

UNIVERSAL EFIMOV PHYSICS IN THREE- AND
FOUR-BODY COLLISIONS

by

YUJUN WANG

B.S., Nanjing University, China, 2002

AN ABSTRACT OF A DISSERTATION

submitted in partial fulfillment of the
requirements for the degree

DOCTOR OF PHILOSOPHY

Department of Physics
College of Arts and Sciences

KANSAS STATE UNIVERSITY

Manhattan, Kansas

2010

Abstract

The Efimov effect plays a central role in few-body systems at ultracold temperature and has thus accelerated a lot of studies on its manifestation in the collisional stability of the quantum degenerate gases. Near broad Feshbach resonances, Efimov physics has been studied both theoretically and experimentally through the *zero-energy* scattering observables. We have extended the theoretical studies of Efimov physics to a much broader extent. In particular, we have investigated the three-body Efimov physics near narrow Feshbach resonances and have also identified the Efimov features beyond the zero temperature limit. We have found, near a narrow Feshbach resonance, the non-trivial contribution from both of the resonance width and the short-range physics to the three-body recombination and vibrational dimer relaxation. Remarkably, the collisional stability of the Feshbach molecules are found to be opposite to that near the broad resonances: an increased stability for molecules made by bosons and a decreased stability for those made by fermions. The universal physics observed near the narrow Feshbach resonances is further found not to be limited to the zero temperature observables. We have found that the general features of Efimov physics and those pertaining to a narrow resonance are manifested in different energy ranges above zero temperature. This opens the opportunity to observe Efimov physics by changing the collisional energy while keeping the atomic interaction fixed. The landscape of the universal Efimov physics is thus delineated in both of the interaction and the energy domain. We have also investigated Efimov physics in heteronuclear four-body systems where the complexity can be reduced by approximations. In particular, we have proposed ways for controllable production of the Efimov tri-atomic molecules by three-body or four-body recombinations involving four atoms. We have also confirmed the existence of four-body Efimov effect in a system of three heavy particles and one light particle, which has resolved a decade-long

controversy on this topic. Finally, we have studied the collisional properties of four identical bosons in 1D, which is important to the experiments on the quantum gases confined in the 1D optical lattices.

UNIVERSAL EFIMOV PHYSICS IN THREE- AND
FOUR-BODY COLLISIONS

by

Yujun Wang

B.S., Nanjing University, China, 2002

A DISSERTATION

submitted in partial fulfillment of the
requirements for the degree

DOCTOR OF PHILOSOPHY

Department of Physics
College of Arts and Sciences

KANSAS STATE UNIVERSITY

Manhattan, Kansas

2010

Approved by:

Major Professor
Dr. Brett D. Esry

Copyright

Yujun Wang

2010

Abstract

The Efimov effect plays a central role in few-body systems at ultracold temperature and has thus accelerated a lot of studies on its manifestation in the collisional stability of the quantum degenerate gases. Near broad Feshbach resonances, Efimov physics has been studied both theoretically and experimentally through the *zero-energy* scattering observables. We have extended the theoretical studies of Efimov physics to a much broader extent. In particular, we have investigated the three-body Efimov physics near narrow Feshbach resonances and have also identified the Efimov features beyond the zero temperature limit. We have found, near a narrow Feshbach resonance, the non-trivial contribution from both of the resonance width and the short-range physics to the three-body recombination and vibrational dimer relaxation. Remarkably, the collisional stability of the Feshbach molecules are found to be opposite to that near the broad resonances: an increased stability for molecules made by bosons and a decreased stability for those made by fermions. The universal physics observed near the narrow Feshbach resonances is further found not to be limited to the zero temperature observables. We have found that the general features of Efimov physics and those pertaining to a narrow resonance are manifested in different energy ranges above zero temperature. This opens the opportunity to observe Efimov physics by changing the collisional energy while keeping the atomic interaction fixed. The landscape of the universal Efimov physics is thus delineated in both of the interaction and the energy domain. We have also investigated Efimov physics in heteronuclear four-body systems where the complexity can be reduced by approximations. In particular, we have proposed ways for controllable production of the Efimov tri-atomic molecules by three-body or four-body recombinations involving four atoms. We have also confirmed the existence of four-body Efimov effect in a system of three heavy particles and one light particle, which has resolved a decade-long

controversy on this topic. Finally, we have studied the collisional properties of four identical bosons in 1D, which is important to the experiments on the quantum gases confined in the 1D optical lattices.

Table of Contents

Table of Contents	viii
List of Figures	xi
List of Tables	xiv
Acknowledgements	xvi
Dedication	xvii
1 Introduction	1
1.1 Efimov effect in three- and four-body systems	1
1.2 Efimov physics in ultracold atomic gases	6
1.2.1 Efimov physics in Bose gases	7
1.2.2 Efimov physics in Fermi gases	12
1.3 Prologue for the work in this thesis	13
2 Theoretical formulation for few-body scattering	16
2.1 Jacobi vectors	17
2.2 Hyperspherical coordinates	20
2.2.1 Delves' hyperspherical coordinates	22
2.2.2 Democratic hyperspherical coordinates	24
2.3 Adiabatic hyperspherical representation	27
2.3.1 Three-body adiabatic equations in Delves' coordinates	28
2.3.2 Three-body adiabatic equations in Smith-Whitten coordinates	30
2.4 Few-body scattering	31
2.5 Adiabatic potentials	34
2.6 Deriving universal expressions for inelastic rates	38
3 Universal Efimov physics in three-body systems	41
3.1 Ultracold three-body collisions near narrow Feshbach resonances	42
3.1.1 Modeling Feshbach resonances	46
3.1.2 Three-body inelastic processes for identical bosons	48
3.1.3 Three-body relaxation for fermionic system (FFF')	55
3.1.4 Adiabatic potentials with the zero-range potential model	56
3.1.5 Summary	58
3.2 Colliding Bose-Einstein condensates to observe Efimov physics	59
3.2.1 Energy-dependent oscillations in K_3 for $a > 0$	60

3.2.2	Higher partial wave contributions	65
3.2.3	Three-body recombination in BEC collisions	68
3.2.4	A multi-channel approach for recombination at finite energies	70
3.2.5	Summary	74
3.3	Universal three-body physics at finite energy near Feshbach resonances	75
3.3.1	Three-body Efimov resonance at finite energy	76
3.3.2	Energy-dependent oscillations in K_3 for $a < 0$	79
3.3.3	Summary	86
4	Universal Efimov physics in four-body systems	87
4.1	Efimov trimer production via four-body recombination	88
4.1.1	Four-body hyperspherical coordinates	89
4.1.2	Four-body adiabatic potentials	91
4.1.3	Four-body recombination	95
4.1.4	Experimental issues	100
4.1.5	Fermi contact potential in adiabatic hyperspherical representation	101
4.1.6	Summary	103
4.2	Four-body Efimov physics induced by three-body Efimov effect	104
4.2.1	Efimov effect with Born-Oppenheimer approximation	105
4.2.2	$HL + H + H$ recombination	109
4.2.3	Four-body Efimov effect	113
4.2.4	Conclusion	118
4.3	Universal four-body physics in one dimension	120
4.3.1	Definitions for two-body scattering in 1D	122
4.3.2	Four-body hyperspherical coordinates in one dimension	123
4.3.3	Four-body adiabatic hyperspherical potentials in 1D	126
4.3.4	Summary	136
	My Publications	137
	References	138
A	A diabatic picture generated by freezing three-body geometry	161
A.1	Method	163
A.2	Applications	165
A.2.1	Three identical particles	165
A.2.2	Two identical particles	180
A.2.3	Calculating adiabatic potentials	182
A.3	Summary	184
B	Single-channel approach for deriving three-body inelastic rates	186
B.1	Zero-energy recombination ($a < 0$) and relaxation ($a > 0$) for large effective-range	187

B.2	Recombination at finite energies ($a < 0$)	189
C	A multi-channel approach for deriving three-body inelastic rates	190
C.1	General formalism	190
C.2	An analytical model	193

List of Figures

1.1	The Efimov spectrum in a three-body system	3
1.2	The wavefunction for a two-body halo state.	5
1.3	Three-body recombination rates for identical bosons near Feshbach resonances.	9
1.4	Three-body loss rates measured for identical ^7Li near a Feshbach resonance.	9
2.1	The three-body Jacobi vectors.	18
2.2	The four-body Jacobi vectors.	19
2.3	A set of adiabatic hyperspherical potentials.	35
2.4	The adiabatic potential model for three-body recombination when $a < 0$	39
3.1	Schematic potentials for a Feshbach resonance.	46
3.2	Comparison between a Feshbach resonance and a shape resonance.	48
3.3	Ultracold three-body recombination rates ($a > 0$) for identical bosons.	49
3.4	Ultracold three-body recombination rates ($a < 0$) and relaxation rates ($a > 0$) for identical bosons.	51
3.5	Schematic adiabatic hyperspherical potentials near a narrow Feshbach resonance.	52
3.6	Adiabatic hyperspherical potentials near a narrow Feshbach resonance.	53
3.7	Relaxation rates for mixed-spin fermions with $a > 0$ and large $ r_{\text{eff}} $	56
3.8	Schematic potentials and pathways for three-body recombination near zero energy ($a > 0$).	61
3.9	Schematic potentials and pathways for three-body recombination at finite energy ($a > 0$, $J = 0$).	62
3.10	The $J=0$ recombination rate K_3 at finite energies.	64
3.11	Scaled numerical three-body recombination rates $K_3(E)E^2$	66
3.12	The $J = 0^+$ contribution to $K_3(E)E^2$ for Cs+Cs+Li with different scattering length.	67
3.13	Atomic losses during BEC collisions.	70
3.14	Schematic adiabatic hyperspherical potentials in the multi-channel model for $a > 0$	71
3.15	A two-channel calculation of the $J=0$ recombination rate K_3 at finite energies using the multi-channel model ($a > 0$).	73
3.16	The $J=0$ recombination rate K_3 at finite energies calculated by using the multi-channel model ($a > 0$).	74
3.17	Three-body Efimov resonance at finite energy manifested in the adiabatic hyperspherical potentials.	77

3.18	The evolution of an Efimov resonance with a in the three-body recombination probability $P^{(a<0)}(E)$	78
3.19	The resonance structures in $J=0$ recombination rate K_3 at finite energies ($a < 0$).	79
3.20	The three-body recombination probabilities for $a < 0$ near broad Feshbach resonances at finite energies.	81
3.21	The three-body recombination probability for $a < 0$ near narrow Feshbach resonances at finite energies.	82
3.22	The three-body relaxation rate for $a > 0$ near narrow Feshbach resonances at finite energies.	84
4.1	The “K”-type Jacobi vectors for $A + A + A + B$ system.	91
4.2	The lowest four-body adiabatic hyperspherical potentials W_ν	96
4.3	The recombination probability for several transitions.	99
4.4	The recombination rates K_3 for the process $HL + H + H \rightarrow HHL + H$ when $M/m = 30$	110
4.5	The schematic effective hyperspherical adiabatic potentials W_ν for $a_{HH}^* \gg a_{HL} \gg r_0$	111
4.6	The recombination rates K_3 for the process $HL + H + H \rightarrow HHL + H$ with $M/m=50$	114
4.7	The lowest three-body continuum adiabatic hyperspherical potential for HHL with different mass ratios.	115
4.8	Schematic Efimov energy spectrum for $HHHL$ four-body system.	117
4.9	The collisional relaxation rates V_{rel} for $(\text{Cs}_2^-)^* + \text{Cs} \rightarrow \text{Cs}_2^- + \text{Cs}$	118
4.10	The “H-type” Jacobi vectors in one dimension.	124
4.11	The two-body coalescence lines ($r_{ij} = 0$) on the hyperangular plane for four particles in 1D.	127
4.12	Avoided crossings in the four-body adiabatic hyperspherical potentials of the three- and four-body continuum channels.	129
4.13	Four-body adiabatic potentials for the dimer-dimer and atom-trimer channels with one two-body bound state.	131
4.14	The comparison between numerically calculated few-body binding energies and the analytical prediction.	133
4.15	The non-adiabatic couplings between the weakly-bound dimer-dimer and atom-trimer channels.	134
4.16	The four-body adiabatic potentials with both weakly-bound and a deeply-bound two-body subsystems.	135
A.1	The shape-diabatic potentials and the adiabatic potentials	166
A.2	Hyperangular wave-functions in shape-diabatic representation.	167
A.3	The diagonal couplings in shape-diabatic representation.	168
A.4	The couplings between the bound channel and continuum channels.	169
A.5	The off-diagonal couplings between the continuum channels.	170

A.6	The shape-diabatic potentials the adiabatic potentials for systems with high angular momentum bound states.	171
A.7	The couplings in the shape-diabatic representation and adiabatic representation.	172
A.8	The diabatic and adiabatic couplings for the channels near a crossing.	173
A.9	Diabatic hyperangular wave-functions.	174
A.10	The shape-diabatic potentials and adiabatic potentials with large scattering length.	175
A.11	The lowest few shape-diabatic potentials and adiabatic potentials for systems with short-range repulsions.	176
A.12	Diabatic hyperangular wave-functions.	177
A.13	The couplings in the shape diabatic representation.	178
A.14	The couplings in the shape diabatic representation.	179
A.15	The diabatic hyperangular wave-functions.	180
A.16	The “ θ -potentials” $u_\lambda(R, \theta)$ at $R = 40$ a.u..	181
A.17	The diabatic hyperangular channel function.	181

List of Tables

2.1	Transformation effect of the permutation operators in Smith-Whitten hyperspherical coordinates.	30
3.1	Effective-range for some selected Feshbach resonances.	44
4.1	Universal coefficients $c_{\nu,\nu'}$ for non-adiabatic couplings $P_{\nu,\nu'}$	95
A.1	The lowest three adiabatic potential energies calculated at $R = 10$ a.u.. . .	183
A.2	The lowest three adiabatic potential energies calculated at $R = 100$ a.u.. . .	183
A.3	The lowest three adiabatic potential energies calculated at $R = 500$ a.u.. . .	184
C.1	Universal coefficients $c_{\nu,\nu'}$ for non-adiabatic couplings $P_{\nu,\nu'}$	195

Acknowledgments

First and foremost, I would like to sincerely thank my advisor Dr. Brett Esry for his guidance and support all through my Ph.D. study. Beginning from the first lecture I have attended in his class, Brett has helped me build a lot of insights in physics, particularly in quantum scattering. Thanks to his patience and “hand-in-hand” directions, I have been able to make fruitful progress in my Ph.D. research. The knowledge I have learned from Brett is certainly not limited to academic area. He has helped me understand how to manage time wisely and collaborate with other people efficiently. This valuable experience will be very helpful for my future life.

During my stay in our research group, I have also been benefited greatly from other group members. The one on the top of the list is Dr. Jose D’Incao, who gave me a nice introduction to the study of few-body physics when I first joined the group. Let alone the help he has offered during the collaborations, I have learned from him to use simple pathway analysis to get quantitative results for quantum scattering, which has been one of the most valuable tools for my research.

Next I would like to thank our group members Dr. Blake Liang and Dr. Jesus Hernández. The discussions we had have helped me make clear a lot of detailed questions in research. I am also thankful for their kind help on reading my thesis. The final version of this thesis has been improved significantly by incorporating their suggestions and comments.

In the following I want to give my appreciation to those who have been helpful for some particular research projects. I am grateful to Dr. Javier von Stecher and Dr. Chris Greene from JILA for the discussions on four-body Efimov effect. And I want to thank Dr. Deote Blume from University of Washington for the discussions on one-dimensional few-body systems. Also, I want to acknowledge Dr. Christophe Näegerl from Innsbruck for his brilliant idea on using BEC collisions to observe Efimov features.

Finally, I want to express my deep gratitude to people who have given me the most

important support in my life. First I want to thank my wife, Jie Chen, who has been along with me through my Ph.D. study. Among all these years, she has given me full support so that I can focus on my work and still have a nice family life. The achievement I have today is made together with her effort. Next I want to thank my parents, especially for their effort in the eariler years in preparing me for getting through difficulties. They are always standing beside me whenever I need their help.

Dedication

To my beloved wife Jie and my respectable parents

Chapter 1

Introduction

1.1 Efimov effect in three- and four-body systems

The Efimov effect is one of the most bizarre few-body phenomena in the quantum world, where the two-body subsystem cannot be bound without the existence of the third particle. More counterintuitively, the Efimov effect is exhibited as an infinite number of three-body bound states when the two-body subsystems have a *zero-energy* bound state and any further increase of the interactions will only result in a *decrease* of three-body bound states to a finite number.

The studies on Efimov physics can be traced back to the seminal work by nuclear physicist Vitaly Efimov [12] in the 1970's. By using the zero-range potential model [13], he solved the Faddeev equation [14] in hyperspherical coordinates [15, 16] analytically, and found a long-range effective three-body interaction which can support an infinite number of bound states when the two-body subsystems have zero-energy bound states. Limited by the computational capacity at that time, numerically solving the three-body Schrödinger equation was formidable, and the existence of the Efimov effect was difficult to confirm. Furthermore, in the context of nuclear physics, experimental observation of the Efimov effect has been more elusive since the interactions between the elementary particles are fixed by nature and a coincidence of zero binding energy is quite unlikely.

The binding energy for two particles E_{2b} is connected to their low-energy scattering

properties when E_{2b} is much smaller than the “natural” energy scale of an interaction, $1/\mu_2 r_0^2$, where μ_2 is the two-body reduced mass and r_0 is the characteristic size of the short-range interaction. In particular, E_{2b} is related to the s -wave scattering length a by $E_{2b} = \hbar^2/2\mu_2 a^2$, where a is defined through the scattering phase shift $\delta(k)$ as

$$a = -\lim_{k \rightarrow 0} \frac{\tan \delta(k)}{k}, \quad (1.1)$$

where $k = \sqrt{2\mu_2 E/\hbar^2}$ is the incident wave number, E is the asymptotic scattering energy and μ_2 is the two-body reduced mass. Physically, the scattering length is a better measure for the Efimov effect than E_{2b} , because more detailed study shows the Efimov effect can be considered as a consequence of the long-range correlations between the pairs when $|a|$ is large [17]. The scattering length a changes from $-\infty$ to $+\infty$ when a two-body state changes from unbound to weakly-bound. The Efimov bound states formed when a is negatively large are called “Borromean” states [18], and are of particular interest due to the fact that none of the two-body subsystems can be bound.

As $|a|$ increases, the number of three-body bound states increases and their energies E_n form a geometric series:

$$E_n = E_0 e^{-2\pi n/s_0}, \quad (n = 0, 1, 2, \dots) \quad (1.2)$$

where the ground state energy E_0 depends on the details of the three-body interactions at short range, and s_0 is a universal constant determined only by the identical particle symmetry and the mass ratio of the three particles. For identical bosons, $s_0 \approx 1.00624$. The maximum value of n is determined by $|a|$ through

$$n_{max} \approx \left\lfloor \frac{s_0}{\pi} \ln(|a|/r_0) \right\rfloor. \quad (1.3)$$

Figure 1.1 shows a sketch of the three-body Efimov bound state spectrum. On the left part of the figure when $a < 0$, three-body Efimov states emerge from the three-body continuum as $1/a$ gets closer to zero. It is interesting to notice that these three-body Efimov states will break when any of the particles are removed from the system. The particles in

such states are highly correlated [18]. On the right part of the figure the Efimov states disappear into the two-body break-up continuum as $1/a$ increases further.

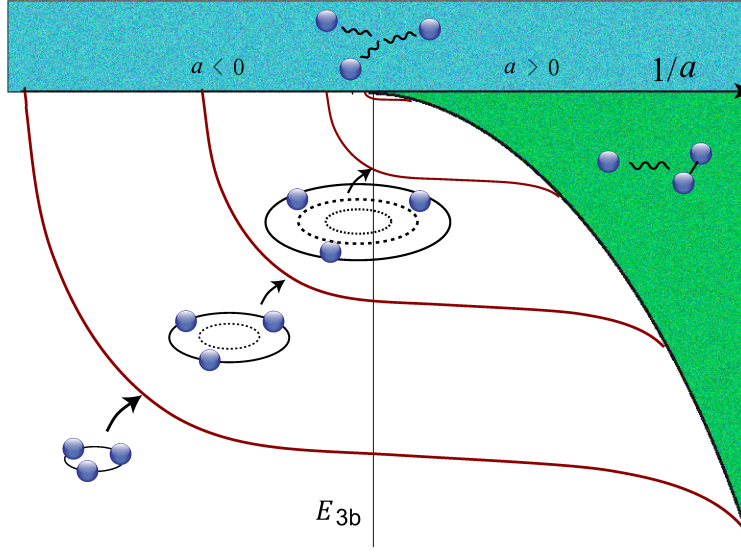


Figure 1.1: The Efimov spectrum in a three-body system. On the negative side of a where weakly-bound two-body state does not exist, three-body Efimov bound states are born directly from the three-body continuum (top blue region) as $|a|$ increases. Infinite number of these states accumulate at $a = \infty$. At positive side of $1/a$ where a weakly-bound two-body state exists, the Efimov trimer states merge into the atom-dimer continuum as a decreases.

There is another bizarre three-body phenomenon which has close relationship with the Efimov effect, which is called Thomas collapse [19]. Compared to the Efimov effect where $|a|$ is taken to the limit of infinity while r_0 is fixed, the Thomas collapse is manifested by taking the opposite limit: for fixed scattering length a , when r_0 decreases the three-body energy spectrum scales as Eq. (1.2), except that the value of n takes $0, -1, -2, \dots$ and E_0 becomes the upper bound of the bound state energies. Thus in the limit $r_0 \rightarrow 0$, a three-body system with finite two-body binding energies, does not have a lower bound in the three-body energy. Since the deeper the energy the smaller the size of the bound state, the three-body system seeking the lowest bound state is expected to collapse to the center, giving rise to the Thomas collapse. Interestingly, in classical mechanics the collapse of an orbital occurs in the case of two particles interacting via an attractive $1/r^2$ potential when

the interaction strength is stronger than the centrifugal potential [20], where r is the inter-particle distance. In fact, as will be discussed in the next chapter, the Efimov effect and the Thomas collapse share the similar physical origin: the “effective” three-body interaction behaves attractively like $1/R^2$, where R is hyperradius [15, 16] which represents the overall size of a three-body system.

The strangeness of the Efimov effect also rises from the way our world is setup by nature. For three identical bosons, the Efimov effect only occurs in the spatial dimension d to be within $2.3 < d < 3.8$ [21]. For systems with unequal masses, the lower and upper limits for the dimensional requirement change, but $d=3$ is the only integer number for the Efimov effect to occur [21].

In addition to the requirement of the spatial dimensionality, it is interesting to investigate the possibility of the Efimov effect in a system with more than three particles. In analogy with the three-body case, the existence of the N -body Efimov effect is tested when a zero-energy $(N - 1)$ -body bound state is formed. For $N = 4$, for instance, the above definition implies that the four-body Efimov effect is completely independent of the three-body one since the two-body scattering length is not required to be large. It turns out for identical particles, the Efimov effect is always absent if the number of particles is beyond three [22]. For a system of particles with unequal masses this question is not well understood. In particular, for a four-body system of three identical heavy particles (H) and one light particle (L), there has been a controversy about the existence of the four-body Efimov effect in the previous studies [23, 24]. But as will be discussed in Sec. 4.2, we have confirmed the existence of the Efimov effect in such a four-body system by numerical calculations. For the first time we give an estimate on the number of four-body Efimov states for finite mass ratios.

Because of the fundamental interest in the Efimov effect, people have made a great effort to identify the possible Efimov states formed in nuclear and atomic systems. One of the most concrete pieces of evidence for the Efimov states is that the spacing between the bound

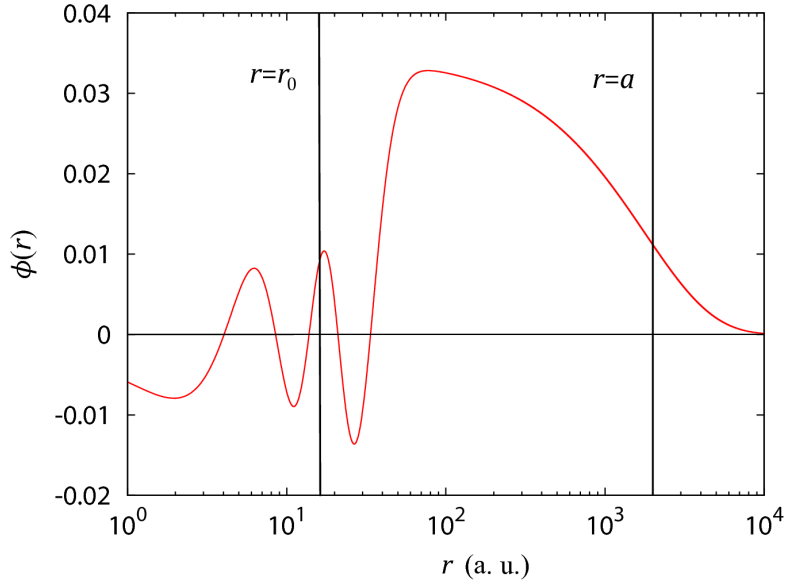


Figure 1.2: The wavefunction for a two-body halo state. The wavefunction has large amplitude outside the interaction region $r \approx r_0$, and falls off exponentially only when the distance is beyond the scattering length a .

state energies follows the prediction from Eq. (1.2). However, the existence of at least one excited Efimov state is necessary, which typically requires $|a|$ to be a few hundred times larger than r_0 . A coincidence of such large scattering length by nature is quite unlikely. In nuclear systems quantum “halo” states whose wavefunctions have a large amplitude in the classically forbidden region as shown in Fig. 1.2, are more frequently found [18]. One example is the ^{11}Li nucleus, which is formed by a ^9Li core surrounded by two far away neutrons [18]. The Efimov states can be viewed as an extreme case of the halo states. The studies of these “halo” nuclei can thus provide understanding for the Efimov states. In atomic systems, people have found that the ^4He trimers are probably the best candidates for the Efimov states [25–30]. Specifically, the only two trimer states in this system have energy spacing close to the expected spacing for Efimov states [25–30].

1.2 Efimov physics in ultracold atomic gases

The development of experimental techniques for cooling atoms into the nano-Kelvin regime [31] has not only successfully led to the realization of Bose-Einstein condensates (BEC) [31–33] and the degenerate Fermi gases, but also opened the great opportunity for the studies of various few- and many-body quantum phenomena.

In studies of many-body physics, for instance, the coherence of the matter wave for a BEC can be used to build interferometers for high precision measurements. For degenerate Fermi gases, a lot of effort has been made toward the understanding of superfluidity [34–37], the energy spectra in the strong interaction regime [35, 38, 39] and the behavior of the many-body system for the BCS-BEC crossover [34]. Weakly-bound diatomic Feshbach “halo” molecules have also been observed [40], and their dynamics probed [41]. In these studies, the strongly interacting systems are especially of interest since the systems are far from the perturbative regime and novel physical behaviors are expected.

In ultracold gases, the interactions are characterized by the two-body scattering length a . With the fast development in recent years, experimentalists are able to tune the scattering length through a huge range of values by use of Feshbach resonances [42, 43]. The atomic system can be easily changed from the weakly interacting regime ($|a| \rightarrow 0$) to the strongly interacting regime ($|a| \rightarrow \infty$).

In the strong interaction regime where $|a|$ is large, Efimov physics comes into play and it can have a significant effect on experimental studies, especially in systems of identical bosons. Near a Feshbach resonance, Efimov physics plays a central role in the stability of atomic components, and weakly-bound molecules in ultracold gases. In ultracold experiments, the loss of atoms in an ultracold gas sample can be reduced to a low level for “one-body” losses [44] with the rates directly proportional to the atomic density n . Such losses are typically caused by a collision with a “hot” particle in the background of the vacuum chamber. Two-body losses occur when two atoms undergo inelastic collisions. The corresponding two-body loss rates are proportional to n^2 . Since the ultracold atomic gases

are very dilute, two-body losses are more likely than one-body losses. These collisions will usually release binding energy and change the internal state of the atoms. The released energy is typically much higher than the trapping potential such that the colliding atoms stop being trapped. But, such losses can be avoided by simply preparing the atomic sample in the ground hyperfine state so that all the energy-releasing two-body inelastic processes are energetically forbidden.

1.2.1 Efimov physics in Bose gases

For bosonic atomic gases, it has been observed that three-body inelastic collisions can lead to huge trap losses near a Feshbach resonance [45–47]. For instance, when $a > 0$ such that atoms can form a highly-excited weakly-bound dimer state A_2^* , the stability of an atomic gas sample is mainly determined by three-body recombination $A+A+A \rightarrow A_2^*+A$. The stability of a molecular gas sample in an atomic bath for the case $a > 0$ is predominantly determined by three-body vibrational relaxation $A_2^*+A \rightarrow A_2+A$, where A_2 represents any of the deeply-bound dimer states. When $a < 0$, only deeply bound dimer states exist, but three-body recombination, $A+A+A \rightarrow A_2+A$, can still lead to a tremendous loss of atoms. The stability of the deeply-bound diatomic molecules A_2 , however, does not have a dramatic change near a Feshbach resonance.

If the loss of atoms is dependent on three-body recombination, for identical bosonic atoms, the density of atoms remaining in the trap is determined by the rate equation:

$$\frac{dn}{dt} = -\frac{3}{3!}K_3n^3, \quad (1.4)$$

where n is the atomic density, K_3 is the rate of the recombination. In the equation above the factor of 3 in the numerator comes from the assumption that all three atoms involved in the recombination event are finally lost. The factor of 3! in the denominator comes from the statistics of the identical bosons when they are in a quantum degenerate state (BEC) [48]. Note that the identical particles here require not only being the same atomic isotope, but also being in the same internal quantum state.

Near a Feshbach resonance, the rate constant K_3 increases sharply, and both theoretical [49–52] and experimental [45, 46] studies show that K_3 follows an overall a^4 scaling. The strong dependence of K_3 on the two-body scattering length a turns out to have a close relationship with the Efimov effect. This connection also celebrates the analytically derived [52, 53], universal formulae for the rate constant near zero temperature:

$$K_3 = 67.1e^{-2\eta} \left(\sin^2[s_0 \ln \frac{a}{r_0} + \Phi] + \sinh^2 \eta \right) \frac{\hbar}{m} a^4, \quad (1.5)$$

for $a > 0$ and

$$K_3 = \frac{4590 \sinh 2\eta}{\sin^2[s_0 \ln(|a|/r_0) + \Phi + 1.53] + \sinh^2 \eta} \frac{\hbar}{m} a^4 \quad (1.6)$$

for $a < 0$. In these equations, r_0 represents the characteristic size of the short-range atomic interactions and m is the atomic mass. Remarkably, the overall behavior of K_3 is determined only by a , while all the complicated atomic interactions at small distances are condensed in the two short-range parameters Φ and η [52, 53]. The parameter Φ is related to the phase of the three-body wavefunction when the three atoms are close together at the distance of r_0 . This parameter is sensitive to the details of the atomic interactions and thus can change dramatically for different atomic species. It can also change across different Feshbach resonances [53]. The other parameter η characterizes the probability for a three-body inelastic process, which have the final products of a free atom and a deeply-bound diatomic molecule [52, 53]. As observed in the experiments [54–57], the parameter η is typically smaller than unity and is on the order of 0.1.

The behavior of the recombination rates K_3 in Eq. (1.5) and Eq. (1.6) is shown in Fig. 1.3. One experimental observation of such behavior can be seen in Fig. 1.4, where the loss rate L_3 due to three-body recombination is shown. The experimental data (symbols) have good agreement with the theoretical prediction (solid black lines) except for very large $|a|$, where the temperature of the atomic gas in the experiment is beyond the zero-energy threshold for the theoretical prediction to be valid [53, 58]. A clear attribute in the recombination rate is logarithmically separated features, characterized by a series of minima for $a > 0$

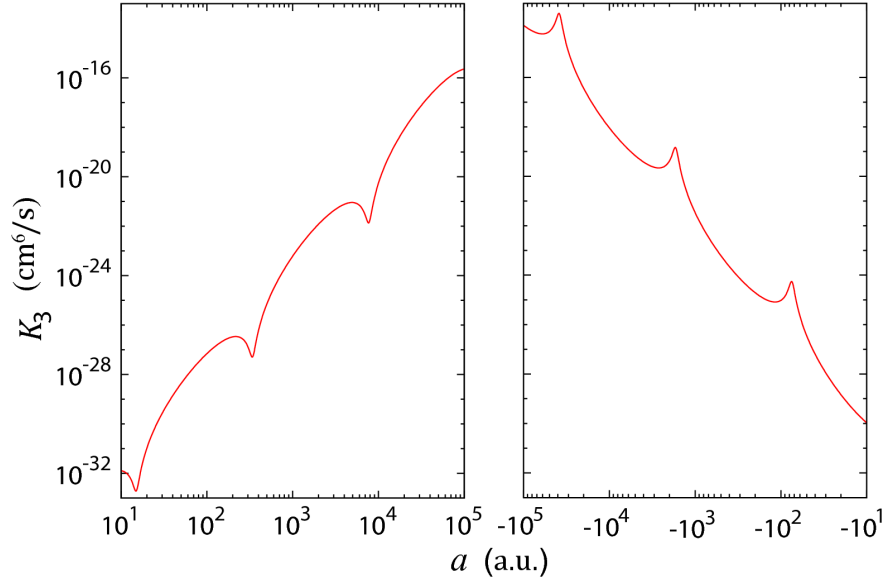


Figure 1.3: Three-body recombination rates for identical bosons near Feshbach resonances. The parameters for Eq. (1.5) and (1.6) are $\Phi = 0$, $r_0 = 15$ a.u. and $\eta = 0.07$. The value of r_0 and η are taken to be close to experimental data [54, 57].

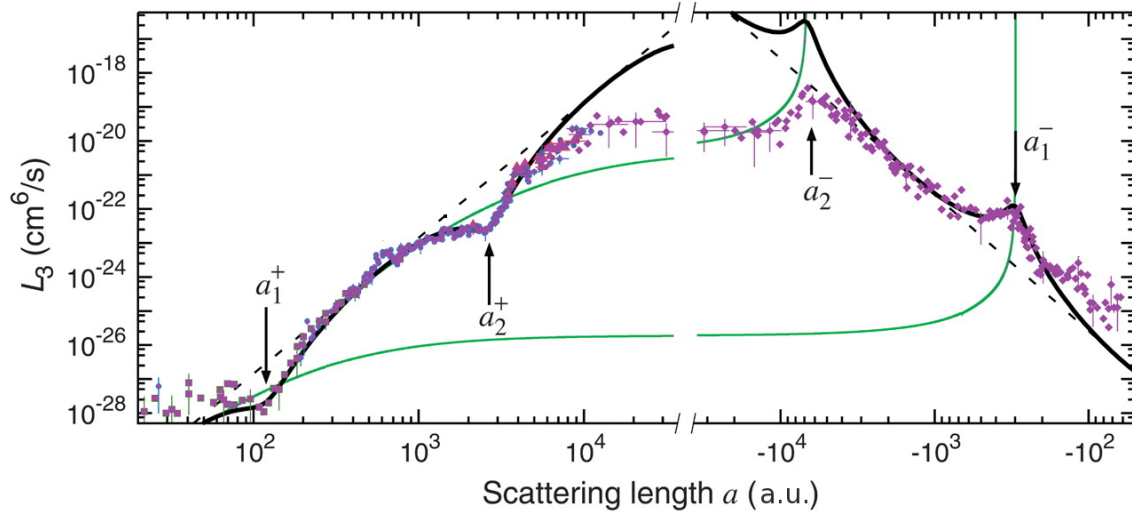


Figure 1.4: Three-body loss rates for identical ${}^7\text{Li}$ measured near the Feshbach resonance located at 737 G. The symbols are from experimental data, and the solid black curves are fits from Eq. 1.5 and 1.6. The green curves indicate the square of the energies of the Efimov trimers, as introduced in Figure 1.1. Figure is adapted from Ref. [57].

and a series of peaks for $a < 0$. As the same scaling behavior is also observed in Eq. (1.2) for the energies of the Efimov states, one may readily speculate the relationship between the behavior of the recombination rates and the Efimov states formed near a Feshbach resonance. In fact, as will be presented in Chap. 2, the minima for $a > 0$ can be understood by the interference effect of two recombination pathways in the presence of the Efimov effect. The peaks for $a < 0$ have a more direct connection to the Efimov effect: they correspond to three-body shape resonances as three-body Efimov bound states form. In particular, these peaks appear exactly at the scattering lengths where the energies of the Efimov states pass across the three-body break-up threshold, as shown in Fig. 1.1.

One of the most striking features in Eq. (1.5) and (1.6) is the universality. For any three-body systems interacting via short-range interactions, Eq. (1.5) and (1.6) always hold as long as $|a|$ is the largest length scale in the system which typically means $|a| \gg r_0$. This is especially surprising considering the complexity of the short-range interactions between the atoms from effects like electron polarization, electron and nucleus exchange, spin-spin interaction, etc. In fact, not limited to the recombination rates for identical bosons, universal behavior is seen in various scattering length scaling laws for three-body inelastic rates. Once these scalings laws are identified, they can be directly applied in other fields like nuclear physics or chemistry.

Though three-body recombination mostly leads to huge loss near Feshbach resonances and is thus the process people try to avoid in the ultracold experiments, it is nevertheless the “smoking gun” for observing the Efimov effect. In fact, the first experimental evidence [54] of the Efimov effect was from the first resonant peak as predicted in Fig. 1.3 when a is tuned from 0 to $-\infty$.

In ultracold experiments, as the Feshbach resonance is scanned from the negative side to the positive side of a , a weakly-bound Feshbach diatomic molecule is formed with size of a . These newly formed molecules in the atomic bath undergo collisions with free atoms and inelastic transitions occur when these weakly-bound molecules in a highly-excited vibrational

state relax into deeply-bound lower vibrational states. Energy conservation requires the released binding energy from the molecule to go to the kinetic energy of the relative motion between the molecule and the free atom involved in the collision, and both of them are lost from the trap. For identical bosons, the rate of the relaxation process near zero temperature is determined by [52]:

$$V_{\text{rel}} = \frac{20.1 \sinh 2\eta}{\sin^2[s_0 \ln(a/r_0) + \Phi + 1.47] + \sinh^2 \eta} \frac{\hbar}{m} a, \quad (1.7)$$

with the parameters defined the same as for the three-body recombination.

The behavior of V_{rel} in Eq. (1.7) is similar to that of K_3 for $a < 0$, as observed in Eq. (1.6). They both feature a series of logarithmically separated peaks, but the overall scaling of the rate with a is only linear. Also, the peaks in V_{rel} have a similar origin as those in K_3 , they appear at the scattering length when an atom and a dimer can form a barely-bound Efimov state. This occurs in Fig. 1.1 when the energies of the Efimov states merge into the atom-dimer continuum. The difference is that for $a < 0$ Efimov states are formed near the three-body break-up threshold while for $a > 0$ Efimov states are formed near the atom-dimer threshold and consequently lead to a diverging atom-dimer scattering length. These physical properties can be more intuitively understood when we introduce the hyperspherical framework in Chap. 2.

The resonantly increasing relaxation rate with increasing scattering length leads to huge trap losses of the of the weakly-bound molecules produced near Feshbach resonances. Though troublesome for the studies of the molecules, it offers an alternative way for observing the Efimov effect, as reported in Ref. [55].

The experimental signatures of the Efimov effect are not limited to the three-body processes mentioned above. The legacy of the three-body Efimov effect has been predicted [59] and observed [57, 60] in the loss signatures of the atoms by four-body recombinations. These signatures are the manifestation of four-body resonances attached to three-body Efimov states. Interestingly, there are always two of such resonant states for each of Efimov state [59], giving rise to two sub-peaks in the loss signal on top of each of the main peaks

observed in Eq. (1.6) [57, 60].

The experimental manifestations of the three-body Efimov effect discussed thus far are for identical bosons. The Efimov effect is altered, in a universal way, when the three-body system includes non-identical particles. It is difficult to obtain large scattering lengths for three pairs independently for non-identical interactions. If two of the particles are identical bosons, and the third particle has a large scattering length with each of them, the Efimov effect shows up and all the three-body inelastic rates are essentially the same as for three identical bosons. The important universal constant s_0 , which determines the ratio of the consecutive Efimov bound state energies and the period of the logarithmically separated features in inelastic rates, increases as the mass ratio between the bosons and the third particle increases. The observation of the Efimov effect is thus favored in the three-body system of two heavy atoms and one light atom where the period in the rates is small.

If there is only one large scattering length in the three-body system, the Efimov effect does not occur and the three-body inelastic rates do not have log-periodic features near Feshbach resonances [61]. However, the rates still have universal scaling with the scattering length. The three-body relaxation rate of the Feshbach molecules is actually suppressed, and scales like $1/a$ [61].

1.2.2 Efimov physics in Fermi gases

As mentioned previously, the occurrence of the Efimov effect also depends on identical particle symmetry. When there are at least two identical fermions, the three-body recombination rates in the zero temperature limit vanish due to Fermi statistics. Fermi gases of different spin mixtures have been studied intensively in recent years due to the close relationship to the study of the superfluidity and superconductivity [34]. In these experiments, the scattering length between dissimilar fermions are typically tuned large to get to the strongly interacting regime. The stability of the gas sample under such conditions is determined by the universal scaling of the three-body collisions with two identical fermions and another

fermion from the same isotope but in a different hyperfine state.

A large scattering length between fermionic atoms in different hyperfine states can be achieved by a Feshbach resonance [43]. The three-body relaxation of Feshbach molecules in the presence of an atom in either of the hyperfine states is suppressed by the large scattering length as $1/a^{3.33}$ [62]. Though the Feshbach molecules are composite bosons, so that they do not have Pauli blocking when they are considered as single particles, the collisional relaxation rate of two such molecules is nevertheless suppressed as $1/a^{3.2}$ when the four-body nature of the collision is considered [63]. These molecules are thus stable under various collisions so that further studies involving Feshbach resonances, such as the BCS-BEC crossover [34] and the production of the ultracold molecule in the absolute ground state [64, 65], are greatly facilitated.

The universal scalings of three- and four-body inelastic processes for all combinations of particles described above can be understood by the same physics as the three-body Efimov effect. A comprehensive list of scaling laws for the corresponding rates has been compiled in Ref. [66, 67]. The extent of Efimov physics, however, is far from being exhausted. In fact, more interesting scattering phenomena related to Efimov physics have recently been identified for both three- [5, 11] and four-body [7][68] systems, and the studies on these systems have been even more active.

1.3 Prologue for the work in this thesis

Before presenting our work for the Efimov-related studies in the few-body systems, I will summarize the contributions I made during my Ph.D. studies.

- Numerical calculation.

In studies of universal physics in few-body systems, I have performed hundreds of three-body scattering calculations to extract the universal behavior and to check the validity of various analytical results. The results of the work will be presented in detail in the following chapters and can also be found in my following works [1, 2, 5, 7, 11].

For a specific atomic system where the two-body spectrum is simple, such as a three-body system comprised of two hydrogen atoms and one alkali atom, I have performed large-scale computations up to 50,000 CPU hours to calculate various three-body scattering observables, where the majority of the computational power was used to solve generalized eigenvalue problem of banded matrix with order about 10^5 and band about 2500. The eigenvalue problem comes from solving a set of coupled 2D differential equations in B-spline basis, as will be discussed in detail in Section 2.3.

- Analytical expression.

Based on the universal scaling behavior generalized from the numerical studies, I have set up simple models to derive analytical expressions for various few-body scattering observables. This analytical work not only gives the correct scaling laws in the universal regime but also provide deep insight on the physical mechanisms which led to these scaling laws. I will present these expressions in the following chapters and will explain their derivation in Appendix B and C. They can also be found in my works [2, 5, 7, 10, 11].

- Numerical methods and algorithmic development.

To handle the numerical difficulty of sharp curve crossings in adiabatic representations [69], and large dimensionality involved with going toward the few-body systems with more particles, I have developed *diabatic* representations for solving the few-body Schrödinger equation. They will be presented in Sec. 4.1.2 and in Appendix A. They can also be found in the following works [3, 10].

- Spanning field study.

The methods we use in few-body scattering do not only pertain to the world of ultra-cold temperatures. I have studied the properties of a hydrogen atom in the presence of an intense laser field by using adiabatic Floquet representation [70] and a curve crossing model [71], which can be found in the work [6].

In the following parts of my thesis, I will present the progress we have made on Efimov physics in three- and four-body systems. These studies have benefited from the universal property of the Efimov physics, where general features in the inelastic processes are predominantly determined by a and the fact that non-universal short-range physics, no matter how complicated it could be, only contributes to only one or two parameters in the rate expressions. Specifically, this allows us to use convenient model potentials to mimic atomic interactions, which greatly simplifies our numerical calculations and the analyses as the realistic atomic interactions in the ultracold experiments are of a multi-channel nature with at least hundreds of two-body ro-vibrational bound states. The model potentials used in our calculations, however, are single-channel and have only a few two-body bound states, which makes the three-body calculations much easier.

Chapter 2

Theoretical formulation for few-body scattering

The few-body problem has been of people's interest since the era of Newtonian mechanics. In fact, after the two-body problem was solved by Newton in the seventeenth century [72], people have made a great effort to find a general solution for the three-body problem, but only realized that this is impossible after nearly three hundred years, as three-body systems usually exhibit chaotic behavior [73]. Nevertheless, studies on three-body problems have high priority in basic scientific research especially in astrophysics. For instance, people have worried about the collapse of celestial bodies interacting with gravitational force in a system of more than two celestial bodies. This concern comes from the fact that the energy of a classical three-body system is not discretized so that one of the bodies can continuously take away binding energy and make the other two finally collapse on each other. Fortunately, in most celestial systems two-body motion contributes dominantly to the dynamics of the whole system while the effect of a third or further bodies can be treated perturbatively. The inter-celestial trajectory in such systems are typically stable.

In the microscopic world such as atoms and molecules however, few-body dynamics are typically non-perturbative and the classical orbitals are mostly unstable. But the situation changes fundamentally in the quantum mechanical world. The quantization of the two most important physical observables: energy and angular momentum lead to stable steady

states for the few-body system under certain circumstances. More importantly, significant progress has been made in three-body [50–52, 66, 74] and four-body [10][59, 63, 68] scattering processes especially under ultracold temperatures.

To solve the few-body scattering problem, one needs to solve the few-body Schrödinger equation and get the corresponding scattering wave-function. There are different ways to achieve this. For instance, instead of solving the Schrödinger equation directly one can solve the Faddeev-Yakubovski equations [14] or Alt-Grassberger-Sandhas (AGS) equations [75]. The benefit of solving these equations is that numerically they better treat the disconnected amplitudes for various fragmentation configurations in the total wavefunction. However, spurious solutions can appear and numerical calculations can be inefficient due to the transformation from one fragmentation configuration to another.

2.1 Jacobi vectors

In our numerical studies, we solve the few-body Schrödinger equation directly. For particles in free space, total linear and angular momentum are conserved. The center of mass motion can be separated out by transforming the position vectors of the particles into Jacobi vectors [15, 16]. The Jacobi vectors are essentially built by connecting the positions of the particles and the centers of mass. These vectors are then scaled by mass factors for further convenience. For a three-body system with masses m_i ($i=1, 2, 3$), there are three different choices of mass-scaled Jacobi vectors, defined by:

$$\vec{\rho}_{ij} = \sqrt{\frac{\mu_{ij}}{\mu_3}}(\vec{r}_i - \vec{r}_j), \quad (2.1)$$

$$\vec{\rho}_{ij,k} = \sqrt{\frac{\mu_{ij,k}}{\mu_3}}\left(\vec{r}_k - \frac{\vec{r}_i + \vec{r}_j}{2}\right), \quad (2.2)$$

where \vec{r}_i ($i=1, 2, 3$) are the lab-frame position vectors. The three-body reduced mass μ_3 is defined as:

$$\mu_3 = \left(\frac{m_1 m_2 m_3}{m_1 + m_2 + m_3}\right)^{\frac{1}{2}}, \quad (2.3)$$

and the reduced masses μ_{ij} , $\mu_{ij,k}$ are defined by

$$\mu_{ij} = \frac{m_i m_j}{m_i + m_j}, \quad \mu_{ij,k} = \frac{m_k (m_i + m_j)}{m_i + m_j + m_k}. \quad (2.4)$$

An illustration of the three-body Jacobi vectors is shown in Fig. 2.1 All three choices of Jacobi vectors are equivalent: they can be transformed to each other by kinematic rotations [76]. In numerical calculations, selecting one particular set of Jacobi vectors can be more convenient for calculating the asymptotic wavefunction when the three-body system breaks up into a $A_2 + A$ configuration where the two-body composite A_2' is connected directly by one of the Jacobi vectors.

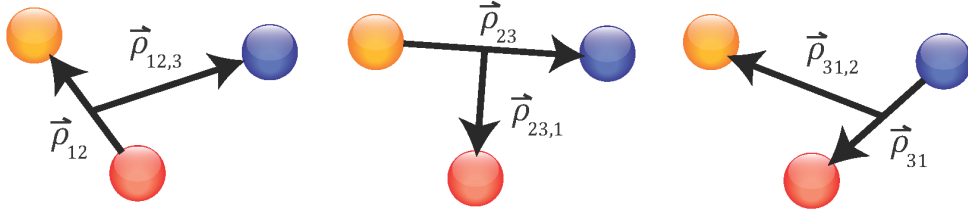


Figure 2.1: The three-body Jacobi vectors.

For a four-body system, there are 18 different definitions of mass-scaled Jacobi vectors. They can be categorized, however, into two groups. One is the so-called ‘‘K-type’’, as defined by

$$\vec{\rho}_{ij} = \sqrt{\frac{\mu_{ij}}{\mu_4}} (\vec{r}_i - \vec{r}_j), \quad (2.5)$$

$$\vec{\rho}_{ij,k} = \sqrt{\frac{\mu_{ij,k}}{\mu_4}} \left(\vec{r}_k - \frac{\vec{r}_i + \vec{r}_j}{2} \right), \quad (2.6)$$

$$\vec{\rho}_{ijk,l} = \sqrt{\frac{\mu_{ijk,l}}{\mu_4}} \left(\vec{r}_l - \frac{\vec{r}_i + \vec{r}_j + \vec{r}_k}{2} \right), \quad (2.7)$$

where $\mu_{ijk,l}$ is the reduced mass between particle l and the other three bodies:

$$\mu_{ijk,l} = \frac{m_l (m_i + m_j + m_k)}{m_i + m_j + m_k + m_l}. \quad (2.8)$$

The four-body reduced mass μ_4 is defined as

$$\mu_4 = \left(\frac{m_1 m_2 m_3 m_4}{m_1 + m_2 + m_3 + m_4} \right)^{\frac{1}{3}}. \quad (2.9)$$

Another group, called ‘‘H-type’’, is constructed by connecting two pairs of particles first and then the center of mass for each pair, and is defined as

$$\vec{\rho}_{ij} = \sqrt{\frac{\mu_{ij}}{\mu_4}}(\vec{r}_i - \vec{r}_j), \quad (2.10)$$

$$\vec{\rho}_{kl} = \sqrt{\frac{\mu_{kl}}{\mu_4}}(\vec{r}_k - \vec{r}_l), \quad (2.11)$$

$$\vec{\rho}_{ij,kl} = \sqrt{\frac{\mu_{ij,kl}}{\mu_4}}\left(\frac{\vec{r}_i + \vec{r}_j}{2} - \frac{\vec{r}_k + \vec{r}_l}{2}\right), \quad (2.12)$$

where $\mu_{ij,kl}$ is the reduced mass between the pairs:

$$\mu_{ij,kl} = \frac{(m_i + m_j)(m_k + m_l)}{m_i + m_j + m_k + m_l}. \quad (2.13)$$

All other sets of Jacobi vectors within each group can be obtained by permutation of the particles. The sets of Jacobi vectors from different group can only be transformed to each other by kinematic rotations. As shown in Fig. 2.2, the ‘‘K-type’’ vectors are better fitted for describing the $A_3 + A$ break-up, while the ‘‘H-type’’ vectors are expected to give a better treatment of $A_2 + A_2$ break-up.

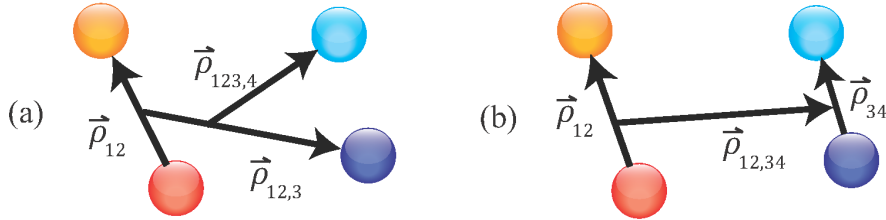


Figure 2.2: The four-body Jacobi vectors of ‘‘K-type’’ (a) and ‘‘H-type’’ (b).

The Jacobi vectors for an N -body system can be defined, in principle, by following the similar procedure of connecting the particles and their center of masses. The N -body reduced mass μ_N can be defined in the way such that the Jacobian has no overall mass factor after the transformation from lab vectors to Jacobi vectors [16]. This leads to

$$\mu_N^{-\frac{N-1}{2}} \left(\prod_{i=2}^N \frac{m_i \sum_{k=1}^{i-1} m_k}{\sum_{j=1}^i m_j} \right)^{\frac{1}{2}} = 1. \quad (2.14)$$

Then μ_N takes the following form which is independent of a specific definition of Jacobi vectors:

$$\mu_N = \left(\prod_{i=1}^N m_i / \sum_{j=1}^N m_j \right)^{\frac{1}{N-1}}. \quad (2.15)$$

2.2 Hyperspherical coordinates

In few-body scattering, different groups of interparticle distances can go to infinity when the system breaks up in various ways. It is numerically inconvenient to deal with more than one coordinate going to infinity and it also requires separate scattering analyses for each of the break-up configurations. However, one can define hyperspherical coordinates [15, 16], as the generalization of spherical coordinates in the two-body case, to represent the break-up of a few-body system by a single coordinate. Hyperspherical coordinates and hyperspherical harmonics were introduced as early as 1935 by Zernike and Brinkman [77]. In the early days when computational capability was very limited, studies on the Schrödinger equation in the hyperspherical coordinates are mostly focused on the transformation properties of the coordinates and the mathematical properties of the hyperspherical harmonics [78, 79].

With the rapid development of computational power, hyperspherical coordinates are being widely adopted in atomic, molecular, and nuclear physics. For instance, in atomic physics hyperspherical coordinates have been used successfully to explain the spectrum of doubly excited states for the He atom and the H^- ion [80]. In molecular physics, hyperspherical coordinates are used to study the ro-vibrational energy spectrum [30, 81, 82] and various scattering processes [83, 84]. The application of hyperspherical coordinates in nuclear physics starts early [15, 16, 21] and is most renowned by studies of halo nuclei [18]. Hyperspherical coordinates have also been widely used in quantum chemistry calculations. For instance, the coordinates have been adopted in calculations for reactive scattering by Launay, *et al.* [85–98], Parker, Pack, *et al.* [99–105]. In addition to the studies of realistic physical systems, hyperspherical coordinates have achieved great success in the study of

universal physics. An approach similar to hyperspherical coordinates had been used for the discovery of the Efimov effect in the early days [12, 106, 107], and different forms of hyperspherical coordinates have been successfully used in studies on the universal scattering properties of the few-body systems in recent years [50, 59, 63, 66, 68, 74].

The coordinate in the hyperspherical coordinates representing break-up is recognized as hyperradius R , defined from the sizes of the mass-scaled Jacobi vectors. Its square is defined by the square sum of all the mass-scaled Jacobi vectors. For instance, for a three-body system it is defined by

$$R^2 = \rho_{ij}^2 + \rho_{ij,k}^2 \quad (2.16)$$

for a three-body system, and defined by

$$R^2 = \rho_{ij}^2 + \rho_{kl}^2 + \rho_{ij,kl}^2 \quad (2.17)$$

for a four-body system if ‘‘H-type’’ Jacobi vectors are used.

One important property of the hyperradius is its invariance under kinematic rotations. This dramatically eases the numerical calculations, as it allows one to use other convenient representations for the remaining degrees of freedom. Since the hyperradius R is invariant, the differences between the hyperspherical representations are contained in the definitions of the hyperangles. Some of these angles describe the spatial rotations and others describe the geometrical configurations. By using a collective coordinate Ω to represent all the hyperangles, the few-body Schrödinger equation takes the following form [108]:

$$\left[-\frac{1}{2\mu_N} \left(\frac{\partial^2}{\partial R^2} + \frac{(N-1)D-1}{R} \frac{\partial}{\partial R} \right) + \frac{\Lambda(\Omega)^2}{2\mu_N R^2} + V(R, \Omega) \right] \Psi = E\Psi, \quad (2.18)$$

where N is the number of particles, D is the spatial dimension and E is the total scattering energy. The first-order hyperradial derivative can be eliminated upon the substitution:

$$\Psi = \sum_{\nu=0}^{\infty} R^{-\frac{(N-1)D-1}{2}} \psi, \quad (2.19)$$

and Eq. (2.20) becomes

$$\left\{ -\frac{1}{2\mu_N} \frac{\partial^2}{\partial R^2} + \frac{\Lambda(\Omega)^2}{2\mu_N R^2} + \frac{[(N-1)D-1][(N-1)D-3]}{8\mu_N R^2} + V(R, \Omega) \right\} \psi = E\psi. \quad (2.20)$$

The square of the generalized angular momentum operator Λ^2 describes the rotation of the system on a $(N-1) \times D$ dimensional sphere and V includes all the interactions between the particles.

Though the definition for the hyperradial part of the Hamiltonian in Eq. (2.20) can be written in a simple general form, the definition for the hyperangles Ω cannot. Even for a particular N and D there are many ways to define a set of hyperangles [108–113]. The definition of the hyperangles Ω is important in the numerical convergence and for imposing identical particle symmetry in the calculations. In the following, we will discuss the hyperangular degrees of freedom specifically for the three-body systems while keeping the hyperradial degrees of freedom as general as possible. The discussion for four-body hyperangles will be presented in Sec. 4.3 for the individual applications.

2.2.1 Delves' hyperspherical coordinates

The key feature of the Delves' hyperspherical coordinates [15, 16] is that the hyperangles representing the configurational motion are defined by the relative size of the Jacobi vectors. In a three-body system there is only one such angle, ϕ , defined as

$$\phi = \tan^{-1} \left(\frac{\rho_{12,3}}{\rho_{12}} \right), \quad (0 \leq \phi \leq \pi/2), \quad (2.21)$$

where we have picked the first set of Jacobi vectors in Fig. 2.1. The rest of the hyperangles can be either defined in a space-fixed frame or a body-fixed frame. In a space-fixed frame, the hyperangles are taken as the polar angles ϑ_{12} , $\vartheta_{12,3}$ and azimuthal angles φ_{12} , $\varphi_{12,3}$ of the Jacobi vectors. The symmetry of the total orbital angular momentum J can be built in the three-body wavefunction ψ by superposing all the partial angular momentum states

$Y_{\ell_{12}m_{12}}, Y_{\ell_{12,3}m_{12,3}}$ with the appropriate Clebsch-Gordon coefficients [114]:

$$\psi = \sum_{\substack{\ell_{12}, m_{12} \\ \ell_{12,3}, m_{12,3}}} f_{\ell_{12}, \ell_{12,3}}(R, \phi) \langle \ell_{12} m_{12} \ell_{12,3} m_{12,3} | JM \rangle Y_{\ell_{12} m_{12}} Y_{\ell_{12,3} m_{12,3}}. \quad (2.22)$$

The indices of m_{12} and $m_{12,3}$ are suppressed in ψ since the equation for ψ in free space is independent of them. The identical particle symmetry for particles 1 and 2 can be imposed by only including the harmonics $Y_{\ell_{12} m_{12}}$ which have the correct permutation symmetry.

This definition of the hyperangles is simple and easy to generalize for more particles. It also has the benefit that the obvious basis functions for the angular degrees of freedom recognized as the spherical harmonics $Y_{\ell m}$ are in analytic form. For some types of interactions V , the matrix elements of the Hamiltonian $\langle Y_{\ell' m'} | H | Y_{\ell m} \rangle$ can be evaluated analytically which means few-body problems that have fast convergence with (ℓ, m) can be solved very efficiently.

However, for describing a $A_2 + A$ break-up where the pair A_2 is not connected directly by the Jacobi vector, lots of partial angular momenta will be required for convergence when the separation of the system becomes large. For instance, using the Delves' hyperspherical coordinates defined above, the number of spherical harmonics required for representing the break-up between the particle 2 and a two-body bound state formed by particle 1 and 3 scales linearly with d/r_0 , where d is the distance between particle 1 and the pair, r_0 is the size of pair bound states.

One approach to deal with this situation is to go to the body-fixed frame. In the body-fixed frame, the overall rotation of the system is characterized by three Euler angles α, β and γ [115]. For a three-body system, in addition to the hyperangle ϕ , the other hyperangle is the angle between the two Jacobi vectors θ ($0 \leq \theta \leq \pi$). We give the explicit form of the square of the generalized angular momentum operator Λ^2 in the body-fixed frame as the following [108]:

$$\Lambda^2 = T_0 + T_1 + T_2 - 2, \quad (2.23)$$

where

$$T_0 = \frac{\partial^2}{\partial \phi^2} - \frac{4}{\sin^2 2\phi} \frac{1}{\sin \theta} \frac{\partial}{\partial \theta} \left(\sin \theta \frac{\partial}{\partial \theta} \right), \quad (2.24)$$

$$T_1 = \frac{4}{\sin^2 2\phi} \frac{1}{\sin^2 \theta} J_z^2 - \frac{1}{\cos^2 \phi} (2J_z^2 - J^2), \quad (2.25)$$

$$T_2 = \frac{1}{\cos^2 \phi} \left(2iJ_y \frac{\partial}{\partial \theta} + 2 \cot \theta J_x J_z \right). \quad (2.26)$$

The operator J^2 is the square of the total orbital angular momentum operator and the operators J_x, J_y, J_z are the projection of J on the principle axes of the moment of inertia and the quantization axis (z -axis) for the angular momentum is taken along the Jacobi vector $\vec{\rho}_i$.

In the body-frame Delves' coordinates, the identical particle symmetry for two particles connected directly by a Jacobi vector can be imposed by restricting the range of the hyperangle θ and requiring appropriate boundary conditions. The detailed procedure will be introduced in Sec. 2.3.

2.2.2 Democratic hyperspherical coordinates

Though the Delves' hyperspherical coordinates are easy to be defined and are intuitively understandable, it is difficult to impose the permutation symmetry of the particles not directly connected by Jacobi vectors. A definition of hyperspherical coordinates which can impose the permutation symmetry with simple operations is thus highly desirable. The "democratic" hyperspherical coordinates are designed to treat all the particles on equal footing regardless of the fact that they have been unequally treated by using the Jacobi vectors.

To build as much of the identical particle symmetry into the hyperspherical coordinates directly it is crucial to finding invariant physical identities under permutation operations. One observation is that the moment of inertia tensor is invariant under permutation of identical particles. Since the invariant coordinates should also not be changed under spatial rotation, we transform the coordinates of the particles in the body-fixed frame so the mo-

ment of inertia tensor is diagonal. The number of independent diagonals in the moment of inertia tensor determines the maximum possible invariant coordinates under identical particle permutations. In general, if the spatial dimension is 3, all three moments of inertia of the particles are independent, implying three invariants can be obtained when defining a set of hyperspherical coordinates. In 2D, though, only two moments of inertia are independent and the third one can be expressed as the sum of the other two. Finally in 1D only one is independent. Thus, in addition to the hyperradius, there will be two invariant hyperangles in 3D and one invariant hyperangle in 2D. No hyperangle is invariant in 1D.

Since in hyperspherical coordinates one of the invariant coordinates has already been defined as the hyperradius, the rest invariant coordinates can be defined as hyperangles. Note that the three-body system is a special case because the particles can always be put in a plane and the number of independent moments of inertia is reduced to two. The number of hyperangles which are changed under permutation is $D(N - 1) - (n_{\text{in}} - 1) - n_{\text{rot}}$, where n_{in} is the number of invariant coordinates and $n_{\text{rot}}=D(D - 1)/2$ is the number of the angles for spatial rotations, which are the polar angle in 2D and the three Euler angles in 3D. The angles for spatial rotations are counted separately since at most they are simply shifted under permutations. Defining democratic hyperspherical coordinates is usually not intuitive, but there are general procedures available to follow [111–113, 116, 117].

For three particles in 3D, we follow the definition of the hyperangles from Smith and Whitten [109, 110]. The quantization axis for angular momentum (z -axis) is chosen to be along the direction perpendicular to the plane containing the three particles. The invariant hyperangle θ and the hyperangle ϕ are related to the Jacobi vectors in the body-fixed frame

by [110, 118]

$$(\vec{\rho}_{12})_x = R \cos(\theta/2 - \pi/4) \cos(\phi/2 + \phi_{12}/2), \quad (2.27)$$

$$(\vec{\rho}_{12})_y = R \sin(\theta/2 - \pi/4) \sin(\phi/2 + \phi_{12}/2), \quad (2.28)$$

$$(\vec{\rho}_{12,3})_x = -R \cos(\theta/2 - \pi/4) \sin(\phi/2 + \phi_{12}/2), \quad (2.29)$$

$$(\vec{\rho}_{12,3})_y = R \sin(\theta/2 - \pi/4) \cos(\phi/2 + \phi_{12}/2), \quad (2.30)$$

where $\phi_{12}=2 \tan^{-1}(m_3/\mu_3)$. The z components of the vectors are zero. The range for θ is $[0, \pi/2]$, and the range for ϕ is $[0, 2\pi]$. The interparticle distances in the Smith-Whitten hyperspherical coordinates are expressed as

$$r_{ij} = 2^{-1/2} d_{ij} R [1 + \sin \theta \cos(\phi + \phi_{ij})]^{1/2}, \quad (2.31)$$

where

$$d_{ij}^2 = \frac{m_k}{\mu_3} \frac{m_i + m_j}{m_i + m_j + m_k}, \quad (2.32)$$

with i, j, k chosen cyclically, and

$$\phi_{12} = 2 \tan^{-1}(m_3/\mu_3), \quad \phi_{23} = 0, \quad \phi_{31} = -2 \tan^{-1}(m_2/\mu_3), \quad (2.33)$$

where $0 < \phi_{12} < \pi$ and $-\pi < \phi_{31} < 0$. Note that the previous discussion argues that there should be two invariant hyperangles when the spatial dimension is 3, regardless the number of particles. Though in above definition for three-body democratic coordinates we have only ϕ invariant, there is actually another invariant hyperangle, but defined exactly as zero [116].

The square of the generalized angular momentum operator Λ^2 in Smith-Whitten hyperspherical coordinates is defined by [116, 119]

$$\Lambda^2 = T_\theta + T_\phi + T_{\text{rot}}, \quad (2.34)$$

where

$$T_\theta = -\frac{4}{\sin 2\theta} \frac{\partial}{\partial \theta} \sin 2\theta \frac{\partial}{\partial \theta}, \quad (2.35)$$

$$T_\phi = \frac{2}{\sin^2 2\theta} \left(i \frac{\partial}{\partial \phi} - \frac{\cos \theta}{2} J_z \right)^2, \quad (2.36)$$

$$T_{\text{rot}} = \frac{2}{1 - \sin \theta} J_x^2 + \frac{2}{1 + \sin \theta} J_y^2 + J_z^2. \quad (2.37)$$

2.3 Adiabatic hyperspherical representation

To solve the few-body Schrödinger equation Eq. (2.20), one needs to solve a $D(N - 1)$ dimensional differential equation. Since the hyperradius R is invariant under all symmetry operations, it is convenient to deal with the hyperradial and hyperangular degrees of freedom separately and build all the symmetry in the hyperangular solutions. Also, since the hyperradius measures the overall size of a few-body system, we can assume it represents a slow motion compared to the hyperangular motions which represent the change of the spatial configuration. As firstly pointed out by Macek as early as in 1968 [120], the hyper-radial and hyperangular motions can be assumed to be approximately separable so that an adiabatic representation can be expected to provide high efficiency in solving Eq. (2.20).

By treating the hyperradius as an adiabatic parameter, we can solve the adiabatic equation

$$\left\{ \frac{\Lambda(\Omega)^2}{2\mu_N R^2} + \frac{[(N - 1)D - 1][(N - 1)D - 3]}{8\mu_N R^2} + V(R, \Omega) \right\} \Phi_\nu(R; \Omega) = U_\nu(R) \Phi_\nu(R; \Omega), \quad (2.38)$$

and obtain a set of hyperangular basis functions $\{\Phi_\nu\}$ parametrized by R . The total wavefunction can be expanded in this basis set as

$$\psi(R, \Omega) = \sum_{\nu=0}^{\infty} F_{E,\nu}(R) \Phi_\nu(R; \Omega). \quad (2.39)$$

Equation (2.20) reduces to a set of coupled 1D equations:

$$\left(-\frac{1}{2\mu_N} \frac{d^2}{dR^2} + U_\nu(R) \right) F_{E,\nu} - \frac{1}{2\mu_N} \sum_{\nu'} \left(2P_{\nu,\nu'} \frac{d}{dR} + Q_{\nu,\nu'} \right) F_{E,\nu'} = E F_{E,\nu}, \quad (2.40)$$

where the non-adiabatic couplings $P_{\nu,\nu'}(R)$ and $Q_{\nu,\nu'}(R)$, which drive inelastic transitions, are defined as

$$P_{\nu,\nu'}(R) = \left\langle\left\langle \Phi_\nu \left| \frac{d}{dR} \right| \Phi_{\nu'} \right\rangle\right\rangle, \quad Q_{\nu,\nu'}(R) = \left\langle\left\langle \Phi_\nu \left| \frac{d^2}{dR^2} \right| \Phi_{\nu'} \right\rangle\right\rangle. \quad (2.41)$$

The double angular bracket here indicates integration over only the hyperangular degrees of freedom. With the above definitions, the Hamiltonian in Eq. (2.40) is not manifestly Hermitian with respect to the indices ν and ν' . That is, the Hamiltonian is not symmetric piece by piece under the exchange of ν and ν' . In numerical calculations the Hermiticity of the Hamiltonian will be lost with finite numerical accuracy. However, we can make the Hamiltonian manifestly Hermitian by rewriting $Q_{\nu,\nu'}$ using the following identity

$$Q_{\nu,\nu'} = \frac{dP_{\nu,\nu'}}{dR} + (P^2)_{\nu,\nu'}, \quad (2.42)$$

where the square of the coupling matrix $P_{\nu,\nu'}$ can be evaluated by

$$(P^2)_{\nu,\nu'} = - \left\langle\left\langle \frac{d\Phi_\nu}{dR} \left| \frac{d\Phi_{\nu'}}{dR} \right\rangle\right\rangle. \quad (2.43)$$

It should be noted that $P_{\nu,\nu'}$ is antisymmetric matrix and $(P^2)_{\nu,\nu'}$ is a symmetric matrix. Writing it this way has the additional benefit that the second order derivative of the adiabatic functions is no longer required, which is usually not easy to evaluate accurately.

Solving the adiabatic equation Eq. (2.38) is typically the most time demanding in our calculations since more degrees of freedom are involved. In free space, the total angular momentum is conserved so that in the body-fixed frame the Euler angles can be separated from the ‘‘internal motion’’ of the system, by expanding the adiabatic wave-function Φ_ν over eigenfunctions of total angular momentum.

2.3.1 Three-body adiabatic equations in Delves’ coordinates

In the following we will give the details for solving the three-body adiabatic equations. The adiabatic wavefunction can be expanded in the following form:

$$\Phi_\nu(R; \Omega) = \sum_{K=K_{\min}}^J u_{\nu,K}(R; \theta, \phi) \tilde{D}_{KM}^{J\Pi}(\alpha, \beta, \gamma), \quad (2.44)$$

where the symmetrized Wigner D -functions $\tilde{D}_{KM}^{J\Pi}$ [108] are the simultaneous eigenfunctions of total angular momentum and total parity Π . They can be expressed by Wigner D -functions as:

$$\tilde{D}_{KM}^{J\Pi}(\alpha, \beta, \gamma) = \frac{1}{4\pi} \sqrt{2J+1} [D_{KM}^J(\alpha, \beta, \gamma) + (-1)^{J+K} \Pi D_{-K,M}^J(\alpha, \beta, \gamma)]. \quad (2.45)$$

Here K and M are the magnetic quantum numbers of the projection of total orbital angular momentum on the body-fixed and space-fixed z -axes, respectively. The eigenvalue of the total parity Π can take values ± 1 , which determines the range of K in the summation in Eq. (2.44): $K_{\min}=0$ for “parity-favored” states when $\Pi=(-1)^J$ and $K_{\min}=1$ for “parity-unfavored” states when $\Pi=-(-1)^J$.

The identical particle symmetry of the particles “1” and “2” which are connected directly by a Jacobi vector can be easily implemented. The permutation operator P_{12} gives the following transformation:

$$P_{12} \tilde{D}_{KM}^{J\Pi} = \Pi (-1)^K \tilde{D}_{KM}^{J\Pi}, \quad (2.46)$$

$$P_{12} \theta \rightarrow \pi - \theta. \quad (2.47)$$

The identical particle symmetry can then be imposed by restricting the range of the hyper-angle θ to be $[0, \pi/2]$, and requiring the following boundary conditions for the body-frame components $u_{\nu,K}(R; \theta, \phi)$:

$$u_{\nu,K}(R; \theta, \phi) \Big|_{\theta=\pi/2} = \mathcal{A} \Pi (-1)^K u_{\nu,K}(R; \theta, \phi) \Big|_{\theta=\pi/2}, \quad (2.48)$$

$$\frac{\partial u_{\nu,K}(R; \theta, \phi)}{\partial \theta} \Big|_{\theta=\pi/2} = \mathcal{A} \Pi (-1)^{K+1} \frac{\partial u_{\nu,K}(R; \theta, \phi)}{\partial \theta} \Big|_{\theta=\pi/2}, \quad (2.49)$$

$$(2.50)$$

where $\mathcal{A} = 1$ for bosons and $\mathcal{A} = -1$ for fermions. The range restriction on θ leads to a 2! reduction in the numerical calculations for a given accuracy. The permutation operation of P_{13} and P_{23} , however, mixes up the hyperangles θ and ϕ so that imposing the identical particle symmetry for these pairs is much harder.

Permutation	ϕ	D_{KM}^J
P_{12}	$2\pi - \phi$	$(-1)^J D_{-KM}^J$
P_{23}	$2\pi/3 - \phi$	$(-1)^J D_{-KM}^J$
P_{31}	$4\pi/3 - \phi$	$(-1)^{J+K} D_{-KM}^J$

Table 2.1: Transformation effect of the permutation operators in Smith-Whitten hyperspherical coordinates. The effects of other two permutation operations $P_{12}P_{23}$ and $P_{12}P_{31}$ can be obtained by applying the individual operators consecutively.

2.3.2 Three-body adiabatic equations in Smith-Whitten coordinates

The permutation symmetry for three identical particles can be most easily imposed in Smith-Whitten coordinates. We expand the adiabatic wavefunction in the basis of Wigner D -functions D_{KM}^J :

$$\Phi_\nu(R; \Omega) = \sum_K u_{\nu,K}(R; \theta, \phi) D_{KM}^J(\alpha, \beta, \gamma). \quad (2.51)$$

For the ‘‘parity-favored’’ states K takes the values of $-J, -(J-2), \dots, J-2, J$, and for the ‘‘parity-unfavored’’ states K takes the values of $-(J-1), -(J-3), \dots, J-3, J-1$. Though Wigner D -functions we are using here is same as those in previous section, the difference in the choices of quantization axis makes the permutation effect on Wigner D -functions no longer the same for the two cases.

The permutation symmetry for two identical particles is also simple in Smith-Whitten coordinates and has been given in Ref. [121]. Here we give the method to impose the permutation symmetry for three identical particles. In Table 2.1, we list the transformation effect of the permutation operators on the hyperangle ϕ and the Wigner D -functions. These transformations are equivalent to the following boundary conditions when we restrict the range of the hyperangle ϕ to be within $[0, \pi/3]$:

$$u_{\nu,K}(R; \theta, 0) = \mathcal{A}(-1)^J u_{\nu,-K}(R; \theta, 2\pi) = \mathcal{A}(-1)^{J+K} u_{\nu,-K}(R; \theta, 0), \quad (2.52)$$

$$\left. \frac{\partial u_{\nu,K}(R; \theta, \phi)}{\partial \phi} \right|_{\phi=0} = \mathcal{A}(-1)^{J+K+1} \left. \frac{\partial u_{\nu,-K}(R; \theta, \phi)}{\partial \phi} \right|_{\phi=0}, \quad (2.53)$$

and

$$u_{\nu,K}(R; \theta, \pi/3) = \mathcal{A}(-1)^J u_{\nu,-K}(R; \theta, \pi/3), \quad (2.54)$$

$$\left. \frac{\partial u_{\nu,K}(R; \theta, \phi)}{\partial \phi} \right|_{\phi=\pi/3} = \mathcal{A}(-1)^{J+1} \left. \frac{\partial u_{\nu,-K}(R; \theta, \phi)}{\partial \phi} \right|_{\phi=\pi/3}. \quad (2.55)$$

Here the restriction of the range on ϕ leads to a 3! reduction for numerical calculations.

In either Delves' or Smith-Whitten coordinates, the adiabatic equation Eq. (2.38) for three-body systems reduces to 2D equations for coupled body-frame components $u_{\nu,K}$. We typically solve these equations by expanding the body-frame components in a 2D direct product B-spline basis $\{B_i(\theta)\} \otimes \{B_j(\phi)\}$. The boundary conditions for imposing the identical particle symmetries are directly built in the basis functions.

We have also solved the 2D equations by solving each dimension consecutively, which can reduce the requirement for computational resources significantly. A generalization of this method to few-body systems with more particles gives hope for performing scattering calculations with more particles. The detailed implementation of this method is presented in Appendix A.

2.4 Few-body scattering

We use the variational method to solve the hyperradial equation Eq. (2.40). Since the form of Eq. (2.40) is independent of the number of particles, the following procedure can be used for solving the N -body hyperradial equation in general. For calculating the bound state energies, we expand the hyperradial functions in a set of finite element basis functions:

$$F_{E,\nu}(R) = \sum_i c_{E,\nu,i} B_i(R). \quad (2.56)$$

The equation for the expansion coefficients c_i is reduced to a generalized eigenvalue equation by applying the variational principle:

$$\mathbf{H}\vec{c} = E\mathbf{S}\vec{c}, \quad (2.57)$$

where the Hamiltonian and the overlap matrices are

$$H_{\nu,i;\nu',j} = \int_0^\infty dR \left[\delta_{\nu,\nu'} \left(\frac{1}{2\mu_N} \frac{dB_i}{dR} \frac{dB_j}{dR} + U_\nu B_i B_j \right) + \frac{1}{2\mu_N} P_{\nu,\nu'} \left(\frac{dB_i}{dR} B_j - \frac{dB_j}{dR} B_i \right) + \frac{1}{2\mu_N} (P^2)_{\nu,\nu'} B_i B_j \right], \quad (2.58)$$

$$S_{\nu,i;\nu',j} = \delta_{\nu,\nu'} \int_0^\infty dR B_i B_j. \quad (2.59)$$

For scattering calculations, the scattering matrix \mathbf{S} for Eq. (2.40) is obtained by using the eigenchannel R -matrix method [122]. Specifically, by applying the variational principle [122, 123] and expanding the total wavefunction Ψ by Eq. (2.39) and (2.56), the few-body Schrödinger equation Eq. (2.20) is reduced to the following generalized eigenvalue problem

$$\mathbf{\Gamma} \vec{c} = b \mathbf{\Lambda} \vec{c} \quad (2.60)$$

for the logarithmic derivative b on the hypersphere

$$b = \frac{\partial \ln \Psi}{\partial R}. \quad (2.61)$$

In our calculations, the non-adiabatic couplings $P_{\nu,\nu'}$ between some channels decay very slowly as $1/R$ [21] so that we need to integrate the hyperradial equation up to $10^6 - 10^7$ a.u. To deal with such situations, we use a propagation method [124] to divide the hyperradii into small boxes of sizes about $10^3 - 10^4$ a.u. so that we are able to integrate millions of oscillations in the hyperradial wavefunctions. Within each box ($R_1 \leq R \leq R_2$), the matrices $\mathbf{\Gamma}$ and $\mathbf{\Lambda}$ are defined as

$$\Gamma_{\nu,i;\nu',j} = \int_{R_1}^{R_2} dR \left\{ \delta_{\nu,\nu'} \left[\frac{1}{2\mu_N} \frac{dB_i}{dR} \frac{dB_j}{dR} + (2\mu_N U_\nu - k^2) B_i B_j \right] + \frac{1}{2\mu_N} P_{\nu,\nu'} \left(\frac{dB_i}{dR} B_j - \frac{dB_j}{dR} B_i \right) + \frac{1}{2\mu_N} (P^2)_{\nu,\nu'} B_i B_j \right\}, \quad (2.62)$$

$$\Lambda_{\nu,i;\nu',j} = \delta_{\nu,\nu'} \sum_{i,j} [B_i(R_1) B_j(R_1) + B_i(R_2) B_j(R_2)]. \quad (2.63)$$

The adiabatic potentials and non-adiabatic couplings are calculated up to the hyperradius where they acquire asymptotic behavior, which is usually about 20 times larger than the two-body scattering length a . We determine some of the power-law behavior for the asymptotic

expansions from Ref. [21]. The rest of the power-law behavior is determined empirically from the numerical data. And we fit the coefficients of the lowest three terms also from the numerical data. These asymptotic expansions are then used in the hyperradial boxes from the distance where the numerical potentials and couplings end to the distance $R = R_m$ where we match the numerical solutions to the asymptotic ones.

After solving the expansion coefficients \vec{c} , the solution matrix \mathbf{F} can be constructed by the linearly-independent solutions after imposing regularity at the origin $R = 0$. The R -matrix \mathbf{R} is obtained by

$$\mathbf{R} = \mathbf{F}\mathbf{F}'^{-1}, \quad (2.64)$$

where \mathbf{F}' is the hyperradial derivative of the solution matrix \mathbf{F} . The reactance matrix \mathbf{K} is evaluated by the following expression at the hyperradius $R = R_m$:

$$\mathbf{K} = (\mathbf{f} - \mathbf{f}'R)(\mathbf{g} - \mathbf{g}'R)^{-1}|_{R=R_m}, \quad (2.65)$$

where the asymptotic solution matrices \mathbf{f} and \mathbf{g} are diagonal whose elements are expressed in terms of the first and the second kind of Bessel functions, as given in Appendix C. The scattering matrix \mathbf{S} is then obtained by

$$\mathbf{S} = (\mathbb{1} + i\mathbf{K})(\mathbb{1} - i\mathbf{K})^{-1}, \quad (2.66)$$

where $\mathbb{1}$ is the unit matrix.

The inelastic collision rates can be immediately obtained once the scattering matrix is calculated. The general expression for N -body recombination has been derived in Ref. [125]. Here we explicitly give the three-body recombination rate which will be used throughout our work:

$$K_3^{J\Pi} = \sum_{f,i} \frac{C\pi^2(2J+1)}{\mu_3 k^4} |(S^{J\Pi})_{f,i}|^2. \quad (2.67)$$

Since the initial plane wave state for the three particles can be written as a superposition of all the hyperspherical continuum channels, the sum of i is over all these three-body

continuum channels. The sum of f is over and all possible final two-body bound channels. The value of the constant C is 192 when all three particles are identical [126] and is 64 when two of the particles are identical [118, 125]. The expressions for three-body relaxation rate follow the two-body ones since in such scattering processes both initial and final channels are the two-body break-up channels.

The adiabatic hyperspherical representation usually has very quick convergence with respect to the adiabatic channels. The physical reason behind is that the hyperradius R is typically a slow dynamical variable compared with the hyperangles. This is in analogy with the Born-Oppenheimer approximation widely used in chemistry, but note that the adiabatic hyperspherical representation is exact and does not break down when the masses are all comparable. An approximate version of the representation can be made, however, by neglecting the couplings. In fact, for some cases these single channel approximations can give quite good estimates of the few-body bound state energies and the positions of resonances [108].

2.5 Adiabatic potentials

As mentioned previously, the adiabatic hyperspherical representation can usually give a good description of the physical properties in a few-body system even under the single-channel approximation. This implies that the diagonals in the hyperradial equation Eq. (2.40) are the most essential for describing the stationary states in a few-body system. In the following we will show the typical behavior for the diagonal potentials

$$W_{\nu,\nu}(R) = U_{\nu}(R) - \frac{1}{2\mu_3}Q_{\nu,\nu}(R) \quad (2.68)$$

in three-body systems.

Assuming that the individual particles are structureless, when the hyperradius R goes to infinity the three-body system can break-up either into three free particles or one free particle and two particles bound together. A typical set of adiabatic potentials for $J = 0^+$

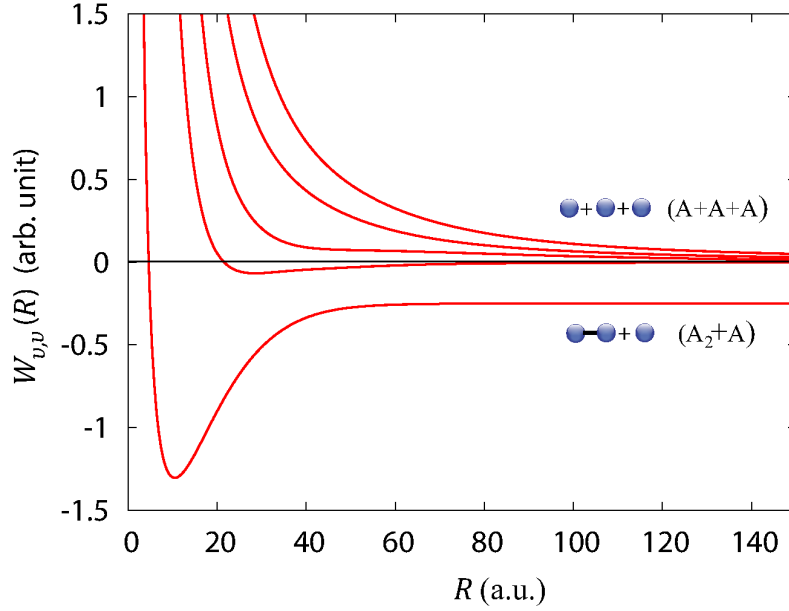


Figure 2.3: A set of adiabatic hyperspherical potentials for $J^{\Pi} = 0^+$ symmetry.

are shown in Fig. 2.3. All the adiabatic potentials behave like $1/R^2$ as $R \rightarrow 0$. Such behavior holds for particles interacting with any potentials which are less singular than $1/R^2$ near origin so that the $1/R^2$ centrifugal potentials dominate at small hyperradii. Specifically, these potentials assume the free-particle behavior [21]:

$$W_{\nu,\nu}(R) = \frac{\lambda(\lambda + 4) + 15/4}{2\mu_3 R^2}, \quad (2.69)$$

where λ s are non-negative integers. When $R \rightarrow \infty$, there are two different behaviors for the potentials. For the channels corresponding to the three-body break-up, the three particles are free asymptotically thus the potentials again behave like Eq. (2.69). For the channels correspond to atom-diatomic break-up the potentials behave like

$$W_{\nu,\nu}(R) = E_{\nu,\ell_0} + \frac{\ell(\ell + 1)}{2\mu_3 R^2}, \quad (2.70)$$

where E_{ν,ℓ_0} is the bound state energy of the diatomic system with vibrational and rotational quantum number of ν and ℓ_0 , respectively, and ℓ is the asymptotic angular momentum between the atom and the diatomic system.

Generally, when three-body break-up needs to be considered, the calculation of the total cross section requires not only the integration over the scattering angles, but also an integration over all possible distributions of the total energy over the two Jacobi vectors. In numerical calculations this requires a discretization scheme which is difficult to implement in a rigorous way. In hyperspherical coordinates, however, the three-body break-up is represented by discrete channels so that the inclusion of the physics from the three-body break-up is simply achieved by the convergence of the observable with respect to the number of three-body continuum channels. This is especially convenient for three-body recombination calculations.

Adiabatic hyperspherical potentials are especially useful in the study of universal physics. In systems with large two-body scattering length a , the scaling of the adiabatic potentials and the non-adiabatic couplings can be derived by solving the Faddeev equations [14] with the zero-range potential model [13], which is the approach also used by Efimov [12, 106, 107] for the discovery of the Efimov effect. Specifically, the three-body solution Ψ takes the functional form for the free-particle solutions with appropriate boundary condition satisfied when the interparticle distances r_{ij} go to 0. This boundary condition can be expressed in a general form as [127]:

$$\frac{\partial}{\partial r_{ij}}(r_{ij}\Psi) = k \cot \delta(k_2)\Psi, \quad (r_{ij} \rightarrow 0) \quad (2.71)$$

where δ is the two-body phase shift and k_2 is the two-body wave number. In general, δ has non-universal dependence on two-body interactions, but at low energies where k_2 is small, the right hand side of Eq. (2.71) can be approximated by using low energy scattering parameters:

$$k \cot \delta(k_2) \approx -\frac{1}{a}, \quad (k_2 \rightarrow 0). \quad (2.72)$$

For three identical bosons, the boundary condition Eq. (2.71) with the low energy approximation Eq. (2.72) leads to a transcendental equation

$$s_\nu \cos\left(\frac{\pi}{2}s_\nu\right) - \frac{8}{\sqrt{3}} \sin\left(\frac{\pi}{6}s_\nu\right) = 12^{-\frac{1}{4}} \sin\left(\frac{\pi}{2}s_\nu\right) \frac{2R}{a}, \quad (2.73)$$

where s_ν is related to the adiabatic hyperspherical potential by

$$U_\nu = \frac{s_\nu^2 - \frac{1}{4}}{2\mu_3 R^2}. \quad (2.74)$$

The lowest potential U_0 , the so called Efimov potential, which represents the weakly-bound $A_2^* + A$ break-up threshold when $a > 0$ or the lowest three-body continuum channel when $a < 0$, is determined by a purely imaginary solution $s_\nu = is_0$ from Eq. (2.73). The potential is attractive and behaves like the following:

$$W_{\nu,\nu}(R) \simeq -\frac{s_0^2 + 1/4}{2\mu_3 R^2}, \quad (r_0 \ll R \ll |a|), \quad (2.75)$$

where the value of s_0 can be obtained by taking the limit $a \rightarrow \infty$, which gives $s_0 \approx 1.00624$. Here we use A to represent an atom and use a superscript $*$ to indicate an excited state. Note that attractive $1/R^2$ potential also shows up in electron-dipole scattering and has been studied in Refs [128–130].

As pointed out by Efimov [131], some of the three-body scattering processes are determined by the universal long-range behavior of a few adiabatic potentials. From our numerical calculations, we have confirmed that in most cases there are only one or two adiabatic potentials as well as the couplings between them are most important. The basic example here is the energies of the Efimov bound states. Within the single-channel approximation, the hyperradial solutions for the three-body bound states in the Efimov potential Eq. (2.75) can be written in terms of the modified Bessel functions with imaginary order:

$$F_{E_n,\nu}(R) = \sqrt{\frac{2\kappa_n^2 \sinh(\pi s_0)}{\pi s_0}} R^{1/2} K_{is_0}(\kappa_n R), \quad (2.76)$$

where $\kappa_n = \sqrt{-2\mu_3 E_n}$ is the bound wavenumber. Since the coefficient for attractive $1/R^2$ potential in Eq. (2.75) is supercritical ($> 1/4$), the system will have the “fall to the center” problem [132], also known as Thomas collapse [19]. This is manifested by an infinite number of oscillations in the hyperradial wavefunction $F_{E_n,\nu}$ when $R \rightarrow 0$. As pointed out by Efimov [12, 106], in reality, when R is near the short-range distance r_0 the behavior of the potential in Eq. (2.75) is overtaken by non-universal short-range details, so that a cutoff for

$F_{E_n, \nu}$ near $R \approx r_0$ is required which gives the short-range dependent ground state energy E_0 . He also pointed out that an infinite number of bound state can accumulate towards the zero-energy threshold, with the energies E_n and the maximum value of n determined by Eq. (1.2) and (1.3), respectively.

The transcendental equations similar to Eq. (2.73) for other combinations of particles will be given in the following chapters when each specific case is addressed.

2.6 Deriving universal expressions for inelastic rates

Our numerical calculations show that at ultracold energies only one or two adiabatic channels are important in determining the universal scaling behaviors for the scattering processes. We can thus design a simple model based on the scaling of a few adiabatic potentials to derive the expressions for the rate constants of three-body inelastic processes. Here we present the method we use for deriving the three-body recombination rate near zero scattering energy when $a < 0$, which had also been used by Jonsell for the same problem [133].

As shown in Fig. 2.4, the recombination starts from the three-body continuum where the adiabatic channels are essentially decoupled ($P_{\nu, \nu'} \sim 1/R^{5/2}$). Near zero scattering energy, only the lowest continuum channel is important since higher channels are more repulsive and thus much more classically forbidden. Inelastic transitions occur at the hyperradii where the coupling between the incident channel and the deeply-bound $A_2 + A$ channels cannot be neglected. We have found from numerical calculations that the non-adiabatic couplings $P_{\nu, \nu'}$ and $Q_{\nu, \nu'}$ between these two channels are only significant near $R \lesssim r_0$. This is not difficult to understand, as the distance between the two particles that will be recombined should be close to the size of the recombined state r_0 and the third particle which is responsible for taking away the binding energy needs to be within the distance of r_0 from the other two so that they can interact and have energy exchange. Thus we assume that the two channels are decoupled for any $R > r_0$. We are able then to write down the hyperradial solution in different regions of hyperradii where the scaling behavior of the potentials is analytically

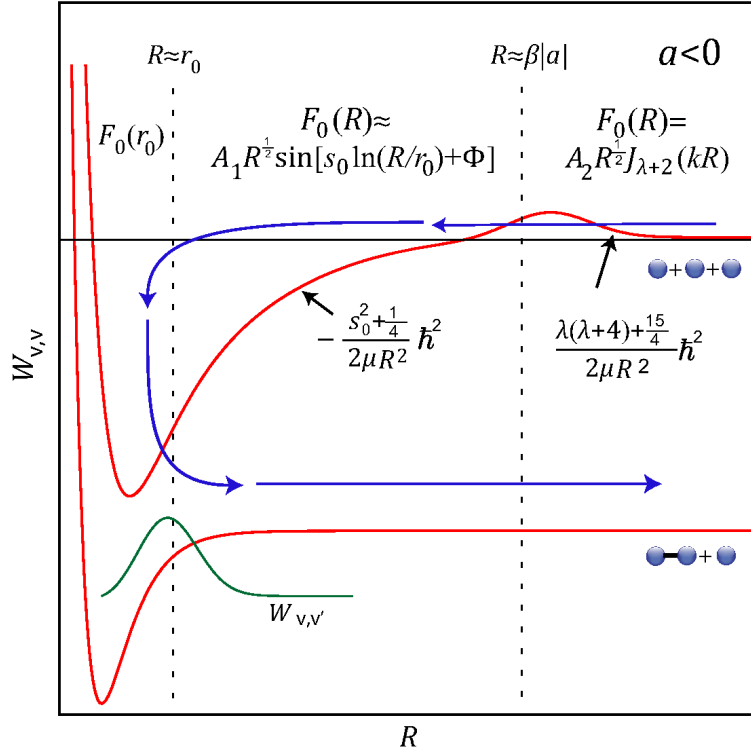


Figure 2.4: The adiabatic potential model for three-body recombination when $a < 0$.

known.

The scaling behavior of the recombination rates can be obtained once the scaling of hyperradial wavefunctions is known. In the present case, we divide the potential for the incident channel into three regions, and assume that the potentials have the following behavior in our model:

$$W_{\nu,\nu}(R) = W_{\nu}(r_0) \quad R \leq r_0, \quad (2.77)$$

$$W_{\nu,\nu}(R) = -\frac{s_0^2 + 1/4}{2\mu_3 R^2} \quad r_0 \leq R \leq \beta|a|, \quad (2.78)$$

$$W_{\nu,\nu}(R) = \frac{15/4}{2\mu_3 R^2} \quad R \geq \beta|a|, \quad (2.79)$$

where β is a parameter reflecting the uncertainty in determining the boundary. The corresponding hyperradial solutions in the Efimov region ($r_0 \leq R \leq |a|$) and the asymptotic region are the Bessel functions of order is_0 and order 2, respectively. We model the inelastic

transition near $R = r_0$ by using a complex phase in $F_\nu(r_0)$, which is equivalent to adding an optical potential [134]. After matching $F_\nu(R)$ at $R = r_0$ and $R = |a|$, we calculate the elastic scattering probability \mathcal{R} in the initial three-body continuum channel and calculate three recombination rate by using the relation

$$K_3 = \frac{192\pi^2}{\mu_3 k^2} (1 - \mathcal{R}). \quad (2.80)$$

The recombination rate K_3 into deep two-body bound channels for $a < 0$ is finally obtained as

$$K_3 = \frac{12\sqrt{3}\pi^3\beta^4 \sin 2\varphi_0 \sinh 2\eta}{\sin^2[s_0 \ln(|\beta a/r_0|) + \Phi] + \sinh^2 \eta} \frac{a^4}{m}. \quad (2.81)$$

For details of the derivation please refer to Appendix B.

Chapter 3

Universal Efimov physics in three-body systems

Recent studies have substantially pushed forward the understanding of the three-body Efimov effect in ultracold atomic gases [49–52, 66]. Since most analytical theories developed thus far [49, 52, 66, 135] assume that the three-body scattering is at zero-energy and the two-body scattering is only determined by the scattering length a , they are valid only under certain experimental conditions. For instance, the Feshbach resonances [42] used for obtaining large a are required to be relatively broad in the magnetic field [43] and the temperature of the gas samples need to be extremely low [58]. In Refs. [136, 137], the authors have employed models which are valid when the width of the resonance is narrow, but with the short-range physics left out. The finite energy effect has been considered in Refs. [53, 138–140] for explaining the experimental data, but only as small corrections. In Sec. 3.1, we have extended our study to narrow Feshbach resonances with the non-trivial short-range physics included, where the material is adapted from a preprint [2]. In Sec. 3.2 and Sec. 3.3, we have identified novel phenomena at higher collisional energies which can be traced back to the Efimov effect. In particular, Sec. 3.2 is adapted from a published paper [11], and Sec. 3.3 is adapted from a preprint [5].

3.1 Ultracold three-body collisions near narrow Feshbach resonances

Strongly interacting three-body systems play an important role in many areas of physics including condensed matter, atomic, molecular, and nuclear physics [18, 52]. Advances in the control of interatomic interactions have made ultracold atomic gases a preferred test bed for many interesting physical phenomena. One of the most important tools for this control is the Feshbach resonance [42, 43, 141–143]. Applying an external field, the s -wave scattering length a between two atoms can be tuned from $-\infty$ to $+\infty$.

A major experimental difficulty encountered for Bose gases in the strongly interacting limit, $|a| \gg r_0$ where r_0 is the characteristic range of the interatomic interactions, is that the system becomes unstable due to three-body collisional loss of atoms and molecules. For a pure atomic sample, the loss is dominated by the three-body recombination, and the density change of the sample is determined by Eq. (1.4). Though in the typical experiments the three-body recombination is not favored for the low density (10^{12} – 10^{15} cm $^{-3}$), the recombination rate surges very quickly as $|a|^4$ near a Feshbach resonance. For the weakly-bound molecules produced through a Feshbach resonance, though the loss rate from atom-dimer relaxation scales more mildly as a , they are lost quickly since the loss rate is both linear in the atomic density and the dimer density.

In ultracold two-component Fermi gases where the components correspond to the same atomic isotope in different hyperfine states F and F' , three-body processes are suppressed near a Feshbach resonance where F and F' interact resonantly. This can be understood by the Pauli exclusion from the two identical fermionic atoms involved in the three-body collisions. In particular, the three-body recombination into a weakly-bound dimer $:F + F + F' \rightarrow (FF')^* + F$ is suppressed as k^2 near zero energy. For the three-body relaxation $(FF')^* + F \rightarrow FF' + F$, the rate is suppressed by $1/a^{3.33}$ even though it is non-zero as $k \rightarrow 0$. This increased stability for two-component Fermi gases allows the experimental realization of a broad range of novel physical phenomena.

For the identical bosons, while the overall behavior of K_3 and V_{rel} is determined by a as shown in Eq. (1.5), (1.6) and (1.7), any comparison with a physical system also requires the short-range three-body parameters Φ and η which cannot, in general, be predicted from two-body physics alone [53].

The past few years have seen the experimental verification [54–57, 60, 144–148] of various predictions for Efimov physics especially for the explicit analytical expressions for the universal inelastic rates. These predictions, except the ones in Ref. [136, 137], were based on the assumption that ultracold scattering properties are universal and depend only on a , which is a good assumption for broad resonances. This focus on broad resonances and the dominance of a was natural given the low-energy expansion of the two-body s -wave scattering phase shift δ ,

$$k_2 \cot \delta = -\frac{1}{a} + \frac{1}{2} r_{\text{eff}} k_2^2 + \dots, \quad (3.1)$$

where k_2 is the two-body wavenumber and r_{eff} is the effective range. For the magnetic Feshbach resonances used in the ultracold experiments, the r_{eff} can be estimated from the resonance parameters by [149]

$$r_{\text{eff}} = -\frac{1}{|\mu_2 a_{\text{bg}} \Delta\mu \Delta B|}, \quad (3.2)$$

where μ_2 is the two-body reduced mass, a_{bg} is the background scattering length, $\Delta\mu$ is the difference of the magnetic moment between the two channels involved in the resonance and ΔB is the resonance width. In Table 3.1, we list the effective-range for some selected Feshbach resonances [43]. Since $|r_{\text{eff}}|$ is inversely proportional to the resonance width for $r_{\text{eff}} < 0$ [136], the second term in Eq. (3.1) is negligible, at low collisional energies for broad resonances. Near a narrow resonance, however, $|r_{\text{eff}}|$ is large and the second term in Eq. (3.1) is no longer negligible even at ultracold collision energies. This implies that r_{eff} should be incorporated in the three-body universal theory for the narrow resonances. While specific systems have been modeled near a resonance [150–153], no simple analytical expressions like those in Equations. (1.5)–(1.7) have yet appeared. Narrow resonances, however, are

Atomic species	Resonance position (G)	a_{bg} (a.u.)	$\Delta\mu$ (μ_B)	ΔB (G)	r_{eff} (a.u.)
^6Li	543.25	60	2	0.1	-71300
^7Li	736.8	-25	2	-192.3	-76
^{23}Na	1195	62	-0.15	1.4	-17100
^{23}Na	907	63	3.8	1	-947
^{23}Na	853	63	3.8	0.0025	-373000
^{87}Rb	1007.2	100	2.79	0.21	-1010
^{87}Rb	911.7	100	2.71	0.0013	-168000
^{87}Rb	685.4	100	1.34	0.006	-73400
^{87}Rb	406.2	100	2.01	0.0004	-734000
^{87}Rb	9.13	99.8	2.00	0.015	-19700
^{133}Cs	47.97	926	1.21	0.12	-287
^{133}Cs	19.84	160	0.57	0.005	-84600
^{133}Cs	53.5	995	1.52	0.0025	-10200
^{52}Cr	589.1	105	2	1.7	-276
^{52}Cr	499.9	107	4	0.08	-2880
$^{39}\text{K}+^{87}\text{Rb}$	317.9	34	2	7.6	-185

Table 3.1: Effective-range for some selected Feshbach resonances.

expected not only to affect Efimov physics [136, 137] but also to modify the BEC-BCS crossover picture for fermionic systems [154].

Furthermore, the physics near narrow Feshbach resonances are regarded as intrinsically different from the physics near broad resonances since the two-body wavefunction is closed-channel dominant and the two resonant ultracold atoms always carry bound state characteristics even if they do not form a bound state. The possibility of new many-body physics near narrow Feshbach resonances has already been proposed theoretically in Refs. [154–156].

In addition, many of the recent experiments on ultracold systems with mixed species are done near relatively narrow Feshbach resonances [157–160]. And with the development of the optical Feshbach resonances [141–143] it is promising to gain experimental fine control over the width of the resonance. It is thus important to develop the universal theory for the three-body physics near narrow resonances.

In the previous works on this topic by Petrov and Gogolin, *et al.* [136, 137], the zero-range potential (ZRP) [13] model is used and the short-range physics is completely neglected.

Though their results give the general scaling for the three-body scattering observables in terms of both the scattering length and effective-range, the validity of these results in the presence of finite-range interactions is missing. Particularly, Petrov calculated the recombination rate for identical bosons near a narrow Feshbach resonance with $a > 0$ using a modified ZRP to include r_{eff} [136]. By solving his model numerically, he found that the minima described by Eq. (1.5) still appear for $a \gg |r_{\text{eff}}|$ but occur at fixed values of $|r_{\text{eff}}|/a$ without any reference to a three-body parameter like Φ . Gogolin *et al.* [137] reproduced these results with a very different method but effectively the same physical model. There are some other theoretical work addressing the modification of the Efimov physics by the effective-range [161–163], where $|r_{\text{eff}}| \approx r_0$ so that a perturbative treatment is still adequate. Their results, however, cannot be applied to the narrow Feshbach resonances.

Here we aim to expand our knowledge of universality near a narrow Feshbach resonance. We are especially interested in the change of the universal behavior for the three-body processes which depends on the short-range physics. In particular, we study the dependence of ultracold three-body collision rates on r_{eff} , obtaining analytic expressions for K_3 and V_{rel} similar to Equations. (1.6) and (1.7), and verified by numerical solutions. Surprisingly, we find that *all* inelastic processes leading to deeply-bound two-boson states are suppressed as $|r_{\text{eff}}|^{-1}$, indicating that Bose gases are more stable near narrow resonances. In contrast, we find that Fermi gases should be less stable due to enhanced losses for large $|r_{\text{eff}}|$.

More fundamentally, and in contrast to [136] and [137], we show that the short-range three-body physics *is* important near a narrow resonance for identical bosons — even in the limit $r_0 \rightarrow 0$. Mathematically, it is true that no three-body parameter is needed since the inclusion of r_{eff} in the zero-range model regularizes it [127][9], removing the Thomas collapse [19]. Physically, however, we will show that a three-body parameter is still needed to represent the short-range three-body physics for any realistic system. Consequently, a and r_{eff} alone are insufficient to describe ultracold three-boson observables.

To this end, we calculate various three-body inelastic rates numerically by solving

Eq. (2.20) for three bodies. In these calculations, we use the adiabatic hyperspherical representation in Smith-Whitten coordinates since we are focusing on the universal physics for identical bosons.

3.1.1 Modeling Feshbach resonances

Feshbach resonances are in general a multi-channel phenomenon. A two-channels picture is sufficient to reproduce the resonant behavior to sufficiently accuracy. As shown in Fig. 3.1,

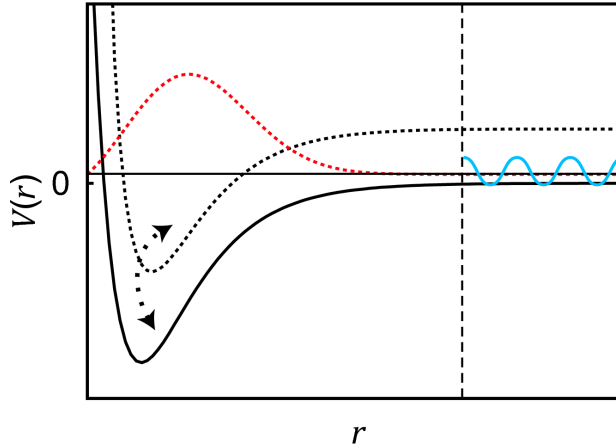


Figure 3.1: Schematic potentials for a Feshbach resonance. The dashed curve with arrows indicate that the two channels are coupled. As the relative separation between the two channels are tuned by the magnetic field in experiment, a Feshbach resonance occurs when the scattering energy (indicated by the horizontal solid black line) matches the bound state energy in the upper channel. Both the scattering amplitude in the lower channel (blue sinusoidal curve) and the amplitude in the upper channel (red dashed curve) are significantly enhanced. In particular, when the energy of a bound state in the upper-channel move across the threshold of the lower channel, the scattering length for the lower channel goes through a pole.

a Feshbach resonance occurs when the collisional energy between two atoms in the lower channel is near the bound state energy in the upper channel. The resonance leads to a large change in the scattering wavefunction, as can be exhibited through the effective-range expansion in Eq. (3.1). In particular, by tuning the relative separation between the two channels the scattering length in the lower channel goes through a pole when a bound state in the upper channel moves across the threshold of the lower channel. The strength of

the coupling between the two channels determines the width of the resonance and controls the size of the effective range r_{eff} in Eq. (3.1). When there is only one open channel, the asymptotic scattering wavefunction for the single-channel model can be made identical to the multichannel case. In other words, the asymptotic wave function does not depend on the short-range two-body physics that generates the resonance [135, 136]. From this spirit, we can model a single-channel two-body potential with a shape resonance to reproduce the same scattering property as for a multi-channel case. The shape resonance we use will then be essentially identical to a multi-channel Feshbach resonance. Specifically, the single-channel two-body interaction we use takes the following form:

$$V_{\text{sech}}(r) = -D\text{sech}^2(3r/r_0) + Be^{-2(3r/r_0-2)^2}, \quad (3.3)$$

where r is the distance between the two atoms. As shown in Fig. 3.2, instead of coupling two different channels in a Feshbach resonance case, we couple the scattering region with the short-range region in our single-channel model, by the use of a potential barrier. The resonance in this model thus corresponds to a shape resonance.

In our three-body calculations, we use a pair-wise sum of model potentials with the form of Eq. (3.3), where the potential depth D primarily controls a , and the barrier height B is adjusted to produce the desired r_{eff} . One indicator of the universal physics is that the change on the short-range physics is very small near the universal scaling limit ($|a| \gg r_0$, for instance). In the present case small changes in short-range physics are required when $|a| \gg r_0$ and $|r_{\text{eff}}| \gg r_0$. With the single-channel potential we use, however, non-negligible change for the short-range physics is required to obtain a large $|a|$ and a large negative r_{eff} simultaneously. The universal scaling behavior is thus entangled with the non-universal change of the short-range behavior. To solve this problem, we introduced a hard wall in $W_{\nu\nu}(R)$ at $R=r_0$ to cut off the short-range behavior which changes non-universally. The behavior of the potentials $W_{\nu\nu}(R)$ beyond $R=r_0$ are universal so that the universal scalings can be extracted. We have verified that our numerical results are not sensitive to the precise location of this hard wall.

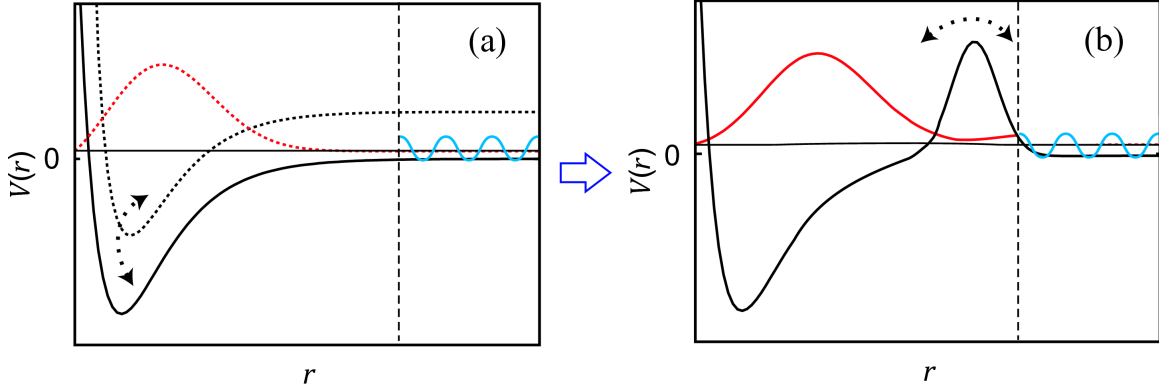


Figure 3.2: Comparison between a Feshbach resonance and a shape resonance. (a) A two-channel representation of a Feshbach resonance. The amplitude at short range (red curve) indicates the amplitude in the closed channel. The amplitude at large distance (blue curve) indicates the asymptotic scattering amplitude in the open channel. The dashed curve with arrows indicates that the two channels are coupled. (b) A schematic show of a shape resonance. One intuitive understanding of the connection to a Feshbach resonance is to consider that for both cases the scattering wavefunction is “coupled” to a short-range component: a component in another channel for a Feshbach resonance and a component behind the barrier for a shape resonance.

3.1.2 Three-body inelastic processes for identical bosons

Figure 3.3 shows our numerical calculations for K_3 when $a > 0$. We generated each curve by varying a at fixed $|r_{\text{eff}}|$, corresponding to tuning across a Feshbach resonance with a particular width. For $|a| \gg |r_{\text{eff}}|$, the rates retain the features predicted in Eq. (1.5), which is expected since the scaling of the inelastic rates should be still be determined by the Efimov physics when a is the largest length scale in the whole system. For $|a| < |r_{\text{eff}}|$, K_3 deviates from this formula and approaches the $(a^7 |r_{\text{eff}}|)^{1/2}$ behavior predicted in [136]. Experimental data for three-body recombination are available for $|r_{\text{eff}}| > a > 0$, where $|r_{\text{eff}}| \approx 1000$ a.u. The figure also shows that the rates seem to converge to a universal curve as $|r_{\text{eff}}|$ increases. Moreover, as the limit $r_0/|r_{\text{eff}}| \rightarrow 0$ is approached, the position of the first Efimov feature (minimum) as a function of $|a|/|r_{\text{eff}}|$ agrees reasonably well with the ZRP predictions from Refs. [136] and [137]. Recalling that r_{eff} is only about -200 a.u. for a 1 G wide resonance, we see that typical experiments will actually fall far from the ZRP results. Any experimental attempts to reduce the loss of the atoms near a Feshbach resonance by tuning the ratio

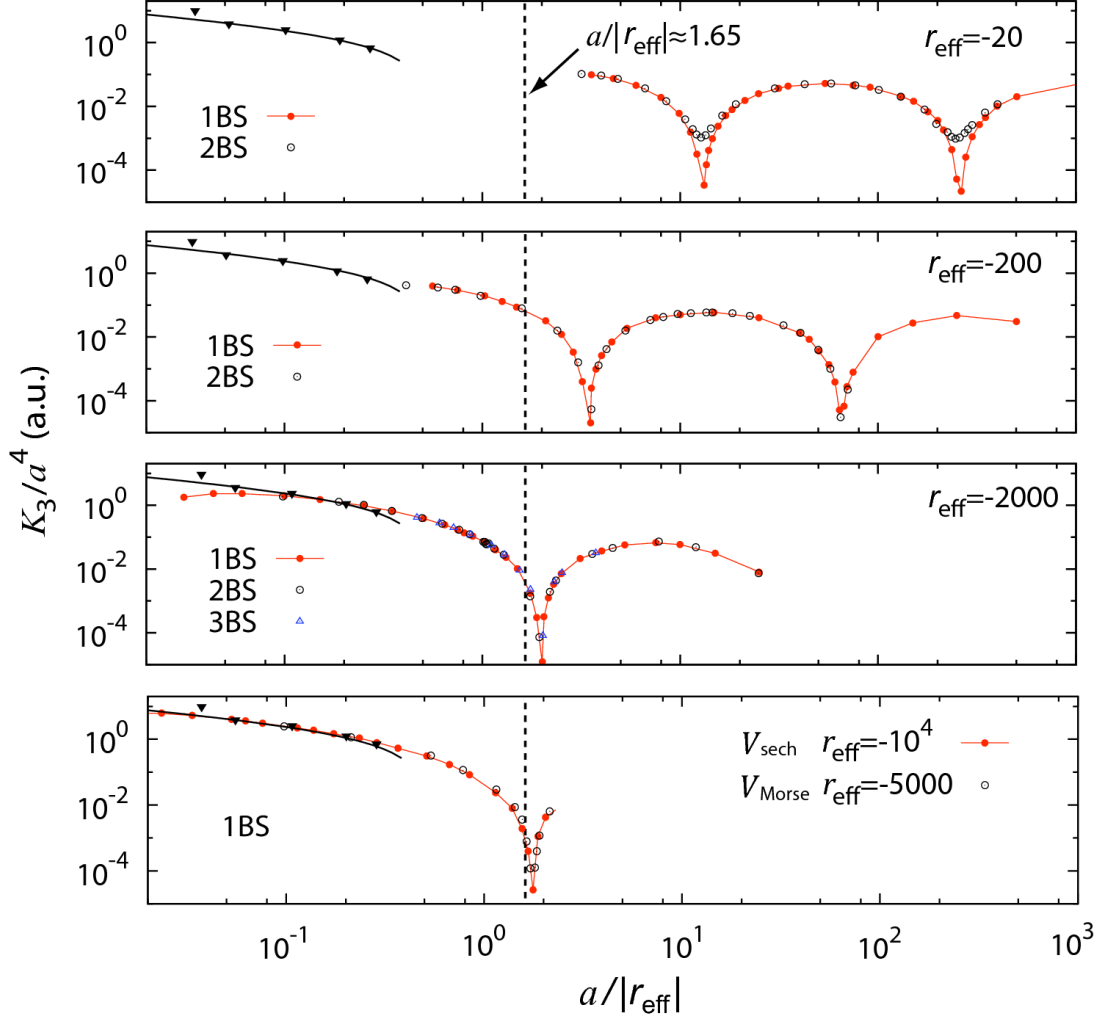


Figure 3.3: Ultracold three-body recombination rates for identical bosons ($a > 0$). The vertical dashed lines indicate the position of the first Efimov feature predicted in Refs. [136, 137]. Here we show K_3 with one or more two-body s -wave bound states (BS), including the analytical result from [136] (thick solid line) and the experimental data of Na at 907 G Feshbach resonance [45] (filled triangles), both scaled to match our data. The experimental data in the lowest panel we show the recombination rates calculated by using two different two-body potentials: the potential defined in Eq. (3.3) and a modified Morse potential². Here $r_0=50$ a.u.. Figure is adapted from Ref. [2].

$a/|r_{\text{eff}}|$ to reach a minimum position of K_3 need substantial calibration that considers the short-range physics.

²The modified Morse potential we use here is $V_{\text{Morse}}(r)=D((1 - e^{-(3r/r_0-1)})^2 - 1) + Be^{-2(3r/r_0-2)^2}$.

One interesting observation in Fig. 3.3 is that the minima in K_3 for more than one two-body bound state become deeper as $|r_{\text{eff}}|$ increases. In fact, if there is only a single two-body state and it is weakly-bound, K_3 is exactly zero at the minima. In realistic atomic systems, however, the recombinations into the deeply-bound two-body channels make K_3 finite at the positions of the minima. This can be clearly seen in Fig. 3.3 for relatively small $|r_{\text{eff}}|$. The deeper minima for larger $|r_{\text{eff}}|$ indicates the suppression of the recombinations into the deeply-bound states. As will be discussed later, this suppression near the narrow Feshbach resonances is the consequence of a new scaling behavior with large $|r_{\text{eff}}|$.

In Fig. 3.4, we show the recombination rates for $a < 0$ and the relaxation rates for $a > 0$. A common property for these three-body processes is that the couplings between the initial and final channels are significant only at short range. The inelastic transitions for these cases thus predominantly occur when the hyperradius $R \lesssim r_0$. As with the K_3 for $a > 0$, the numerical rates on each curve are calculated by changing a with a fixed r_{eff} . When $|r_{\text{eff}}|$ increases, the curves seemingly converge to a limit, and we compare the positions for the first peak in both K_3 ($a < 0$) and V_{rel} ($a > 0$) with their corresponding ZRP predictions. In particular, the K_3 ($a < 0$) prediction is based on the location of the first Efimov state in [137] and the V_{rel} prediction is based on the position of the first pole in the atom-dimer scattering length in [136].

One important feature in Fig. 3.4 is that the rate curves for each inelastic process have similar magnitude when multiplied by $|r_{\text{eff}}|$, which indicates a $1/|r_{\text{eff}}|$ suppression in both of the inelastic processes. To understand this new scaling behavior, we study the scaling of the corresponding adiabatic hyperspherical potentials.

Figure 3.5 shows the idealized $W_{\nu\nu}(R)$ for three identical bosons with $r_0 \ll |r_{\text{eff}}| \ll |a|$. Two numerical examples which have the same r_{eff} but different numbers of s -wave two-body bound states are shown in Fig. 3.6. The main effect of a large $|r_{\text{eff}}|$ on $W_{\nu\nu}(R)$ is that the weakly-bound atom-dimer potential is modified in the range $r_0 \ll R \ll |r_{\text{eff}}|$, taking the Coulomb-like form $c_0/(2\mu|r_{\text{eff}}|R)$ [136] instead of the usual attractive $1/R^2$ Efimov potential.

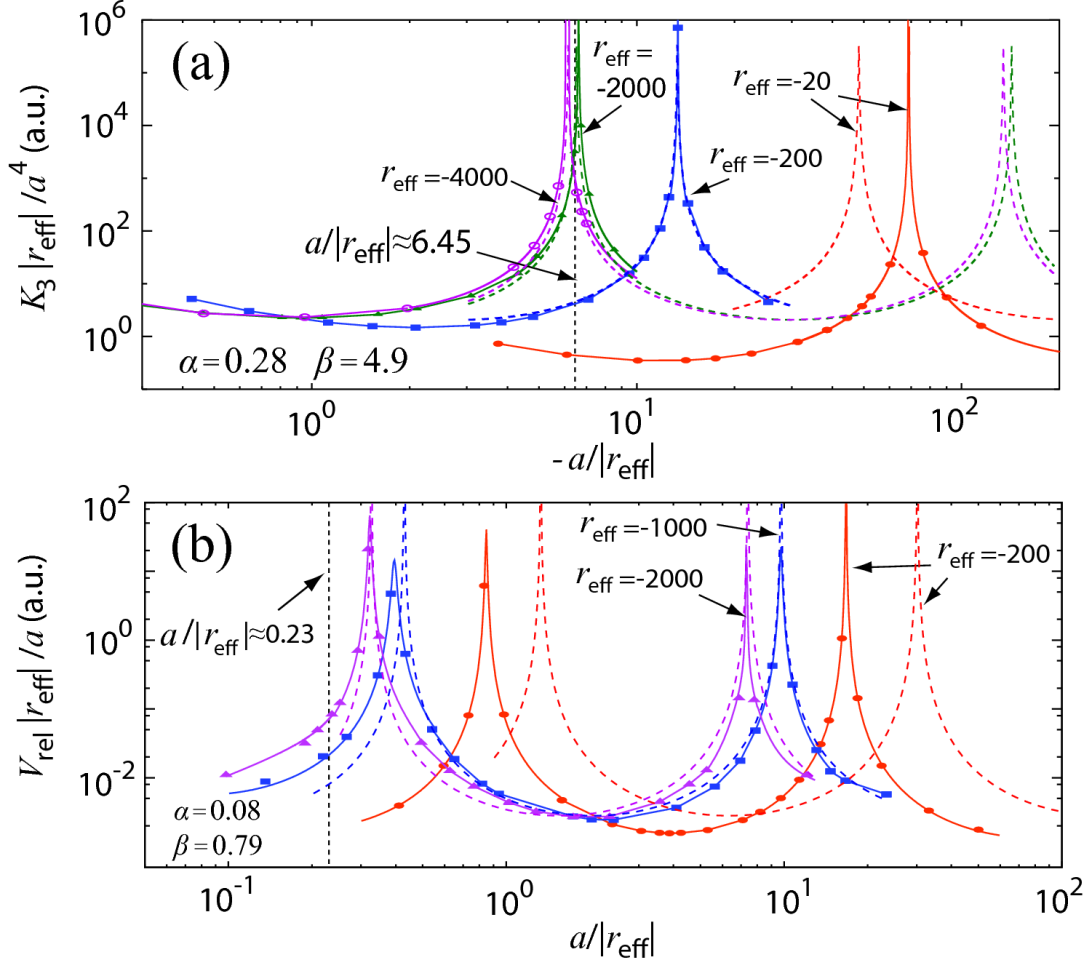


Figure 3.4: Ultracold three-body recombination rates ($a < 0$) (a) and relaxation rates ($a > 0$) (b) for identical bosons. The solid lines are to guide the eye, while the dashed lines are the analytical results from Equations. (3.9) and (3.4), respectively, using the α and β indicated from a fit in the limit $|r_{\text{eff}}| \rightarrow \infty$. In both cases, $r_0 = 50$ a.u.. Figure is adapted from Ref. [2].

The Coulomb-like behavior is actually the residue of a cancellation of potential $U_\nu(R)$ and the contribution from diagonal coupling $Q_{\nu,\nu}/2\mu_3$ in Eq. (2.68). Both of these two terms have same attractive $1/R^2$ leading behavior. Compared to the broad Feshbach resonances where the diagonal coupling $Q_{\nu,\nu}/2\mu_3$ is of a higher order $\sim 1/R^3$ in the region $r_0 \ll R \ll |a|$, the attractive $1/R^2$ behavior in $Q_{\nu,\nu}/2\mu_3$ observed here is a surprise, and it suppresses the Efimov behavior in the potential in the region $r_0 \ll R \ll |r_{\text{eff}}|$. Studies [9] have shown that this new behavior in $Q_{\nu,\nu}/2\mu_3$ comes from the short-range component of the two-body wavefunction,

which is generally absent in the ZRP treatments. Our numerical analysis indicates, however, that the coefficient c_0 is not universal — even changing from attractive to repulsive when more s -wave two-body states are added (see Fig. 3.6). This non-universality makes it even more surprising that the rates in Fig. 3.3 are universal, which we have verified by repeating the calculations with other model potentials and with varying numbers of deeply-bound two-body states.

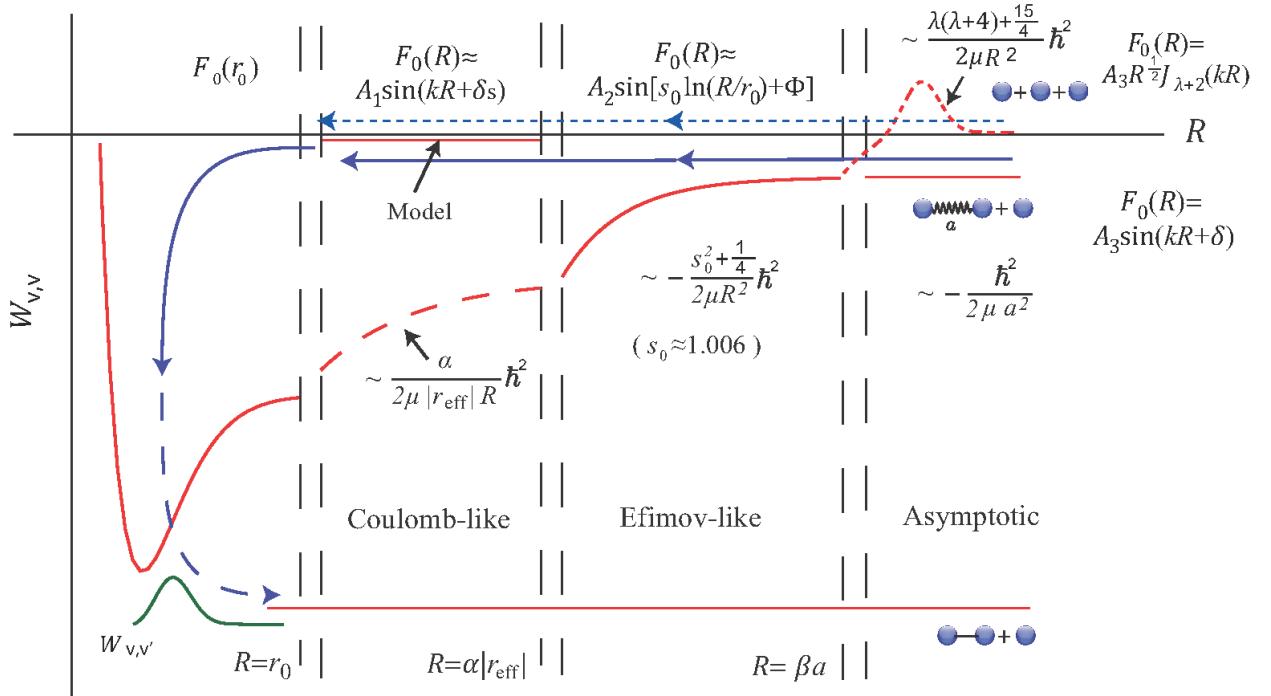


Figure 3.5: Schematic $W_{\nu\nu}(R)$ used to derive Eq. (3.4) and (3.9) with $r_0 \ll |r_{\text{eff}}| \ll |a|$. The difference in the potentials between the two processes is only in the asymptotic region. In the Coulomb-like region, we set the potential to be zero in our model since the potential can be attractive or repulsive (see Fig. 3.6) without changing the physical observables.

The idealized $W_{\nu\nu}(R)$ in Fig. 3.5 can be used to derive quantitative, analytic expressions for the collision rates by using the approach introduced in Sec. 2.6. By realizing that the Coulomb-like potential in the region $r_0 \ll R \ll |r_{\text{eff}}|$ is actually much weaker compared with the free-particle energy scale $\sim 1/R^2$, and with the extra confidence from the empirical

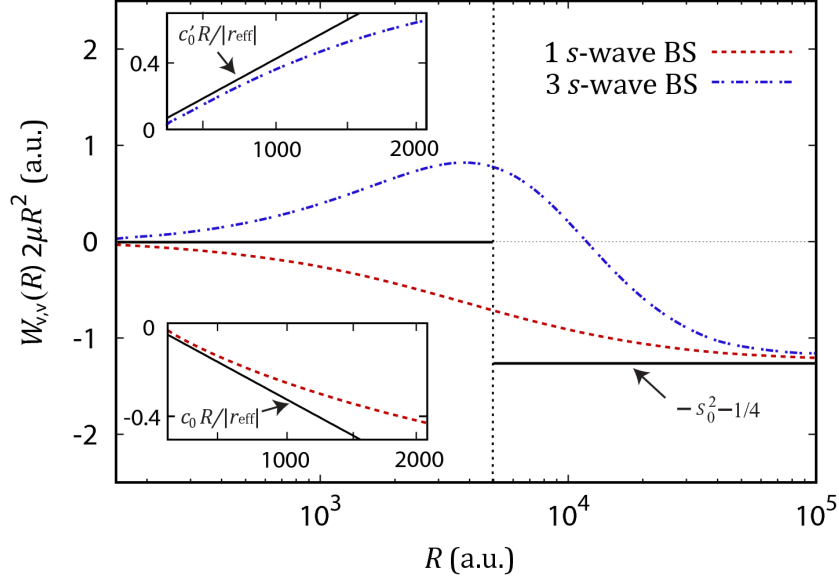


Figure 3.6: Adiabatic hyperspherical potentials near a narrow Feshbach resonance. Numerical $W_{\nu\nu}(R)$ multiplied by $2\mu R^2$ with $r_{\text{eff}} = -5000$ a.u. and $|a| = \infty$. The lower curve in from the calculations with a single $A_2 + A$ s -wave bound channel and the upper one is from the calculations with three $A_2 + A$ s -wave bound channel. The potentials in the region $R \ll |a|$ are not universal. When $R \gg |r_{\text{eff}}|$ the potentials recover the universal Efimov behavior. Figure is adapted from Ref. [2].

observation that the change of c_0 across zero does not affect the numerical rates, we simply set the potential to be zero in our model in the region $r_0 \ll R \ll |r_{\text{eff}}|$ to facilitate the derivations. The existence of the Coulomb-like region physically separates the short-range region and the Efimov region at larger hyperradii. This allows the parametrization of the short-range wavefunction by a complex three-body short-range scattering length A , where the real part $\text{Re}A$ characterizes the low-energy scattering property and the imaginary part $\text{Im}A$ accounts for the short-range inelastic transitions to deeply-bound two-body states. When $a > 0$, for instance, we calculate V_{rel} by considering incidence in the weakly-bound atom-dimer channel with the transition to the deeper two-body channels driven by non-adiabatic coupling localized in the region $R \lesssim r_0$. Following the procedure for deriving the analytic scaling laws introduced in Sec. 2.5, for $\beta a \gg \alpha |r_{\text{eff}}| \gg r_0$ the hyperradial scattering wavefunction is found by matching the analytic solutions from each region at the boundaries $\alpha |r_{\text{eff}}|$ and $\beta |a|$ [125, 133], where α and β reflect the uncertainty in defining these

boundaries [164] and will be determined by fitting our final expression to the numerical results. The relaxation rate is then obtained from $V_{\text{rel}}^{(B)} = \pi(1 - \mathcal{R})/\mu k$ where \mathcal{R} is the elastic scattering probability, yielding³

$$V_{\text{rel}}^{(B)} = \frac{2\sqrt{3}\pi\beta \sin 2\varphi_0 \sinh 2\eta}{\sin^2[s_0 \ln(|a/r_{\text{eff}}|) + \Phi + \varphi]} \frac{a}{m} \quad (3.4)$$

where

$$\tan \Phi = 2s_0 \frac{\alpha - \text{Re}A/|r_{\text{eff}}|}{\alpha + \text{Re}A/|r_{\text{eff}}|}, \quad (3.5)$$

$$\sinh \eta = \left| \frac{\text{Im}A}{\alpha r_{\text{eff}}} \right| \csc(2\varphi_0) \sin^2(\Phi + \varphi_0), \quad (3.6)$$

and

$$\varphi = s_0 \ln(\beta/\alpha) + \varphi_0, \quad (3.7)$$

$$\tan \varphi_0 = 2s_0. \quad (3.8)$$

with a virtually identical analysis, for $\beta|a| \gg \alpha|r_{\text{eff}}| \gg r_0$ $K_3^{(a<0)}$ can be derived to be,

$$K_3^{(a<0)} = \frac{12\sqrt{3}\pi^3\beta^4 \sin 2\varphi_0 \sinh 2\eta}{\sin^2[s_0 \ln(|a/r_{\text{eff}}|) + \Phi + \varphi]} \frac{a^4}{m}. \quad (3.9)$$

Note that α and β can take on different values than for $V_{\text{rel}}^{(B)}$ and that here $\tan \varphi_0 = s_0/2$. Similar expressions can be derived for other low-energy scattering observables.

The comparison of Equations (3.4) and (3.9) with Equations (1.7) and (1.6), respectively, shows that r_0 is replaced by $|r_{\text{eff}}|$, as might be expected, but there are also other modifications due to $|r_{\text{eff}}|$. These expressions justify, for instance, the scaling of the rates with $|r_{\text{eff}}|$ used in Fig. 3.4: the factor $\sinh 2\eta$ introduces a $|r_{\text{eff}}|^{-1}$ suppression. This reduction of η , which represents transitions to deeply-bound two-body states, is also responsible for the more pronounced minima in Fig. 3.3 as $|r_{\text{eff}}|$ increases for those calculations with multiple two-body bound states. The observation of interference minima in K_3 is thus more favorable near a narrow Feshbach resonance.

³For a detailed derivation procedure, please refer to Appendix B

Equations (3.4) and (3.9) further reveal the fundamental importance of the short-range three-body physics through their dependence on A in both η and Φ . This physics is absent from the zero-range treatments [136, 137], so the agreement in Figs. 3.3 and 3.4 between our numerical results and the ZRP predictions for the position of the first Efimov feature is rather fortuitous. We see from the arguments of \sin^2 in Eqs. (3.4) and (3.9) that A -independent Efimov feature positions — as predicted in [136, 137] — are found only in the limit $\text{Re}A/|r_{\text{eff}}| \rightarrow 0$. For the numerical examples in the numerical results shown above, $\text{Re}A \sim r_0$, but this need not be true in general. Particularly, if there is a short-range three-body resonance near the break-up threshold, the value of $\text{Re}A$ can, in principle, take any value from $-\infty$ to $+\infty$.

3.1.3 Three-body relaxation for fermionic system ($FF'F'$)

To get a sense of the effect of large $|r_{\text{eff}}|$ on fermion collisions, we have studied the three-body relaxation process $(FF')^* + F \rightarrow FF' + F$. For broad resonances $|r_{\text{eff}}| \simeq r_0$, the $a^{-3.33}$ suppression of $V_{\text{rel}}^{(F)}$ [62] originates from a repulsive barrier in the adiabatic potential

$$W_{\nu\nu}(R) \simeq \frac{p_0^2 - 1/4}{2\mu_3 R^2} \quad (3.10)$$

in the range $r_0 \ll R \ll a$ [67], where the universal constant $p_0 \approx 2.166$ is determined by the transcendental equation from the ZRP model

$$\sqrt{\frac{\pi}{2}} p_0 \cos\left(\frac{\pi}{2} p_0\right) - 2\sqrt{\frac{2}{3}} Q_{p_0-1/2}^{1/2}\left(\frac{\sqrt{3}}{2}\right) = \frac{R}{a} \sqrt{\pi} 3^{-1/4} \sin\left(\frac{\pi}{2} p_0\right), \quad (3.11)$$

by taking the limit $R/a \rightarrow 0$. The function $Q_l^m(x)$ is the Legendre function of the second kind. For finite values of R/a , p_0 becomes R -dependent and Eq. (3.11) can be used to calculate the adiabatic hyperspherical potentials.

When $|r_{\text{eff}}| \gg r_0$, however, $W_{\nu\nu}(R)$ is modified in the range $r_0 \ll R \ll |r_{\text{eff}}|$ by the emergence of a Coulomb-like potential, just as for bosons. Therefore, the repulsive barrier in that region is weakened, leading to enhanced vibrational relaxation. Moreover, when $a \ll |r_{\text{eff}}|$, the dependence of the rate on a is altered, much like for bosons with $a \ll |r_{\text{eff}}|$ in Fig. 3.3.

All of these effects can be seen in our numerical calculations shown in Fig. 3.7. For $a < |r_{\text{eff}}|$, relaxation scales as $(a/|r_{\text{eff}}|)^{-1}$, a much weaker suppression than for broad resonances. For $a > |r_{\text{eff}}|$, we can apply the same kind of analysis as for bosons, using the fact that the idealized potential behaves as in Eq. (3.10) for $|r_{\text{eff}}| \ll R \ll a$ and assuming the potential is zero for $r_0 \ll R \ll |r_{\text{eff}}|$:

$$V_{\text{rel}}^{(F)} = \frac{256\pi\sqrt{3}p_0^2 \text{Im}A/m}{(1 - 4p_0^2)(\text{Re}A/|\alpha r_{\text{eff}}|)^2 + (2p_0 + 1)^2} \left(\frac{\beta a}{|\alpha r_{\text{eff}}|} \right)^{1-2p_0}. \quad (3.12)$$

We thus recover the broad resonance scaling with a , $V_{\text{rel}}^{(F)} \propto (a/|r_{\text{eff}}|)^{-3.33}$, but with a much larger overall magnitude due to the dependence on r_{eff} .

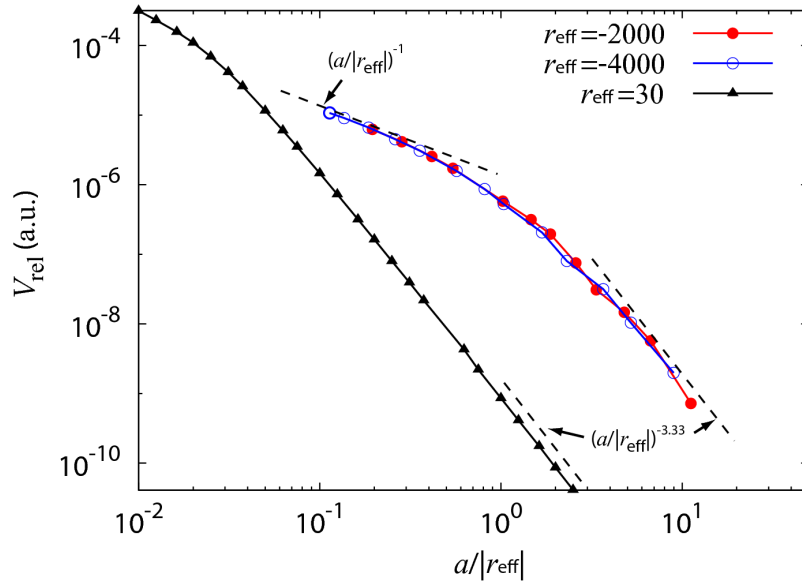


Figure 3.7: Relaxation rates for mixed-spin fermions with $a > 0$ and large $|r_{\text{eff}}|$. The relaxation rate for small $|r_{\text{eff}}|$ is also plotted, showing the same scaling with a but not with $|r_{\text{eff}}|$ since it is not in the universal limit. Figure is adapted from Ref. [2].

3.1.4 Adiabatic potentials with the zero-range potential model

Before finishing the discussion on the three-body Efimov physics near narrow Feshbach resonances, we will show the adiabatic hyperspherical potentials obtained with ZRP model and show their difference from the full numerical potentials. There have been some work

based on ZRP model by taking account of the effective-range correction [9][127, 161–163, 165], and particularly Thøgersen has shown that the ZRP model cannot represent three-body physics correctly without considering the short-range effect [9].

Here we extend the ZRP treatment introduced in Sec. 2.5 by including up to the effective-range term in the low-energy expansion of the two-body scattering phase shift to better represent the two-body scattering properties at finite energy:

$$\frac{\partial}{\partial r_{ij}}(r_{ij}\Psi) = \left(-\frac{1}{a} + \frac{1}{2}r_{\text{eff}}k_2^2\right)\Psi, \quad (r_{ij} \rightarrow 0) \quad (3.13)$$

where r_{ij} is the interparticle distance. Treating k_2^2 as proportional to two-body kinetic energy operator $\nabla_{\mathbf{r}_{ij}}^2$, the above boundary condition leads to the transcendental equation:

$$s_0 \cosh\left(\frac{\pi}{2}s_0\right) - \frac{8}{\sqrt{3}} \sinh\left(\frac{\pi}{6}s_0\right) = 12^{-\frac{1}{4}} \sinh\left(\frac{\pi}{2}s_0\right) \left(\frac{2R}{a} + \frac{r_{\text{eff}}}{R}s_0^2\right), \quad (3.14)$$

where s_ν is related to the adiabatic hyperspherical potential by

$$U_\nu = -\frac{s_\nu^2 + \frac{1}{4}}{2\mu_3 R^2}. \quad (3.15)$$

As mentioned earlier, without taking account of two-body short-range amplitude near r_0 , the diagonal coupling $Q_{\nu,\nu}/2\mu_3$ is of higher order than $1/R^2$ and is thus negligible. The lowest effective adiabatic potential $W_0(R)$ then behaves like

$$W_0(R) \simeq -\frac{c_0}{2\mu|r_{\text{eff}}|R} - \frac{1/4}{2\mu R^2}, \quad (3.16)$$

in the region $r_0 \ll R \ll |r_{\text{eff}}|$, with $c_0 \approx 1.68$. As mentioned previously, due to the largeness of $|r_{\text{eff}}|$, the potential in Eq. (3.16) is actually dominated by the $1/R^2$ term. The form of the zero-range three-body potential thus disagrees with the numerical result for the Coulomb-like potential by having an additional $1/R^2$. Further, the non-universal property of the three-body potentials seen in the numerical calculations in this region is not manifested in the ZRP potential at all. The behavior of the potentials for the continuum channels in the region $r_0 \ll R \ll |r_{\text{eff}}|$, however, agrees with the numerical results. They both behave like the free particle potentials as shown in Eq. (2.69). In the Efimov region $|r_{\text{eff}}| \ll R \ll |a|$

and asymptotic region $R \gg |a|$, the leading behavior of the zero-range three-body potentials agrees with the numerical results, as they both recover the behavior of the potentials for small $|r_{\text{eff}}|$ case.

3.1.5 Summary

We have studied ultracold collisions of three identical bosons and of mixed-spin fermions near a narrow Feshbach resonance using the connection between r_{eff} for the two-body interaction and the width of the resonance. We were able to identify the key modifications to the three-body adiabatic hyperspherical potentials and thus derive analytical expressions for the rate constants. From these analytical expressions, we showed that short-range three-body physics is still important, even near a narrow Feshbach resonance. This result is, perhaps, unfortunate for experimentalists since the positions of the Efimov features are, in general, still dependent on short-range physics, making it difficult to locate *a priori* a minimum of K_3 as suggested in [136]. On the other hand, our analysis has shown that bosonic recombination and relaxation to deeply-bound two-body states are suppressed near a narrow resonance which might prove beneficial experimentally. Similarly, our analysis suggests that long-lived weakly-bound FF' molecules are most easily obtained near a broad resonance.

3.2 Colliding Bose-Einstein condensates to observe Efimov physics

Though the Efimov effect is renowned by the emergence of infinite number of three-body bound states, in ultracold gases, however, evidence of the Efimov effect does not stem from observation of the bound spectrum. Rather, it traces the signature of such states through their impact on ultracold three-body scattering processes, usually through the loss of atoms or molecules. Therefore, the “smoking gun” for Efimov physics has become the observation of log-periodic features in any physical observable — not just the bound spectrum. Moreover, in most experimental observations to date [54–56, 144, 145], it is the comparison with theory that finally serves to establish the connection with Efimov physics.

Nevertheless, ultracold gases have a significant advantage over other weakly-bound systems such as the halo nuclei [18] and weakly interacting ^4He atoms, since the interatomic interactions — and thus the Efimov physics — can be controlled by Feshbach resonances. The signature of Efimov physics in experiments so far has been the appearance of features as a function of a that follow the predicted behavior as shown in Eqs. (1.5)–(1.7).

One of the most dramatic consequences of the Efimov effect is the infinite number of three-body features. Previous studies all assumed that these features only manifest as a function of the scattering length near zero collisional energy. Unfortunately, no more than two of these features in any single sequence have yet been observed, so the fundamental log-periodic behavior has not been experimentally verified. The main reasons are the technical challenges of fine tuning a near a Feshbach resonance to achieve extremely large $|a|$ and keeping the temperature T in the threshold regime $T \lesssim \hbar^2/2\mu_3 a^2$ to prevent thermal and unitarity effects [58].

Here we propose an entirely new way to observe the features associated with Efimov states: tuning the relative energy of two colliding Bose-Einstein condensates (BECs). The core of our proposal relies on the key insight that Efimov physics extends to finite energy three-body scattering observables. Current thinking is that Efimov physics appears only in

the a -dependence of *zero*-energy scattering observables. We show, however, that at fixed a the energy-dependent rate for three-body recombination of bosons B , $B+B+B \rightarrow B_2+B$, shows the log-periodic oscillations characteristic of Efimov physics. By extending the pathway analysis for explaining the *zero*-energy Efimov features in the three-body recombination rates [66] to finite energies, we connect the energy-dependent oscillations one-to-one with the previously known a -dependent oscillations and the Efimov states themselves. With the recently-realized ability to collide BECs [166–168] where the collision energy can be precisely tuned through a large range., we show that the atomic loss signals are ideal for observing Efimov oscillations through the three-body recombinations during BEC collisions.

3.2.1 Energy-dependent oscillations in K_3 for $a > 0$

Recalling that in Eq. (1.5) the three-body recombination rate K_3 for $a > 0$ features the log-periodic oscillations which reflects the Efimov effect, these features have been interpreted in the adiabatic hyperspherical representation in Refs. [49, 50, 66]. In particular, in these studies it has been shown that the coupling between the initial continuum channel and the final weakly-bound two-body channel is the most significant near $R \approx a$. The inelastic transition is thus expected to occur predominantly near $R \approx a$. As shown in Fig. 3.8, the inelastic transition leads to two different pathways for recombination, which finally give the log-periodic oscillations through interference [66]. In fact, these same two recombination pathways provide a natural way to understand how Efimov physics extends to finite energies. Using an analysis very similar to that presented in Ref. [66], we trace the pathways through the idealized adiabatic hyperspherical potentials for total orbital angular momentum $J=0$ and sketch the result in Fig. 3.9. As described in Ref. [66], these potentials are universal for $R \geq r_0$, so we expect the rates to be universal for collision energies E less than about $\hbar^2/2\mu_3 r_0^2$. For clarity, we present here a somewhat heuristic derivation that nevertheless captures the essential details and agrees with the fully-numerical results.

Similar to the recombination near zero energy, when $a \gg r_0$, recombination at finite en-

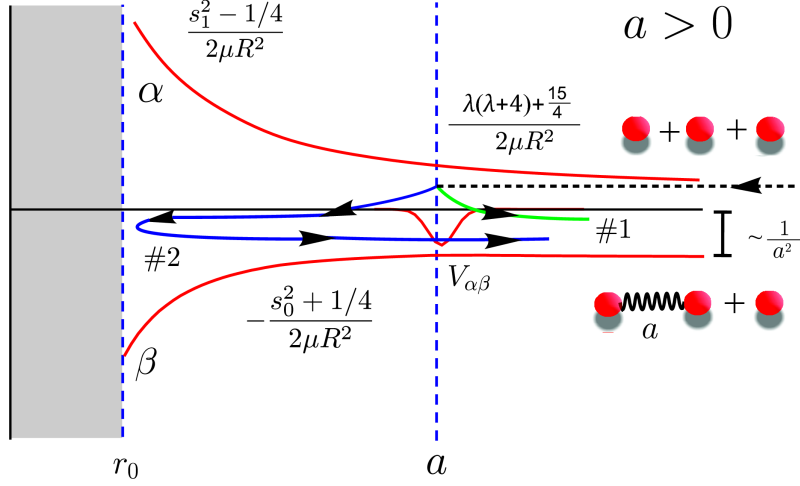


Figure 3.8: Schematic potentials and pathways for three-body recombination near zero energy ($a > 0$). The pathways are indexed as #1 (green) and #2 (blue). Channel α represents three free atoms; channel β , the atom plus dimer; and $V_{\alpha\beta}$, the coupling between the two channels. To clarify the channel each pathway is attached to, the pathways are drawn at different heights. But notice that they all have the same total energy.

ergies occurs predominantly at $R \approx a$ which leads to the two pathways indicated in Fig. 3.9. We can write the amplitudes for these two pathways as $\mathbf{A}_j = A_j e^{i\phi_j}$; A_j^2 includes the probability both for the three free particles to get from $R = \infty$ to $R \approx a$ and for the transition to the atom-dimer channel at $R \approx a$. Near zero energy, A_j mainly results from tunneling and scales like $k^2 a^2$ [66], where $k = \sqrt{2\mu_3 E}/\hbar$ is the three-body incident wavenumber. For higher energies such that $a^{-1} \ll k \ll r_0^{-1}$, the A_j are essentially independent of both a and k .

The phases ϕ_j from Fig. 3.9 can be obtained via the WKB approximation [66]. Since the recombination probability P is proportional to $|\mathbf{A}_1 + \mathbf{A}_2|^2$, only the phase difference matters, giving:

$$\begin{aligned} \phi_1 - \phi_2 = & \sqrt{k^2 a^2 + s_0^2} - \sqrt{k^2 a^2 - s_1^2} - \sqrt{k^2 r_0^2 + s_0^2} - s_0 \ln \left(\frac{s_0 + \sqrt{k^2 a^2 + s_0^2} r_0}{s_0 + \sqrt{k^2 r_0^2 + s_0^2} a} \right) \\ & + \Phi' - \frac{\pi}{2} s_1 + s_1 \tan^{-1} \left(\frac{s_1}{\sqrt{k^2 a^2 - s_1^2}} \right). \end{aligned} \quad (3.17)$$

For identical boson systems, $s_0=1.006$ and $s_1=4.46$ which are determined by Eq. 2.73. Since

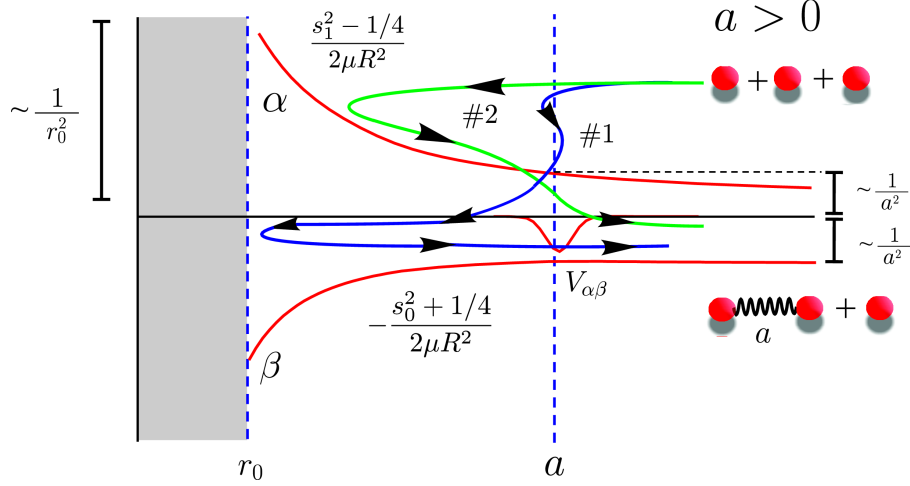


Figure 3.9: Schematic potentials and pathways for three-body recombination at finite energy ($a > 0$, $J = 0$). The pathways are indexed as #1 (blue) and #2 (green). Channel α represents three free atoms; channel β , the atom plus dimer; and $V_{\alpha\beta}$, the coupling between the two channels. Figure is adapted from Ref. [11]

the Efimov effect is more favored in a heteronuclear system of two heavy identical bosons and one distinguishable particle [169] in the sense that the value of s_0 is larger which gives smaller spacing between the Efimov features, we will particularly discuss the energy-dependent Efimov features for a experimentally realizable atomic system: Cs+Cs+Li. The universal constants in this system are determined as $s_0=1.85$ and $s_1=2.76$, by the following transcendental equation:

$$\sqrt{\frac{\pi}{2}} i s_0 \cosh\left(\frac{\pi}{2} s_0\right) + C_1 Q_{i s_0 - 1/2}^{1/2} \left(\sqrt{\frac{m_{\text{Li}} + m_{\text{Cs}}}{m_{\text{Cs}}}} C_1 \right) = i C_2 \frac{R}{a} \sqrt{\frac{\pi}{2}} \sinh\left(\frac{\pi}{2} s_0\right), \quad (3.18)$$

when the limit $R/a \rightarrow 0$ is taken. The constant s_1 is the lowest solution of Eq. (3.18) after replacing s_0 by $i s_1$. The mass-dependent coefficients C_1 and C_2 are

$$C_1 = \sqrt{\frac{m_{\text{Li}} m_{\text{Cs}} (m_{\text{Li}} + 2m_{\text{Cs}})}{(m_{\text{Li}} + m_{\text{Cs}})^3}}, \quad C_2 = \frac{\sqrt{m_{\text{Li}} + m_{\text{Cs}}}}{[m_{\text{Li}} (m_{\text{Li}} + 2m_{\text{Cs}})]^{1/4}}, \quad (3.19)$$

where the masses m_{Li} and m_{Cs} are the masses for Li and Cs atoms, respectively.

For incident energies such that $a^{-1} \ll k \ll r_0^{-1}$, the phase difference in Eq. (3.17) can be simplified as

$$\phi_1 - \phi_2 = -s_0 \ln(kr_0) + \Phi \quad (3.20)$$

to a good approximation (Φ combines Φ' with other universal constants for compactness). Using $K_3 \propto P/k^4$, the recombination rate in this energy range is thus

$$K_3 \propto k^{-4} [c_1 + c_2 \sin^2(-s_0 \ln(kr_0) + \Phi)], \quad (3.21)$$

where c_1 and c_2 can be written in terms of A_1 and A_2 . They can also be obtained — along with Φ — by fitting to the numerically-obtained K_3 .

Equation (3.21) thus summarizes one of our main results in this section: energy-dependent log-periodic oscillations that are intimately connected with Efimov physics. An important feature of Eq. (3.21) is that the oscillatory structure in the energy range $a^{-1} \ll k \ll r_0^{-1}$ is independent of a . So, the energy dependence measured at different, convenient a can, in principle, be combined to produce the full energy range.

The one-to-one connection between the well-known a -dependent oscillations at zero energy and the E -dependent oscillations from Eq. (3.21) is contained in Eq. (3.17) but is more easily seen in Fig. 3.10. Figure 3.10 shows Eq. (3.17) through the whole energy range $0 < k \lesssim r_0^{-1}$ where recombination is expected to be universal. Note that Eq. (1.5) applies in the lower left half of Fig. 3.10 while Eq. (3.21) applies in the upper right half.

One interesting observation in Fig. 3.10 is that each oscillation in E corresponds with one oscillation in a at zero energy. Since the number of the Efimov bound states is determined by a , it is natural to make a connection between the bound states and the energy-dependent oscillations. This connection can be understood qualitatively by the following arguments. In the phase difference expression Eq. (3.17), the log term gives the energy-dependent log-period oscillations in the recombination probability. In the energy range $0 < k < 1/r_0$, the number of oscillations n are given by the change of the phase difference $\phi_1 - \phi_2$:

$$n \approx \left\lfloor \frac{s_0}{\pi} \ln(|a|/r_0) \right\rfloor, \quad (3.22)$$

which is same as the number of Efimov bound states given by Eq. (1.3). Since the energy separation for each energy-dependent oscillation is same as the separation between the

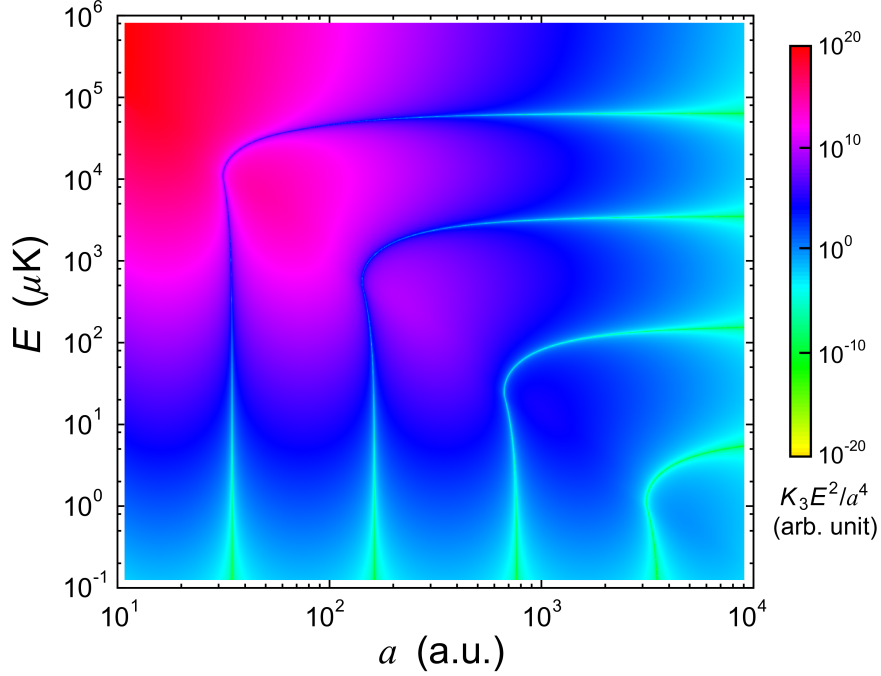


Figure 3.10: The $J=0$ recombination rate K_3 at finite energies⁵. The rate is scaled as $K_3 E^2 / a^4$ to emphasize the Efimov oscillations, especially the connection between the a -dependence and the E -dependence from equations (1.5) and (3.21), respectively. Equation (3.17) was used with Cs+Cs+Li masses, $\Phi'=0$, and $r_0=15$ a.u.. The amplitudes of the two interfering pathways were assumed equal to emphasize the oscillations. Figure is adapted from Ref. [11].

bound states, a one-to-one correspondence between the energy-dependent oscillations and the Efimov bound states can be made.

Before continuing our discussion, we want to emphasize that our results are not in the category of “finite-energy corrections”. Though there are theoretical works addressing the finite-energy effect in the recombination rates for better fitting the experimental results measured at finite temperature [53, 138–140], our work is fundamentally different. In these works, the energy range considered is limited to $E \lesssim 1/2\mu_3 a^2$, where the recombination rate is still in the zero-energy regime and the finite-energy effect can be treated as corrections. The energy-dependent oscillations we are showing here, however, appear at much higher energy where the energy-dependence is no longer perturbative.

⁵Collision energies are reported in Kelvin using the conversion $T = E/k_b$. 1 Kelvin corresponds to 3.1668×10^{-6} a. u. of energy.

3.2.2 Higher partial wave contributions

The discussion so far has been limited to $J=0$, which is the dominant contribution near zero scattering energy for identical bosons. At finite collision energies, however, the total K_3 has contributions from $J>0$ that must be included. Should these higher partial waves also support Efimov states — which does occur in some systems [169] — then the corresponding oscillations in their partial recombination rates would generally add out-of-phase, washing out all evidence of Efimov physics. In fact, this is why no such oscillations in the total rate have been observed in electron-polar molecule scattering, where the scattering potentials also have an attractive $1/R^2$ behavior for several angular momenta [130, 170]. In the cases we consider here, however, there are no attractive $1/R^2$ Efimov potentials for $J>0$ [169]. The higher partial wave contributions are expected to behave smoothly without oscillatory structures across the energy range we are considering here. Thus, the oscillatory structure predicted in Eq. (3.21) and shown in Fig. 3.10 should be visible in the total rate.

Besides $J>0$ contributions, higher collision energies also require taking into account the thermal distribution of velocities [58, 171], if considering the conventional loss experiments on quantum gases. In this case, the energy-dependent rate $K_3(E)$ must be converted to a temperature-dependent rate $\langle K_3(T) \rangle$ via thermal averaging [171].

To verify the predictions above, we calculate K_3 by solving the three-body Schrödinger equation numerically in Smith-Whitten hyperspherical coordinates [109, 110] (see Sec. 2.2, 2.3 and 2.4). We first consider three bosonic ^{133}Cs atoms, assuming a pair-wise sum of short-range, single-channel, two-body model potentials in the following form:

$$V_{ij} = D \operatorname{sech}(r_{ij}/r_0)^2. \quad (3.23)$$

To illustrate the effect of higher partial waves, we have calculated recombination for the lowest two angular momenta relevant for recombination. For Cs atoms they are the $J = 0^+, 2^+$ contributions. The results are shown in Fig. 3.11(a). To more clearly show the oscillations, we plot $K_3 E^2$, which is proportional to the recombination probability. The oscillatory modu-

lation in the total rate, though small, is still discernible. Upon thermal averaging, however, the oscillations are no longer apparent. Also, three identical bosons require temperature changes of $e^{2\pi/s_0} \approx 515$ to observe a single period, which is experimentally challenging at the present time [172].

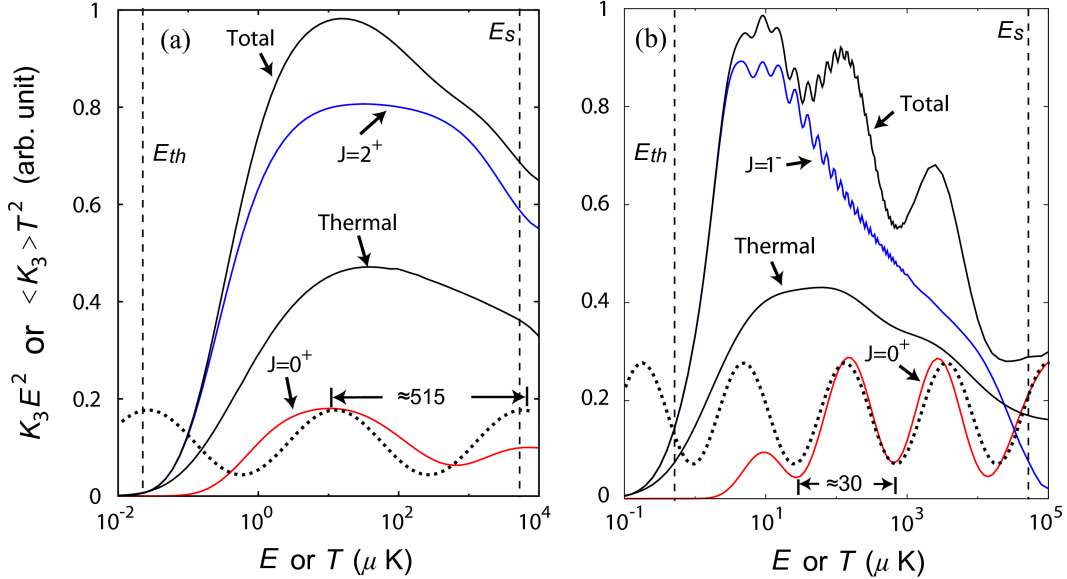


Figure 3.11: Scaled numerical three-body recombination rates $K_3(E)E^2$ for (a) Cs+Cs+Cs with $a_{\text{Cs+Cs}}=8000$ a.u. and (b) Cs+Cs+Li with $a_{\text{Cs+Li}}=5000$ a.u.. The lowest two contributing angular momenta are shown along with their sum and its thermal average, $\langle K_3(T) \rangle T^2$. The dotted lines are from Eq. (3.21). The expected lower and upper limit of universal behavior are indicated by the dashed lines at $E_{th} \approx \hbar^2/2\mu_3 a^2$ and $E_s \approx \hbar^2/2\mu_3 r_0^2$, respectively. The rapid oscillations in the $J = 1^-$ contribution in (b) are not related to the Efimov effect. Figure is adapted from Ref. [11].

This factor can be reduced, however, by seeking three-body systems with larger s_0 . Fortunately, as already mentioned previously, this is readily achieved for two heavy, identical bosons with mass m_B and a third lighter partner with mass m_X and resonant interactions are between the heavy-light pairs. In principle, the larger the mass ratio m_B/m_X the better, given that the mass ratio is still smaller than the critical value where the Efimov effect starts appearing in the higher partial waves. For two identical bosons and one light atom, the Efimov effect never shows up in $J = 1^-$ partial wave for any mass ratio [169] and

the next lowest partial wave which can have an Efimov effect is $J = 2^+$ which gives the critical mass ratio about 38.6 [169]. One of the best available candidates is the Cs+Cs+Li system with a period of $e^{2\pi/s_0} \approx 30$ for the energy-dependent oscillations. The lowest partial wave contributions are from $J = 0^+, 1^-$ in this case. The numerically-calculated Cs+Cs+Li recombination rates are shown in Fig. 3.11(b). The oscillatory Efimov structure appears very clearly in the total rate, but is still virtually eliminated by thermal averaging. The period of the oscillations has indeed shrunk to about 30, making the observation of multiple cycles much more accessible experimentally.

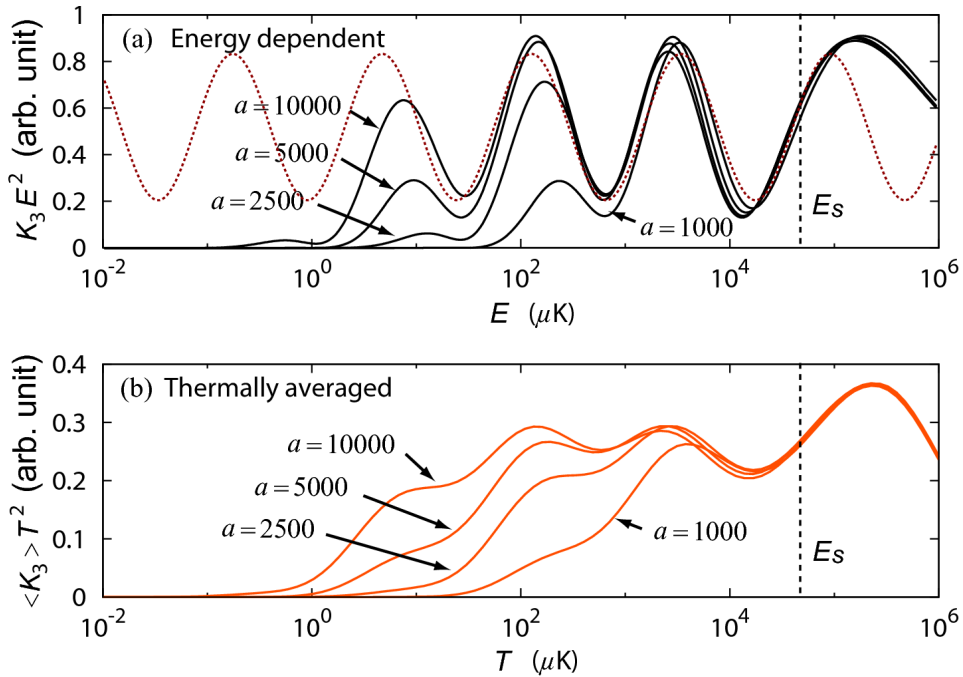


Figure 3.12: The $J = 0^+$ contribution to $K_3(E)E^2$ for Cs+Cs+Li with different scattering length ($a_{\text{Cs+Li}}$). (a) Energy-dependent rates. (b) Thermally-averaged results. At $a_{\text{Cs+Li}}=1000$ a.u., the two oscillations as E decreases from E_s correspond to the ground and first excited Efimov states, respectively. At $a_{\text{Cs+Li}}=5000$ a.u., the second excited Efimov state appears since the number of oscillations increases to three. The dotted line is from Eq. (3.21). Figure is adapted from Ref. [11].

While Fig. 3.11 verifies our basic prediction of energy-dependent oscillations, it does not address the interplay between a and E . Figure 3.12, however, shows the numerical results that confirm this component of our prediction. It shows that as a increases, the Efimov

features appear at lower energies — in agreement with Eq. (3.17) and Fig. 3.10.

3.2.3 Three-body recombination in BEC collisions

To avoid the thermal averaging that obscures the Efimov features, we propose to measure the losses during collisions of two BECs instead of simply raising the temperature in thermal gases. Using this approach, the collision energy can be set accurately and can be tuned easily through orders of magnitude with a so-called BEC accelerator [173]. Due to the complicated many-body dynamics during such a collision, though, it is not completely obvious that the final atomic loss will correctly reflect the Efimov physics we seek. We thus solved the following coupled time-dependent mean-field equations for colliding transversely-confined condensates with the loss terms [174] corresponding to all possible recombination processes:

$$\begin{aligned}
 i\frac{\partial}{\partial t}\phi_{\text{Cs}}(\vec{r}_{\text{Cs}}, t) = & \left(h_{\text{Cs}} + \frac{2\pi a_{\text{CsCs}}}{\mu_{\text{CsCs}}}(N_{\text{Cs}} - 1)|\phi_{\text{Cs}}|^2 + \frac{2\pi a_{\text{CsLi}}}{\mu_{\text{CsLi}}}N_{\text{Li}}|\phi_{\text{Li}}|^2 \right) \phi_{\text{Cs}} \\
 & - \frac{i}{4}(N_{\text{Cs}} - 1)(N_{\text{Cs}} - 2)K_{3,\text{CsCsCs}}|\phi_{\text{Cs}}|^4\phi_{\text{Cs}} \\
 & - \frac{i}{2}(N_{\text{Cs}} - 1)N_{\text{Li}}K_{3,\text{CsCsLi}}|\phi_{\text{Cs}}|^2|\phi_{\text{Li}}|^2\phi_{\text{Cs}} \\
 & - \frac{i}{4}N_{\text{Li}}(N_{\text{Li}} - 1)K_{3,\text{CsLiLi}}|\phi_{\text{Li}}|^4\phi_{\text{Cs}}, \tag{3.24}
 \end{aligned}$$

$$\begin{aligned}
 i\frac{\partial}{\partial t}\phi_{\text{Li}}(\vec{r}_{\text{Li}}, t) = & \left(h_{\text{Li}} + \frac{2\pi a_{\text{LiLi}}}{\mu_{\text{LiLi}}}(N_{\text{Li}} - 1)|\phi_{\text{Li}}|^2 + \frac{2\pi a_{\text{CsLi}}}{\mu_{\text{CsLi}}}N_{\text{Cs}}|\phi_{\text{Cs}}|^2 \right) \phi_{\text{Li}} \\
 & - \frac{i}{4}(N_{\text{Li}} - 1)(N_{\text{Li}} - 2)K_{3,\text{LiLiLi}}|\phi_{\text{Li}}|^4\phi_{\text{Li}} \\
 & - \frac{i}{2}(N_{\text{Li}} - 1)N_{\text{Cs}}K_{3,\text{CsCsLi}}|\phi_{\text{Cs}}|^4\phi_{\text{Li}} \\
 & - \frac{i}{4}N_{\text{Cs}}(N_{\text{Cs}} - 1)K_{3,\text{CsLiLi}}|\phi_{\text{Cs}}|^2|\phi_{\text{Li}}|^2\phi_{\text{Li}}, \tag{3.25}
 \end{aligned}$$

where ϕ_{Cs} and ϕ_{Li} are the mean-field wavefunction for Cs and Li BECs, N_{Cs} and N_{Li} are the number of Cs and Li atoms, respectively. The reduced mass μ_{AB} and scattering length a_{AB} are between the two atoms indicated by the subscripts. The physical density n for a BEC can be obtained by simply multiplying the number of atoms by the corresponding mean-field wavefunction. The single-particle Hamiltonian h_{Cs} and h_{Li} are defined as the

following, which includes kinetic energy operator and a transverse harmonic trap:

$$h_{\text{Cs}} = -\frac{1}{2m_{\text{Cs}}}\nabla_{\text{Cs}}^2 + \frac{1}{2}m_{\text{Cs}}\omega_{\text{Cs}}\rho_{\text{Cs}}^2, \quad (3.26)$$

$$h_{\text{Li}} = -\frac{1}{2m_{\text{Li}}}\nabla_{\text{Li}}^2 + \frac{1}{2}m_{\text{Li}}\omega_{\text{Li}}\rho_{\text{Li}}^2, \quad (3.27)$$

where m_{Cs} and m_{Li} are the atomic masses, ω_{Cs} and ω_{Li} are the transverse trapping frequencies, ρ_{Cs} and ρ_{Li} are the transverse radius of the condensates.

The three-body collision energies are assumed to be time-independent and are calculated as the total initial kinetic energy in the center of mass frame of the three relevant atoms. We take $a_{\text{Cs+Li}}=5000$ a.u., which produces three full oscillations, yet is still likely achievable experimentally. We use typical values for $a_{\text{Cs+Cs}}$ and $a_{\text{Li+Li}}$, namely 500 a.u. and 4 a.u., respectively [175, 176]. The condensate collision takes place within a quasi-one-dimensional geometry with transverse trapping frequencies of 800 Hz for ^{133}Cs and 2240 Hz for ^7Li [177] and no longitudinal confinement.

In Fig. 3.13, we show the results of the mean-field calculations. Figure 3.13(a) shows the Cs and Li densities as a function of time for a typical collision and the time-dependent loss associated with it. We find that Cs and Li are lost at approximately a 2:1 ratio at all energies we have calculated, indicating that the Cs+Cs+Li process dominates. The number of atoms lost, though, depends on the interaction time as well as the recombination rates. If the relative velocity of the condensates is initially v , then the interaction time scales as $v^{-\gamma}$ with γ between 0 (corresponding to the condensates sticking to each other) and 1 (the condensates pass without interacting). Since K_3 itself scales like E^{-2} , the final loss will scale like $E^{-2-\gamma/2}$. Figure 3.13(b) thus shows the loss multiplied by $E^{2+\gamma/2}$ for $\gamma=0,1$. The Efimov oscillations are seen in both cases with only the relative magnitudes of the peaks changing slightly.

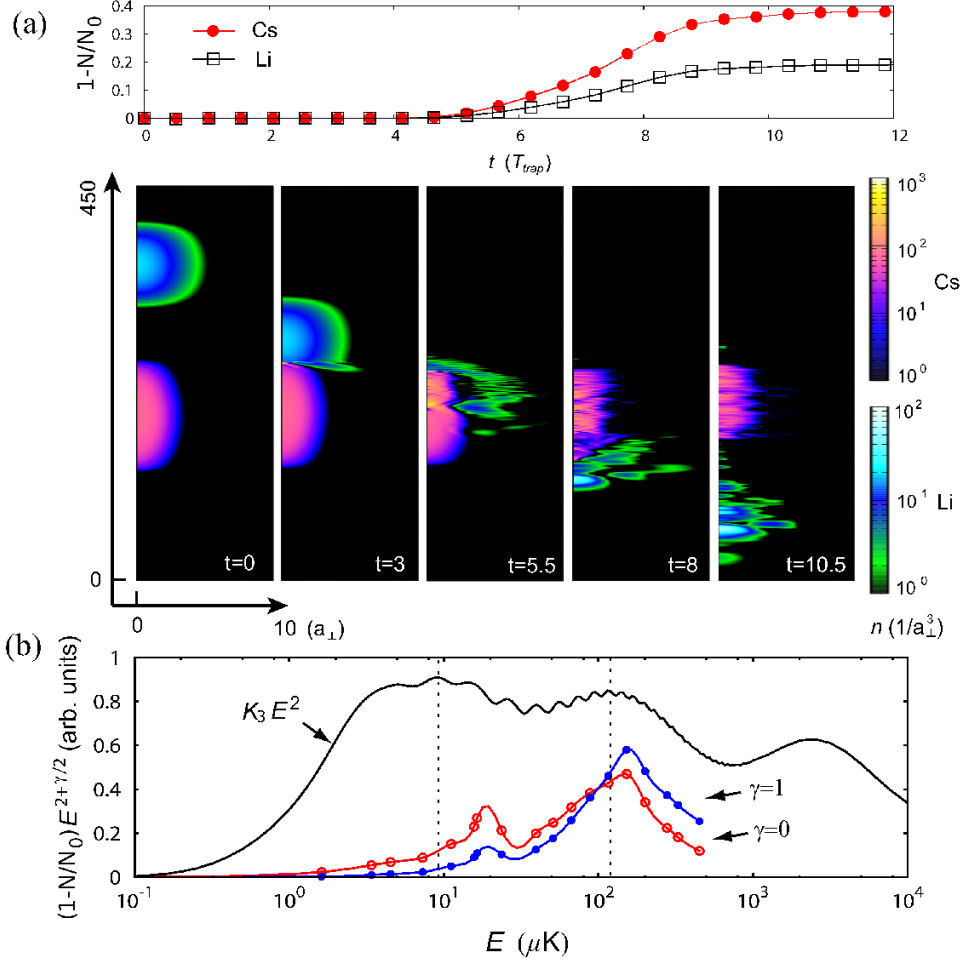


Figure 3.13: Atomic losses during BEC collisions. (a) The time-dependent fractional atom loss, $1 - N(t)/N_0$, during the collision of a Li BEC with a Cs BEC at $E=4 \mu\text{K}$ along with snapshots of the atomic densities in the overall center-of-mass frame. Though the condensate dynamics are quite complicated, the loss is always smooth during the collision. Initially, there are 10^4 atoms in each condensate and $a_{\perp} = \sqrt{\hbar/m_{\text{Cs}}\omega_{\text{Cs}}}$ with $\omega_{\text{Cs}} = 2\pi \times 800$ Hz. (b) The final loss fraction of Cs atoms is multiplied by $E^{2+\gamma/2}$ (filled and open circles) to show the Efimov oscillations. Oscillations are seen in both cases, and their positions correspond to those seen in $K_3 E^2$ (no symbols).

3.2.4 A multi-channel approach for recombination at finite energies

In Sec. 3.2.1, the pathway analysis gives a simple formula for the three-body recombination at finite energies. The method is intuitive, although heuristic. By using the adiabatic hyperspherical representation, here we formulate a more rigorous treatment for the three-

body recombination at finite energies.

Noticing that the three-body recombination is a multi-channel phenomenon when $a > 0$, the single-channel approach used for deriving the recombination rate when $a < 0$ in Sec. 3.1 is not adequate for the present case. To this end, we develop a simple multi-channel model which provides a rigorous and convenient description for the recombination process we are interested in.

Our model for applying multi-channel treatment is similar to the single-channel case, where the adiabatic potentials are divided into different regions. For simplicity here we only consider the broad Feshbach resonances for $J = 0^+$. The schematic adiabatic potentials are shown in Fig. 3.14. The behavior of the adiabatic potentials in the Efimov region

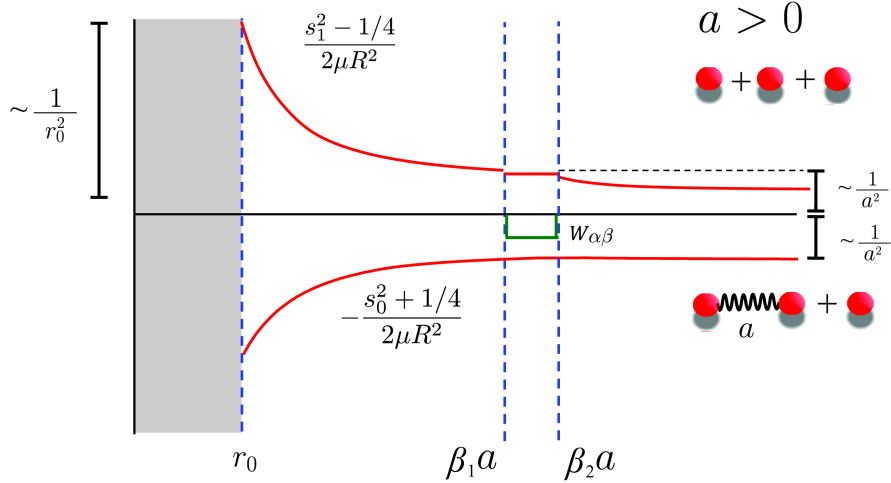


Figure 3.14: Schematic adiabatic hyperspherical potentials used in the multi-channel model for $a > 0$.

($r_0 \ll R \ll a$) is determined by Eq. (2.75). In the asymptotic region ($R \gg a$), the behavior is determined by Eq. (2.69) and (2.70).

The main idea for this approach is to write down the multi-channel hyperradial solutions in each region and extract the scattering matrix \mathbf{S} after matching the solutions at all of the boundaries. The success of the pathway analysis in the previous sections as well as in Refs. [66] indicates that the basic idea in the pathway analysis — the transitions occur pre-

dominantly over certain range of the hyperradii — is concrete rather than speculative. This idea is further supported by the numerical study on the scaling behavior of the non-adiabatic couplings [164]. In particular, for $a > 0$ recombination, the non-adiabatic couplings between the initial (three-body continuum channels) channels and the final channel (weakly-bound atom-dimer channel) peak near $R = a$. We thus model that the couplings are non-zero only in the region $\beta_1 a \leq R \leq \beta_2 a$, where the parameters β_1 and β_2 can be adjusted to give better agreement with the full numerical results. Outside this region the channels are treated as uncoupled. As will be presented in detail in Appendix C, the scattering matrix is written in terms of the multi-channel solutions in each hyperradial region, which gives a general expression for K_3 valid for the whole range of energy where the rate is universal ($k \ll 1/r_0$). In particular, by using the two-channel approximation, the $J = 0$ partial three-body recombination rate acquires a simple analytical form when the scattering energy is in the range $1/a \ll k \ll 1/r_0$:

$$K_3 = \frac{192\pi^2}{\mu_3 k^4} \left| \frac{e^{4c\beta_1} - e^{4c\beta_2}}{2ie^{2c(\beta_1+\beta_2)} \cot(\phi_0 + s_1\pi/2) + e^{4c\beta_1} + e^{4c\beta_2}} \right|^2, \quad (3.28)$$

$$\tan \phi_0 = \tanh \frac{\pi}{2} \tan(\Phi + \gamma - s_0 \ln \frac{kr_0}{2}), \quad (3.29)$$

$$\gamma = \tan^{-1} \frac{\text{Im}[\Gamma(is_0)]}{\text{Re}[\Gamma(is_0)]}, \quad (3.30)$$

where $c = c_{1,0} \approx 0.17$ as listed in Appendix C. The short-range phase Φ is the same as those in Eq. (1.5)-(1.7). Though formally different from Eq. (3.21), Eq. (3.28) nevertheless features a series of log-periodic oscillations in K_3 , which is essentially the same as in Eq. (3.21).

In Fig. 3.15, we show the $J=0$ three-body recombination rates calculated with the multi-channel model with only the lowest three-body continuum channel included. The features resemble those in Fig. 3.10, with the difference in the period for both scattering length and energy since the present result is for identical bosons. There are some small unphysical structures in the plot near the region $E \approx 1/2\mu_3 a^2$, which are due to the discontinuous behavior of the potentials and the couplings used in our model. But these small defects do not change the features in the rates.

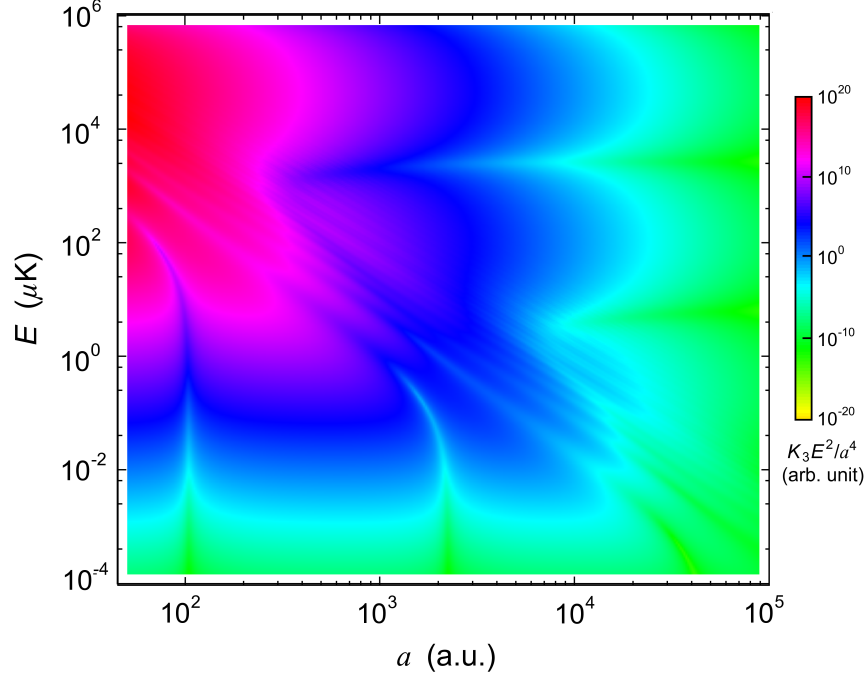


Figure 3.15: The $J=0$ recombination rate K_3 at finite energies calculated by using the multi-channel model ($a > 0$). Only the lowest three-body continuum channel is included. The rate is scaled as K_3E^2/a^4 to emphasize the Efimov oscillations.

By including more continuum channels in the multi-channel model, we have calculated more accurate recombination rates than the two-channel approximations Eq. (3.21) and (3.28). In Fig. 3.16, we show the $J=0$ recombination rates calculated with the lowest three continuum channels. Compared with the energy-dependent oscillatory features in Fig. 3.15, the minima in the oscillations shown in Fig. 3.16 are less pronounced. This difference comes from the contributions from the higher continuum channels included in the multi-channel model.

Finally, it is easy to apply the model for higher partial waves once the constants in the couplings are extracted from the numerical potentials. The converged universal recombination rates at finite energy can then be calculated including all the necessary partial waves. In addition to their value in the theoretical study of universal physics, the results will be greatly helpful for the prediction of the losses in the quantum thermal gas experiments at

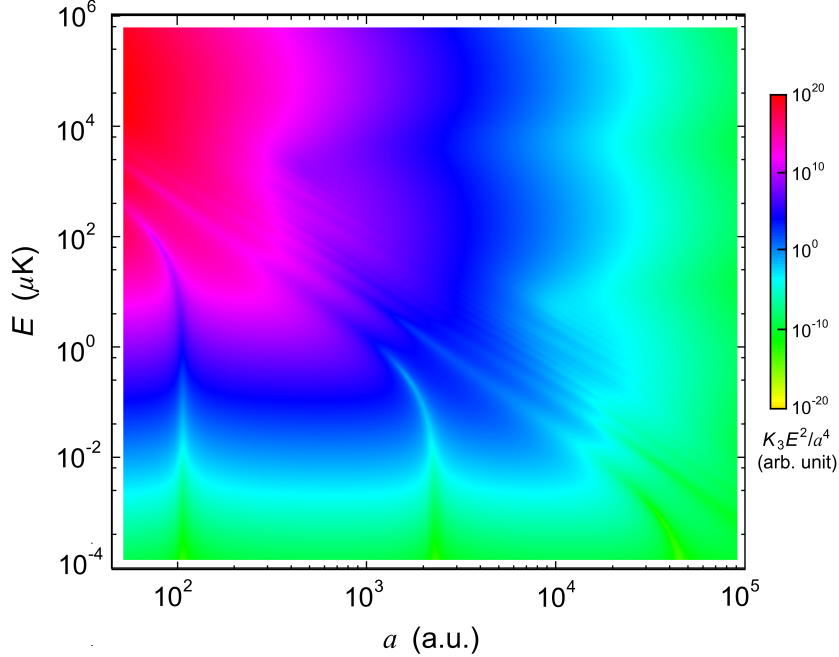


Figure 3.16: The $J=0$ recombination rate K_3 at finite energies calculated by using the multi-channel model ($a > 0$). The rate is scaled as $K_3 E^2 / a^4$ to emphasize the Efimov oscillations.

finite temperatures.

3.2.5 Summary

To summarize, we have identified a powerful new manifestation of the Efimov effect in the energy dependence of the three-body recombination rate. These features can be understood by either simple pathway analysis or more rigorous multi-channel formalism. They can be used to confirm the geometric scaling of Efimov physics — a property not experimentally seen so far due to the difficulty of changing the scattering length over many orders of magnitude. To take advantage of this new prediction, we proposed to utilize a novel new tool: the ability to controllably collide two Bose-Einstein condensates. This technique has promise for the study of few-body collisions at low energies beyond the ultracold regime.

3.3 Universal three-body physics at finite energy near Feshbach resonances

In Sec. 3.2, we have presented the manifestations of Efimov effect in the energy-dependence of K_3 for $a > 0$. It is natural to ask if such phenomena also persist for $a < 0$. Further, recalling that the scaling of K_3 for $a < 0$ near zero energy in Eq. (3.9) is modified near a narrow Feshbach resonance, one interesting question is that if and how this modification will show up in the energy dependence.

In Sec. 3.1, the adiabatic hyperspherical potentials are divided into the following universal scaling regions: the Coulomb-like region ($r_0 \ll R \ll |r_{\text{eff}}|$), the Efimov region ($|r_{\text{eff}}| \ll R \ll |a|$) and the asymptotic region ($R \gg |a|$). For three-body recombination, these regions become classically allowed at different ranges of collisional energies. Specifically, beyond the energy $E_{2b} = 1/\mu_3 a^2$, the Efimov region is classically allowed; beyond the energy $E_{\text{eff}} = 1/\mu_3 |\alpha r_{\text{eff}}|^2$ where $\alpha \approx 0.28$ is the constant appearing in Eq. (3.5)-(3.8), the Coulomb-like region becomes classically allowed. Since the adiabatic potentials and the non-adiabatic couplings have different scaling behavior in different regions, we expect that these scaling behavior will be reflected in the three-body recombination at different energy ranges.

In this section, we will show that for three-body recombination $B + B + B \rightarrow B_2 + B$ at fixed a ($a < 0$), universal scalings with the characteristics of Efimov physics show up in “Efimov” energy range, where the scattering energy E changes from E_{2b} to a higher “cut-off” energy, which is the short-range energy $E_s = 1/2\mu_3 r_0^2$ for a broad resonance and the effective-range energy E_{eff} for a narrow Feshbach resonance. Here μ_3 is the three-body reduced mass and r_0 is the characteristic range for the pair interactions. We also show that in the presence of a narrow Feshbach resonance, the unusual energy scaling for the recombination rates ($a < 0$) and the rates for vibrational relaxation of the weakly-bound dimer $B_2^* + B \rightarrow B_2 + B$ ($a > 0$) in the effective-range energy region $E_{2b} < E < E_{\text{eff}}$ can be traced back to be the suppression of the inelastic processes near zero energy as shown in

Sec. 3.1.2.

Similar to the study on the energy dependence of K_3 for $a > 0$, we will perform both full numerical studies by solving the three-body Schrödinger equation exactly and analytical analysis based on the scaling of the adiabatic hyperspherical potentials. In the numerical calculations, we use a pair-wise sum of single-channel two-body potentials. In particular, we use Eq. (3.23) as the two-body potentials for a broad resonance, and use Eq. (3.3) for a narrow resonance.

To facilitate the discussion below, we introduce the recombination probability P , which is related to K_3 by [49, 50]

$$K_3 = \frac{192\pi^2}{\mu_3 k^4} P, \quad (3.31)$$

where $k = \sqrt{2\mu_3 E}$ is the three-body wavenumber. Beyond the threshold collisional energy, the higher partial wave ($J > 0$) contributions to the inelastic rates are not suppressed by the Wigner threshold law [178]. However, we will show later that for $a < 0$ these contributions are still negligible in the energy range we are considering. In the following we discuss first the dominant contribution from the $J = 0^+$ symmetry.

3.3.1 Three-body Efimov resonance at finite energy

As has been shown in Eq. (1.6) from Sec. 1.2, when $a < 0$, the three-body recombination rate K_3 near zero energy features a series of logarithmically-separated resonance peaks on top of the overall a^4 scaling. The series of peaks appearing in K_3 manifest that as $|a|$ increases, consecutive Efimov states move across three-body break-up threshold ($E=0$) and become bound [179, 180]. When an Efimov state exists as a shape resonance at finite energy above the three-body break-up threshold, increasing the collisional energy across the resonant energy will lead to a resonant peak in K_3 [50]. This process is illustrated in Fig. 3.17. Near the resonant energy the amplitude of the hyperradial wavefunction of the incident channel behind the barrier is greatly enhanced, the three-body system thus has much larger probability to stay in the short-range region. The enhanced recombination then occurs by

the coupling between the incident channel and the deeply-bound atom-dimer channel at short range. One should be aware, however, that the height of the barrier in Fig. 3.17 is $\sim 1/2\mu_3 a^2$, indicating that the resonant behavior in K_3 can only be observed for the energies below $1/2\mu_3 a^2$. Below this energy, the barrier can only confine a resonant Efimov state with size on the order of $|a|$, which implies that at most one Efimov resonance can be observed for a fixed scattering length.

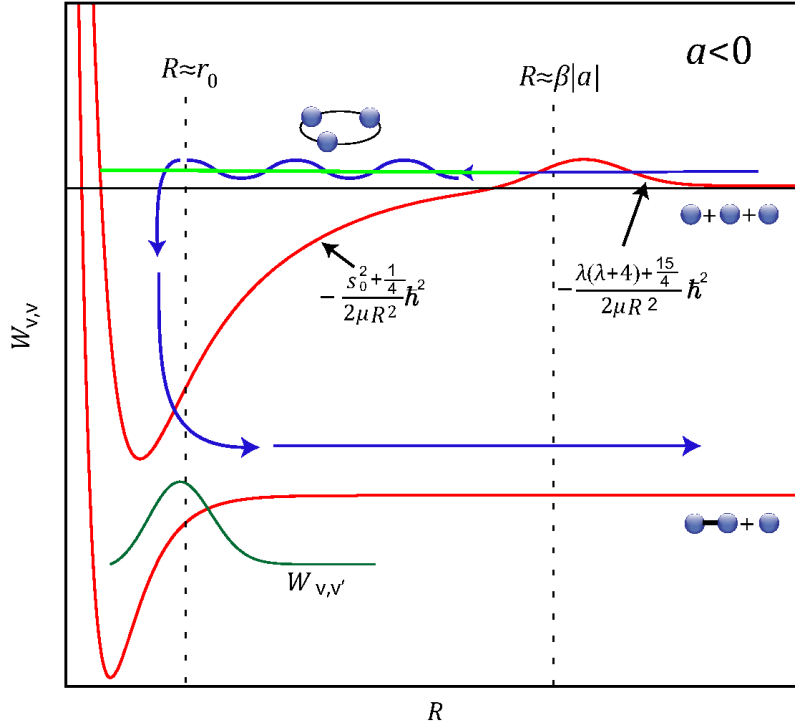


Figure 3.17: Three-body Efimov resonance at finite energy manifested in the adiabatic hyperspherical potentials.

The Wigner threshold law for three-body system [178] shows that $P \propto k^4$ when $E \ll E_{\text{res}}$ where $E_{\text{res}} \leq E_{2b}$ is the resonance energy of the Efimov state. The resonant behavior can thus be observed at finite energy when $E \leq E_{2b}$. In Fig. 3.18, we show the evolution of a resonance peak from finite energy to zero energy as $|a|$ increases. When a peak moves below zero energy, an oscillatory structure appears in the recombination probability P beyond the

threshold energy $E > E_{2b}$,

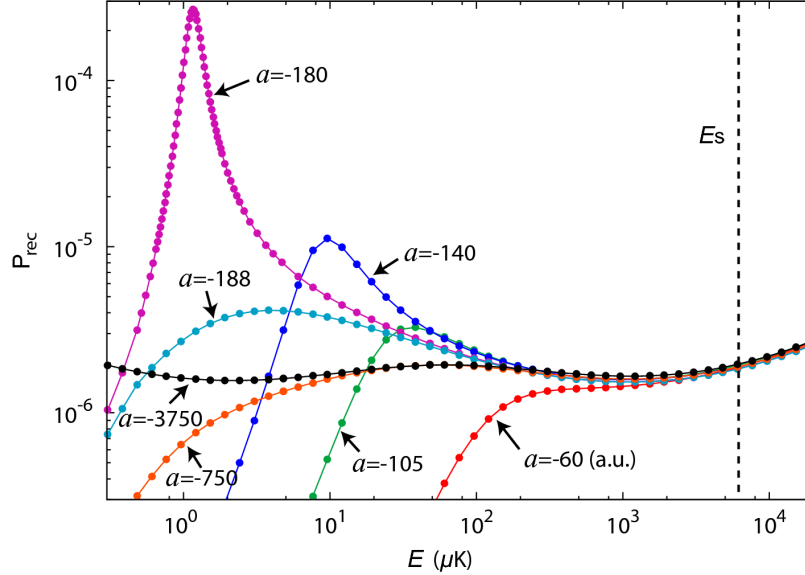


Figure 3.18: The evolution of an Efimov resonance with a in the three-body recombination probability $P^{(a<0)}(E)$ for three identical Cs atoms when a resonant Efimov trimer state is above the three-body break-up threshold. As the scattering length increases the resonant peak moves towards the break-up threshold and finally disappears, while an oscillatory structure is formed instead.

In the ultracold experiments to observe the Efimov effect by three-body recombinations [54, 56, 57], the losses of the atoms for different scattering lengths are typically measured at the same temperature. For the measurements at large scattering lengths such that the recombination is no longer in the zero-energy threshold regime, the measured Efimov features may deviate from the zero-energy prediction in Eq. (1.6). In particular, the positions of the peaks will be shifted to smaller $|a|$ [53] and the peak structure will be smoothed. These effects have been addressed in Refs. [53, 138–140] particularly for the first experimental evidence of Efimov effect in the Innsbruck experiment [54].

By extending the single-channel analysis for recombination for $a < 0$ introduced in Sec. 2.5 to finite energies⁶, we are able to calculate the recombination rate analytically. For low energies, our result in Fig. 3.19 shows that the recombination rate is characterized by

⁶For a detailed derivation please refer to Appendix B.

resonant peaks, but they are shifted to small scattering lengths when the energy is increased.

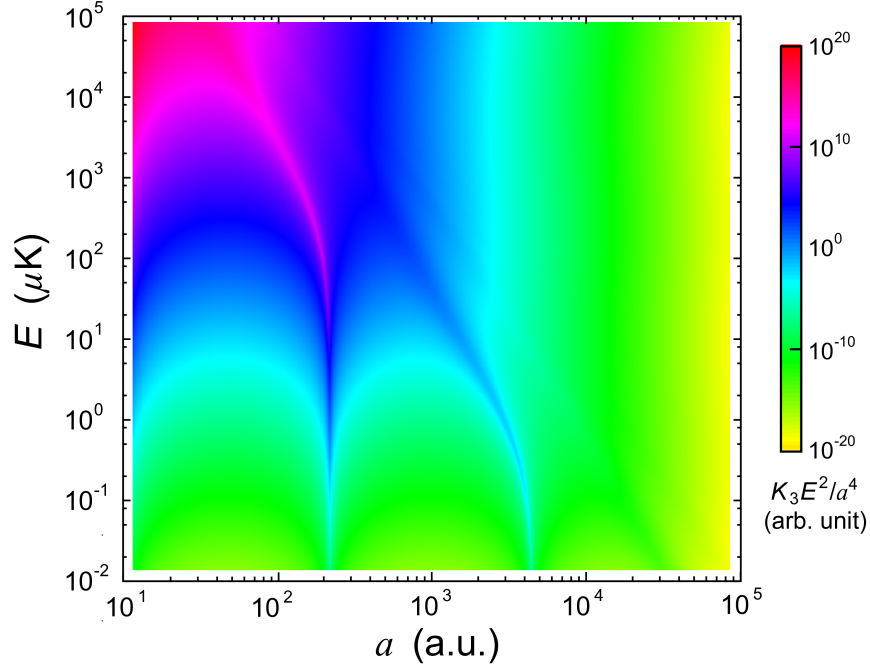


Figure 3.19: The resonance structures in $J=0$ recombination rate K_3 at finite energies ($a < 0$). The rate is scaled as K_3E^2/a^4 to better show the traces of the resonant peaks.

3.3.2 Energy-dependent oscillations in K_3 for $a < 0$

In the energy range $E_{2b} \ll E \ll E_s$, the recombination rate have the following simple form:

$$P^{(a<0)} = \frac{2 \sinh(\pi s_0) \sinh(2\eta)}{\cosh(\pi s_0) + \sin[-2s_0 \ln(kr_0) + 2\Phi - 2\varphi_0]}, \quad (3.32)$$

where the constant phase φ_0 is determined by

$$\tan \varphi_0 = \frac{\text{Re}[\Gamma(is_0)] - \text{Im}[\Gamma(is_0)]}{\text{Re}[\Gamma(is_0)] + \text{Im}[\Gamma(is_0)]}. \quad (3.33)$$

In the energy range we are considering the change in the short-range scattering wavefunction is small. The energy dependence in the short-range phase Φ and the parameter η is negligible so that they both reduce to those defined in Eqs. (1.5)-(1.7).

The log-periodic oscillations in Eq. (3.32) manifests the formation of Efimov states as $|a|$ is increased. Like the energy-dependent oscillation observed for $a > 0$, the overall phase of the oscillations only depends on the short-range physics so when $|a|$ is increased more oscillations will appear towards zero-energy limit while those have already appeared in $E \gg E_{2b}$ will keep unchanged. As mentioned in Sec. 3.2, in the ultracold experiments for measuring the zero-energy recombination rates the temperature is required to be lower as $|a|$ increases. These requirements make the observation of multiple Efimov features quite challenging. Measuring the Efimov features via the energy-dependent oscillations instead can make the experimental requirement less demanding. As in Eq. (3.21) and (3.28) for $a > 0$, where the energy-dependent oscillations are independent of the scattering length a , the independence of a in Eq. (3.32) also provides the convenience of measuring the energy-dependent oscillations by sections at different a , provided that $|a| \geq 1/k$. One should note that if there is an Efimov resonance present at finite energy, the oscillations at higher energies may be destroyed by thermal averaging. Therefore, the scattering length a where the measurements are carried out should be chosen to be far away from resonant peaks.

Equation (3.32) also applies to three-body systems with two identical bosons. In such systems, the Efimov effect is generally more favorable if the two identical bosons are much heavier than the distinguishable one [169], in the sense that the universal constant s_0 can be larger as the mass ratio increases so that the period of the logarithmic oscillations in the collisional rates decreases. For the energy-dependent oscillations, however, increasing s_0 also makes the oscillatory modulations smaller. In Fig. 3.20(a), we show the mass ratio effect for some typical three-body atomic systems. For three identical Cs atoms, the ratio of the modulation to the background is about 0.18; for two identical Cs atoms with one Cs atom in different spin state, the ratio is about 2.1; and for two identical Cs atoms with one Li atom, the ratio is about 0.0079.

Though in the zero-energy limit the features of the relaxation rates $V_{\text{rel}}(a > 0)$ resemble those of the recombination rates ($a < 0$), they differ dramatically at higher energies. The

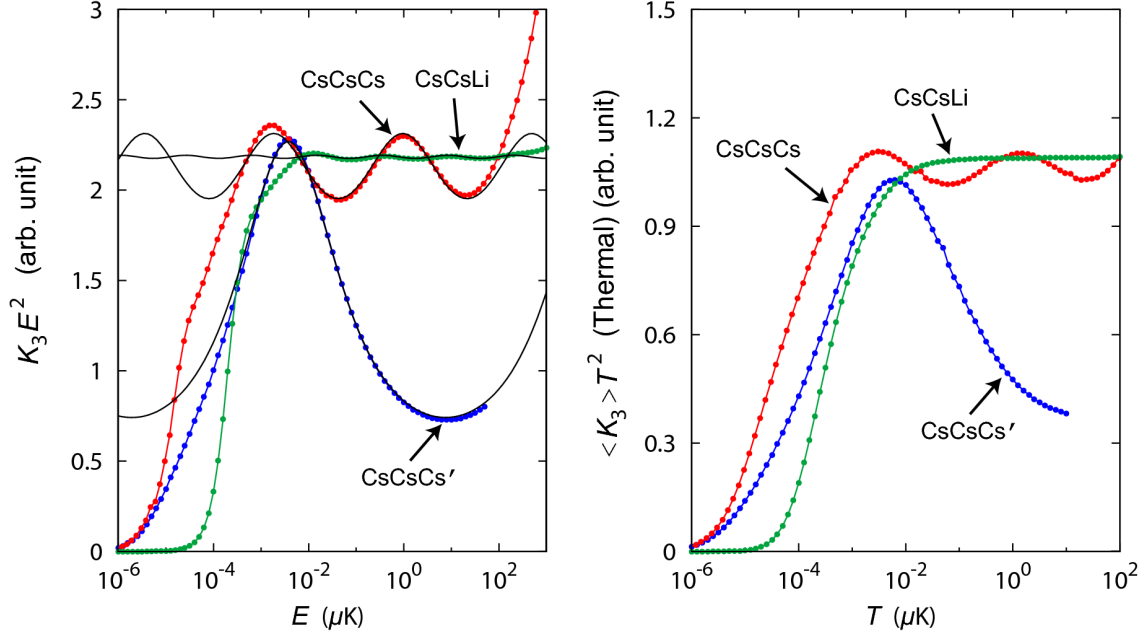


Figure 3.20: Three-body recombination probability for $a < 0$ near broad Feshbach resonances at finite energies. (a) The energy-dependent three-body recombination probability $P^{(a < 0)}(E)$ for three identical Cs atoms, two identical Cs atoms with one Cs atom in a different spin state (Cs') and two identical Cs atoms with one Li atom. The symbols are numerical results and the black solid lines are from Eq. 3.32. The scattering length for the numerical calculations are 2×10^5 a.u., 6×10^5 a.u. and 10^5 a.u., respectively. (b) The recombination probability after thermal averaging. To make a clear comparison between the three different systems, $P^{(a < 0)}$ for CsCsCs' and CsCsLi has been multiplied by 3 and 2, respectively.

zero scattering energy is referred as the atom-dimer break-up threshold for relaxation and as the three-body break-up threshold for recombination. Applying the Wigner threshold law for atom-dimer collision leads to constant V_{rel} below the energy E_{th} where V_{rel} shows the zero-energy behavior as given in Eq. (1.7). Generally $E_{\text{th}} \approx E_{2b}$ except $V_{\text{rel}}(E \rightarrow 0)$ is near a resonant peak where the atom-dimer scattering length $|a_{\text{ad}}| \gg |a|$. In this case E_{th} is close to the least bound Efimov trimer binding energy $1/2\mu_{\text{ad}}a_{\text{ad}}^2$, where μ_{ad} is the atom-dimer reduced mass. Beyond E_{th} and below the short-range energy E_s , V_{rel} scales like

$$V_{\text{rel}} = Ck^{-1} \quad (3.34)$$

except in a small energy range $E \approx E_{2b}$, due to the non-analytic behavior near the three-

body break-up threshold. The constant C depends on the short-range physics and is related to the η parameter in Eq. (1.7). Unlike the three-body recombination rate, the relaxation rate does not show the Efimov-like oscillations.

As presented in Sec. 3.1, near a narrow Feshbach resonance, the behavior of the effective hyperspherical potential $W_{\nu\nu}(R)$ in the region $|r_{\text{eff}}| \ll R \ll |a|$ is replaced by a weak Coulomb behavior instead of the attractive $1/R^2$ form. The observable effect is that for identical bosons, when $|a| \gg |r_{\text{eff}}|$ the weak Coulomb potential leads to $1/|r_{\text{eff}}|$ suppression in the inelastic rates leading to deeply-bound states. Using the same modeling technique for a narrow Feshbach resonance in Sec. 3.1 to model a three-body system near a narrow Feshbach resonance by using pairwise potentials in Eq. (3.3), we have calculated K_3 for $a < 0$ up to the short-range energy scale E_s .

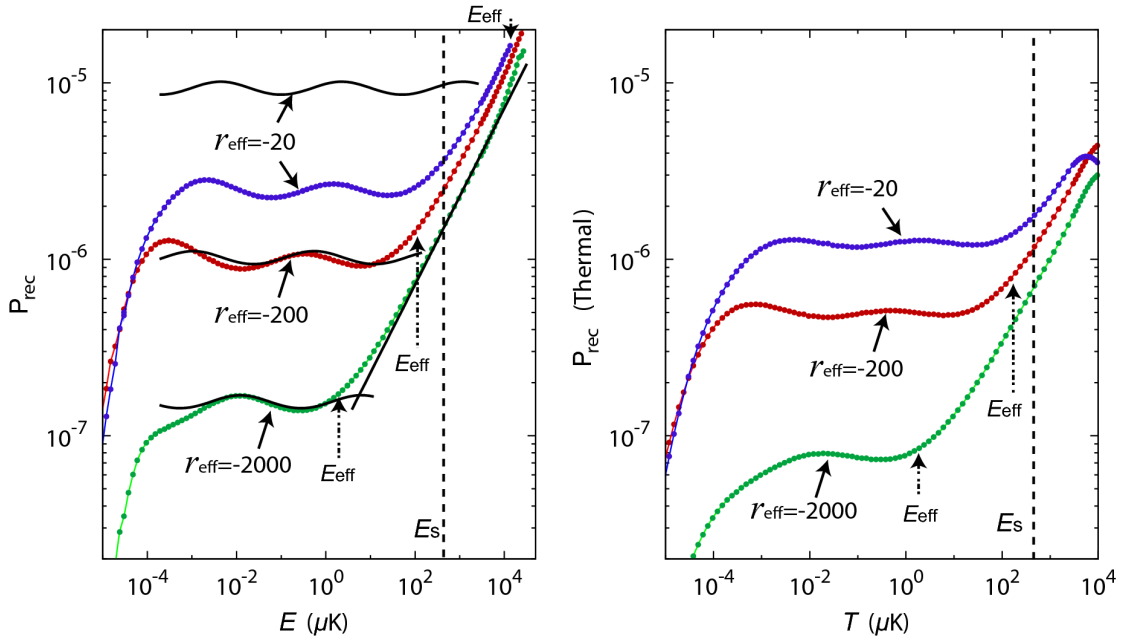


Figure 3.21: The energy-dependent three-body recombination probability for $a < 0$ near narrow Feshbach resonances. (a) The energy-dependent recombination probability $P^{(a < 0)}(E)$ near narrow Feshbach resonances with $r_{\text{eff}} = -20$ a.u., -200 a.u. and -2000 a.u.. The symbols are the numerical results and the back solid lines are from Eq 3.32. The parameter α is fitted as 0.25, consistent with the result in Ref. [2]. (b) The recombination probability from numerical calculations after thermal averaging.

We have found that without looking at the effective-range dependence in the inelastic rates, the $1/|r_{\text{eff}}|$ suppression is manifested in the energy dependence of the inelastic rates for a fixed effective range. As shown in Fig. 3.21(a), the recombination probability $P^{(a<0)}$ in the short-range energy scale $E \approx E_s$ has a similar magnitude for different r_{eff} , since the short-range behavior of the three-body system has only small changes. In the effective-range energy region $E_{\text{eff}} < E < E_s$ instead, $P^{(a<0)} \propto k$. Thus as the energy gets smaller, the recombination probability decreases monotonically until the energy reaches $E \approx E_{\text{eff}}$, where oscillatory behavior similar to Eq. (3.32) takes place. Compared with the situation near a broad resonance, P is suppressed by a factor of $1/|r_{\text{eff}}|$ around $E \approx E_{\text{eff}}$ before it connects to the oscillatory behavior at lower energy. Consequently, the recombination rates at lower energies are all suppressed by $1/|r_{\text{eff}}|$. Following the similar procedure for deriving the recombination rate for small $|r_{\text{eff}}|$, $P^{(a<0)}$ for large $|r_{\text{eff}}|$ acquires the same form in the Efimov energy range as Eq. 3.32, with r_0 replaced by $\alpha|r_{\text{eff}}|$ and the parameters Φ and η connected to the real and imaginary part of the three-body short-range scattering length $\text{Re}A$ and $\text{Im}A$:

$$\tan \Phi = 2s_0 \frac{\alpha - \text{Re}A/|r_{\text{eff}}|}{\alpha + \text{Re}A/|r_{\text{eff}}|}, \quad \sinh \eta = 2 \left| \frac{\text{Im}A}{\alpha r_{\text{eff}}} \sin 2\Phi \right|, \quad (3.35)$$

where the parameter α comes from the uncertainty in defining the boundary of the Coulomb-like region and is fitted to be $\alpha = 0.25$ from our numerical results. In the effective-range energy range, P takes the following simple analytical form:

$$P = 4k|\text{Im}A|. \quad (3.36)$$

The behavior of P near a narrow Feshbach resonance leads to the change of the energy scaling k^{-4} in the ‘‘Efimov’’ energy range ($E_{2b} \leq E \leq E_{\text{eff}}$) to k^{-3} in the effective-range energy region ($E_{\text{eff}} \leq E \leq E_s$). The $1/|r_{\text{eff}}|$ suppression can thus be observed experimentally through the change of the energy scaling.

A similar change in scaling also occurs in the same energy range for relaxation. As shown in Fig. 3.22, As $|r_{\text{eff}}|$ increases, instead of k^{-1} scaling for broad Feshbach resonances

as shown in Eq. (3.34), a plateau region shows up in V_{rel} , extending from short-range energy down to the effective-range energy. Similar to recombination, this change also connects to the $1/|r_{\text{eff}}|$ suppression of the rates near zero energy and can be used for observing the effective-range effect near narrow Feshbach resonances.

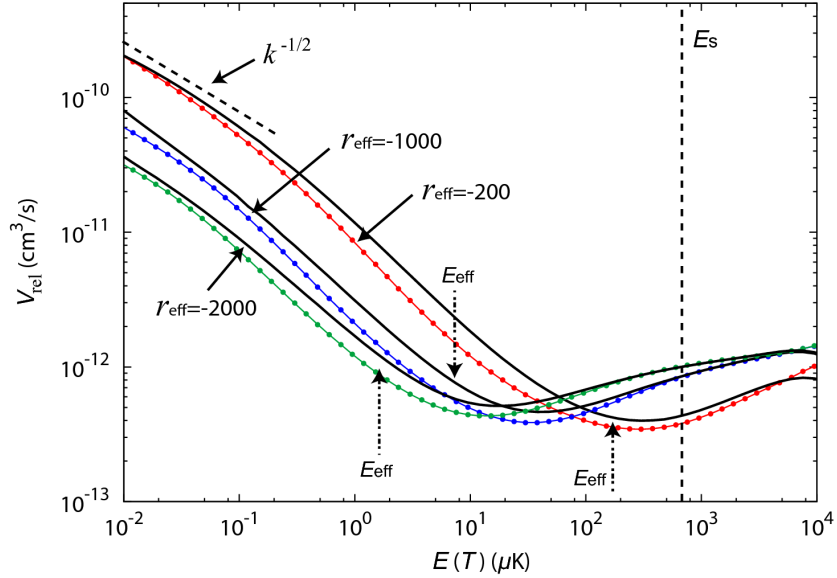


Figure 3.22: The three-body relaxation rates for $a > 0$ near narrow Feshbach resonances with $r_{\text{eff}} = -200$ a.u., -1000 a.u. and -2000 a.u.. The scattering length is 10^4 a.u. for all cases. The rates are shown for the collisional energy beyond the three-body break-up threshold, where no resonant peaks are present so that the energy scaling behavior is easy to be seen. The symbols are the numerical results and the black solid lines are thermally-averaged results.

Next we will discuss how the higher partial waves contribute to the total inelastic rates. For three-body recombination at $a < 0$ and relaxation at $a > 0$, the inelastic processes require transitions at short-range $R \leq r_0$. For $J > 0$, in the three-body systems where the Efimov effect does not occur for $J > 0$ [169], the effective hyperspherical potentials are all repulsive for $R > r_0$, leading to great suppression when $E < E_s$. Specifically, using a WKB analysis [66] we can show that the probability for such inelastic transitions scales like $(kr_0)^{2p_0}$, where the universal constant $p_0 > 2$ for identical bosons and increases with J in general. Our numerical calculations also show that for $E < E_s$, $K_3^{(J>0)}$ is smaller than $K_3^{(J=0)}$ by many orders of magnitude.

Finally we address the thermal effect on the inelastic rates in the quantum gas experiments. By assuming a Boltzmann distribution of the thermal energy, we have performed a thermal average on the energy-dependent inelastic rates we have calculated. The results are shown in Fig. 3.20(b) and 3.22(b) for recombination and are shown together with the energy-dependent rates in Fig. 3.22 for relaxation. In the ‘‘Efimov’’ energy range, the oscillatory structures in $P^{(a<0)}$ generally become less clear after thermal average. In presence of an Efimov resonance near the three-body break-up threshold, the observability of the oscillatory structures in the Efimov energy region can be further reduced. For the three-body systems of two identical bosons and one distinguishable atom with a small value of s_0 , the oscillatory structures are well-preserved after thermal average, with the trade-off that the oscillatory periods are spanning a larger energy range. In the effective-range energy region, however, the thermal average does not change the observability of the specific energy scalings near the narrow resonances for recombination or relaxation processes.

Before concluding, we discuss the possible application of the energy-dependent Efimov features identified for both $a > 0$ and $a < 0$ cases to studies in nuclear physics. Though the scattering length-dependent predictions for the three-body inelastic rates have been successfully applied to the ultracold experiments for the observation of the Efimov effect, they are less helpful in the context of nuclear physics where the discussions on the Efimov effect first originated. The reason is simple: the nuclear interactions are predetermined by nature and there is no known way to experimentally control these interactions. The scattering length a between the nucleons is thus not tunable and the scattering length dependent Efimov features are generally not observable. As we have extended Efimov physics into the energy domain from the three-body collisions, the information of the three-body Efimov state can be obtained without tuning the interactions. In particular, if the recombination is difficult to realize in some systems, one can always look at the three-body dissociation signals in the collisional process $B_2^* + B \rightarrow B + B + B$, the time reversal of the three-body recombination. The energy-dependent Efimov features are expected to show up in exactly the same way as

for the recombinations.

3.3.3 Summary

To summarize, we have studied the three-body collisions at incident energies up to the short-range energy regime near both broad and narrow Feshbach resonances. We have identified the universal energy dependence as a manifestation of Efimov effect in three-body recombination probability in the Efimov energy range when $a < 0$. Near narrow Feshbach resonances, we have also found the universal energy scaling in the effective-range energy region for recombination rates ($a < 0$) and relaxation rates ($a > 0$), which have a close relationship to the $1/|r_{\text{eff}}|$ suppression in those rates near zero-energy [2]. By understanding the physical processes in hyperspherical representation, we derived simple analytical expressions for the universal energy-dependent features, supported by the results from solving the Schrodinger equation numerically. These energy-dependent features can be conveniently used for the experimental observation of the Efimov effect and the suppression effect near narrow Feshbach resonances. Our study brings the universal three-body physics from the ultracold quantum degenerate regime to the cold atoms regime, where richer universal physics can be discovered both theoretically and experimentally.

Chapter 4

Universal Efimov physics in four-body systems

In the quest for exploring universal physics in few-body systems, three-body Efimov physics has been regarded as the key to obtaining universal scaling behavior in the three-body systems. Since the ultimate goal for the study of universal physics is to build connections between few-body systems and many-body systems, the natural next step is to study universal physics in a four-body system. The addition of only one particle to a three-body system causes fundamental changes. First of all, it has been proven that the Efimov effect does not exist for N *identical* bosons when $N \geq 4$. Some fundamental questions then arise for a four-body system: Are there still some universal behaviors? If there are, do they originate from the three-body Efimov physics or from some new mechanism? Studies on these topics have shown fruitful progress in recent years [10][59, 62, 63, 68, 181–183]. Furthermore, there will be more few-body scattering processes in a four-body system, including recombinations, relaxations and reactive processes. Each of these processes may have unique universal scaling behavior, which provides broad applications in controlled chemistry. In this chapter, the material for Sec. 4.1 and 4.2 is adapted from a published paper [10] and a preprint [7], respectively. We discuss how the three-body Efimov effect appears in four-body systems and how to use the four-body consequences of this effect to gain control over four-body scattering processes. The material for Sec. 4.3 is also adapted from a preprint [4], in which

we discuss universal four-body physics in a one dimensional system where the Efimov effect does not show up for any number of particles.

4.1 Efimov trimer production via four-body recombination

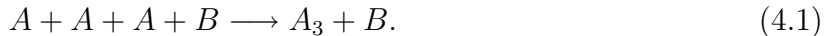
The exquisite experimental control on the interactions in an ultracold quantum gas has opened the era of controlled quantum chemistry. In particular, both weakly-bound [40, 41, 184] and ground state diatomic molecules [64, 64, 65] have been produced by using magnetic Feshbach resonance [42, 43] and STIRAP [185, 186]. Experimental observations of the three-body Efimov effect [54–57, 60, 144–148] give hope for quantum chemistry on triatomic molecules. Predictions and proposals on this topic have appeared recently, such as four-body recombination for identical bosons [59] and the conversion of dimers into an Efimov trimer by tuning their relative energies [68]. When producing Efimov trimers by collisional means, one extra atom or molecule needs to be involved to carry away the extra energy released from the binding, which pushes theoretical studies on this topic to be at least a four-body problem.

Our goal is to explore the possibility of producing Efimov trimers via four-body recombination. A scheme for doing this in the tight confinement of an optical lattice has been proposed [187] which takes advantage of the magnetic field dependence of Efimov trimer energy levels near a Feshbach resonance. Here we investigate the possibility for producing them in free space with four-body recombination. Our approach is similar to one of the experimental techniques used for producing weakly-bound dimers by three-body recombination, where an atomic gas sample is held at a fixed magnetic field near a Feshbach resonance [176, 188]. In such experiments the three-body recombination does not directly lead to trap loss because the energy released from the binding of the weakly-bound dimer does not exceed the height of the trapping potential.

Besides the intrinsic interest of Efimov states, it is also important to develop a theory

of the fundamental process of four-body recombination quantum mechanically. Compared with three-body collisions, our knowledge of ultracold four-body collisions is still quite rudimentary. The reason is clear: solving the Schrödinger equation with three additional degrees of freedom is a much more difficult task. There have, of course, been many studies of four-body systems, and some which have relevance to ultracold quantum gases have appeared recently [59, 62, 63, 68, 181–183, 189]. In particular, in Ref. [59] four-body recombination of four identical bosons has been addressed and a class of universal four-body states has been predicted. This theoretical prediction was later confirmed by experiments [60].

The system we consider here is an ultracold mixture of atoms A and B . We take A to be bosons distinguishable from B . Our goal is to produce Efimov trimers A_3 via the four-body recombination process



To this end, we will assume that the two-body s -wave scattering length among A atoms a_{AA} is infinite to give the most favorable case for Efimov states. We will also assume that the interspecies scattering length a_{AB} is finite and that any dimer states, which are likely for real systems, lie much deeper than the Efimov trimer states. As we will show below, monitoring the loss of B atoms provides a convenient indicator for the formation of A_3 with many advantages over alternative schemes.

4.1.1 Four-body hyperspherical coordinates

Our treatment of this process is asymmetrical in A and B , mirroring the differences in a_{AA} and a_{AB} . The two-body interactions for the A_3 subsystem are well-described by the zero-range model [13] which has been discussed to some extent in Sec. 2.5. The advantage of this model is that the three-body solutions are especially simple in the $|a_{AA}| \rightarrow \infty$ limit [12, 106, 107]. This simplicity partially comes from the simple connection between the two-body zero-range boundary conditions and the boundary condition for the adiabatic hyperangular wavefunction in Eq. (2.38). Extending this model to four-body systems is not

straightforward, however. Our analysis has shown that in the four-body case, the zero-range boundary conditions need to be imposed along complicated trajectories on the hyperangular surface and there is hardly any hope for them to reduce to simple expressions. Instead, we borrow an idea from Rydberg physics [190] — and from many-body theories of Bose-Einstein condensates [31–33] — to model the AB interaction. In the ultracold regime, the kinetic energies of the A atoms are near zero when they are free, so that the wavelength of the A atoms will be much larger than the size of atom B . If the A atoms are bound in an Efimov molecule, they will still have tiny kinetic energies since the Efimov molecules are so weakly-bound. In any case, the AB interactions can be regarded as point interactions and when a_{AB} is not dramatically larger than the size of the short-range interaction r_0 . These interactions can be approximated by the Fermi contact potential [191] instead of using the zero-range boundary conditions as were used for treating the $A + A$ interactions:

$$V_{AB}(r_{i4}) = \frac{2\pi a_{AB}}{\mu_{AB}} \delta(r_{i4}), \quad i = 1, 2, 3, \quad (4.2)$$

where μ_{AB} is the two-body reduced mass and r_{i4} is one of the AB interparticle distances.

Given the success of the adiabatic hyperspherical representation in describing the three-body continuum [49, 50], we will use it here to treat the four-body continuum as well. Since we want to use known solutions for the A_3 subsystem, we build the four-body hyperspherical coordinates from the three-body ones. In particular, as shown in Fig. 4.1 we set up the coordinates by using the “K”-type Jacobi vectors. The four-body hyperradius R_4 and hyperangle α_4 are thus defined as

$$\mu_4 R_4^2 = \mu_{3,4} \rho_3^2 + \mu_3 R_3^2 \quad (4.3)$$

$$\tan \alpha_4 = \sqrt{\frac{\mu_3}{\mu_{3,4}}} \frac{R_3}{\rho_3}. \quad (4.4)$$

Here, $\mu_3 = m_A / \sqrt{3}$ is the three-body reduced mass, $\mu_{3,4} = 3m_A m_B / (3m_A + m_B)$ is the reduced mass between the AAA trimer and the B atom, and $\mu_4 = \sqrt{\mu_3 \mu_{3,4}}$ is the four-body reduced mass. Finally, ρ_3 denotes the distance from the A_3 center of mass to B ; R_3 , the three-body hyperradius; and α_3 , the three-body Delves’ hyperangle as introduced in Sec. 2.2.1.

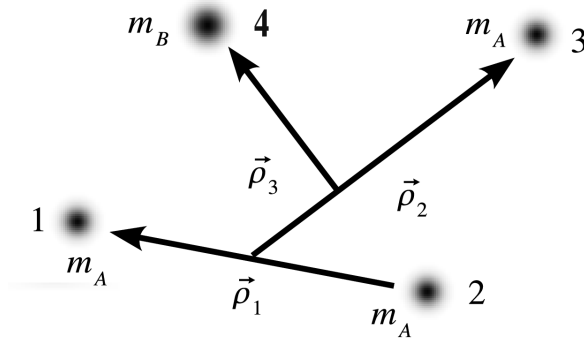


Figure 4.1: The “K”-type Jacobi vectors for $A + A + A + B$ system.

4.1.2 Four-body adiabatic potentials

To properly treat the strong interactions between the A atoms and the weak interactions between A and B atoms, we will not use exactly the same representation introduced in Sec. 2.3. Since the Efimov trimer states are the result of the resonant $A + A$ interactions and recombination is driven by the $A + B$ interactions, we will use a representation which treats the $A + A$ interactions separately from the $A + B$ interactions. Specifically, our representation is not fully adiabatic where we do not include V_{AB} in the adiabatic Hamiltonian H_{ad} . Rather, we will include them later as coupling between channels in the representation where atom B has been treated as free. This choice, together with our definition of coordinates, permits separation of variables in the adiabatic equation, utilizing the known solutions for the A_3 subsystem. Mathematically, this procedure begins with the four-body Schrödinger equation

$$[T_{R_4} + V_{AB}(r_{14}) + V_{AB}(r_{24}) + V_{AB}(r_{34}) + H_{\text{ad}}] \Psi = E\Psi,$$

where T_{R_4} is the hyperradial kinetic energy and

$$H_{\text{ad}} = T_{\Omega_4} + T_{\Omega_3} + V_{123}, \quad (4.5)$$

which includes the hyperangular kinetic energies T_{Ω_i} and all of the interactions among A atoms in V_{123} . The notation Ω_3 denotes collectively all of the three-body hyperangles; Ω_4 includes the four-body hyperangle α_4 and the two spatial angles for the Jacobi vector $\vec{\rho}_3$

shown in Fig. 4.1. For four-body recombination in the ultracold limit, we know from the generalized Wigner threshold law [178] that only the zero total orbital angular momentum solution is relevant and all the higher partial wave contributions are suppressed by the low collisional energy. And, since for identical bosons the three-body Efimov states only exist for zero orbital angular momentum, the angular momentum of B relative to A_3 must also be zero by the addition rule of the angular momentum. The channels for the four-body problem are thus defined from

$$H_{\text{ad}}\Phi_{\nu}^{(4)} = U_{\nu}(R_4)\Phi_{\nu}^{(4)}. \quad (4.6)$$

Since we are using the zero-range model for the three A atoms, the four-body adiabatic wavefunction $\Phi_{\nu}^{(4)}$ is required to satisfy the zero-range boundary condition in Eq. (2.71) and (2.72) when the distance between the A atoms r_{ij} ($i, j = 1, 2, 3$) goes zero. When a is infinite, Eq. (2.71) only depends on the three-body hyperangles Ω_3 , we can thus separate the variables and write $\Phi_{\nu}^{(4)}$ in the following form:

$$\Phi_{\nu}^{(4)}(R_4; \Omega_4, \Omega_3) = u_{\beta n}(R_4; \Omega_4)\Phi_{\beta}^{(3)}(\Omega_3), \quad (4.7)$$

where the channel index ν represents the combination of indices $\{\beta, n\}$.

In our study of four-body recombination into trimer states, we will solve for both of the $A_3 + B$ bound channels and the four-body continuum channels $A + A + A + B$ separately. Under the condition $a_{AA} \rightarrow \infty$ and $a_{AB} \approx r_0$, no weakly-bound dimer channels exist, and all the other channels involving deeply-bound dimers — which exist in a real system — can be neglected since they lie much deeper than the atom-Efimov trimer channels.

For the $A_3 + B$ channels ($\beta=0$), the solutions for the three-body hyperangular motion is analytically known as [106]

$$\Phi_0^{(3)}(\Omega_3) = N_3 \sum_{l=1}^3 \frac{2 \sinh(s_0 \alpha_3^{(l)})}{\sin(2\alpha_3^{(l)})}, \quad (4.8)$$

where $s_0 \approx 1.00624$ is determined by Eq. (2.73), replacing s_{ν} with is_0 . The normalization

factor N_3 is calculated numerically. Equation (4.8) solves

$$(T_{\Omega_3} + V_{123})\Phi_0^{(3)} = -\frac{s_0^2 + \frac{1}{4}}{2\mu_3 R_3^2}\Phi_0^{(3)}. \quad (4.9)$$

The summation in Eq. (4.8) is over the three possible three-body Jacobi sets as shown in Fig. 2.1, each with its own Delves' hyperangle $\alpha_3^{(l)}$. Substituting Eq. (4.8) into Eq. (4.7), and the result into Eq. (4.6), we obtain the following equation for the $A_3 + B$ channels:

$$\left(-\frac{d^2}{d\alpha_4^2} - \frac{s_0^2 + \frac{1}{4}}{\sin^2 \alpha_4}\right)u_{0n} = \lambda_{0n}^2 u_{0n}. \quad (4.10)$$

The physically acceptable solution of Eq. (4.10) which is regular at $\rho_3 = 0$ is

$$u_{0n}(R_4; \alpha_4) = N_4 \cos \alpha_4 \sin^{\frac{1}{2} + is_0}(\alpha_4) {}_2F_1\left(\frac{3}{4} + \frac{is_0}{2} - \frac{\lambda_{0n}}{2}, \frac{3}{4} + \frac{is_0}{2} + \frac{\lambda_{0n}}{2}; \frac{3}{2}; \cos^2 \alpha_4\right) \quad (4.11)$$

where ${}_2F_1$ is the hypergeometric function and the normalization constant N_4 is determined by

$$N_4^2 = \left|\frac{\pi}{2}\Gamma\left(\frac{3}{2}\right)^2 \frac{\Psi(b) + \Psi(c) - \Psi(g) - \Psi(h)}{\lambda_{0n}\Gamma(b)\Gamma(c)\Gamma(g)\Gamma(h)\sinh(\lambda_{0n}\pi)}\right|^{-1}, \quad (4.12)$$

where

$$\begin{aligned} b &= \frac{3}{4} + \frac{1}{2}is_0 - \frac{1}{2}\lambda_{0n}, & c &= \frac{3}{4} - \frac{1}{2}is_0 + \frac{1}{2}\lambda_{0n}, \\ g &= \frac{3}{4} + \frac{1}{2}is_0 + \frac{1}{2}\lambda_{0n}, & h &= \frac{3}{4} - \frac{1}{2}is_0 - \frac{1}{2}\lambda_{0n}. \end{aligned} \quad (4.13)$$

The $\Gamma(z)$ is the Gamma function and $\Psi(z)$ is the Digamma function $d \ln \Gamma(z)/dz$. The adiabatic potentials defined in Eq. (4.6) are connected to the eigenvalues λ_{0n} by:

$$U_{0n} = \frac{\lambda_{0n}^2 - \frac{1}{4}}{2\mu_4 R_4^2}. \quad (4.14)$$

Note that U_{0n} goes below zero when λ_{0n} is purely imaginary.

The solution in Eq. (4.11) has no restriction on the eigenvalue λ_{0n} . This seems bizarre at first glance since it implies that the adiabatic potential $U_\nu(R_4)$ can take any value from $-\infty$ to ∞ . In fact, this is exactly the manifestation of Thomas collapse. This collapse comes from the the zero-range model description of the $A + A + A$ subsystem, as indicated by the

three-body adiabatic potential in Eq. (2.75) which is singular when the size of the $A + A + A$ subsystem is zero. This collapse is then manifested in the $A_3 + B$ system. To avoid this, we simply require that the three-body hyperradial wave functions vanish for $R_3 \leq R_0$ where R_0 roughly represents the size of the ground Efimov state and determines the ground state energy E_0 in Eq. (1.2). This effectively regularizes the singular behavior of the A_3 subsystem at small distance and leads to a transcendental equation for λ_{0n} :

$${}_2F_1\left(\frac{3}{4} + \frac{is_0}{2} - \frac{\lambda_{0n}}{2}, \frac{3}{4} + \frac{is_0}{2} + \frac{\lambda_{0n}}{2}; \frac{3}{2}; \cos^2 \alpha_{4,0}\right) = 0, \quad (4.15)$$

where $\cos^2 \alpha_{4,0} = 1 - R_0^2/R_4^2$. Through the asymptotic behavior of transcendental equation, the Efimov trimer energies are recovered from U_{0n} in the limit $R_4 \rightarrow \infty$:

$$U_\nu(R_4) \simeq -\frac{2}{\mu_3 R_0^2} e^{-\frac{2}{s_0}(n\pi + \gamma)} - \frac{c_2}{2\mu_4 R_4^2} + O\left(\frac{1}{R_4^3}\right), \quad (4.16)$$

where $c_2 \approx 0.667$ is fitted from the potential obtained by solving the root of Eq. (4.15). The constant γ is

$$\gamma = \tan^{-1} \left[\frac{1}{\text{Arg}\Gamma(is_0)} \right] \approx 0.30103. \quad (4.17)$$

The attractive $1/R^2$ behavior in the potentials U_ν is cancelled by the leading order term from the diagonal coupling $Q_{\nu\nu} = \left\langle \left\langle \frac{d\Phi_\nu}{dR_4} \middle| \frac{d\Phi_\nu}{dR_4} \right\rangle \right\rangle$ when we look at the more physical effective potential $W_\nu(R_4) = U_\nu(R_4) - \frac{1}{2\mu_4} Q_{\nu\nu}(R_4)$.

For $R_4 \gg r_0$ but $W_\nu > 0$, the effective potentials behave like

$$W_\nu(R_4) \approx \left[\frac{2(n + \gamma) - s_0}{\pi} + \frac{1}{2} - \frac{s_0}{\pi} \ln \left(\frac{\mu_4 R_4^2}{\mu_3 R_0^2} \right) \right] \frac{1}{2\mu_4 R_4^2}. \quad (4.18)$$

As will be shown later, this behavior determines the structure of the crossings between the $A_3 + B$ channels and the $A + A + A + B$ channels, which is crucial for the inelastic transitions in four-body recombination.

We follow the same logic for the $A + A + A + B$ channels. The only difference is that $\Phi_\beta^{(3)}$ is now a three-body continuum function, but still for $|a_{AA}| \rightarrow \infty$. This is done by replacing

s_β	m	$\lambda_{\beta m}$
4.465	0	5.965
4.465	1	7.965
6.818	0	8.318
4.465	2	9.965
6.818	1	10.318
9.324	0	10.824

Table 4.1: The lowest few asymptotic eigenvalues $\lambda_{\beta m}$ for the $A + A + A + B$ channels.

s_0 by is_β ($\beta > 0$) so that the three-body hyperangular solutions are

$$\Phi_0^{(3)}(\Omega_3) = N_3 \sum_{l=1}^3 \frac{2 \sin(s_\beta \alpha_3^{(l)})}{\sin(2\alpha_3^{(l)})}, \quad (4.19)$$

which give the counterpart of Eq. (4.10) for $A + A + A + B$ channels:

$$\left(-\frac{d^2}{d\alpha_4^2} + \frac{s_\beta^2 - \frac{1}{4}}{\sin^2 \alpha_4} \right) u_{\beta m} = \lambda_{\beta m}^2 u_{\beta m}. \quad (4.20)$$

The universal constants s_β are real numbers determined by Eq. (2.73) in the limit $a \rightarrow \infty$. The four-body hyperangular solution $u_{\beta m}$ takes the same form as Eq. (4.11) with s_0 replaced by is_β . The boundary condition for $u_{\beta m}$ is obtained after replacing s_0 by is_β in Eq. (4.15). After solving the eigenvalues $\lambda_{\beta m}$, we get the four-body adiabatic potentials for $A + A + A + B$ channels

$$U_{\beta m} = \frac{\lambda_{\beta m}^2 - \frac{1}{4}}{2\mu_4 R_4^2}. \quad (4.21)$$

Asymptotically, $\lambda_{\beta m} \rightarrow s_\beta + 2m + \frac{3}{2}$ with $m=0,1,2,\dots$ labeling the four-body continuum states possible for each β . The four-body continuum potentials thus behave as

$$U_{\beta m} = \frac{(s_\beta + 2m + \frac{3}{2})^2 - \frac{1}{4}}{2\mu_4 R_4^2} \quad (4.22)$$

for $R_4 \gg R_0$. We list the lowest few asymptotic eigenvalues $\lambda_{\beta m}$ in Table 4.1.

4.1.3 Four-body recombination

If we expand the total four-body wave function as

$$\Psi(R_4, \Omega_4, \Omega_3) = \sum_{\nu} F_{\nu}(R_4) \Phi_{\nu}^{(4)}(R_4; \Omega_4, \Omega_3), \quad (4.23)$$

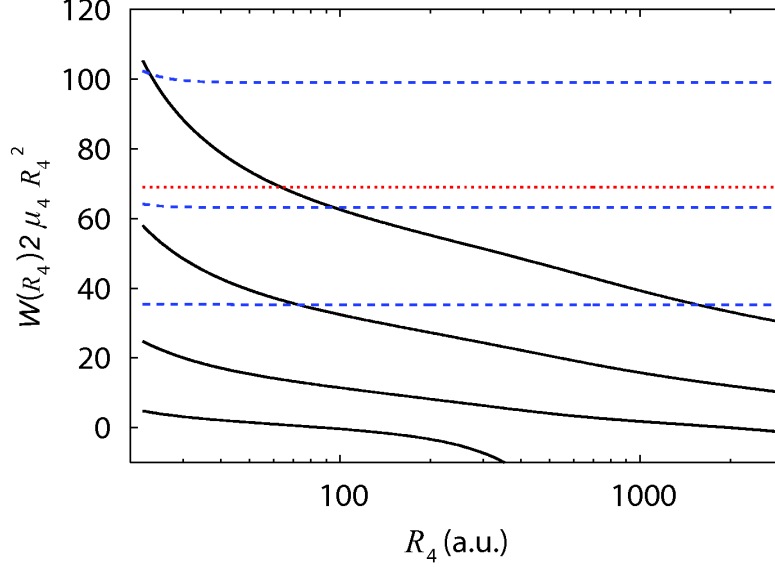


Figure 4.2: The lowest four-body adiabatic hyperspherical potentials W_ν multiplied by $2\mu_4 R_4^2$ to better show their behavior. Black solid lines denote atom-trimer potentials for $\beta=0$ and $n=1,2,3,4$; blue dashed lines, four-body continuum potentials for $\beta=1$ ($s_1=4.465$) and $m=0,1,2$; and the red dotted line, the four-body continuum potential with $\beta=2$ ($s_2=6.818$) and $m=0$. We take $R_0=10$ a.u. for all curves. Figure is adapted from Ref. [10].

then the non-adiabatic couplings

$$P_{\nu\nu'} = \left\langle\left\langle \Phi_\nu \left| \frac{d}{dR_4} \right| \Phi_{\nu'} \right\rangle\right\rangle, \quad Q_{\nu\nu'} = \left\langle\left\langle \frac{d\Phi_\nu}{dR_4} \left| \frac{d\Phi_{\nu'}}{dR_4} \right\rangle\right\rangle \quad (4.24)$$

between four-body continuum and atom-trimer channels vanish since $\Phi_\beta^{(3)}$ are independent of R_3 and form an orthonormal set. Recombination is thus driven only by the diabatic couplings

$$V_{\nu'\nu} = \langle \nu' | V_{AB}(r_{14}) + V_{AB}(r_{24}) + V_{AB}(r_{34}) | \nu \rangle \quad (4.25)$$

and occurs predominantly at the crossings in Fig. 4.2 which shows the lowest atom-trimer and four-body continuum potentials multiplied by R_4^2 for clarity. In the vicinity of the crossings, the coupling $V_{\nu'\nu}$ behaves as $\zeta a_{AB}/R_4^3$ to a good approximation. The unitless constant ζ which originates from the numerical evaluation of $V_{\nu'\nu}$, has a weak dependence on the channel numbers, and is on the order of 10^{-3} . While the two sets of potentials in Fig. 4.2 cross in several places, the lowest two A_3+B potentials do not cross a continuum

channel. In our model then, the lowest two Efimov trimers can only be populated by weak non-adiabatic transitions between atom-trimer channels. This conclusion is independent of R_0 , but for more realistic, finite range two-body potentials all the channels will likely be coupled at small R_4 .

Knowing the behavior of the potentials allows us to address a fundamental question in few-body scattering about the existence of a four-body parameter [182, 183]. This question can be described as: with all the low-energy scattering properties we know for a $(N-1)$ -body system, can we describe the N -body low-energy scattering without additional information? For $N = 3$, this question becomes if low-energy three-body scattering can be fully described by the two-body scattering length. In the presence of the three-body Efimov effect, the short-range three-body potential needs to be regularized by a three-body parameter, which can be, for instance, R_0 in Eq. (4.15) or the short-range phase Φ in Eq. (1.5)-(1.7). For $N = 4$, as in the present case, the relevant question is if the two-body scattering length a_{AB} and the three-body cutoff parameter R_0 are sufficient to describe four-body scattering. The scattering length a_{AA} is not counted since we have taken the limit $a_{AA} \rightarrow \infty$. Note that because all of the states of interest here display strongly repulsive potentials at small R_4 (as seen in Fig. 4.2) and the potentials beyond the repulsive region are universally determined by the R_0 and the universal constants s_0 and s_β , no four-body parameter is required in the description of four-body recombination to Efimov trimers.

The four-body recombination rate K_4 is related to the recombination probability $|T_{fi}|^2$ by $K_4 \propto |T_{fi}|^2/k^7$ where $k = \sqrt{2\mu_4 E}$ is the incident four-body wave vector and the unknown proportionality constant is a number that depends on the number of identical particles. By using the Landau-Zener approximation, we expect that peaks of $|T_{fi}|^2$ will occur at $E \approx W_\nu(R_c)$,

$$W_\nu(R_c) \approx \frac{(s_\beta + 2m + \frac{3}{2})^2}{2\mu_{3,4}R_0^2} e^{-\frac{\pi}{s_0}(2n - s_\beta - 2m + \frac{2\gamma - s_0}{\pi} - 1)}. \quad (4.26)$$

where

$$R_c \approx R_0 \sqrt{\frac{\mu_3}{\mu_4}} e^{\frac{\pi}{s_0}(n - \frac{1}{2}\lambda_\nu^c + \frac{2\gamma - s_0}{2\pi} + \frac{1}{4})} \quad (4.27)$$

is the value of R_4 at the crossing determined by the universal behavior of the $A + A + A + B$ channels in Eq. (4.22) and the $A + A + A + B$ channels in Eq. (4.18) and

$$\lambda_\nu^c \approx \sqrt{(s_\beta + 2m + \frac{3}{2})^2 - \frac{1}{4}} \quad (4.28)$$

is the eigenvalue of Eq. (4.10) evaluated at the crossing. We can estimate the transition probability using the Landau-Zener approximation if $E > W_\nu(R_4^c)$, In this approximation, the recombination probability is given by $P_{LZ} = 4T(1 - T) \cos^2 \Delta\phi$. The relative phase $\Delta\phi$ is approximately zero since the potentials are nearly parallel near the crossings, and T is

$$T = \exp \left[-\sqrt{\frac{\mu_3}{\mu_4}} \left(\frac{\mu_3}{\mu_{AB}} \frac{a_{AB}}{R_c} \right)^2 \frac{\zeta^2}{kR_0} \frac{2\pi}{(2\frac{s_0}{\pi} \lambda_\nu^c + \frac{1}{4})} \right], \quad (4.29)$$

This expression shows that for a given initial channel (s_β, m) there is a geometrically spaced sequence of peaks in *energy* for recombination to Efimov trimers n . This characteristic feature of three-body Efimov physics is thus evident in four-body physics as well. Moreover, the spacing of the features is $\exp(-2\pi/s_0)$ just as one would predict from the three-body physics.

To illustrate this point, we show in Fig. 4.3 $P = |T_{fi}|^2$ for several transitions from different initial channels by numerically solving the hyperradial equation. Specifically, we calculated $|T_{fi}|^2$ for recombination from the lowest continuum channel $(s_1, 0)$ into the $n=4$ and 5 states including only these three channels in the Schrödinger equation. These numerical solutions show that the recombination probability does indeed peak at the crossings, thus showing the expected log-periodic spacing of peaks. Since this calculation confirmed our predictions and a full calculation is prohibitively expensive, we estimate the other peaks in Fig. 4.3 by shifting the peaks from the three-channel calculation based on the crossing energy (4.26) and scaling them taking into account the difference in the peak magnitude.

Up to this point, our analysis has assumed $|a_{AA}| = \infty$. If we let it be finite instead, then the above analysis applies in the regime $|a_{AA}| \gg |a_{AB}|$. We further require $a_{AA} < 0$ so that there are no weakly-bound dimers and thus no three-body recombination of A atoms to compete with four-body recombination. Under these conditions, the four-body adiabatic

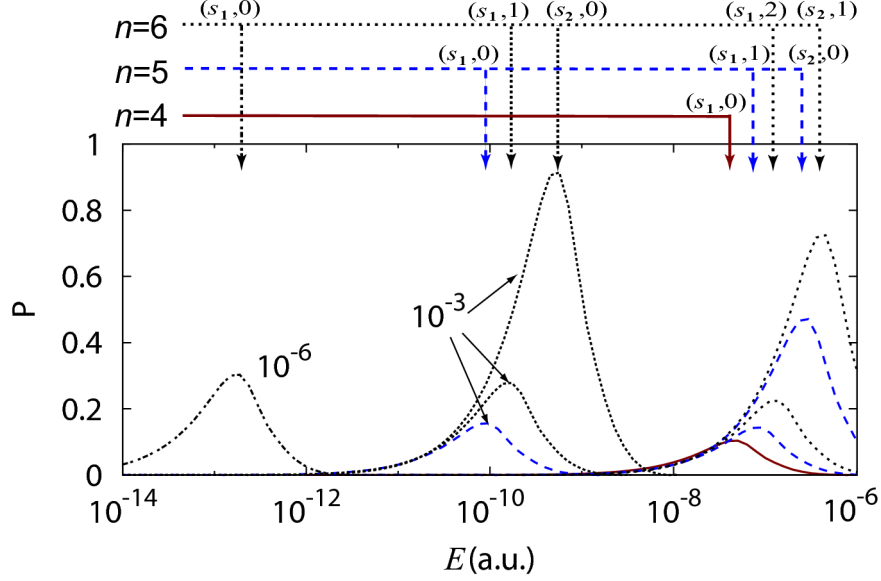


Figure 4.3: The recombination probability for several transitions; (s_β, m) labels the initial continuum channel and n labels the final state of the Efimov trimer. The probabilities must be multiplied by the factors indicated. We have taken $R_0=10$ a.u. and $a_{AB}=100$ a.u.. Figure is adapted from Ref. [10].

potentials behave as described above for $|a_{AB}| \ll R_4 \ll |a_{AA}|$. For $R_4 \gg |a_{AA}|$, the $A+A+A+B$ potentials approach the four-body hyperspherical harmonic potentials

$$W_\nu \approx \frac{\lambda(\lambda + 7) + 12}{2\mu_4 R_4^2} \quad (4.30)$$

where λ a non-negative integer, and the A_3+B potentials approach the trimer bound energies. It follows that at energies $a_{AA}^{-1} \ll k \ll a_{AB}^{-1}$ K_4 keeps the structure described above.

In analogy to three-body recombination, the effects of finite a_{AA} are most easily shown in the zero energy limit. When $E \rightarrow 0$, recombination into the most weakly-bound Efimov trimer dominates. Since the size of this trimer is on the order of $|a_{AA}|$, we expect recombination to occur at $R_4 \approx |a_{AA}|$. So, by employing a WKB analysis similar to that described in Ref. [66], we find that the recombination probability is

$$P = C(a_{AB})(k|a_{AA}|)^7 \sin^2(k_n|a_{AA}| + \Phi), \quad (4.31)$$

where C is a proportionality constant, Φ is a constant phase determined by the universal

shape of the $A_3 + B$ potentials but is independent of a_{AA} , and $k_n = \frac{2}{R_0} \frac{\mu_4}{\mu_3} \exp[-(n\pi + \gamma)/s_0]$ is the wave number for the final trimer state n at $E=0$. When $|a_{AA}|$ increases by a factor of 22.7, a new atom-trimer channel appears and k_n changes to k_{n+1} which, in turn, changes the period of the a_{AA} -dependent oscillations. It turns out that recombination into a particular atom-trimer state will show about seven full oscillations in K_4 as a function of a_{AA} . From the relation $K_4 \propto P/k^7$, Eq. (4.31) also shows that K_4 will be constant in the threshold regime, $ka_{AA} \lesssim 1$, and proportional to $|a_{AA}|^7$. This scaling will apply to K_4 for any system without identical fermions.

4.1.4 Experimental issues

If the trimers cannot be experimentally observed directly, then their production can be measured through the loss of either A or B atoms. In an ultracold mixture of the two, it is much better to observe the B atoms, however, as other few-body processes will lead to loss of A atoms and thus mask the effects we predict. The best choice is to make the B atoms spin-polarized fermions. In this case, $A+A+A+B$ recombination is unaffected, but the competing loss processes involving two or more B atoms can be avoided as they will be suppressed near threshold [178]. There remains the possibility for loss of B atoms in $A+A+B$ collisions, but for $|a_{AA}|=\infty$ or a_{AA} finite but negative, the three-body potentials are all repulsive [61] and only deeply-bound dimer channels are available. The various loss rates for this system are thus small [61]. Measuring the loss of B atoms should then provide a signature of Efimov trimer formation.

The primary processes competing with $A+A+A+B$ recombination for $|a_{AA}|\rightarrow\infty$ are three- and four-body recombination of A atoms since they will deplete the A atoms. If, as we have assumed, there are no A_2 bound states, then there is no $A+A+A$ recombination. For realistic systems with A_2 states, however, we can consider the effect of $A+A+A$ recombination via the rate equations. From the three-body rate equation Eq. (1.4) and the

four-body rate equation:

$$\frac{dn_A}{dt} = -\frac{3}{3!}K_4n_A^3n_B, \quad (4.32)$$

$$\frac{dn_B}{dt} = -\frac{1}{3!}K_4n_A^3n_B, \quad (4.33)$$

we conclude that $A+A+A+B$ recombination can be made dominant by increasing the density n_B of B atoms. To estimate the required n_B , we require that the rate of depletion of A atoms is dominated by four-body recombination, or $K_4n_B > K_3$. The density n_B required for observing the three sets of peaks shown in Fig. 4.3 can thus be estimated by assuming that the overall constants in K_3 and K_4 are of similar magnitude. By using $|T_{fi}|^2 = 10^{-7}$, 10^{-4} , and 10^{-1} from Fig. 4.3 for the three sets of peaks in order of increasing energy of the peaks, the density n_B is estimated to be on the order of 10^{15} , 10^{15} , and 10^{17} atoms/cm³, respectively. For the three-body recombination probability, we use 10^{-3} [50]. These probabilities, however, are not expected to be universal as they depend on short range physics. Consequently, our density estimates can change — assuming equal three- and four-body probabilities, for instance, gives n_B of 10^{11} , 10^{14} , and 10^{19} atoms/cm³. So, with this level of uncertainty, there is hope that the first two peaks might be within experimental reach. The competing $A+A+A+A$ recombination process can be estimated by the theoretical work in Ref. [59] and experimental observations [57, 60], and the conclusion is that the loss from $A+A+A+A$ recombination is at most the same order of magnitude as $A+A+A$ recombination for the densities considered here. By making $n_B \gg n_A$, though, this process might be made less important than $A+A+A+B$ recombination. These two processes can also be separated by the dependence of the latter on a_{AB} [192].

4.1.5 Fermi contact potential in adiabatic hyperspherical representation

Before concluding, we will show the validity of the Fermi contact potential Eq. (4.2) in an adiabatic hyperspherical representation. For simplicity, we discuss the effect on three-body adiabatic potentials, and the conclusion on its validity is expected to hold for four-body

potentials. We consider two atoms (m_A) which are identical bosons and in resonance ($a \rightarrow \infty$), and another atom (m_B) which is a different species having scattering length a_0 with each of the bosons.

First, we solve the potentials by treating the interactions between the third atom and the bosons as a perturbation. We get the unperturbed three-body potential by assuming that the third atom does not interact with the others. Using ZRP model, the only boundary condition on three-body wave function is from the identical bosons. The potential is determined as

$$U(R_3) = \frac{n^2 - \frac{1}{4}}{2\mu_3 R_3^2}, \quad (4.34)$$

where $n = 1, 3, 5, \dots$ is an odd integer. The diagonal corrections are 0 for these potentials.

The perturbation to the adiabatic potential is calculated by using a Fermi contact potential,

$$U^{(1)}(R_3) = \frac{4}{\pi} \sqrt{\frac{\mu_{AB}}{\mu_3^3}} \left(\frac{2 \cos n\alpha^{(12)}}{\sin 2\alpha^{(12)}} \right)^2 \frac{a_0}{R_3^3} \quad (4.35)$$

where $\alpha^{(12)}$ and $\alpha^{(13)}$ are constants for kinematic rotations between Jacobi sets

$$\alpha^{(12)} = \frac{m_A}{m_A + m_B}, \quad \alpha^{(13)} = \sqrt{\frac{m_B}{2(m_A + m_B)}}. \quad (4.36)$$

If we attribute all the interactions between three pairs of atoms to the three boundary conditions in ZRP model, the adiabatic potential $U(R_3) = \frac{s^2 - \frac{1}{4}}{2\mu_3 R_3^2}$ is determined by the transcendental equation

$$\begin{aligned} \cos\left(\frac{\pi}{2}s\right)s \left[\cos\left(\frac{\pi}{2}s\right)s - \frac{\sin(s\alpha^{(12)})}{\sin^{\frac{3}{2}}\alpha^{(12)} \cos^{\frac{1}{2}}\alpha^{(12)}} - \sqrt{\frac{\mu_3}{\mu_{13}}} \frac{R_3}{a_0} \sin\left(\frac{\pi}{2}s\right) \right] \\ = 8 \left[\frac{\sin s\left(\frac{\pi}{2} - \alpha^{(13)}\right)}{\sin 2\alpha^{(13)}} \right]^2 \end{aligned} \quad (4.37)$$

The asymptotic expansion $s(R_3) = C_0 + \frac{C_1}{R_3} + O\left(\frac{1}{R_3^2}\right)$ gives the first two terms of the potential:

$$U(R_3) = \frac{n^2 - \frac{1}{4}}{2\mu_3 R_3^2} + \frac{4}{\pi} \sqrt{\frac{\mu_{AB}}{\mu_3^3}} \left(\frac{2 \cos n\alpha^{(12)}}{\sin 2\alpha^{(12)}} \right)^2 \frac{a_0}{R_3^3} \quad (4.38)$$

where n is a positive integer. The even n solutions here correspond to trivial solutions when the atom B is treated as free. The odd n solutions give the potentials which have one-to-one correspondence to those in Eq. (4.34). By asymptotic expansion we have found the diagonal corrections for these channels is of higher order: $Q_{nn} \sim O(\frac{1}{R_3^4})$. Thus the result from the ZRP model and from perturbation agree exactly in the leading order in the asymptotic region ($R_3 \gg a_0$). This gives the same result as in many-body theory, where the adoption of Fermi contact potential gives the answer exact in the lowest order.

4.1.6 Summary

To summarize, we have taken the first steps in understanding ultracold four-body recombination into Efimov trimers. By setting up the problem in a mixed diabatic and adiabatic representation, we were able to obtain largely analytical results. In the process, we showed that the four-body recombination should show prominent, geometrically spaced energy-dependent peaks that reflect the three-body Efimov physics. In fact, these peaks are separated by precisely the factor one expects from the three-body physics. Further, we proposed a potentially useful scheme using the spectator B atoms to detect these trimer-forming events. Observing the four-body recombination loss is only the first step — studying the trimers produced is the real goal.

4.2 Four-body Efimov physics induced by three-body Efimov effect

For systems with four identical particles, remnants of the three-body Efimov effect have been predicted and observed [59, 60, 181, 183], extending universal physics from three-body to four-body systems. In particular, they have found that there are two universal four-body resonance states attaching each of the atom-trimer break-up channel. The Efimov effect in a heteronuclear atomic system near overlapping Feshbach resonances has recently been of both theoretical and experimental interest [67, 144–146, 148, 193, 194], where the mass ratio and the scattering lengths between the atoms from different species provide additional knobs for the studies of Efimov physics. However, the experimental studies suffer from the fact that the magnetic field dependence of the scattering lengths are determined by the nature of atomic interactions and thus cannot be tuned independently.

Here we propose studying Efimov physics in a heteronuclear atomic system with large mass ratio m_H/m_L , where m_H and m_L are the masses of the heavy and light atoms, respectively. In such a system, the motion of the light atom interacting with the heavy ones can be treated by the Born-Oppenheimer approximation, which mediate effective interactions between the heavy ones even if they do not interact by themselves.

As will be shown below, the ratio of the scattering length between heavy and light atoms a_{HL} and the effective scattering length between the heavy atoms a_{HH}^* can be tuned at will with the help of a Feshbach resonance between the heavy and light atoms. Here we study a four-body system with three heavy identical bosons and one light atom, where we show the embedded three- and four-body Efimov physics in ultracold collisions and the production of Efimov triatomics with non-zero angular momenta. In particular, we show that these novel Efimov features are manifested in the recombination process



where a collisional process determines the stability of the Feshbach molecule HL formed in

a bath of H atoms.

One may notice that the above process also produces an Efimov molecule, but there are some differences between this process and the four-body recombination process $A + A + A + B \rightarrow A_3 + B$ we have introduced in Sec. 4.1, making them appropriate for different purposes. First, the process we introduce here produces a heteronuclear Efimov molecule while the process of four-body recombination gives a homonuclear Efimov trimer. Second, the process we introduce here is essentially a three-body recombination process, which typically has a higher rate than a four-body recombination process in the ultracold experiments, but it requires one more step of producing a sample of HL diatomic molecules. For the four-body recombination process, however, this step is not required. We will also address the question of the four-body Efimov effect, where contrary to the conventional wisdom that no true four-body Efimov effect is possible, we verify the existence of the four-body Efimov effect in the previously mentioned four-body system with very large mass ratios.

4.2.1 Efimov effect with Born-Oppenheimer approximation

To facilitate our discussion, in $HHLL$ system, we first review the Efimov effect in a three-body system with two heavy and one light particles. The origin of the Efimov effect can be easily demonstrated using the Born-Oppenheimer (BO) approximation [23, 195]. Though mostly used in molecular systems with Coulomb interactions, the BO approximation works perfectly well for treating the motions of the light particles in a neutral heteronuclear system with short-range interactions. When the scattering length between the heavy and light particles a_{HL} becomes much larger than their characteristic interaction range r_0 , the Born-Oppenheimer potential $U(\rho)$ induced by exchange of the light particle has the universal long-range behavior [195]

$$U(\rho) = -\chi_0^2/2m\rho^2, \quad (r_0 \ll \rho \ll |a_{HL}|) \quad (4.40)$$

where m is the mass of the light particle, ρ is the distance between the heavy particles and $\chi_0 \approx 0.567143$ [195].

A procedure for deriving Eq. (4.40) has been shown in Ref. [195], but here we just give a simple summary. Since solving the two-body Schrödinger equation with a separable potential is very simple in the momentum space, we take a s -wave separable potential as the interaction between the H and L :

$$v = |g\rangle\lambda\langle g|, \quad (4.41)$$

where λ determines the strength of the interaction and the ket $|g\rangle$ determines the actual shape of the potential when a particular representation is chosen. For the convenience of analytical derivation, here we take the Yamaguchi [196] form in the momentum space

$$\langle \vec{p}|g\rangle = \frac{1}{p^2 + p_0^2}, \quad (4.42)$$

where \vec{p} is the momentum vector and p_0 is the low-energy cut-off which is related to the range of the potential by $r_0 = 3/p_0$. Note that there is at most one bound state for a separable potential. Writing the two-body Schrödinger equation in the momentum space for solving the bound states gives

$$\frac{p^2}{2\mu_2}\psi(\vec{p}) + \frac{\lambda}{p^2 + p_0^2} \int \frac{\psi(\vec{p}')}{p'^2 + p_0^2} dp'^3 = -\frac{\kappa_{2b}}{2\mu_2}\psi(\vec{p}). \quad (4.43)$$

where κ_{2b} is the two-body binding wave number. Noticing that

$$N = \int \frac{\psi(\vec{p}')}{p'^2 + p_0^2} dp'^3 \quad (4.44)$$

is just a number, Eq. (4.43) can be solved algebraically as

$$\psi(\vec{p}) = N \frac{-\lambda}{p^2 + p_0^2} \frac{2\mu_2}{p^2 + \kappa_{2b}^2}. \quad (4.45)$$

Consistency of Eq. (4.45) with Eq. (4.44) then gives

$$\kappa_{2b} = \pi \sqrt{(-\lambda)\mu_2/p_0} - p_0, \quad (4.46)$$

where μ_2 is the two-body reduced mass.

Efimov physics in the HHL system

For the HHL system, with the BO approximation the Schrödinger equation for the light particle is

$$(p^2 + \mathcal{O}|g\rangle\lambda\langle g|\mathcal{O}^{-1} + \mathcal{O}^{-1}|g\rangle\lambda\langle g|\mathcal{O})|\Phi\rangle = U(\rho)|\Phi\rangle, \quad (4.47)$$

where $\mathcal{O} = e^{ip\rho/2}$ is the translation operator. Solving Eq. (4.47) in the momentum space leads to a transcendental equation

$$1 - J(0) - \Lambda J(\rho) = 0, \quad (4.48)$$

where $\Lambda = \pm 1$ represents the symmetry of the wavefunction for L under the exchange of the two identical H 's.

$$J(\rho) = -\frac{4\lambda m\pi^2}{\rho} \left[\frac{e^{-s\rho} - e^{-p_0\rho}}{(p_0^2 - s^2)^2} - \frac{e^{-p_0\rho} p_0\rho}{2p_0^2(p_0^2 - s^2)} \right]. \quad (4.49)$$

The the BO potential is then determined by

$$U = -s^2/2m. \quad (4.50)$$

When $|a_{HL}| \gg r_0$, Eq. (4.50) reduces to the BO potential in Eq. (4.40).

For the heavy particles H moving in the BO potential of Eq. (4.40), the bound state energies then satisfy the structure of an Efimov spectrum:

$$E_{n+1}/E_n = e^{-2\pi/s_0}, \quad (n = 0, 1, 2, \dots) \quad (4.51)$$

for states below the $HL + H$ break-up threshold such that $|E_n| \leq \chi_0^2/2ma_{HL}^2$, where $s_0^2 = \chi_0^2 M/m$ with M being the mass of the heavy particle. The Efimov effect, i.e., an infinite number of states, thus occurs in the limit $|a_{HL}| \rightarrow \infty$, corresponding to a zero-energy HL bound state. In general, the heavy particles H also interact among themselves. But since the H - H interaction is short-range, it can only change the short-range behavior of the BO potential and will keep the long-range behavior in Eq. (4.40) unchanged. Addition of any

H - H interaction will then change the position of the ground Efimov state energy E_0 , but the scaling behavior Eq. (4.51) and all the resulting Efimov features in scattering observables will not be changed.

The low-energy scattering properties of the heavy particles are thus closely connected to the HHL Efimov state: whenever an Efimov state appears at finite $|a_{HL}|$, the effective scattering length a_{HH}^* goes through a pole. For the Borromean case where $a_{HL} < 0$, the BO approximation has difficulty when ρ is beyond the distance where HL becomes unbound so that Eq. (4.48) does not have a solution. Special treatment should be made for this situation. For $a_{HL} > 0$, no special attention is required since HL remains bound for all value of ρ , and Eq. (4.48) always has solutions. In the following we will discuss the two cases separately.

Efimov physics in the $HHHL$ system

For simplicity, we will assume that the H 's do not interact directly. Our analysis, however, will apply so long as the scattering length from direct interactions between H 's is small so that H - H interactions will change only the short-range physics of the $HHHL$ system without modifying the long-range behavior. Then neglecting such interactions will have negligible effect on the scattering processes in which we are interested. Following the similar procedure for obtaining the BO potential for HHL system, for $a_{HL} > 0$, we integrate out the light particle motion, producing the interaction potential surface for three the H 's [23]. The motion of the H 's is then solved in hyperspherical coordinates [109, 110] (see Secs. 2.2, 2.3 and 2.4).

As for three-body systems, the universal behavior of the four-body system can be learned from the scaling of the adiabatic hyperspherical potentials. The effective adiabatic potentials $W_\nu(R) = U_\nu(R) - Q_{\nu\nu}(R)/2\mu_3$ asymptotically connect to all the possible break-up configurations such as the $HHL + H$ two-body break-up and $HL + H + H$ three-body break-up, where $\mu_3 = M/\sqrt{3}$, R is the hyperradius for three H particles. Their scaling behavior with R is the most significant in determining the scattering length scaling properties

of various collisional rates in the few-body systems. For the $HHHL$ problem, $U_\nu(R)$ are obtained from solving the hyperangular equation:

$$\left[\frac{\Lambda^2}{2\mu_3 R^2} + V(R, \Omega) \right] \Phi(R; \Omega) = U_\nu(R) \Phi(R; \Omega), \quad (4.52)$$

where Λ is the grand angular momentum operator Eq. (2.34) for the three H 's, V is the Born-Oppenheimer potential, and Ω denotes all the hyperangles.

We tune a_{HL} such that a HHL bound state is weakly-bound. As mentioned above, this tuning can be characterized by the effective scattering length a_{HH}^* . The numerical calculations show that the lowest adiabatic hyperspherical potential has a long-range form

$$W_0 = -\frac{g_0^2 + 1/4}{2\mu_3 R^2}, \quad (a_{HL} \ll R \ll |a_{HH}^*|) \quad (4.53)$$

where the universal constant g_0 is numerically determined to be $g_0 \approx 1.006$. This is expected from the argument of three-body Efimov effect, since here we have effectively a HHH three-body system with large scattering lengths from the short-range interactions mediated by the L . When a_{HL} is tuned to some value \tilde{a}_{HL} where $a_{HH}^* \rightarrow +\infty$, the long-range behavior in the effective adiabatic potential in Eq. (4.53) extends to $R = \infty$ and an infinite series of four-body bound states accumulate in the long-range potential with the energy scaling $E_{n+1}/E_n = e^{-2\pi/g_0} \approx 1/515$. Note that the emergence of such states are not regarded as four-body Efimov effect, since their existence depends on the HL subsystem being bound.

4.2.2 $HL + H + H$ recombination

The long-range scaling in Eq. (4.53) for the HHH hyperspherical potential leads to universal scaling for the recombination process $HL + H + H \rightarrow HHL + H$. We have calculated $HL + H + H$ recombination rates by numerically solving the coupled hyperradial equation Eq. (2.40) for three H 's. Fig. 4.4 shows sequence of overlapping resonant features in the recombination rates K_3 as a_{HL} increases when the mass ratio $m_H/m_L = 30$. The main resonant features (two major peaks) correspond to the emergence of the lowest two HHL

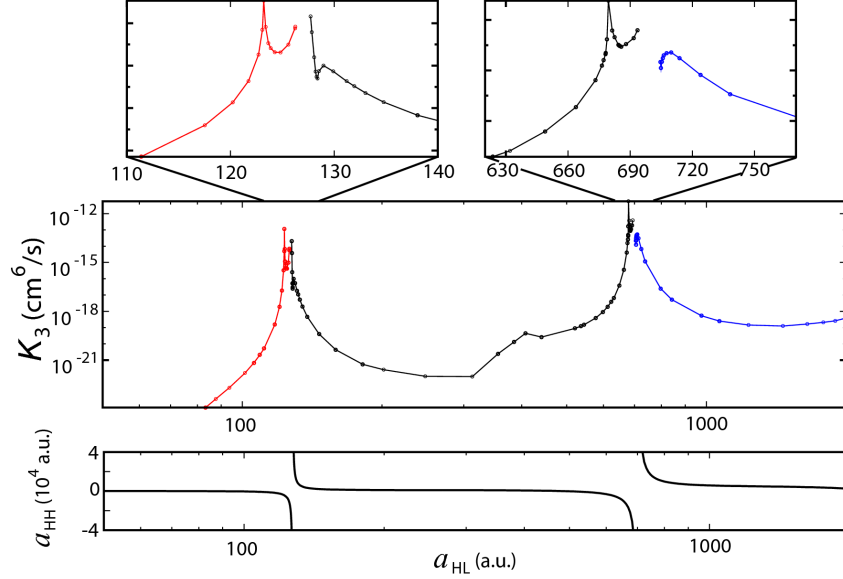


Figure 4.4: The recombination rates K_3 for the process $HL + H + H \rightarrow HHL + H$ when $M/m = 30$. The major peaks occur near the region where a_{HH}^* diverges. The sequences of sub-peaks and sub-minima indicate the formation of the four-body bound states. The universal three-body Efimov physics of the HHL subsystem is manifested by the separation between the major peaks. Figure is adapted from Ref. [7].

Efimov states. Their separation is determined by the universal constant s_0 from the three-body Efimov effect in the HHL system. The value of s_0 is determined by Eq. (3.18) and gives $a_{HL}^{(2)}/a_{HL}^{(1)} = e^{\pi/s_0} \approx 3.96$. The observed separation is 5.5 due to the fact that the criterion for universal physics $a_{HL} \gg r_0$ is not well satisfied for the first two peaks. The features on top of a major peak are seen as sub-peaks and local minima on the $a_{HH}^* < 0$ and $a_{HH}^* > 0$ ridges, respectively. These features come from the formation of the series of the four-body bound states mentioned above and is the consequence of the universal scaling of the hyperspherical potential in Eq. (4.53).

Near the major peaks where $|a_{HH}^*| \gg a_{HL} \gg r_0$, the behavior of the effective hyperspherical potentials are schematically shown in Fig. 4.5. The universal behavior of the potentials

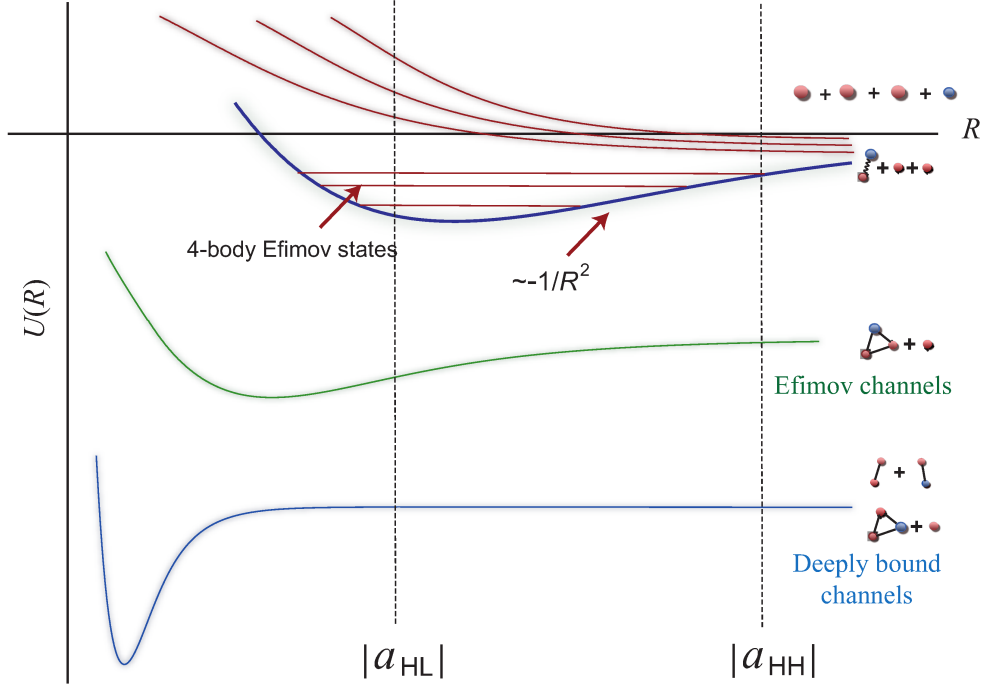


Figure 4.5: The effective hyperspherical adiabatic potentials W_ν for three heavy atoms when $a_{HH}^* \gg a_{HL} \gg r_0$. The deeply-bound channels are not considered in our model, and their effects are expected to be small since they lie much deeper than the atom-Efimov trimer channels.

gives the following universal formula for the rates by WKB analysis [66]:

$$K_3^{(a_{HH}^* > 0)} = \frac{C}{\mu} \sin^2[g_0 \ln(a_{HH}^*/a_{HL}) + \Phi] a_{HH}^{*4}, \quad (4.54)$$

$$K_3^{(a_{HH}^* < 0)} = \frac{C'}{\mu} \frac{\sinh(2\eta) |a_{HH}^*|^4}{\sin^2[g_0 \ln(|a_{HH}^*|/a_{HL}) + \Phi'] + \sinh^2(\eta)} \quad (4.55)$$

where C is a universal constant while C' , Φ , Φ' and η depend on the property of the recombined weakly-bound HHL triatomic states. These expressions have the same form as those for three-body recombination Eq. (1.5) and (1.6), with the short-range distance r_0 changed to a_{HL} , which determines the range of $H+L$ interaction. Also, as will be shown later from the numerical calculation, the phases Φ and Φ' are universal since recombined HHL triatomic states have universal properties. Similar to the atom-dimer scattering length in case of three-body Efimov effect [52], the relationship between a_{HH}^* and a_{HL} can be derived

to be:

$$a_{HH}^* \approx D \cot[s_0 \ln(a_{HL}/r_0 + \Phi_0)] a_{HL}, \quad (4.56)$$

where D is a universal constant and Φ_0 depends on the short-range detail of the interaction between H and L when their distance is about r_0 . The effective scattering length between the heavy particles can thus be tuned across a huge range through small changes of a_{HL} . Considering the experimental limit in obtaining the large scattering length a_{HL} via the tuning of magnetic field, this level of magnification can greatly improve the attainable value of the two-body scattering length, which gives access to much larger space in the study of many-body physics under unitarity limit [197, 198].

More interestingly, by tuning the mass ratio, HHL Efimov states with non-zero angular momentum can be formed. When the mass ratio is large enough, the attractive interaction induced by the light particle can overcome the centrifugal barrier between the two heavy particles, which gives the three-body Efimov effect in high angular momentum states. The scaling of the bound state energies also follows Eq (4.51), but the scaling constant s_0 will depend on the angular momentum of the HHL Efimov state j . These higher angular momentum Efimov states have not been observed because experiments thus far have mostly focused on identical particles which have no such states.

In contrast to the zero angular momentum HHL Efimov states, the emergence of these nonzero angular momentum states near the threshold does not lead to long-range scaling of the hyperspherical potentials. In particular, the long-range attractive $1/R^2$ potential does not show up in the $HHL(j > 0) + H$ channel when the $HHL(j > 0)$ states are weakly-bound. An infinite number of four-body bound states is thus not expected, however, the universal scaling feature is nevertheless marked in the separation between the simple peaks of the recombination rates, as shown in Fig. 4.6. For the mass ratio $M/m=50$, HHL Efimov states with $j = 2$ also appear, while the $j = 1$ states do not exist due to the identical particle symmetry of the heavy particles. The separation for the $j = 0$ major peaks is expected to change to $a_{HL}^{(N+1)}/a_{HL}^N \approx 2.94698$. In Fig. 4.6, the separations between the first three major

peaks are 4.7 and 3.4, which are not very close to the expected universal value. The reason is that a_{HL} is not dramatically larger than r_0 . For $j = 2$, the separation between the peaks is expected to be $a_{HL}^{(N+1)}/a_{HL}^N \approx 9.46665$. The finite range effect is more dramatic in this case, resulting a separation of 17.5 for the first two peaks. Near a major peak, the separation of the sub-peaks and minima carry the scaling signature of the universal four-body states with an expected value $|a_{HH}^{*(n+1)}/a_{HH}^{*(n)}| = e^{\pi/g_0} \approx 22.7$ ($a_{HH}^* \gg a_{HL}$ and $a_{HH}^* \gg r_0$). The finite-range effect changes separations of the first two sub-peak and minima to 19.3 and 14.6, respectively.

Another interesting observation is about the phases Φ and Φ' in Eqs. (4.54) and (4.55). Though they typically depend on the mass ratio, but as shown in Fig. 4.6, they are independent of a_{HL} and stay unchanged across the major peaks. As mentioned above, this universal behavior can be understood by the fact that the short-range physics for the $HL + H + H \rightarrow HHL + H$ recombination process is determined near $R \approx a_{HL} \gg r_0$, where the potentials are still universal.

4.2.3 Four-body Efimov effect

For $a_{HL} < 0$, we focus on the existence of the four-body Efimov effect. We will follow a definition of the N -body Efimov effect from Ref. [22, 23]. Analogous to the three-body case, for a four-body Efimov effect to exist, the four-body system must possess an infinite number of stable bound states when there is a zero-energy three-body bound state (and also no two-body bound states) [23]. Under these conditions, the four-body Efimov effect is completely independent of any three-body Efimov effect, so that it is fundamentally different from the universal four-body states discussed in the previous section and those discussed in Refs. [59, 181, 183]. Since it has been shown [22] that no Efimov effect occurs for four identical particles, we consider instead an $HHHL$ system. One of the previous works on such a system [23] was based only on analyzing the BO potential surface, and it concluded that there was no such effect. Another work [24] also based on BO approximation used

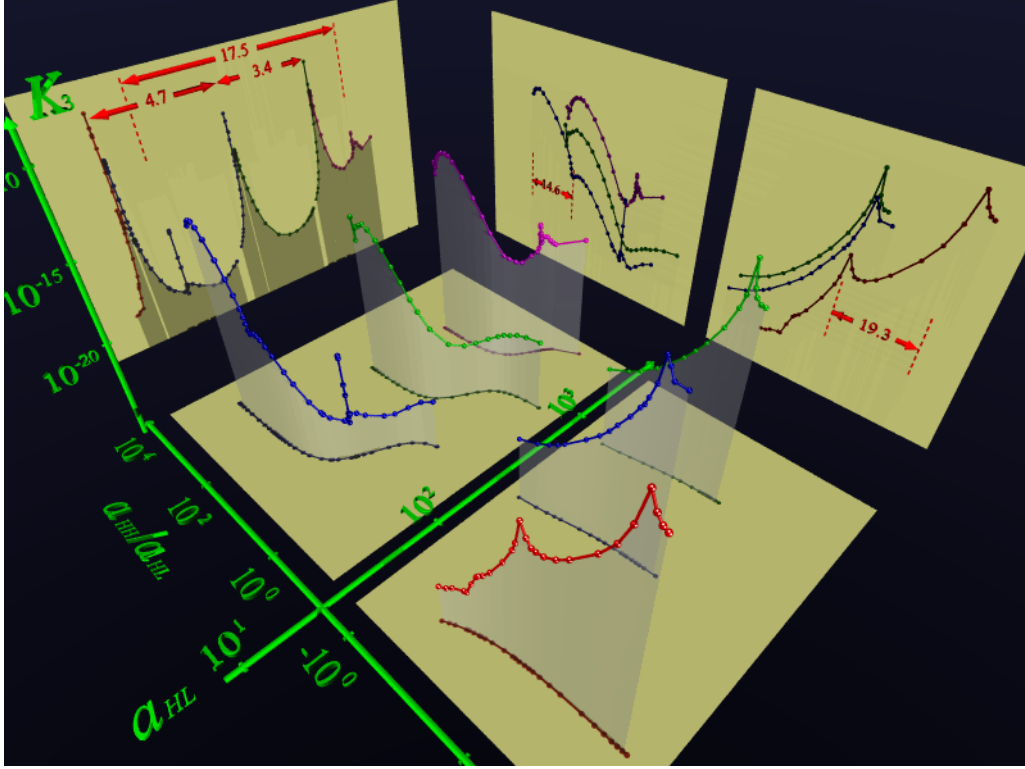


Figure 4.6: The recombination rates K_3 for the process $HL + H + H \rightarrow HHL + H$ with $M/m=50$. The effective scattering length a_{HH}^* is also plotted as one axis to show the universal four-body scalings. The sharp simple peaks indicate the formation of $j=2$ HHL Efimov states. The sub-peak (minima) structure can be seen from projection on the $K_3 - a_{HH}^*$ plane. The separation between the sub-peaks (minima) shows the scaling character of the universal four-body Efimov physics. Figure is adapted from Ref. [7].

general criteria for the Efimov effect and concluded that there was an effect. Though this disagreement has been overlooked and the four-body Efimov effect is generally regarded impossible, here we reaffirm the conclusion in Ref. [24] that argues that such an effect exists by numerically solving the three-body Schrödinger equation of the H particles and further giving qualitative arguments on how the non-BO effect modifies the result.

The difficulty in handling the L particle with the BO approximation for $a_{HL} < 0$ comes from the fact that L become unbound when the distance between two H particle exceeds $|a_{HL}|$. A non-rigorous way to deal with this situation is simply to set the BO potential to be zero. Then an effective scattering length a_{HH}^* can still be defined as for $a_{HL} > 0$, and

the long-range hyperspherical potential Eq. (4.53) appears when $a_{HH}^* \rightarrow \infty$. This implies that an infinite series of four-body bound states will show up as the manifestation of the four-body Efimov effect. However, after some discussion with von Stecher and Greene [199] about the connection of a BO potential to a hyperspherical potential, we have investigated the connection further and have found that setting the BO potential as zero is inappropriate since a zero-energy HHL bound state is actually confined within a long-range barrier in the view of the adiabatic hyperspherical potential for HHL system. On the other hand, as the mass ratio increases, the height of the barrier decreases, and the barrier is pushed to a larger distance, $R \sim |a_{HL}|(M/m)^{1/4}$, as shown in Fig. 4.7. From this argument, in the BO

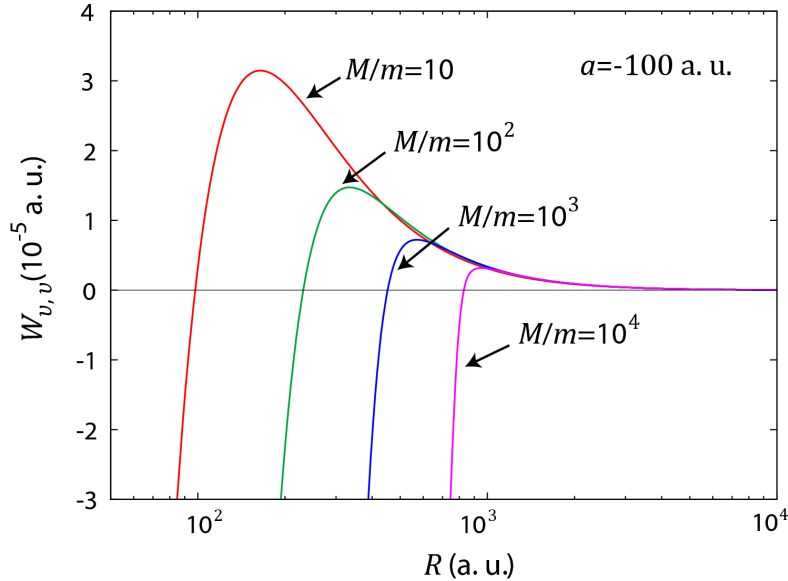


Figure 4.7: The lowest three-body continuum adiabatic hyperspherical potential for HHL with different mass ratios.

limit $M/m \rightarrow \infty$ it is valid to set the BO potential to be zero when L becomes unbound. However, this limit is very slowly approached for a finite value of M/m . Particularly, the maximum possible number of four-body Efimov states can be estimated by the largest size of such states determined by the position of the barrier as:

$$n \approx \left\lfloor \frac{g_0}{\pi} \ln \left[\left(\frac{M}{m} \right)^{1/4} \right] \right\rfloor. \quad (4.57)$$

a_{HL} is canceled in the expression because the value of a_{HL} at which the first HHL zero-energy state appears is comparable to the size of short-range interactions r_0 .

In Fig. 4.8, we show a schematic four-body Efimov energy spectrum. The four-body Efimov bound states appear in the upper-left corner of the diagram, where the lowest three-body bound state passes across the four-body break-up threshold. The four-body states which persist across the zero of $1/|a_{HL}|$ are the those sitting in the lower atom-Efimov trimer channels (green potential curves shown in Fig. 4.5). They are attached to the HHL three-body Efimov states and are not Efimov states. These states are of the same nature as the universal four-body states in Ref. [59, 60, 181, 183].

Nevertheless, the requirement for a large mass ratio reveals the class of exotic four-body Efimov states constituted by one electron and three atoms. We demonstrate the formation of the four-body Efimov states with the atoms being ^{133}Cs where $n = 1$ excited four-body Efimov state can be formed. Since the interaction between the atoms can be tuned more easily in ultracold experiments than the $\text{Cs}+e^-$ interaction, we keep the $\text{Cs}+e^-$ interaction fixed with fixed $a_{HL} = -22$ a.u. [200] and tune the $\text{Cs}+\text{Cs}$ interaction instead. For studying the universal physics for this system, we can use model short-range potentials for both $\text{Cs}+e^-$ and $\text{Cs}+\text{Cs}$ interactions without loss of generality. For $(\text{Cs}_2^-)^*$ anion where $\text{Cs}+\text{Cs}$ is in the highest vibrational state, a bound state with zero binding energy is obtained when $a_{HH}^* \rightarrow \infty$, which can be achieved by tuning the $\text{Cs}+\text{Cs}$ direct interaction with a scattering length $a_{HH} < 0$.

If $(\text{Cs}_2^-)^*$ anions coexist with ultracold Cs atoms, the four-body Efimov effect can be manifested through the vibrational relaxation process



analogous to the resonant atom-dimer relaxation due to the three-body Efimov effect [107, 138, 201]. Experimentally, the resonant relaxation can be detected by the loss of Cs atoms. One may also look at the four-body recombination process $\text{Cs} + \text{Cs} + \text{Cs} + e^- \rightarrow \text{Cs}_2^- + \text{Cs}$, but this requires ultracold electron gas which is very difficult to be realized experimen-

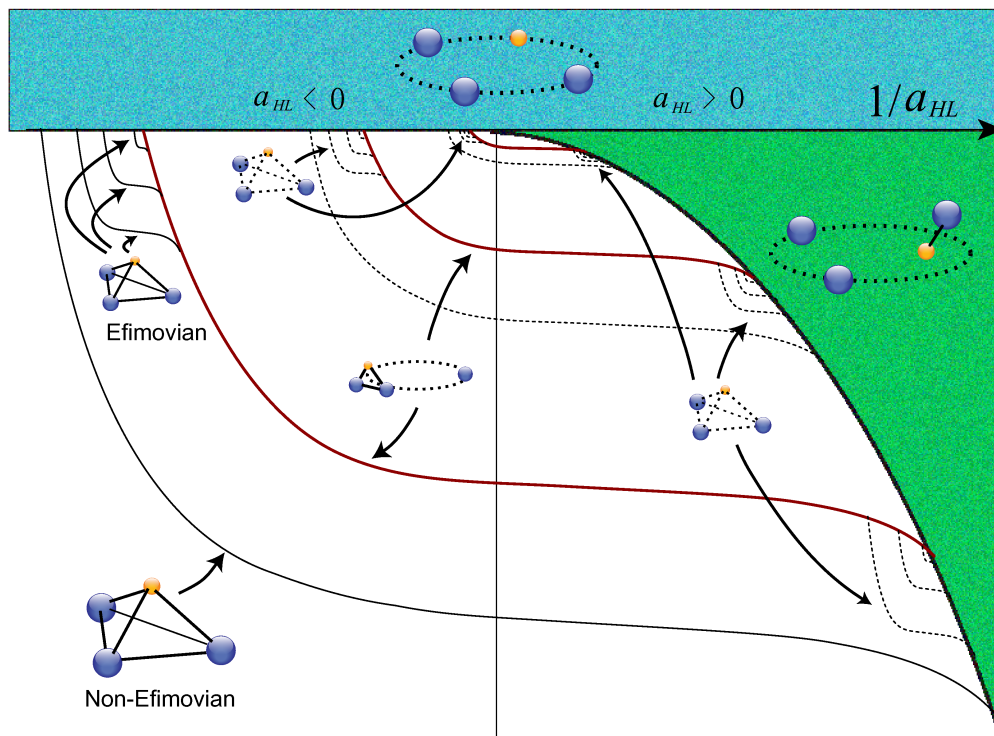


Figure 4.8: Schematic Efimov energy spectrum for $HHHL$ four-body system. The blue-colored region is the $H+H+H+L$ four-body break-up continuum; the green-colored region is $HL+H+H$ three-body break-up continuum. The red lines indicate the energy of HHL three-body states, and the four-body states corresponding to these lines are the $HHL+H$ scattering states. When $1/a_{HL} \rightarrow 0$, these three-body states are the Efimov states having universal properties. The light black lines under the three-body bound energies are the energies of four-body bound states (solid lines) or resonance states (dashed lines). The four-body states (resonances) whose energies do not merge into the three-body states are not considered as four-body Efimov states.

tally [202].

We calculate the rates for the above relaxation process without including relaxation channels containing the two-body bound states Cs_2 and Cs^- in our model. Their effects, however, can be neglected since they are much deeper than the energy scale considered here. As shown in Fig. 4.9, the resonant peaks in the relaxation rates V_{rel} indicate the formation of the four-body Efimov states Cs_3^- near the $(\text{Cs}_2^-)^* + \text{Cs}$ threshold, where the collisional relaxation of the excited $(\text{Cs}_2^-)^*$ anions is greatly enhanced. Though the relationship be-

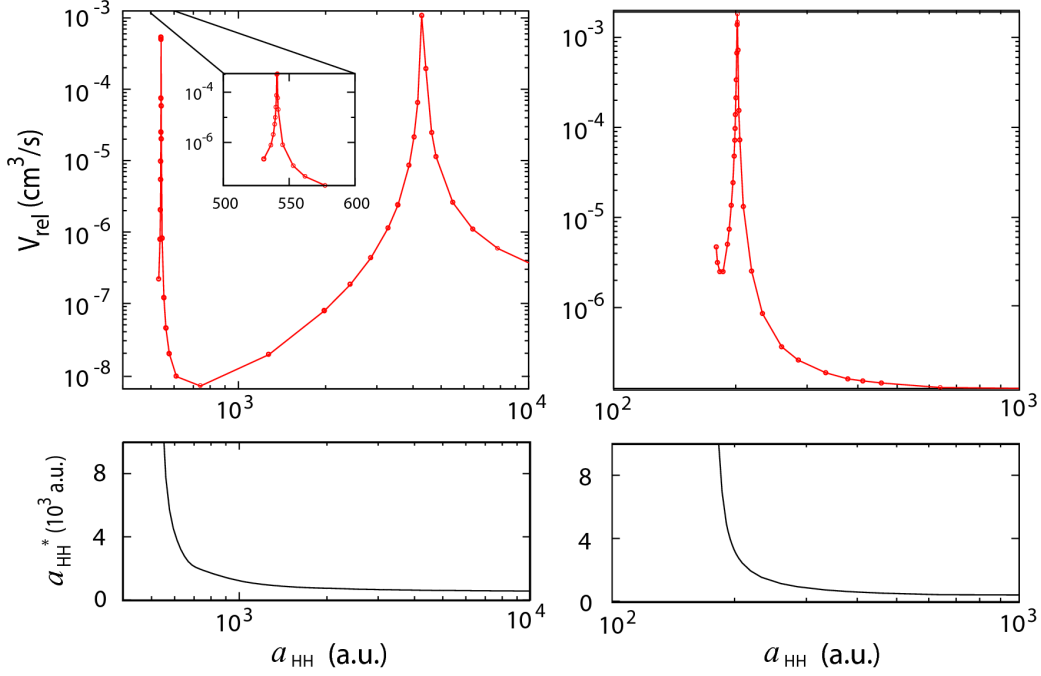


Figure 4.9: The collisional relaxation rates V_{rel} for $(\text{Cs}_2^-)^* + \text{Cs} \rightarrow \text{Cs}_2^- + \text{Cs}$ for different $(\text{Cs}_2^-)^*$ Borromean states in (a) and (b). The Cs-Cs interaction is tuned such that a weakly-bound $(\text{Cs}_2^-)^*$ state is below the four-body break-up threshold. The rates surge up to large value when a_{HH}^* is large, and the peaks occur when a four-body Efimov state Cs_3^- is near the $(\text{Cs}_2^-)^* + \text{Cs}$ threshold. Figure is adapted from Ref. [7].

tween a_{HH} and a_{HH}^* is generally non-universal, for $a_{\text{HH}}^* \gg |a_{\text{HL}}| > 0$ the four-body Efimov effect leads to universal scaling behavior of V_{rel} with a_{HH}^* , which can be obtained by WKB analysis [66] as

$$V_{\text{rel}}^{(a_{\text{HH}}^* > 0)} = \frac{A_\eta \sinh(2\eta)}{\sin^2[s_0 \ln(a_{\text{HH}}^*/r_0) + \Phi] + \sinh^2(\eta)} a_{\text{HH}}^*, \quad (4.59)$$

where A_η , η and Φ all depend on the short-range detail of the relaxed Cs_2^- bound state.

4.2.4 Conclusion

To conclude, we have studied the four-body Efimov physics in a heteronuclear atomic system $HHHL$. In such a system the ratio of the scattering lengths from the distinct pairs can be tuned to an arbitrary value, making such a system an ideal testbed for the study of the universal physics near overlapping resonances. For $a_{\text{HL}} > 0$, we have studied the three-body

recombination of the weakly-bound HL molecule with two H atoms, where the embedded three- and four-body features are observed as a particular effect for overlapping resonances. Our study also shows that this process can be used as an efficient way for producing Efimov molecules [10] (see Sec. 4.1). For $a_{HL} < 0$, we have confirmed the existence of the four-body Efimov effect and have given the qualitative condition for its existence. An experimental approach is further proposed for observing the effect.

4.3 Universal four-body physics in one dimension

The rapid development of optical techniques in recent years has realized various trapping geometries for ultracold quantum gases. For instance, toriodal traps have been used for the study of superfluidity for quantum degenerate gases [203, 204] and more importantly, optical lattices have been realized to mimic the lattice structures in condensed matter systems by superposing counter-propagating laser beams [205]. In contrast to the real lattices in the condensed matter world, the structure and the dimensionality of the optical lattices can be tuned very easily.

In low dimensional systems, the physical properties of the quantum systems are usually quite different from their 3D properties. For instance, Bose gases can behave like Fermi gases [206, 207] when the 1D coupling constant [208] becomes large, and such gases are called the Tonks-Girardeau gas and have been realized experimentally [209]. It has also been shown that inelastic transitions are forbidden in 1D — in the zero-range limit of the interactions — which is a good example of a bizarre physical law when the system becomes integrable [210, 211]. The 1D few-body and many-body systems thus become the frontier for looking for novel phenomena. Furthermore, the solutions for many physical problems can be written down in general form in 1D. One of most brilliant examples is the general N -body solutions with contact potential $V = g\delta(x_i - x_j)$ [207], where x_i, x_j are the position of the particles. The coupling constant g is related to the 1D scattering length a by

$$g = -\frac{1}{\mu_2 a}. \quad (4.60)$$

Based on this general solution, a lot of studies have been performed on the energy spectra and thermodynamical properties of the general N -body system in 1D or quasi-1D confinement. In particular, for $g < 0$ there is always one N -body bound state. For a system of identical bosons, the bound state energy is given by [212]

$$E_N = -\frac{N(N^2 - 1)}{6ma^2}, \quad (4.61)$$

where m is the atomic mass. In a 1D model with the contact potential, the connection to the fermionization of bosons is made when $g \rightarrow \infty$, where $a \rightarrow 0$. Here we are interested in the other extreme where a is large. In the low energy limit where the two-body scattering behavior is universally determined by a , we expect that the four-body low energy scattering also shows universal scaling behavior.

The Efimov effect is known to exist only in 3D space [21]. For few-body systems in lower dimensions, however, the inelastic scattering rates may still be universal when the scattering length is large. In particular, for the atoms confined in an elongated quasi-1D trap, the 1D scattering length can be tuned essentially at will with CIR. It is thus important to study the universal behavior of the few-body system in one dimension near a CIR.

Generally speaking, treating a few-body system more realistically in a quasi-1D trap requires taking into account the finite size of the transverse confinement, which is highly demanding in either analytical or numerical studies. The reason that calculations for quasi-1D geometries are more demanding than for fully 3D geometries is that there are fewer conserved quantities, requiring the calculations to treat more degrees of freedom explicitly. For instance, for three identical particles in a quasi-1D trap the dimensionality of the problem is five compared to three for particles in 3D free space because total angular momentum is no longer conserved. One strategy to simplify the problem is to study the systems in pure 1D which has a much lower dimensionality. This has the following advantages: first, these studies may give the limiting results for systems under tight transverse confinement. Second, solutions for a quasi-1D system can be built on the solutions for a pure 1D system which can, sometimes give more physical insight like the solutions for a two-body system in quasi-1D confinement [208]. Finally, some fundamental few-body questions which show up both in 1D and higher dimensions can get a more focused investigation in 1D where the situation is usually simpler.

Three-body recombination in one dimension has been studied in detail in Ref. [123], where the universal threshold laws and the scattering length scaling laws are given for both

bosons and fermions. In the following we will study the universal properties for four identical bosons in one dimension.

4.3.1 Definitions for two-body scattering in 1D

To avoid the possible ambiguity in the definitions used in 1D scattering, we will first give the definitions used in our study.

For symmetric interactions [$v(x)=v(-x)$] in one dimension, there exist only two “partial waves”, corresponding to the even and odd parities. We define that the even and odd parity states take the following asymptotic form:

$$\psi_e \simeq \cos(k|x| + \delta_e), \quad \psi_o \simeq \text{sign}(x) \sin(k|x| + \delta_o), \quad (4.62)$$

so that the phase shifts δ_e and δ_o are both zero for the non-interacting case. Two-body scattering in one dimension has a significant distinction from 3D scattering near zero energy. In 3D scattering, the scattering phase shifts approach $n\pi$ near zero energy unless there exists a zero-energy bound state; for 1D scattering, however, the phase shift for even parity approaches $n\pi + \pi/2$ with our definition regardless the existence of a zero-energy bound state. The definition for the 1D scattering length, which is determined from the low energy expansion of the phase shift, becomes ambiguous. For the study of universal physics in few-body systems, the more relevant quantity is the size of the low-energy wavefunction instead of the mathematical expression. Considering the connection of the scattering length to the low-energy wavefunction in 3D, we define the scattering length 1D in the same fashion and obtain the following relationship between the scattering length a and the even phase shift:

$$\lim_{k \rightarrow 0} k \tan \delta_e(k) = -1/a. \quad (4.63)$$

With this definition, the connection between the scattering length and the binding energy of the two-body weakly-bound state is the same as for the 3D case: $E_{2b} \approx -1/2\mu_2 a^2$ when $a \gg r_0$.

4.3.2 Four-body hyperspherical coordinates in one dimension

For four particles moving in one dimension with coordinates $\{x_i \ (i = 1, 2, 3, 4)\}$, the center of mass motion is separated from the internal motion when we transform the coordinates to Jacobi vectors as introduced in Sec. 2.1. Since the definition of the hyperspherical coordinates is formally independent of the type of the Jacobi set, we will call the three 1D Jacobi vectors ρ_1 , ρ_2 and ρ_3 , from either “K-type” or “H-type” Jacobi set. The value of these Jacobi coordinates can take from $-\infty$ to ∞ . To simplify the operations of identical particle permutations, we want to define a set of democratic hyperspherical coordinates. In the following, we use a formal method for defining the democratic hyperspherical coordinates used in Refs. [111–113, 116, 117]. However, from the discussion in Sec. 2.2.2 we know that only one independent moment of inertia implies there is only one invariant coordinate in 1D systems: the hyperradius R . We will show in the following that the 1D democratic hyperspherical coordinates are the same as the Delves’ coordinates. For a four-body system in 1D, the lab-frame coordinate tensor for the mass-scaled Jacobi vectors is a 1×3 matrix (ρ_1, ρ_2, ρ_3) , which can be written as the product of the transformation matrices as the following [111–113, 116, 117]:

$$(\rho_1, \rho_2, \rho_3) = \tilde{\mathbf{D}}\mathbf{\Lambda}\mathbf{K}, \quad (4.64)$$

where the transpose of the 1D spatial rotational matrix $\tilde{\mathbf{D}} = \mathbb{1}$ and the diagonal matrix $\mathbf{\Lambda} = R\mathbb{1}$ is connected to the trace of the inertia tensor and is invariant under permutation of the particles. Finally, the 1×3 matrix \mathbf{K} is

$$\mathbf{K} = (1, 0, 0)\bar{\mathbf{K}}, \quad (4.65)$$

where $\bar{\mathbf{K}}$ is the kinematic rotational matrix in the two hyperangles ϕ_1 , ϕ_2 and is defined as

$$\bar{\mathbf{K}} = \begin{pmatrix} \cos(\pi/2 - \phi_2) & 0 & \sin(\pi/2 - \phi_2) \\ 0 & 1 & 0 \\ -\sin(\pi/2 - \phi_2) & 0 & \cos(\pi/2 - \phi_2) \end{pmatrix} \begin{pmatrix} \cos \phi_1 & \sin \phi_1 & 0 \\ -\sin \phi_1 & \cos \phi_1 & 0 \\ 0 & 0 & 1 \end{pmatrix}. \quad (4.66)$$

The mass-scaled Jacobi coordinates are then expressed in terms of the hyperspherical coordinates as

$$\rho_1 = R \sin \phi_2 \cos \phi_1, \quad \rho_2 = R \sin \phi_2 \sin \phi_1, \quad \rho_3 = R \cos \phi_2, \quad (4.67)$$

where the ranges for ϕ_1 and ϕ_2 are $[0, 2\pi]$ and $[0, \pi]$, respectively. This definition is exactly the same if one follows the procedure for defining a Delves' coordinates.

The form of the 1D four-body Schrödinger equation in the hyperspherical coordinates we just defined takes exactly the same form as that for one particle in 3D:

$$-\frac{1}{2\mu_4} \left(\frac{\partial^2}{\partial R^2} + \frac{2}{R} \frac{\partial}{\partial R} + \frac{\Lambda^2}{R^2} \right) \psi + \sum_{i<j} v(r_{ij}) \psi = E\psi. \quad (4.68)$$

where

$$\Lambda^2 = \frac{1}{\sin \phi_2} \frac{\partial}{\partial \phi_2} \sin \phi_2 \frac{\partial}{\partial \phi_2} + \frac{1}{\sin \phi_2^2} \frac{\partial^2}{\partial \phi_1^2}. \quad (4.69)$$

Since we are essentially working with the Delves' hyperspherical coordinates, both of the interparticle distances r_{ij} and the permutation operations will depend critically on the choice of the Jacobi vectors. We want more particles to be connected directly with the Jacobi vectors so that the permutation of the particles can be easier. We thus use the “H-type” Jacobi set, as shown in Fig. 4.10.

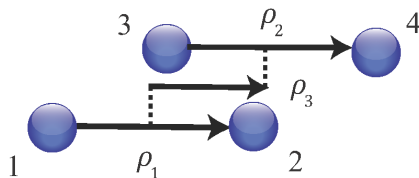


Figure 4.10: The “H-type” Jacobi vectors in one dimension.

The interparticle distances r_{ij} can be written in terms of the hyperspherical coordinates

via the following expressions:

$$\begin{aligned}
 r_{12} &= A_1|\rho_1|, & r_{34} &= A_2|\rho_2|, \\
 r_{13} &= |C_1\rho_1 - C_2\rho_2 + C_3\rho_3|, & r_{23} &= |C_1\rho_1 + C_2\rho_2 - C_3\rho_3|, \\
 r_{14} &= |C_1\rho_1 - C_2\rho_2 - C_3\rho_3|, & r_{24} &= |C_1\rho_1 + C_2\rho_2 + C_3\rho_3|,
 \end{aligned} \tag{4.70}$$

where the mass factors A_i and C_i are

$$\begin{aligned}
 A_1 &= \sqrt{\frac{\mu_4}{\mu_{12}}}, & A_2 &= \sqrt{\frac{\mu_4}{\mu_{34}}}, \\
 C_1 &= \sqrt{\frac{\mu_4 m_2}{m_1(m_1 + m_2)}}, & C_2 &= \sqrt{\frac{\mu_4 m_4}{m_3(m_3 + m_4)}}, & C_3 &= \sqrt{\frac{\mu_4(m_1 + m_2 + m_3 + m_4)}{(m_1 + m_2)(m_3 + m_4)}}.
 \end{aligned} \tag{4.71}$$

The permutations of the particles which are connected directly by the Jacobi vectors give simple transformation of the hyperangles:

$$P_{12} \begin{pmatrix} \phi_1 \\ \phi_2 \end{pmatrix} \rightarrow \begin{pmatrix} \pi - \phi_1 \\ \phi_2 \end{pmatrix}, \quad P_{34} \begin{pmatrix} \phi_1 \\ \phi_2 \end{pmatrix} \rightarrow \begin{pmatrix} 2\pi - \phi_1 \\ \phi_2 \end{pmatrix}. \tag{4.72}$$

The permutations of the particles not connected by a Jacobi vector, however, mix up the hyperangles. For instance, the permutation operator P_{24} gives the following transformation:

$$P_{24} \begin{pmatrix} \phi_1 \\ \phi_2 \end{pmatrix} \rightarrow \begin{pmatrix} \tan^{-1} \left[\frac{\sin \phi_2 \sin(\phi_1 + \pi/4) - \cos \phi_2}{\sin \phi_2 \sin(\phi_1 + \pi/4) + \cos \phi_2} \right] \\ \cos^{-1}[\sin \phi_2 \sin(\pi/4 - \phi_1)] \end{pmatrix}. \tag{4.73}$$

The quadrant for ϕ_1 after the transformation is determined by the signs of the numerator and the denominator in the argument of the inverse tangent function. Since the effect of P_{24} on the hyperangles is not independent of each of the hyperangles, the permutation symmetries for these operations can not be satisfied by simply imposing the boundary conditions along the coordinates lines, as has been discussed in Sec. 2.3. For four identical particles, the permutation symmetry from P_{13} and P_{24} can be partially imposed by the using operator $P_{13}P_{24}$, which gives a simple transformation of the hyperangles:

$$P_{13}P_{24} \begin{pmatrix} \phi_1 \\ \phi_2 \end{pmatrix} \rightarrow \begin{pmatrix} \pi/2 - \phi_1 \\ \pi - \phi_2 \end{pmatrix}. \tag{4.74}$$

Finally, the total parity operator Π transforms the hyperangles as the following:

$$\Pi \begin{pmatrix} \phi_1 \\ \phi_2 \end{pmatrix} \rightarrow \begin{pmatrix} \pi + \phi_1 \\ \pi - \phi_2 \end{pmatrix}. \quad (4.75)$$

These permutation operations can be understood qualitatively by looking at the two-body coalescence lines ($r_{ij} = 0$) on the hyperangular plane, as shown in Fig. 4.11. Since the permutation of two particles will keep their coalescence lines unchanged, the permutation symmetry then requires that the adiabatic wavefunction $\Phi(R, \phi_1, \phi_2)$ is symmetric or anti-symmetric with respect to the coalescence lines. These symmetries are easily imposed if the coalescence lines are parallel to the coordinate lines, as the coalescence lines with $r_{12} = 0$ and $r_{34} = 0$, but are difficult to impose if they are curves, as the coalescence lines for the other pairs.

4.3.3 Four-body adiabatic hyperspherical potentials in 1D

Solving the adiabatic equation

To study the universal behavior of a system of four identical bosons, we calculate the adiabatic hyperspherical potentials by solving the adiabatic equation

$$\frac{\Lambda^2}{2\mu_4 R^2} \Phi_\nu(R; \phi_1, \phi_2) = U_\nu(R) \Phi_\nu(R; \phi_1, \phi_2). \quad (4.76)$$

We impose the symmetry of the total parity and permutation operators P_{12} , P_{34} and $P_{13}P_{24}$ by restricting the range of the hyperangles ϕ_1 and ϕ_2 to $[0, \pi/4]$ and $[0, \pi/2]$ then imposing the following boundary conditions:

$$\left. \frac{\partial \Phi(R; \phi_1, \phi_2)}{\partial \phi_1} \right|_{\phi_1=0} = 0, \quad \left. \frac{\partial \Phi(R; \phi_1, \phi_2)}{\partial \phi_1} \right|_{\phi_1=\pi/4} = 0, \quad \left. \frac{\partial \Phi(R; \phi_1, \phi_2)}{\partial \phi_2} \right|_{\phi_2=\pi/2} = 0, \quad (4.77)$$

for even parity $\Pi = +1$ and

$$\left. \frac{\partial \Phi(R; \phi_1, \phi_2)}{\partial \phi_1} \right|_{\phi_1=0} = 0, \quad \Phi(R; \pi/4, \phi_2) = 0, \quad \Phi(R; \phi_1, \pi/2) = 0, \quad (4.78)$$

for odd parity $\Pi = -1$. This restriction on the range of the hyperangles gives a factor of 16 reduction in our calculations. Note that when each time a two-body permutation symmetry

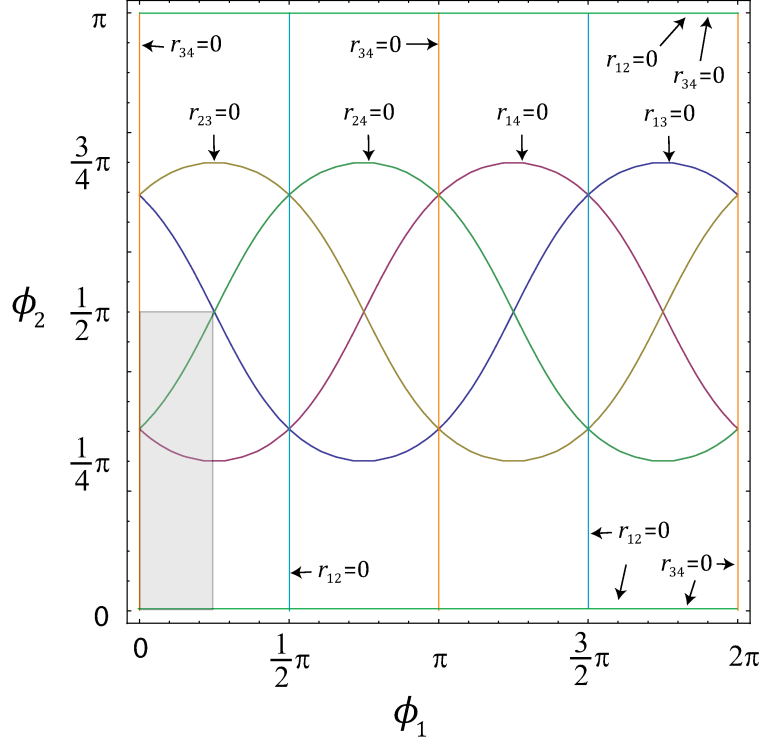


Figure 4.11: The two-body coalescence lines ($r_{ij} = 0$) on the hyperangular plane for four particles in 1D. The coalescence lines for particles connected directly by Jacobi vectors are straight lines parallel to the coordinate lines, which implies simple transformation of the hyperangles under permutation of the two particles. The coalescence lines for particles not connected directly by Jacobi vectors are more complicated and imply complicated transformation on the hyperangles under the permutations. The shaded region indicates the range of the hyperangles in our calculations for identical bosons.

is imposed to restrict the range of the hyperangles, it does not always reduce the range by a factor of 2. The adiabatic wavefunctions Φ_ν satisfying the above boundary conditions are not all fully symmetrized, and we identify those which have correct symmetry by calculating the expectation value for one of the permutation operator $\langle\langle\Phi_\nu|P_{24}|\Phi_\nu\rangle\rangle$.

We use two types of two-body potentials in our calculations. The first one is purely attractive :

$$V_{\text{sech}}(r) = -D\text{sech}^2(r/r_0), \quad (4.79)$$

where r is the interparticle distance. For 1D application however, this potential is incon-

venient for getting an infinite scattering length with only a single bound state, since the infinite scattering length with a single bound state for the potential in Eq. (4.79) occurs in the limit of $D \rightarrow 0$ where the interactions vanish. This is because a purely attractive potential in 1D always has a bound state for any non-zero potential depth [213]. The universality of the scaling behavior extracted in this limit is also questionable. Thus, we also use another potential shown in Eq. (4.80), which is characterized by a repulsive barrier for small interparticle distances, and an attractive $1/r^6$ van der Waals [214] tail for large interparticle distances.

$$V_{\text{vdW}}(r) = -D \frac{(r/r_0)^2}{1 + (r/r_0)^8} + B \frac{1}{1 + (r/r_0)^8}. \quad (4.80)$$

The existence of the repulsive barrier in Eq. (4.80) makes the pole of the 1D scattering length occur only at finite potential depths. We take $r_0 = 15$ a.u. for all our following numerical calculations.

Three- and four-body continuum potentials

A four-body system can break up into various configurations. When the two-body bound subsystems can form bound states, the four-body system can break up into $A_2 + A + A$ configurations. A three-body continuum is associated to each of such configurations, which is manifested by infinite number of adiabatic hyperspherical continuum channels for each of the $A_2 + A + A$ break-up thresholds. The four-body system can also break up into four free particles which leads to infinite number of adiabatic channels associated with the four-body break-up threshold.

As shown in Fig. 4.12, since the three- and four-body break-ups have different thresholds, asymptotically the three- and four-body continuum has an infinite number of avoided crossings. These crossings become sharper when the hyperradius R increases. This indicates the adiabatic potentials for three- and four-body continuum channels should better be traced “diabatically” by treating the avoided crossings as real crossings. In the adiabatic representation, even though the inelastic transitions between the three-body continuum and

the four-body continuum are expected to be negligible asymptotically, sharp peaks occur in the non-adiabatic couplings $P_{\nu,\nu'}$ and $Q_{\nu,\nu'}$ near those sharp avoided crossings which are very difficult to be traced out accurately in numerical calculations. The sharp structure in the non-adiabatic couplings lead to strong transitions in the adiabatic channels which are physically unnecessary since these transitions are just from the labeling change of an adiabatic channel from one group of continuum to another. A diabatic representation is thus necessary for a simpler treatment of the three- and four-body continuum. For total scattering energies well below the four-body break-up threshold, however, the four-body continuum channels are energetically forbidden so that the effects from sharp crossings between the three- and four-body continuum are not expected to be significant. In our present study, we will focus on the scattering processes where the four-body continuum does not play an important role.

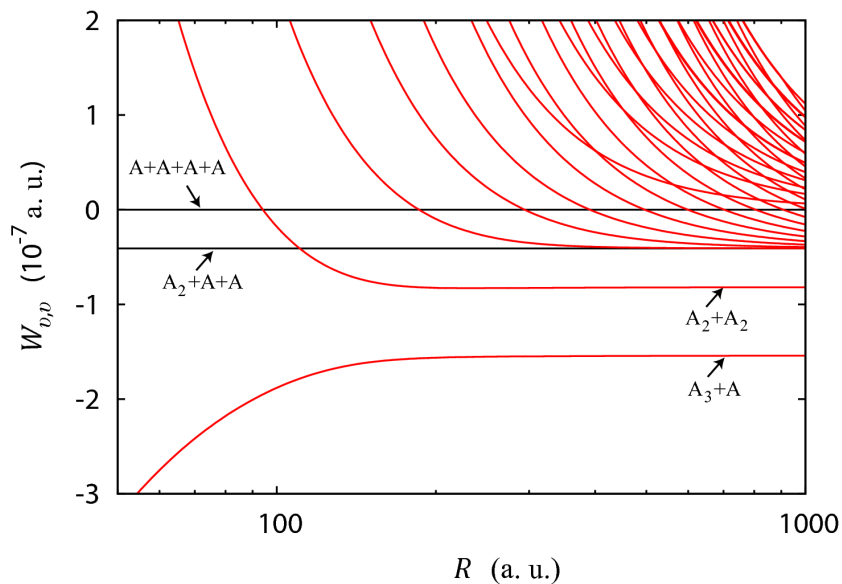


Figure 4.12: Avoided crossings in the four-body adiabatic hyperspherical potentials of the three- and four-body continuum channels. The potentials are calculated with the two-body potential V_{sech} . There is only one two-body bound state in the two-body subsystems.

Universal scaling for dimer-dimer relaxation

If the ultracold weakly-bound dimers are produced in an quasi-one dimensional atomic trap, an important question arises on the collisional stability of these molecules. If the atoms are converted to weakly-bound dimers with high efficiency so that few free atoms are left, the dominant collisional decay will be from the inelastic collisions between the two weakly-bound dimers. In the following we will discuss the universal scaling behavior of such collisional processes near zero-energy with large 1D scattering length.

Since the scaling of the inelastic rates depends crucially on the behavior of the adiabatic potentials in the initial and final channels, we will first discuss the behavior of the weakly-bound dimer-dimer potential and the lower lying atom-trimer potentials. In Fig. 4.13, we show the four-body adiabatic potentials with only a single two-body bound state. The adiabatic potentials calculated by using two-body potential V_{sech} and V_{vdW} are shown together to demonstrate the universality. The dimer-dimer potential behaves universally like $1/R^2$ for hyerradius $R \lesssim a$ and goes to the asymptotic value $-1/ma^2$ for hyerradius $R \gtrsim a$. For low-energy dimer-dimer collisions, the strong repulsive behavior in the $R \lesssim a$ region leads to a small probability for the system to be at short-range distances. All the inelastic dimer-dimer collisional processes require transitions at short-range region, will thus be strongly suppressed.

As shown in Fig. 4.13, the adiabatic potential for the atom-trimer channel with diagonal coupling $Q_{0,0}/2\mu_4$ included, behaves like:

$$W_0(R) = -\frac{c_0}{2\mu_4 a R} \quad (4.81)$$

in the region $R \lesssim a$. The coefficient $c_0 \approx 8$. Though the potential in Eq. (4.81) is Coulomb-like which decreases slowly with R , it is not expected to have physical significance due to the smallness of the effective charge, which makes the potential in this region much smaller than the free particle energy scale, $1/R^2$. This is the same situation as the Coulomb-like potential discussed in Sec. 3.1.2. By using the same argument for atom-dimer relaxation in Sec. 3.1.2,

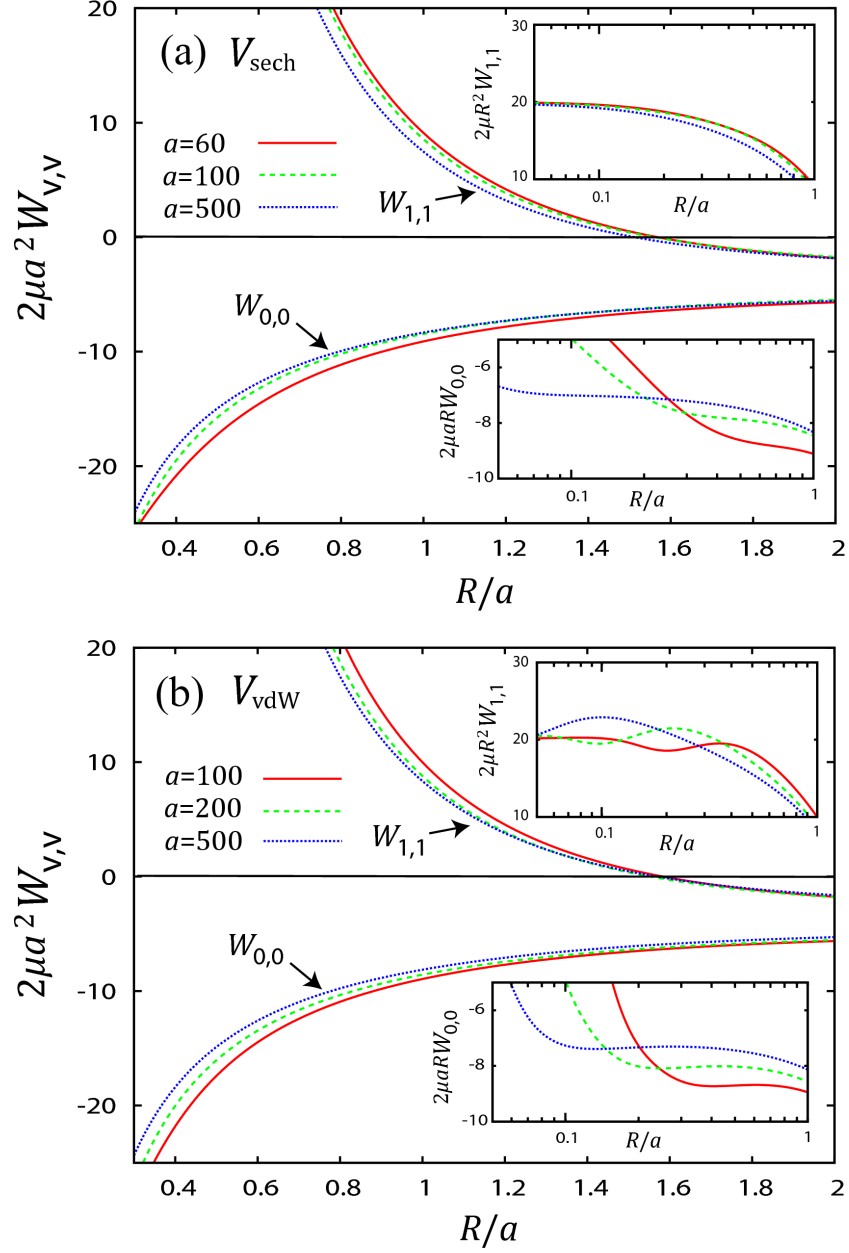


Figure 4.13: Four-body adiabatic potentials $W_{\nu,\nu}$ for the dimer-dimer and the atom-trimer channels with one two-body bound state. The potentials in panel (a) are calculated with two-body potentials in Eq. (4.79) and those in panel (b) are calculated with two-body potentials in Eq. (4.80). The potentials and the hyperradius are scaled to show their universal behavior. In the insets, the dimer-dimer potential and the atom-trimer potential are scaled differently by multiplying $2\mu_a R^2$ and $2\mu_a R$, respectively, to show the universal coefficients in their scaling behavior. Figure is adapted from Ref. [4].

we expect any short-range inelastic transition from the atom-trimer channel to lower lying channels, if any, will be suppressed by the existence of the Coulomb region, compared to a small scattering length case. Asymptotically ($R \gtrsim a$), the atom-trimer potential goes to the three-body bound state energy, which is approximately $-4/ma^2$ for $a \gg r_0$ as expected from Eq. (4.61). To examine the effects of finite-range two-body interactions on the energies of the weakly-bound states, we compare the numerical two- and three-body bound state energies with the analytical result from Eq. (4.61). To give a clear comparison, we define

$$\kappa_n = [6ma\Delta E_n/N(N^2 - 1)]^{1/2}. \quad (4.82)$$

The analytical result from Eq. (4.61) then gives $\kappa_n = 1/a$. The fractional difference between numerical and analytical energies can be viewed from $\kappa_n a - 1$, which is shown Fig. 4.14. It can be seen that the numerical energies approach the analytical prediction in the limit $1/a \rightarrow 0$, except for the three- and four-body bound state energies with V_{vdW} interactions. Though the deviation is still small (about 10^{-2} for relative difference), the break down of the zero-range prediction requires further investigation. In other cases, deviation of the numerical energies from the zero-range results becomes negligible when a is about one order of magnitude larger than the range of the interactions r_0 .

As seen in the previous chapters, the behavior of the couplings between the initial and the final channels determines over what range of hyperradii the inelastic transitions will occur. This information typically gives the overall power law scaling of the inelastic rates on the scattering length [66]. In Fig. 4.15, we show the behavior of the non-adiabatic couplings $P_{0,1}$ between the dimer-dimer and the atom-trimer channels for different a with the two different two-body potentials. The most striking feature of these couplings is the pronounced peaks around $R = 2a$. The width of these peaks scale with a and the heights scale with $1/a$, which is similar to the scaling behavior of the non-adiabatic couplings between the lowest three-body continuum channel and the weakly-bound atom-dimer channel in the case of three-body recombination for $a > 0$ in 3D case. Beyond $R \approx 2a$ the couplings quickly become negligible because of exponential decay. We can then directly conclude that the

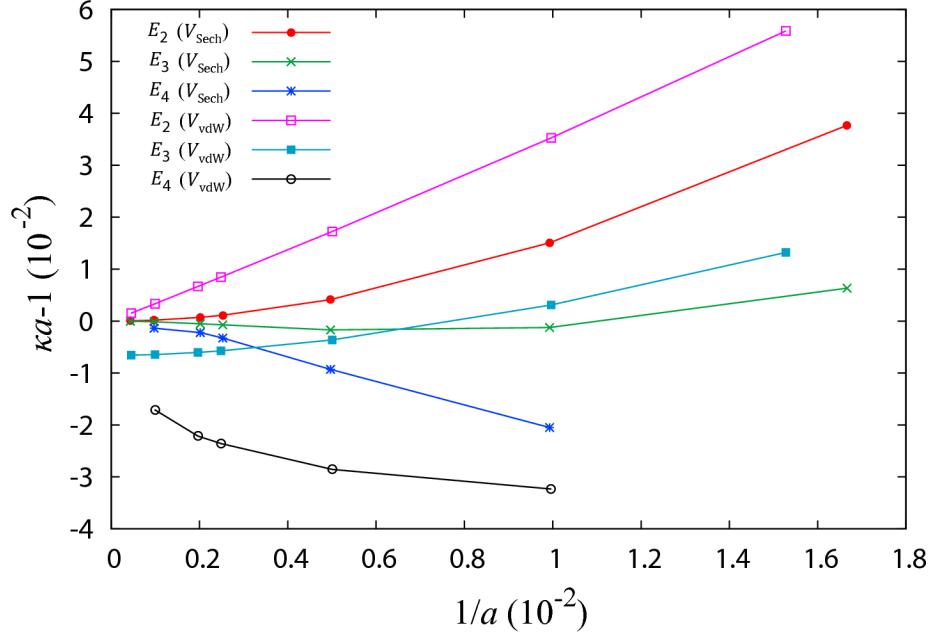


Figure 4.14: The comparison between numerically calculated two- and three-body binding energies and the analytical prediction from Eq. (4.61). The numerical energies E_n are scaled according to Eq. (4.82) to remove the N dependence. The unitless quantity $\kappa a - 1$ is plotted to show the fractional difference between numerical and analytical energies. The lines through the numerical data points are for eye guide.

relaxation in the dimer-dimer collision occurs dominantly around $R = 2a$.

The method required for deriving the scaling law for the relaxation rate is the same for three-body recombination when $a > 0$. Here we follow the simple pathway analysis introduced in Ref. [66] and used in Sec. 3.2.1. The zero-energy dimer-dimer relaxation rate V_{rel} has the following simple scaling with a without modulations from resonance or interference effect:

$$V_{\text{rel}} = Ca, \quad (4.83)$$

where C is a universal constant and can be obtained by fitting Eq. (4.83) to numerical results.

Equation (4.83) indicates the relaxation of weakly-bound dimers in 1D will be enhanced for large scattering lengths. With the prediction of the universal two- and three-body bound

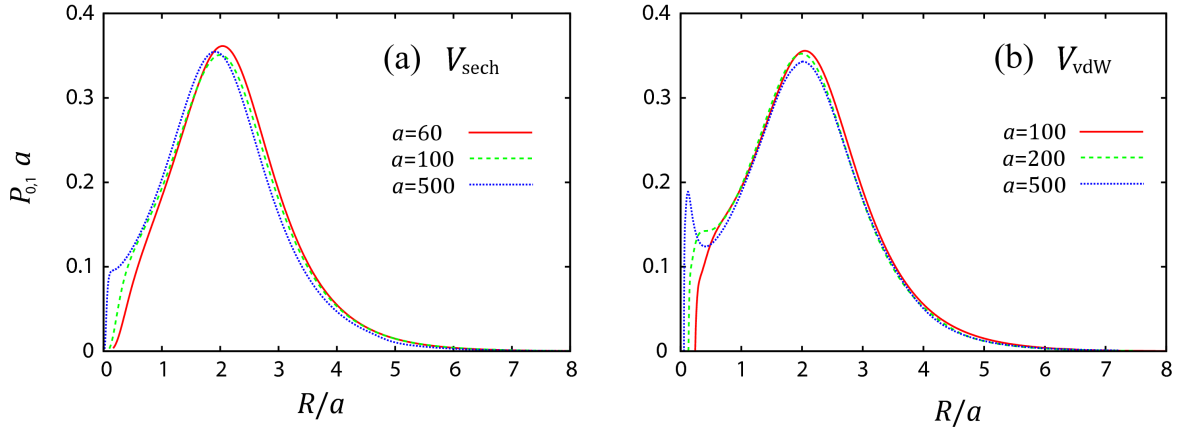


Figure 4.15: The non-adiabatic couplings between the weakly-bound dimer-dimer and atom-trimer channels. Both the hyperradius and couplings are scaled to show the universal scaling. Figure is adapted from Ref. [4].

state energies in Eq. (4.61), the energy release from each relaxation event is also universal: $\Delta E = 3/ma^2$. For moderate values of scattering length $a < 10^4$ a.u., the energy release is large enough to kick the relaxed atom and trimer out of the trap for a typical experimental setup. And thus, a sample of ultracold weakly-bound 1D dimers is expected to suffer dramatic losses. Though this is unfortunate for experiments requiring stable dimers, it can potentially provide a novel method for producing atomic or molecular beam collimated by the 1D trap, if the depth of the trap in transversal direction can be made still deep enough to hold the relaxation products.

Four-body adiabatic potentials with a deeply-bound two-body state

As mentioned previously, in four-body adiabatic hyperspherical potentials a set of three-body continuum channels is associated to each of the distinct $A_2 + A + A$ three-body break-up thresholds. Thus, for a four-body system with more than one two-body bound states, the three-body continuum potentials going to different $A_2 + A + A$ break-up threshold will cross and give an infinite number of avoided crossings. This is seen in Fig. 4.16, where the adiabatic potentials are calculated by using the two-body potential V_{sech} with a weakly-bound and a deeply-bound state. Due to the existence of multiple three-body continua,

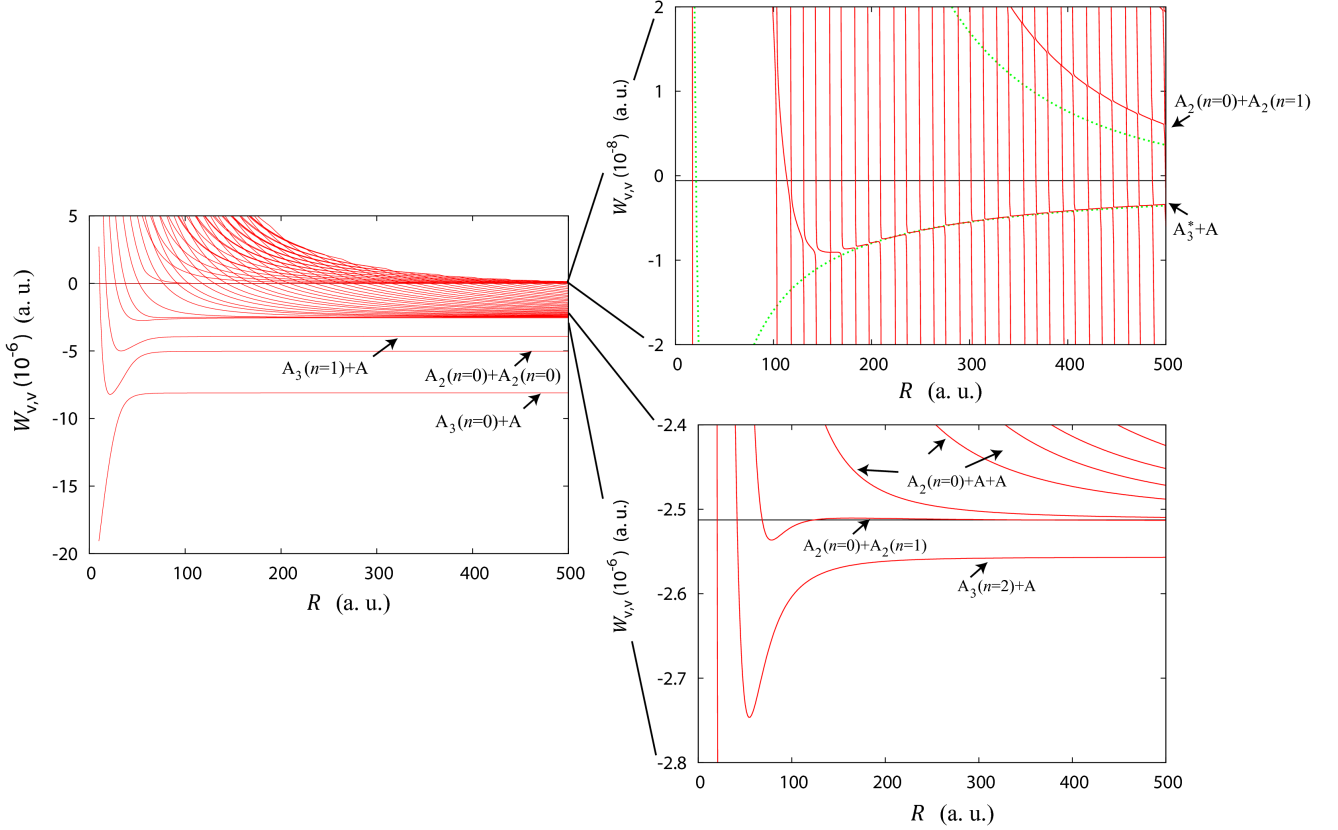


Figure 4.16: The four-body adiabatic potentials with both weakly-bound and a deeply-bound two-body subsystems. The lower right panel shows the potentials near $A_2(n=0) + A + A$ break-up threshold, and the upper right panel shows the potentials near $A_2(n=1) + A + A$ break-up threshold, where the potentials cross with the three-body continuum potentials from $A_2(n=0) + A + A$ break-up threshold. The green dotted curves are the weakly-bound atom-trimer and the dimer-dimer potentials with the same scattering length calculated by using the two-body potential Eq. (4.80). Here n is the vibrational quantum number for a dimer and the superscript $*$ indicates a resonant state. The black lines in the zoom-in panels give the $A_2 + A + A$ break-up threshold. Figure is adapted from Ref. [4].

it becomes increasingly difficult to get to the weakly-bound $A_2(n=1) + A + A$ break-up threshold for large hyperradius, since a large number of adiabatic potentials need to be calculated. One need to note that the weakly-bound atom-trimer channel $A_3^* + A$ in this case is only a resonance state and does not correspond to a real scattering threshold, since A_3^* can decay by itself into an atom and a more deeply-bound dimer.

In the right panels in Fig. 4.16, we zoom in on the regions near the $A_2 + A + A$ break-up

thresholds. In particular, in the upper panel we show the potentials near the weakly-bound $A_2(n = 1) + A + A$ break-up thresholds. To get a sense for universality, we have shown the atom-trimer and dimer-dimer potentials for the same scattering length with a single two-body bound state by using V_{vdW} . For the atom-trimer channel, the positions of the potential minima is different for the two cases. For R larger than the positions of the potential minima, both potentials behave like Eq. (4.81). For the dimer-dimer channel with deeply-bound two-body state, the potential still behaves like $1/R^2$ when $R \lesssim a$ but has a larger coefficient than that for the single two-body bound state case. The potentials for the two cases start to merge near $R = a$. Due to the tremendous number of avoided crossings in the dimer-dimer and atom-trimer potentials in the presence of deeply-bound two-body state, it is not practical to extract the coupling between these channels. However, since the qualitative behavior of the potentials is not changed by having more two-body bound states, we expect the coupling between them is qualitatively the same. The conclusion for the scattering length scaling of the relaxation rate in Eq. (4.83) is thus expected to hold in general.

4.3.4 Summary

To summarize, we have studied the universal scaling behavior of four identical bosons in one dimension. The scaling of the potentials in the presence of multiple three-body continua is shown and their effects are discussed. We have observed the complicated behavior of the potentials when the different sets of continuum potentials cross with each other, implying rich physics even for a one-dimensional system. By analyzing the scaling behavior of the four-body adiabatic potentials and the non-adiabatic couplings, we predict a linear in a enhancement of the vibrational relaxation involving two weakly-bound dimers. The weakly-bound dimers in a 1D confinement are thus expected to be unstable due to collisional decay. This enhancement, however, can be used to produce highly controllable collimated atomic or molecular beams.

My Publications

- [1] Y. Wang, J. P. D’Incao, and B. D. Esry, “*Cold three-body collisions in hydrogen-hydrogen-alkali atomic system,*” Phys. Rev. A (to be submitted).
- [2] Y. Wang, J. P. D’Incao, and B. D. Esry, “*Ultracold three-body collisions near narrow Feshbach resonances,*” Phys. Rev. A (to be submitted).
- [3] Y. Wang and B. D. Esry, “*A diabatic picture generated by freezing three-body geometry,*” Phys. Rev. A (to be submitted).
- [4] Y. Wang and B. D. Esry, “*Stability of weakly-bound dimers in one-dimension,*” (in preparation).
- [5] Y. Wang and B. D. Esry, “*Universal three-body physics at finite energy near Feshbach resonances,*” New J. Phys. (to be submitted).
- [6] Y. Wang, J. V. Hernández, and B. D. Esry, “*Adiabatic Floquet picture for hydrogen atom in laser field,*” Phys. Rev. A (to be submitted).
- [7] Y. Wang, W. B. Laing, and B. D. Esry, “*Four-body Efimov physics induced by three-body Efimov effect,*” Phys. Rev. Lett. (to be submitted).
- [8] B. D. Esry, Y. Wang, and J. P. D’Incao, “*Alternative paths to observing Efimov physics,*” Few-body Sys. **43**, 63 (2008).
- [9] M. Thøgersen, D. V. Fedorov, A. S. Jensen, B. D. Esry, and Y. Wang, “*Conditions for Efimov physics for finite-range potentials,*” Phys. Rev. A **80**, 013608 (2009).
- [10] Y. Wang and B. D. Esry, “*Efimov Trimer Formation via Ultracold Four-Body Recombination,*” Phys. Rev. Lett. **102**, 133201 (2009).

- [11] Y. Wang, J. P. D’Incao, H.-C. Nägerl, and B. D. Esry, “*Colliding Bose-Einstein Condensates to Observe Efimov Physics,*” Phys. Rev. Lett. **104**, 113201 (2010).

References

- [12] V. Efimov, “Energy levels arising from resonant two-body forces in a three-body system,” *Phys. Lett. B* **33**, 563 (1970).
- [13] Y. N. Demkov and V. N. Ostrovskii, *Zero-Range Potentials and Their Applications in Atomic Physics* (New York : Plenum Press, 1988).
- [14] L. D. Faddeev, “Scattering theory for a three particle system,” *Sov. Phys. JETP* **12**, 1014 (1961).
- [15] L. M. Delves, “Tertiary and general-order collisions,” *Nucl. Phys.* **9**, 391 (1959).
- [16] L. M. Delves, “Tertiary and general-order collisions (II),” *Nucl. Phys.* **20**, 275 (1960).
- [17] J. von Stecher, *Trapped Ultracold Atoms with Tunable Interactions*, Ph.D. thesis, University of Colorado (2008).
- [18] A. S. Jensen, K. Riisager, D. V. Fedorov, and E. Garrido, “Structure and reactions of quantum halos,” *Rev. Mod. Phys.* **76**, 215 (2004).
- [19] L. H. Thomas, “The interaction between a neutron and a proton and the structure of ${}^3\text{H}$,” *Phys. Rev.* **47**, 903 (1935).
- [20] L. D. Landau and E. M. Lifshitz, *Mechanics*, vol. 3rd Ed. (Butterworth-Heinemann).
- [21] E. Nielsen, D. Fedorov, A. Jensen, and E. Garrido, “The three-body problem with short-range interactions,” *Phys. Rep.* **347**, 373 (2001).
- [22] R. D. Amado and F. C. Greenwood, “There is no Efimov effect for four or more particles,” *Phys. Rev. D* **7**, 2517 (1973).

- [23] S. K. Adhikari and A. C. Fonseca, “Four-body Efimov effect in a Born-Oppenheimer model,” *Phys. Rev. D* **24**, 416 (1981).
- [24] H. Naus and J. Tjon, “The Efimov effect in a four-body system,” *Few-Body Syst.* **2**, 121 (1987).
- [25] T. Cornelius and W. Glöckle, “Efimov states for three He atoms?” *J. Chem. Phys.* **85**, 3906 (1986).
- [26] S. Huber, “Efimov states in ^4He trimers by two-body effective-range and scattering-length analysis: A comparison with Faddeev calculations,” *Phys. Rev. A* **31**, 3981 (1985).
- [27] T. K. Lim, S. K. Duffy, and W. C. Damer, “Efimov state in the ^4He trimer,” *Phys. Rev. Lett.* **38**, 341 (1977).
- [28] H. Huber and T. Lim, “A study of the Efimov states and binding energies of the helium trimer through the Faddeev-coordinate-momentum approach,” *J. Chem. Phys.* **68**, 1006 (1978).
- [29] S. Nakaichi-Maeda and T. K. Lim, “Zero-energy scattering and bound states in the ^4He trimer and tetramer,” *Phys. Rev. A* **28**, 692 (1983).
- [30] B. D. Esry, C. D. Lin, and C. H. Greene, “Adiabatic hyperspherical study of the helium trimer,” *Phys. Rev. A* **54**, 394 (1996).
- [31] C. J. Pethick and H. Smith, *Bose-Einstein Condensation in Dilute Gases* (Cambridge University Press, Cambridge, 2001).
- [32] F. Dalfovo, S. Giorgini, L. P. Pitaevskii, and S. Stringari, “Theory of Bose-Einstein condensation in trapped gases,” *Rev. Mod. Phys.* **71**, 463 (1999).
- [33] L. P. Pitaevskii and S. Stringari, *Bose-Einstein Condensation* (Clarendon Press, Oxford, 2003).

- [34] S. Giorgini, L. P. Pitaevskii, and S. Stringari, “Theory of ultracold atomic Fermi gases,” *Rev. Mod. Phys.* **80**, 1215 (2008).
- [35] M. J. Wright, S. Riedl, A. Altmeyer, C. Kohstall, E. R. S. Guajardo, J. H. Denschlag, and R. Grimm, “Finite-temperature collective dynamics of a Fermi gas in the BEC-BCS crossover,” *Phys. Rev. Lett.* **99**, 150403 (2007).
- [36] B. Clancy, L. Luo, and J. E. Thomas, “Observation of nearly perfect irrotational flow in normal and superfluid strongly interacting Fermi gases,” *Phys. Rev. Lett.* **99**, 140401 (2007).
- [37] M. Zwierlein, J. Abo-Shaeer, A. Schirotzek, C. Schunck, and W. Ketterle, “Vortices and superfluidity in a strongly interacting Fermi gas,” *Nature* **435**, 1047 (2005).
- [38] D. Blume, J. von Stecher, and C. H. Greene, “Universal properties of a trapped two-component Fermi gas at unitarity,” *Phys. Rev. Lett.* **99**, 233201 (2007).
- [39] J. von Stecher, C. H. Greene, and D. Blume, “Energetics and structural properties of trapped two-component Fermi gases,” *Phys. Rev. A* **77**, 043619 (2008).
- [40] S. Jochim, M. Bartenstein, A. Altmeyer, G. Hendl, S. Riedl, C. Chin, J. Hecker Denschlag, and R. Grimm, “Bose-Einstein condensation of molecules,” *Science* **302**, 2101 (2003).
- [41] C. Chin, T. Kraemer, M. Mark, J. Herbig, P. Waldburger, H.-C. Nägerl, and R. Grimm, “Observation of Feshbach-like resonances in collisions between ultracold molecules,” *Phys. Rev. Lett.* **94**, 123201 (2005).
- [42] H. Feshbach, “A unified theory of nuclear reactions. II,” *Ann. Phys.* **19**, 287 (1962).
- [43] C. Chin, R. Grimm, P. Julienne, and E. Tiesinga, “Feshbach resonances in ultracold gases,” *Rev. Mod. Phys.* **82**, 1225 (2010).

- [44] T. Walker and P. Feng, *Adv. At. Mol. Opt. Phy.*, edited by B. Bederson and H. Walther, vol. Vol. 34 (Academic, San Deigo).
- [45] J. Stenger, S. Inouye, M. R. Andrews, H.-J. Miesner, D. M. Stamper-Kurn, and W. Ketterle, “Strongly enhanced inelastic collisions in a Bose-Einstein condensate near Feshbach resonances,” *Phys. Rev. Lett.* **82**, 2422 (1999).
- [46] T. Weber, J. Herbig, M. Mark, H.-C. Nägerl, and R. Grimm, “Three-body recombination at large scattering lengths in an ultracold atomic gas,” *Phys. Rev. Lett.* **91**, 123201 (2003).
- [47] C. A. Regal, M. Greiner, and D. S. Jin, “Lifetime of molecule-atom mixtures near a Feshbach resonance in ^{40}K ,” *Phys. Rev. Lett.* **92**, 083201 (2004).
- [48] K. Yu., S. B. V., and S. G. V., “Effect of Bose condensation on inelastic processes in gases,” *JETP Lett.* **42**, 209 (1985).
- [49] E. Nielsen and J. H. Macek, “Low-energy recombination of identical bosons by three-body collisions,” *Phys. Rev. Lett.* **83**, 1566 (1999).
- [50] B. D. Esry, C. H. Greene, and J. P. Burke, “Recombination of three atoms in the ultracold limit,” *Phys. Rev. Lett.* **83**, 1751 (1999).
- [51] P. F. Bedaque, E. Braaten, and H.-W. Hammer, “Three-body recombination in Bose gases with large scattering length,” *Phys. Rev. Lett.* **85**, 908 (2000).
- [52] E. Braaten and H. Hammer, “Universality in few-body systems with large scattering length,” *Phys. Rep.* **428**, 259 (2006).
- [53] J. D’Incao, C. Greene, and B. Esry, “The short-range three-body phase and other issues impacting the observation of Efimov physics in ultracold quantum gases,” *J. Phys. B* **42**, 044016 (2009).

- [54] T. Kraemer, M. Mark, P. Waldburger, J. Danzl, C. Chin, B. Engeser, A. Lange, K. Pilch, A. Jaakkola, H. Nägerl, and R. Grimm, “Evidence for Efimov quantum states in an ultracold gas of caesium atoms,” *Nature* **440**, 315 (2006).
- [55] S. Knoop, F. Ferlaino, M. Mark, M. Berninger, H. Schöbel, H. Nägerl, and R. Grimm, “Observation of an Efimov-like trimer resonance in ultracold atom–dimer scattering,” *Nature Phys.* **5**, 227 (2009).
- [56] M. Zaccanti, B. Deissler, C. D’Errico, M. Fattori, M. Jona-Lasinio, S. Müller, G. Roati, M. Inguscio, and G. Modugno, “Observation of an Efimov spectrum in an atomic system,” *Nature Phys.* (2009).
- [57] S. Pollack, D. Dries, and R. Hulet, “Universality in Three-and Four-Body Bound States of Ultracold Atoms,” *Science* **326**, 1683 (2009).
- [58] J. P. D’Incao, H. Suno, and B. D. Esry, “Limits on universality in ultracold three-boson recombination,” *Phys. Rev. Lett.* **93**, 123201 (2004).
- [59] J. von Stecher, J. D’Incao, and C. Greene, “Signatures of universal four-body phenomena and their relation to the Efimov effect,” *Nature Phys.* **5**, 417 (2009).
- [60] F. Ferlaino, S. Knoop, M. Berninger, W. Harm, J. P. D’Incao, H.-C. Nägerl, and R. Grimm, “Evidence for universal four-body states tied to an Efimov trimer,” *Phys. Rev. Lett.* **102**, 140401 (2009).
- [61] J. P. D’Incao and B. D. Esry, “Suppression of molecular decay in ultracold gases without Fermi statistics,” *Phys. Rev. Lett.* **100**, 163201 (2008).
- [62] D. S. Petrov, C. Salomon, and G. V. Shlyapnikov, “Weakly bound dimers of fermionic atoms,” *Phys. Rev. Lett.* **93**, 090404 (2004).
- [63] J. P. D’Incao, S. T. Rittenhouse, N. P. Mehta, and C. H. Greene, “Dimer-dimer

- collisions at finite energies in two-component Fermi gases,” *Phys. Rev. A* **79**, 030501 (2009).
- [64] J. Danzl, E. Haller, M. Gustavsson, M. Mark, R. Hart, N. Bouloufa, O. Dulieu, H. Ritsch, and H. Nagerl, “Quantum gas of deeply bound ground state molecules,” *Science* **321**, 1062 (2008).
- [65] J. Deiglmayr, A. Grochola, M. Repp, K. Mörtilbauer, C. Glück, J. Lange, O. Dulieu, R. Wester, and M. Weidemüller, “Formation of ultracold polar molecules in the rovibrational ground state,” *Phys. Rev. Lett.* **101**, 133004 (2008).
- [66] J. P. D’Incao and B. D. Esry, “Scattering length scaling laws for ultracold three-body collisions,” *Phys. Rev. Lett.* **94**, 213201 (2005).
- [67] J. P. D’Incao and B. D. Esry, “Ultracold three-body collisions near overlapping Feshbach resonances,” *Phys. Rev. Lett.* **103**, 083202 (2009).
- [68] J. P. D’Incao, J. von Stecher, and C. H. Greene, “Universal four-boson states in ultracold molecular gases: Resonant effects in dimer-dimer collisions,” *Phys. Rev. Lett.* **103**, 033004 (2009).
- [69] T. Pacher, L. S. Cederbaum, and H. Kppel, “Adiabatic and quasidiabatic states in a gauge theoretical framework,” *Adv. Chem. Phys.* **84**, 293 (1993).
- [70] S.-I. Chu and D. A. Telnov, “Beyond the floquet theorem: generalized Floquet formalisms and quasienergy methods for atomic and molecular multiphoton processes in intense laser fields,” *Phys. Rep.* **390**, 1 (2004).
- [71] C. Zener, “Non-adiabatic crossing of energy levels,” *Proc. R. Soc. London, Ser. A* **137**, 696 (1932).
- [72] S. I. Newton, *Principia (On the Shoulders of Giants)* (Running Press, 2005).

- [73] T.-Y. Li and J. A. Yorke, “Period three implies chaos,” *American Mathematics Monthly* **82**, 985 (1975).
- [74] E. Nielsen, D. V. Fedorov, and A. S. Jensen, “The structure of the atomic helium trimers: halos and Efimov states,” *J. Phys. B* **31**, 4085 (1998).
- [75] E. O. Alt, P. Grassberger, and W. Sandhas, “Reduction of the three-particle collision problem to multi-channel two-particle Lippmann-Schwinger equations,” *Nucl. Phys. B* **2**, 167 (1967).
- [76] F. T. Smith, “Generalized angular momentum in many-body collisions,” *Phys. Rev.* **120**, 1058 (1960).
- [77] F. Zernike and H. C. Brinkman, *Proc. K. Ned. Akad. Wett.* **38**, 161 (1935).
- [78] A. J. Dragt, “Classification of three-particle states according to SU_3 ,” *J. Math. Phys.* **6**, 533 (1965).
- [79] J. S. Avery, *Hyperspherical Harmonics: Applications in Quantum Theory* (Springer, 1989).
- [80] C. Lin, “Doubly-excited states, including new classification schemes,” *Adv. Atom. Mol. Phys* **22**, 77 (1986).
- [81] A. Bastida, A. Requena, and J. Zuniga, “Generalized hyperspherical coordinates for molecular vibrations,” *J. Phys. Chem.* **97**, 5831 (1993).
- [82] A. R. Cooper, S. Jain, and J. M. Hutson, “Methods for calculating the bound state energies of van der Waals trimers: Applications to Ar_3 ,” *J. Chem. Phys.* **98**, 2160 (1993).
- [83] A. Ohsaki and H. Nakamura, “Hyperspherical coordinate approach to atom-diatom chemical reactions in the sudden and adiabatic approximations,” *Phys. Rep.* **187**, 1 (1990).

- [84] G. Nyman and H.-G. Yu, “Quantum theory of bimolecular chemical reactions,” *Rep. Prog. Phys.* **63**, 1001 (2000).
- [85] J. M. Launay and M. L. Dourneuf, “Hyperspherical description of collinear reactive scattering,” *J. Phys. B* **15**, L455 (1982).
- [86] B. Lepetit, M. L. Dourneuf, J. M. Launay, and F. X. Gadéa, “Quantum dynamics of the collinear CsHH system,” *Chem. Phys. Lett.* **135**, 377 (1987).
- [87] J. M. Launay and B. Lepetit, “Three-dimensional quantum study of the reaction $\text{H}+\text{FH}(\nu j)\rightarrow\text{HF}(\nu' j')+\text{H}$ in hyperspherical coordinates,” *Chem. Phys. Lett.* **144**, 346 (1988).
- [88] B. Lepetit and J. M. Launay, “A quantum-mechanical study of the reaction $\text{H}+\text{HF}(\nu j m_j)\rightarrow\text{HF}(\nu' j' m'_j)+\text{H}$: Exact and centrifugal decoupling calculations in hyperspherical coordinates,” *Chem. Phys. Lett.* **151**, 287 (1988).
- [89] J. M. Launay and M. L. Dourneuf, “Hyperspherical close-coupling calculation of integral cross sections for the reaction $\text{H}+\text{H}_2\rightarrow\text{H}_2+\text{H}$,” *Chem. Phys. Lett.* **163**, 178 (1989).
- [90] J. M. Launay and M. L. Dourneuf, “Quantum-mechanical calculation of integral cross sections for the reaction $\text{F}+\text{H}_2(v = 0, j = 0)\rightarrow\text{FH}(v' j')+\text{H}$ by the hyperspherical method,” *Chem. Phys. Lett.* **169**, 473 (1990).
- [91] J. M. Launay, “Computation of cross-sections for the $\text{F}+\text{H}_2(v = 0, j = 0)\rightarrow\text{FH}(v' j')+\text{H}$ reaction by the hyperspherical method,” *Theoretica Chimica Acta* **79**, 183 (1991).
- [92] B. Lepetit and J. M. Launay, “Quantum mechanical study of the reaction $\text{He}+\text{H}_2^+\rightarrow\text{HeH}^++\text{H}$ with hyperspherical coordinates,” *J. Chem. Phys.* **95**, 5159 (1991).

- [93] S. E. Branchett, S. B. Padkjaer, and J. M. Launay, “Quantum dynamical study of the $\text{H} + \text{HCl} \rightarrow \text{H}_2 + \text{Cl}$ reaction,” *Chem. Phys. Lett.* **208**, 523 (1993).
- [94] P. Honvault and J. M. Launay, “Quantum mechanical study of the $\text{F} + \text{D}_2 \rightarrow \text{DF} + \text{D}$ reaction,” *Chem. Phys. Lett.* **287**, 270 (1998).
- [95] P. Honvault and J. M. Launay, “A quantum-mechanical study of the dynamics of the $\text{N}(^2\text{D}) + \text{H}_2 \rightarrow \text{NH} + \text{H}$ reaction,” *J. Chem. Phys.* **111**, 6665 (1999).
- [96] F. Huarte-Larranaga, X. Gimenez, J. M. Lucas, A. Aguilar, and J. M. Launay, “Detailed Energy Dependences of Cross Sections and Rotational Distributions for the $\text{Ne} + \text{H}_2^+ \rightarrow \text{NeH}^+ + \text{H}$ Reaction,” *J. Phys. Chem. A* **104**, 10227 (2000).
- [97] P. Honvault and J. M. Launay, “A quantum-mechanical study of the dynamics of the $\text{O}(^1\text{D}) + \text{H}_2 \rightarrow \text{OH} + \text{H}$ insertion reaction,” *J. Chem. Phys.* **114**, 1057 (2001).
- [98] L. Banares, F. Aoiz, P. Honvault, and J. Launay, “Dynamics of the $\text{S}(^1\text{D}) + \text{H}_2$ insertion reaction: A combined quantum mechanical and quasiclassical trajectory study,” *J. Phys. Chem. A* **108**, 1616 (2004).
- [99] G. A. Parker, R. L. Snow, and R. T. Pack, “Intermolecular potential surfaces from electron gas methods. I. angle and distance dependence of the $\text{He}-\text{CO}_2$ and $\text{Ar}-\text{CO}_2$ interactions,” *J. Chem. Phys.* **64**, 1668 (1976).
- [100] R. T. Pack and G. A. Parker, “Quantum reactive scattering in three dimensions using hyperspherical (APH) coordinates,” *J. Chem. Phys.* **87**, 3888 (1987).
- [101] G. A. Parker, R. T. Pack, B. J. Archer, and R. B. Walker, “Quantum reactive scattering in three dimensions using hyperspherical (APH) coordinates. tests on $\text{H} + \text{H}_2$ and $\text{D} + \text{H}_2$,” *Chem. Phys. Lett.* **137**, 564 (1987).

- [102] R. T. Pack and G. A. Parker, "Quantum reactive scattering in three dimensions using hyperspherical (aph) coordinates. III. small theta behavior and corrigenda," *J. Chem. Phys.* **90**, 3511 (1989).
- [103] J. D. Kress, Z. Bacic, G. A. Parker, and R. T. Pack, "Quantum effects in the $F+H_2\rightarrow HF+H$ reaction. accurate 3d calculations with a realistic potential energy surface," *Chem. Phys. Lett.* **157**, 484 (1989).
- [104] Z. Bacic, J. D. Kress, G. A. Parker, and R. T. Pack, "Quantum reactive scattering in three dimensions using hyperspherical(APH) coordinates. IV. Discrete variable representation(DVR) basis functions and the analysis of accurate results for $F+H_2$," *J. Chem. Phys.* **92**, 2344 (1990).
- [105] G. A. Parker, A. Laganà, S. Crocchianti, and R. T. Pack, "A detailed three-dimensional quantum study of the $Li+FH$ reaction," *J. Chem. Phys.* **102**, 1238 (1995).
- [106] V. Efimov, "Weakly-bound states of three resonantly-interacting particles," *Sov. J. Nucl. Phys* **12**, 589 (1971).
- [107] V. Efimov, "Energy levels of three resonantly interacting particles," *Nucl. Phys. A* **210**, 157 (1973).
- [108] C. D. Lin, "Hyperspherical coordinate approach to atomic and other coulombic three-body systems," *Phys. Rep.* **257**, 1 (1995).
- [109] B. R. Johnson, "On hyperspherical coordinates and mapping the internal configurations of a three body system," *J. Chem. Phys.* **73**, 5051 (1980).
- [110] R. C. Whitten and F. T. Smith, "Symmetric representation for three-body problems. II. motion in space," *J. Math. Phys.* **9**, 1103 (1968).
- [111] V. Aquilanti and S. Cavalli, "The quantum-mechanical Hamiltonian for tetraatomic

- systems in symmetric hyperspherical coordinates,” *J. Chem. Soc., Faraday Trans.* **93**, 801 (1997).
- [112] A. Kuppermann, “Reactive scattering with row-orthonormal hyperspherical coordinates. 2. transformation properties and Hamiltonian for tetraatomic systems,” *J. Phys. Chem. A* **101**, 6368 (1997).
- [113] A. Kuppermann, “Reactive scattering with row-orthonormal hyperspherical coordinates. 3. Hamiltonian and transformation properties for pentaatomic systems,” *J. Phys. Chem. A* **113**, 4518 (2009).
- [114] A. R. Edmonds, *Angular Momentum in Quantum Mechanics* (Princeton, New Jersey, 1957).
- [115] H. Goldstein, *Classical Mechanics*, vol. 2nd ed.
- [116] A. Kuppermann, “Reactive scattering with row-orthonormal hyperspherical coordinates. 1. Transformation properties and Hamiltonian for triatomic systems,” *J. Phys. Chem.* **100**, 2621 (1996).
- [117] V. Aquilanti and S. Cavalli, “Coordinates for molecular dynamics: Orthogonal local systems,” *J. Chem. Phys.* **85**, 1355 (1986).
- [118] H. Suno and B. D. Esry, “Adiabatic hyperspherical study of triatomic helium systems,” *Phys. Rev. A* **78**, 062701 (2008).
- [119] B. K. Kendrick, R. T. Pack, R. B. Walker, and E. F. Hayes, “Hyperspherical surface functions for nonzero total angular momentum. I. Eckart singularities,” *J. Chem. Phys.* **110**, 6673 (1999).
- [120] J. Macek, “Properties of autoionizing states of He,” *J. Phys. B* **1**, 831 (1968).
- [121] H. Suno and B. D. Esry, “Three-body recombination in cold helium–helium–alkali-metal-atom collisions,” *Phys. Rev. A* **80**, 062702 (2009).

- [122] M. Aymar, C. H. Greene, and E. Luc-Koenig, “Multichannel Rydberg spectroscopy of complex atoms,” *Rev. Mod. Phys.* **68**, 1015 (1996).
- [123] N. P. Mehta, B. D. Esry, and C. H. Greene, “Three-body recombination in one dimension,” *Phys. Rev. A* **76**, 022711 (2007).
- [124] J. P. Burke Jr., *Theoretical Investigation of Cold Alkali Atom Collisions*, Ph.D. thesis, University of Colorado (1999).
- [125] N. P. Mehta, S. T. Rittenhouse, J. P. D’Incao, J. von Stecher, and C. H. Greene, “General theoretical description of N -body recombination,” *Phys. Rev. Lett.* **103**, 153201 (2009).
- [126] H. Suno, B. D. Esry, C. H. Greene, and J. P. Burke, “Three-body recombination of cold helium atoms,” *Phys. Rev. A* **65**, 042725 (2002).
- [127] D. V. Fedorov and A. S. Jensen, “Regularization of a three-body problem with zero-range potentials,” *J. Phys. A* **34**, 6003 (2001).
- [128] M. J. Seaton, “Strong coupling in optically allowed atomic transitions produced by electron impact,” *Proc. Phys. Soc.* **77**, 174 (1961).
- [129] M. Gailitis and R. Damburg, “The influence of close coupling on the threshold behaviour of cross sections of electron-hydrogen scattering,” *Proc. Phys. Soc.* **82**, 192 (1963).
- [130] C. H. Greene and A. R. P. Rau, “Dipole threshold laws for single and double detachment from negative ions,” *Phys. Rev. A* **32**, 1352 (1985).
- [131] V. Efimov, “Low-energy properties of three resonantly interacting particles,” *Sov. J. Nucl. Phys* **29**, 546 (1979).
- [132] A. M. Perelomov and V. S. Popov, “Fall to the center in quantum mechanics,” *Theor. Math. Phys.* **4**, 664 (1970).

- [133] S. Jonsell, “Efimov states for systems with negative scattering lengths,” *Europhys. Lett.* **76**, 8 (2006).
- [134] K. M. Watson, “Implications of the direct-interaction model for nuclear structure,” *Rev. Mod. Phys.* **30**, 565 (1958).
- [135] S. Jonsell, “Universality of the three-boson system close to a Feshbach resonance,” *J. Phys. B* **37**, S245 (2004).
- [136] D. S. Petrov, “Three-boson problem near a narrow Feshbach resonance,” *Phys. Rev. Lett.* **93**, 143201 (2004).
- [137] A. O. Gogolin, C. Mora, and R. Egger, “Analytical solution of the bosonic three-body problem,” *Phys. Rev. Lett.* **100**, 140404 (2008).
- [138] E. Braaten, D. Kang, and L. Platter, “Universality constraints on three-body recombination for cold atoms: From ^4He to ^{133}Cs ,” *Phys. Rev. A* **75**, 052714 (2007).
- [139] E. Braaten, H.-W. Hammer, D. Kang, and L. Platter, “Three-body recombination of identical bosons with a large positive scattering length at nonzero temperature,” *Phys. Rev. A* **78**, 043605 (2008).
- [140] L. Platter and J. R. Shepard, “Scaling functions applied to three-body recombination of ^{133}Cs atoms,” *Phys. Rev. A* **78**, 062717 (2008).
- [141] J. L. Bohn and P. S. Julienne, “Prospects for influencing scattering lengths with far-off-resonant light,” *Phys. Rev. A* **56**, 1486 (1997).
- [142] F. K. Fatemi, K. M. Jones, and P. D. Lett, “Observation of optically induced Feshbach resonances in collisions of cold atoms,” *Phys. Rev. Lett.* **85**, 4462 (2000).
- [143] M. Theis, G. Thalhammer, K. Winkler, M. Hellwig, G. Ruff, R. Grimm, and J. H. Denschlag, “Tuning the scattering length with an optically induced Feshbach resonance,” *Phys. Rev. Lett.* **93**, 123001 (2004).

- [144] T. B. Ottenstein, T. Lompe, M. Kohnen, A. N. Wenz, and S. Jochim, “Collisional stability of a three-component degenerate Fermi gas,” *Phys. Rev. Lett.* **101**, 203202 (2008).
- [145] J. H. Huckans, J. R. Williams, E. L. Hazlett, R. W. Stites, and K. M. O’Hara, “Three-body recombination in a three-state Fermi gas with widely tunable interactions,” *Phys. Rev. Lett.* **102**, 165302 (2009).
- [146] G. Barontini, C. Weber, F. Rabatti, J. Catani, G. Thalhammer, M. Inguscio, and F. Minardi, “Observation of heteronuclear atomic Efimov resonances,” *Phys. Rev. Lett.* **103**, 043201 (2009).
- [147] N. Gross, Z. Shotan, S. Kokkelmans, and L. Khaykovich, “Observation of universality in ultracold ${}^7\text{Li}$ three-body recombination,” *Phys. Rev. Lett.* **103**, 163202 (2009).
- [148] J. R. Williams, E. L. Hazlett, J. H. Huckans, R. W. Stites, Y. Zhang, and K. M. O’Hara, “Evidence for an excited-state Efimov trimer in a three-component Fermi gas,” *Phys. Rev. Lett.* **103**, 130404 (2009).
- [149] G. M. Bruun, A. D. Jackson, and E. E. Kolomeitsev, “Multichannel scattering and Feshbach resonances: Effective theory, phenomenology, and many-body effects,” *Phys. Rev. A* **71**, 052713 (2005).
- [150] O. I. Kartavtsev and J. H. Macek, “Low-Energy Three-Body Recombination Near a Feshbach Resonance,” *Few-Body Syst.* **31**, 249 (2002).
- [151] G. Smirne, R. M. Godun, D. Cassettari, V. Boyer, C. J. Foot, T. Volz, N. Syassen, S. Dürr, G. Rempe, M. D. Lee, K. Góral, and T. Köhler, “Collisional relaxation of Feshbach molecules and three-body recombination in ${}^{87}\text{Rb}$ Bose-Einstein condensates,” *Phys. Rev. A* **75**, 020702 (2007).

- [152] P. Massignan and H. T. C. Stoof, “Efimov states near a Feshbach resonance,” *Phys. Rev. A* **78**, 030701 (2008).
- [153] N. P. Mehta, S. T. Rittenhouse, J. P. D’Incao, and C. H. Greene, “Efimov states embedded in the three-body continuum,” *Phys. Rev. A* **78**, 020701 (2008).
- [154] S. D. Palo, M. L. Chiofalo, M. J. Holland, and S. J. J. M. F. Kokkelmans, “Resonance effects on the crossover of bosonic to fermionic superfluidity,” *Phys. Lett. A* **327**, 490 (2004).
- [155] O. S. Sørensen, N. Nygaard, and P. B. Blakie, “Statistical mechanics of a Feshbach-coupled Bose-Fermi gas in an optical lattice,” *Phys. Rev. A* **79**, 053601 (2009).
- [156] O. S. Sørensen, N. Nygaard, and P. B. Blakie, “Adiabatic cooling of a tunable Bose-Fermi mixture in an optical lattice,” *Phys. Rev. A* **79**, 063615 (2009).
- [157] C. A. Stan, M. W. Zwierlein, C. H. Schunck, S. M. F. Raupach, and W. Ketterle, “Observation of Feshbach resonances between two different atomic species,” *Phys. Rev. Lett.* **93**, 143001 (2004).
- [158] E. Wille, F. M. Spiegelhalter, G. Kerner, D. Naik, A. Trenkwalder, G. Hendl, F. Schreck, R. Grimm, T. G. Tiecke, J. T. M. Walraven, S. J. J. M. F. Kokkelmans, E. Tiesinga, and P. S. Julienne, “Exploring an ultracold Fermi-Fermi mixture: Interspecies Feshbach resonances and scattering properties of ^6Li and ^{40}K ,” *Phys. Rev. Lett.* **100**, 053201 (2008).
- [159] A.-C. Voigt, M. Taglieber, L. Costa, T. Aoki, W. Wieser, T. W. Hänsch, and K. Dieckmann, “Ultracold heteronuclear Fermi-Fermi molecules,” *Phys. Rev. Lett.* **102**, 020405 (2009).
- [160] K. Pilch, A. D. Lange, A. Prantner, G. Kerner, F. Ferlaino, H.-C. Nägerl, and

- R. Grimm, “Observation of interspecies feshbach resonances in an ultracold Rb-Cs mixture,” Phys. Rev. A **79**, 042718 (2009).
- [161] E. Braaten and H.-W. Hammer, “Universality in the three-body problem for ^4He atoms,” Phys. Rev. A **67**, 042706 (2003).
- [162] H.-W. Hammer, T. A. Lähde, and L. Platter, “Effective-range corrections to three-body recombination for atoms with large scattering length,” Phys. Rev. A **75**, 032715 (2007).
- [163] L. Platter, C. Ji, and D. R. Phillips, “Range corrections to three-body observables near a Feshbach resonance,” Phys. Rev. A **79**, 022702 (2009).
- [164] J. P. D’Incao and B. D. Esry, “Manifestations of the Efimov effect for three identical bosons,” Phys. Rev. A **72**, 032710 (2005).
- [165] J. P. D’Incao, “Private communications.” .
- [166] N. R. Thomas, N. Kjærgaard, P. S. Julienne, and A. C. Wilson, “Imaging of s and d partial-wave interference in quantum scattering of identical bosonic atoms,” Phys. Rev. Lett. **93**, 173201 (2004).
- [167] C. Buggle, J. Léonard, W. von Klitzing, and J. T. M. Walraven, “Interferometric determination of the s and d -wave scattering amplitudes in ^{87}Rb ,” Phys. Rev. Lett. **93**, 173202 (2004).
- [168] A. Perrin, H. Chang, V. Krachmalnicoff, M. Schellekens, D. Boiron, A. Aspect, and C. I. Westbrook, “Observation of atom pairs in spontaneous four-wave mixing of two colliding Bose-Einstein condensates,” Phys. Rev. Lett. **99**, 150405 (2007).
- [169] J. P. D’Incao and B. D. Esry, “Mass dependence of ultracold three-body collision rates,” Phys. Rev. A **73**, 030702 (2006).

- [170] N. F. Lane, “The theory of electron-molecule collisions,” *Rev. Mod. Phys.* **52**, 29 (1980).
- [171] H. Suno, B. D. Esry, and C. H. Greene, “Recombination of three ultracold fermionic atoms,” *Phys. Rev. Lett.* **90**, 053202 (2003).
- [172] F. Ferlaino, (Private Communication).
- [173] S. Schmid, G. Thalhammer, K. Winkler, F. Lang, and J. H. Denschlag, “Long distance transport of ultracold atoms using a 1D optical lattice,” *New J. Phys.* **8**, 159 (2006).
- [174] T. Lahaye, J. Metz, B. Fröhlich, T. Koch, M. Meister, A. Griesmaier, T. Pfau, H. Saito, Y. Kawaguchi, and M. Ueda, “*d*-wave collapse and explosion of a dipolar Bose-Einstein condensate,” *Phys. Rev. Lett.* **101**, 080401 (2008).
- [175] C. Chin, V. Vuletić, A. J. Kerman, S. Chu, E. Tiesinga, P. J. Leo, and C. J. Williams, “Precision Feshbach spectroscopy of ultracold Cs₂,” *Phys. Rev. A* **70**, 032701 (2004).
- [176] S. Jochim, M. Bartenstein, A. Altmeyer, G. Hendl, C. Chin, J. H. Denschlag, and R. Grimm, “Pure gas of optically trapped molecules created from fermionic atoms,” *Phys. Rev. Lett.* **91**, 240402 (2003).
- [177] A. Mosk, S. Kraft, M. Mudrich, K. Singer, W. Wohlleben, R. Grimm, and M. Weidemüller, “Mixture of ultracold lithium and cesium atoms in an optical dipole trap,” *Appl. Phys. B* **73**, 791 (2001).
- [178] B. D. Esry, C. H. Greene, and H. Suno, “Threshold laws for three-body recombination,” *Phys. Rev. A* **65**, 010705 (2001).
- [179] F. Bringas, M. T. Yamashita, and T. Frederico, “Triatomic continuum resonances for large negative scattering lengths,” *Phys. Rev. A* **69**, 040702 (2004).
- [180] B. D. Esry and J. P. D’Incao, “Efimov physics in ultracold three-body collisions,” *J. Phys: Conf. Ser.* **88**, 012040 (2007).

- [181] L. Platter, H.-W. Hammer, and U.-G. Meißner, “Four-boson system with short-range interactions,” *Phys. Rev. A* **70**, 052101 (2004).
- [182] M. T. Yamashita, L. Tomio, A. Delfino, and T. Frederico, “Four-boson scale near a Feshbach resonance,” *Europhys. Lett.* **75**, 555 (2006).
- [183] H. W. Hammer and L. Platter, “Universal properties of the four-body system with large scattering length,” *Eur. Phys. J. A* **32**, 113 (2007).
- [184] C. A. Regal, M. Greiner, and D. S. Jin, “Observation of resonance condensation of fermionic atom pairs,” *Phys. Rev. Lett.* **92**, 040403 (2004).
- [185] K. Winkler, F. Lang, G. Thalhammer, P. v. d. Straten, R. Grimm, and J. H. Denschlag, “Coherent optical transfer of Feshbach molecules to a lower vibrational state,” *Phys. Rev. Lett.* **98**, 043201 (2007).
- [186] K. Bergmann, H. Theuer, and B. W. Shore, “Coherent population transfer among quantum states of atoms and molecules,” *Rev. Mod. Phys.* **70**, 1003 (1998).
- [187] M. Stoll and T. Köhler, “Production of three-body Efimov molecules in an optical lattice,” *Phys. Rev. A* **72**, 022714 (2005).
- [188] M. W. Zwierlein, C. A. Stan, C. H. Schunck, S. M. F. Raupach, S. Gupta, Z. Hadzibabic, and W. Ketterle, “Observation of Bose-Einstein condensation of molecules,” *Phys. Rev. Lett.* **91**, 250401 (2003).
- [189] J. von Stecher and C. H. Greene, “Spectrum and dynamics of the BCS-BEC crossover from a few-body perspective,” *Phys. Rev. Lett.* **99**, 090402 (2007).
- [190] C. H. Greene, A. S. Dickinson, and H. R. Sadeghpour, “Creation of polar and nonpolar ultra-long-range Rydberg molecules,” *Phys. Rev. Lett.* **85**, 2458 (2000).
- [191] E. Fermi, *Nuovo Cimento* **11**, 157 (1934).

- [192] S. Knoop, (Private Communication).
- [193] E. Braaten, H.-W. Hammer, D. Kang, and L. Platter, “Three-body recombination of ${}^6\text{Li}$ atoms with large negative scattering lengths,” *Phys. Rev. Lett.* **103**, 073202 (2009).
- [194] P. Naidon and M. Ueda, “Possible Efimov trimer state in a three-hyperfine-component lithium-6 mixture,” *Phys. Rev. Lett.* **103**, 073203 (2009).
- [195] A. C. Fonseca, E. F. Redish, and P. E. Shanley, “Efimov effect in an analytically solvable model,” *Nucl. Phys. A* **320**, 273 (1979).
- [196] Y. Yamaguchi, “Two-nucleon problem when the potential is nonlocal but separable. i,” *Phys. Rev.* **95**, 1628 (1954).
- [197] S. Cowell, H. Heiselberg, I. E. Mazets, J. Morales, V. R. Pandharipande, and C. J. Pethick, “Cold Bose gases with large scattering lengths,” *Phys. Rev. Lett.* **88**, 210403 (2002).
- [198] H. Heiselberg, “Bosons and fermions near Feshbach resonances,” *J. Phys. B* **37**, S141 (2004).
- [199] J. von Stecher and C. H. Greene, (Private Communication).
- [200] C. Bahrim and U. Thumm, “Low-lying ${}^3P^o$ and ${}^3S^e$ states of Rb^- , Cs^- , and Fr^- ,” *Physical Review. A* **61**, 022722 (2000).
- [201] E. Nielsen, H. Suno, and B. D. Esry, “Efimov resonances in atom-diatom scattering,” *Phys. Rev. A* **66**, 012705 (2002).
- [202] T. Killian, T. Pattard, T. Pohl, and J. Rost, “Ultracold neutral plasmas,” *Phys. Rep.* **449**, 77 (2007).

- [203] C. Ryu, M. F. Andersen, P. Cladé, V. Natarajan, K. Helmerson, and W. D. Phillips, “Observation of persistent flow of a Bose-Einstein condensate in a toroidal trap,” *Phys. Rev. Lett.* **99**, 260401 (2007).
- [204] A. L. Fetter, “Rotating trapped Bose-Einstein condensates,” *Rev. Mod. Phys.* **81**, 647 (2009).
- [205] I. Bloch, “Ultracold quantum gases in optical lattices,” *Nature Physics* **1**, 23 (2005).
- [206] M. Girardeau, “Relationship between systems of impenetrable bosons and fermions in one dimension,” *J. Math. Phys.* **1**, 516 (1960).
- [207] E. H. Lieb and W. Liniger, “Exact analysis of an interacting Bose gas. I. the general solution and the ground state,” *Phys. Rev.* **130**, 1605 (1963).
- [208] M. Olshanii, “Atomic scattering in the presence of an external confinement and a gas of impenetrable bosons,” *Phys. Rev. Lett.* **81**, 938 (1998).
- [209] B. Paredes, A. Widera, V. Murg, O. Mandel, S. Fölling, I. Cirac, G. Shlyapnikov, T. Hänsch, and I. Bloch, “Tonks–Girardeau gas of ultracold atoms in an optical lattice,” *Nature* **429**, 277 (2004).
- [210] J. B. McGuire, “Study of exactly soluble one-dimensional N-body problems,” *J. Math. Phys.* **5**, 622 (1964).
- [211] V. A. Yurovsky, A. Ben-Reuven, and M. Olshanii, “One-dimensional Bose chemistry: Effects of nonintegrability,” *Phys. Rev. Lett.* **96**, 163201 (2006).
- [212] E. Tempfli, S. Zilner, and P. Schmelcher, “Excitations of attractive 1D bosons: binding versus fermionization,” *New J. Phys.* **10**, 103021 (2008).
- [213] H. Ezawa, “Constructive proof of the existence of bound state in one dimension,” *Found. Phys.* **98**, 1495 (1997).

- [214] L. D. Landau and E. M. Lifshitz, *Electrodynamics of Continuous Media*, vol. 2nd Ed. (Butterworth-Heinemann).
- [215] A. Simoni, J.-M. Launay, and P. Soldán, “Feshbach resonances in ultracold atom-molecule collisions,” *Phys. Rev. A* **79**, 032701 (2009).
- [216] M. A. J. D. R. Gurout, P. Soldn and O. Dulieu, “Core repulsion effects in alkali trimers,” *Int. J. Quantum Chem* **109**, 3387 (2009).
- [217] P. Soldán, “Lowest quartet states of Li_2A ($\text{A}=\text{Na}$, K , Rb , Cs),” *Phys. Rev. A* **77**, 054501 (2008).
- [218] M. Lysebo and L. Veseth, “Cold collisions between atoms and diatomic molecules,” *Phys. Rev. A* **77**, 032721 (2008).
- [219] G. Quéméner, J.-M. Launay, and P. Honvault, “Ultracold collisions between Li atoms and Li_2 diatoms in high vibrational states,” *Phys. Rev. A* **75**, 050701 (2007).
- [220] M. T. Cvitaš, P. Soldán, J. M. Hutson, P. Honvault, and J.-M. Launay, “Interactions and dynamics in $\text{Li} + \text{Li}_2$ ultracold collisions,” *J. Chem. Phys.* **127**, 074302 (2007).
- [221] M. T. Cvitaš, P. Soldán, J. M. Hutson, P. Honvault, and J.-M. Launay, “Ultracold $\text{Li}+\text{Li}_2$ collisions: Bosonic and fermionic cases,” *Phys. Rev. Lett.* **94**, 033201 (2005).
- [222] G. Quéméner, P. Honvault, and J.-M. Launay, “Sensitivity of the dynamics of $\text{Na} + \text{Na}_2$ collisions on the three-body interaction at ultralow energies,” *Eur. Phys. J. D* **30**, 201 (2004).
- [223] P. Soldán, M. T. Cvitaš, J. M. Hutson, P. Honvault, and J.-M. Launay, “Quantum dynamics of ultracold $\text{Na}+\text{Na}_2$ collisions,” *Phys. Rev. Lett.* **89**, 153201 (2002).
- [224] M. Hesse, A. T. Le, and C. D. Lin, “Protonium formation in the \bar{p} -H collision at low energies by a diabatic approach,” *Phys. Rev. A* **69**, 052712 (2004).

- [225] B. D. Esry and H. R. Sadeghpour, “Split diabatic representation,” *Phys. Rev. A* **68**, 042706 (2003).
- [226] L. C. T. Pacher and H. Kppel, *Adv. Chem. Phys.* **34**, 293 (1993).
- [227] T. G. Heil, S. E. Butler, and A. Dalgarno, “Charge transfer of multiply charged ions at thermal energies,” *Phys. Rev. A* **23**, 1100 (1981).
- [228] A. B. Alekseyev, H.-P. Liebermann, R. J. Buenker, N. Balakrishnan, H. R. Sadeghpour, S. T. Cornett, and M. J. Cavagnero, “Spin-orbit effects in photodissociation of sodium iodide,” *J. Chem. Phys.* **113**, 1514 (2000).
- [229] O. I. Tolstikhin, S. Watanabe, and M. Matsuzawa, ““Slow” variable discretization: a novel approach for Hamiltonians allowing adiabatic separation of variables,” *J. Phys. B* **29**, L389 (1996).
- [230] Z. Zhen and J. Macek, “Loosely bound states of three particles,” *Phys. Rev. A* **38**, 1193 (1988).
- [231] D. V. Fedorov and A. S. Jensen, “Efimov effect in coordinate space Faddeev equations,” *Phys. Rev. Lett.* **71**, 4103 (1993).
- [232] H. li Han, Y. Li, X. zhou Zhang, and T. yun Shi, “Hyperspherical coupled channel calculations for the spectra and structure parameters of rare gas trimers NeAr_2 and Ne_2Ar ,” *J. Chem. Phys.* **127**, 154104 (2007).
- [233] D. Blume, C. H. Greene, and B. D. Esry, “Comparative study of He_3 , Ne_3 , and Ar_3 using hyperspherical coordinates,” *J. Chem. Phys.* **113**, 2145 (2000).
- [234] A. R. Cooper, S. Jain, and J. M. Hutson, “Methods for calculating the bound state energies of van der Waals trimers: Applications to Ar_3 ,” *J. Chem. Phys.* **98**, 2160 (1993).

Appendix A

A diabatic picture generated by freezing three-body geometry

Quantum mechanical calculations for realistic three-body systems have been pursued for many years. In the field of quantum chemistry and ultracold quantum gases, the three-body scattering processes are especially of interest because of their close relationship to the molecular formations and stabilities of the quantum gases. Some precursory calculations have been available, but they are mostly restricted to the systems where particles interact very weakly, such as three He atoms [118, 126]. For the three-body systems involving stronger interactions, like the alkali atoms which are widely used in the experiments on ultracold quantum gases, exact three-body calculations are only available for the processes involving a few of the lowest two-body channels [215–223].

Among the various numerical methods developed to perform three-body calculations, the hyperspherical close coupling method has many advantages. In the hyperspherical coordinates, the overall size of the three-body system is measured by the hyperradius R , while all the other degrees of freedom are defined via two hyperangles. The three-body Schrödinger equation is usually solved by treating the hyperradius as an adiabatic parameter. The adiabatic hyperradial potentials and the non-adiabatic couplings for each R are then calculated by solving the resulting hyperangular equation. The adiabatic hyperspherical potentials have some similarity with the Born-Oppenheimer potentials. Especially, in the limit of one

particle much lighter than the other two, the adiabatic hyperradial potentials reduces to the Born-Oppenheimer potentials. But for the cases where all three particles have comparable masses, unlike the Born-Oppenheimer potentials, the hyperradial potentials are still of physical significance due to the fact that the hyperradius is generally a slowly varying variable. Further, the three-body break-up continuum is rigorously discretized, which greatly facilitates numerical calculations involving the three-body continuum. An exact solution of the three-body equation can in principle be obtained by solving the hyperradial equation, including all the adiabatic potentials and the non-adiabatic couplings. However, in most three-body systems with realistic atomic interactions, the adiabatic hyperspherical potential curves bearing different characteristics, such as different partial angular momenta or two-body affinities, can have sharp avoided crossings. Near such crossings, the non-adiabatic couplings exhibit δ -function like behavior. It is very challenging to either trace out such sharp peaks or to use them to perform hyperradial calculations.

Due to these difficulties, much effort has been made to find a diabatic representation which is also of physical significance [224–228]. Some of the schemes, called “diabatization”, are based on post-processing the adiabatic potentials, trying to connect the sharp avoided crossings as real ones, as called “diabatization”. However, it is hard to find a general criterion to decide which avoided crossings should be connected *a priori*. Even if this can be achieved, the coupling information is generally missing, making the picture incomplete. Another useful diabatic picture, the “slow variable discretization” (SVD) [229], is an exact representation. It is defined in a unified form which facilitates its applications. However, in this representation the hyperradial and hyperangular motions are coupled, making it more numerical rather than physical. This representation imposes the inconvenience of storing the hyperangular wave-function for consecutive steps.

In an adiabatic representation, the potential energy operator is made diagonal. However, in a diabatic representation the potential energy operator is not diagonalized, which allows great flexibility in defining a diabatic representation. [10]. As mentioned above, for a pair of

adiabatic potentials bearing distinct characteristics, sharp avoided crossings may occur. This usually implies the presence of some “nearly” good quantum numbers (from approximate symmetries), or “flavors”, for the channels. A diabatic representation is most useful if these “flavors” are used to label the channels [226]. However, the difficulty is that the “flavors” usually have very different physical nature, and in most cases it is hard to define an appropriate physical quantity to represent these “flavors” *a priori*.

In three-body systems, states with distinct “flavors” usually have different geometric configurations. The emergence of the sharp avoided crossings can be understood by the fact that the geometric configuration of the three-body system is not likely to change abruptly. The shape of the system is then a slowly-varying characteristic which can be used to produce a diabatic representation with a unified form. Based on this idea, here we develop a *shape*-diabatic representation. This representation is superior in the short and intermediate distances to treat the complicated three-body dynamical processes and can provide more physical insights to the geometric changes. Combined with the adiabatic representation in the asymptotic region, this representation is complete provides an efficient method for solving three-body problems of realistic systems with more complicated interactions. Further, we find the adiabatic equation can be solved with better memory efficiency in the shape-diabatic representation, making it an appealing numerical strategy for adiabatic calculations.

A.1 Method

We set up our method in the Smith-Whitten hyperspherical coordinates as introduced in Sec. 2.2.2. To build the information of the geometric configurations into the hyperangular basis, we treat both R and θ as adiabatic parameters, since θ characterizes the geometrical configuration of the three particles. The basis functions for shape-diabatic representation is written as

$$\Phi_{\nu,\lambda}(R; \theta, \varphi) = \Theta(R; \theta)_{\nu,\lambda} \phi_{\lambda}(R, \theta; \varphi), \quad (\text{A.1})$$

where ϕ_λ solves

$$[T_\varphi + V(R, \theta; \varphi)] \phi_\lambda(R, \theta; \varphi) = u_\lambda(R, \theta) \phi_\lambda(R, \theta; \varphi), \quad (\text{A.2})$$

and $\Theta_{\nu,\lambda}$ is the solution of

$$\left[T_\theta + \frac{15}{8\mu_3 R^2} + u_\lambda(R, \theta) \right] \Theta_{\nu,\lambda}(R; \theta) = U_{\nu,\lambda}(R) \Theta_{\nu,\lambda}(R; \theta). \quad (\text{A.3})$$

Since the coordinate θ determines the three-body geometry, the functions $\Theta_{\nu,\lambda}$ then provide an overall “envelope” of the geometric configurations, on top of the details given by the φ -channel functions ϕ_λ . Expanding the total wave-function ψ in the shape-diabatic basis $\Phi_{\nu,\lambda}$,

$$\psi = \sum_{\nu,\lambda} F_{\nu,\lambda}(R) \Phi_{\nu,\lambda}(R; \theta, \varphi), \quad (\text{A.4})$$

we arrive at the hyperradial equation in the shape-diabatic basis:

$$\begin{aligned} \left[-\frac{1}{2\mu} \frac{\partial^2}{\partial R^2} + U_{\nu,\lambda}(R) \right] F_{\nu,\lambda}(R) - \frac{1}{2\mu} \sum_{\nu',\lambda'} \left[2P_{\nu\lambda,\nu'\lambda'}(R) \frac{d}{dR} \right. \\ \left. + Q_{\nu\lambda,\nu'\lambda'}(R) + \mathcal{W}_{\nu\lambda,\nu'\lambda'}(R) \right] F_{\nu',\lambda'}(R) = E F_{\nu,\lambda}(R). \end{aligned} \quad (\text{A.5})$$

The shape non-adiabatic couplings $P_{\nu\lambda,\nu'\lambda'}(R)$ and $Q_{\nu\lambda,\nu'\lambda'}(R)$, involving derivatives with respect to R , are defined similarly as the non-adiabatic couplings $P_{n,n'}$ and $Q_{n,n'}$ in the adiabatic picture (n and n' are the adiabatic channel function indices) as

$$P_{\nu\lambda,\nu'\lambda'}(R) = \left\langle\left\langle \Phi_{\nu,\lambda} \left| \frac{d}{dR} \right| \Phi_{\nu',\lambda'} \right\rangle\right\rangle, \quad Q_{\nu\lambda,\nu'\lambda'}(R) = \left\langle\left\langle \Phi_{\nu,\lambda} \left| \frac{d^2}{dR^2} \right| \Phi_{\nu',\lambda'} \right\rangle\right\rangle, \quad (\text{A.6})$$

where the double bracket indicates integration over the hyperangles θ and φ . The diabatic couplings $\mathcal{W}_{\nu\lambda,\nu'\lambda'}$ arise from the non-adiabaticity in the θ coordinate, and are defined by

$$\mathcal{W}_{\nu\lambda,\nu'\lambda'}(R) = \left\langle \Theta_{\nu\lambda,\nu'\lambda'} \left| 4\mathcal{P}_{\lambda,\lambda'}(\theta) \frac{\partial}{\partial \theta} + 2\mathcal{Q}_{\lambda,\lambda'}(\theta) + 8 \cot 2\theta \mathcal{P}_{\lambda,\lambda'}(\theta) \right| \Theta_{\nu\lambda,\nu'\lambda'} \right\rangle_\theta. \quad (\text{A.7})$$

Here the single bracket indicates integration over the hyperangle θ . The shape non-adiabatic couplings $\mathcal{P}_{\lambda,\lambda'}(\theta)$ and $\mathcal{Q}_{\lambda,\lambda'}(\theta)$ are defined similarly as their hyperradial counterparts:

$$\mathcal{P}_{\lambda,\lambda'}(\theta) = \left\langle \phi_\lambda \left| \frac{\partial}{\partial \theta} \right| \phi_{\lambda'} \right\rangle_\varphi, \quad \mathcal{Q}_{\lambda,\lambda'}(\theta) = \left\langle \phi_\lambda \left| \frac{\partial^2}{\partial \theta^2} \right| \phi_{\lambda'} \right\rangle_\varphi, \quad (\text{A.8})$$

where the integration is over the hyperangle φ .

A.2 Applications

A.2.1 Three identical particles

System with single s -wave bound channel

Without loss of generality, we assume that all the identical particles are bosons. We first apply the shape-diabatic representation to a simple three-body system, where the two-body subsystem has only one bound state. We use the following two-body model potential for inter-particle interactions:

$$V(r_{ij}) = -D \operatorname{sech}^2(r_{ij}/r_0) \quad (\text{A.9})$$

The diabatic potentials are shown in Fig. A.1. The adiabatic potentials are shown together for comparison. As seen in the figure, the diabatic potentials follow the adiabatic potentials closely in the short-range region: $R \lesssim 5r_0$. Similar to the adiabatic potentials, the lowest diabatic potential asymptotically goes to a bound state energy, while the higher ones go to the energy of hyperspherical harmonics. However, the energy of the lowest diabatic potential does not match the two-body bound state energy, implying strong couplings between the channels even in the asymptotic region. We also see some of the continuum potentials exchange their ordering asymptotically, for example, the channels $\nu = 3, \lambda = 1$ (dark blue circles) and $\nu = 1, \lambda = 2$ (light pink balls). We show the corresponding hyperangular wave-functions for these two channels from $\varphi = 0$ to $\varphi = 2\pi/3$ in Fig. A.2 at different hyperradii. Due to identical particle symmetry, the part of the wave-function shown is repeated on the rest of the hyperangular plane. As seen from the wave-functions, the exchange of the ordering is direct result of the shrinking of one nodal line into the two-body potential region for $\Phi_{3,1}$ and the emerging of a nodal line from the two-body potential region for $\Phi_{1,2}$.

The diagonal couplings, $Q_{\nu\lambda,\nu\lambda}$ and $\mathcal{W}_{\nu\lambda,\nu\lambda}$, which are important to make the potentials more physical, are shown in Fig. A.3. It is seen that the diagonal term $\mathcal{W}_{1,1,1,1}$ for the two-body bound channel approaches a constant value asymptotically. The coupling term $Q_{1,1,1,1}$ behaves like $1/R^2$ asymptotically. But still the diagonal diabatic potential for the bound

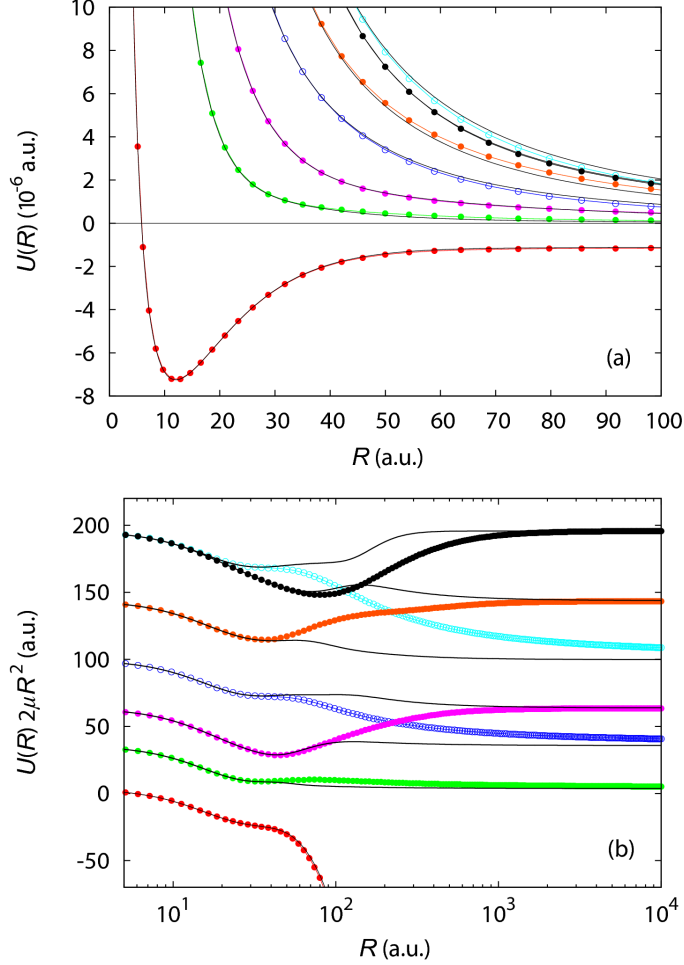


Figure A.1: The shape-diabatic potentials (lines with symbols) and the adiabatic ones (black lines). (a) The potentials at small distances. (b) The potentials multiplied by $2\mu R^2$. Here, $m = 7292.3$ a.u., $r_0 = 15$ a.u. and $D = 4.79 \times 10^{-6}$ a.u.

channel $W_{11,11} = U_{11} - \frac{1}{2\mu}(Q_{11,11} + \mathcal{W}_{11,11})$ does not go to the dimer energy asymptotically, so that the diabatic bound channel potential can not represent the asymptotic $A_2 + A$ configuration by itself. The diagonal couplings $\mathcal{W}_{\nu\lambda,\nu\lambda}$ for continuum channels have two different asymptotic behaviors. The diagonal couplings $\mathcal{W}_{\nu 1,\nu 1}$ behave like $\sim 1/R^2$, while other ones decrease like $1/R$ asymptotically. Since these couplings are of the same order or lower order as the potential energies $U_{\nu\lambda}$ themselves in $1/R$, the diabatic continuum channels do not approach the free particles configurations asymptotically. These diabatic channels then will be coupled together to give the correct physical asymptotic configurations.

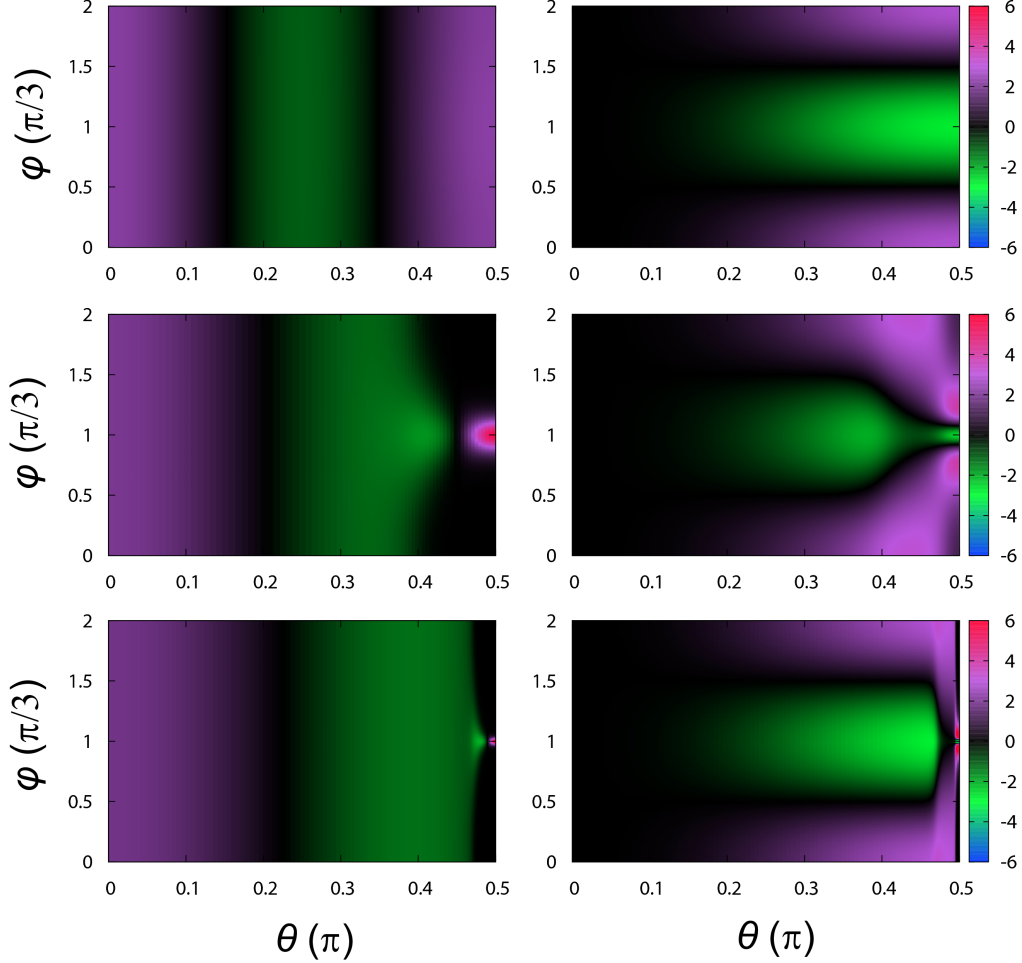


Figure A.2: Hyperangular wave-functions $\Phi_{3,1}$ (left column) and $\Phi_{1,2}$ (right column) at $R = 20$ (top panel), 200 (middle panel) and 2000 a.u. (bottom panel).

For three-body recombination and dissociation processes, the couplings between the bound channel and the continuum channels are the most important. As shown in Fig. A.4, the couplings $\mathcal{W}_{\nu\lambda,11}$ are generally dominant over the corresponding P and Q coupling terms. The coupling terms $\mathcal{W}_{\nu 1,11}$ have very slow decaying behavior as $\sim 1/R$, indicating long-range couplings from the continuum channels come from the same φ -channel ϕ_1 as the bound channel. As seen from the figure, though the other $\mathcal{W}_{\nu\lambda,11}$ coupling terms decay quicker as $\sim 1/R^2$, the terms for higher λ become dominant at larger R . This implies that when R increases, higher continuum channels need to be included to get the correct $A_2 + A$

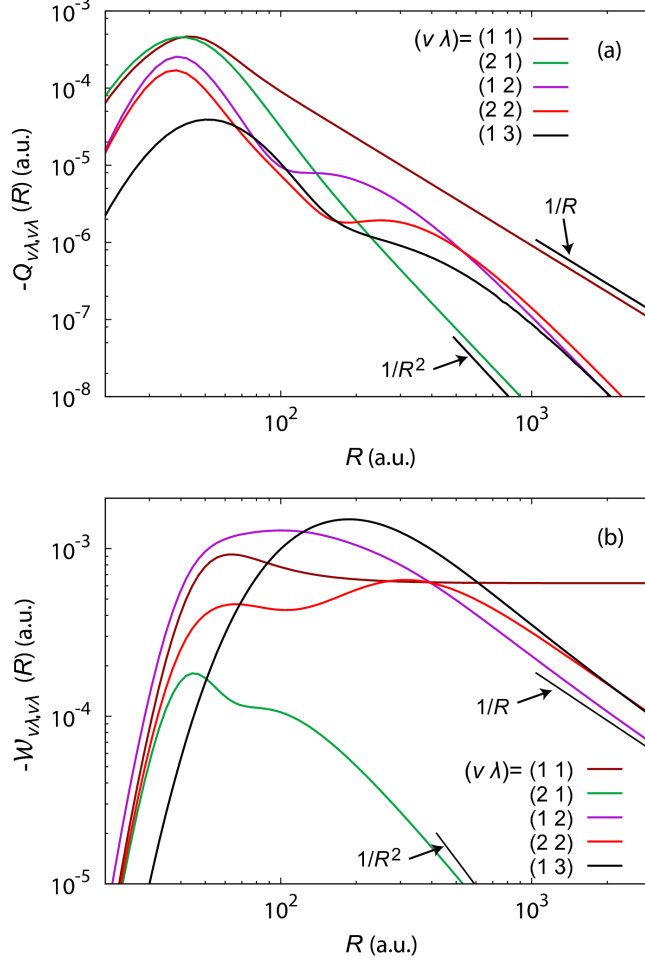


Figure A.3: The diagonal couplings $-Q_{\nu\lambda,\nu\lambda}$ and $-W_{\nu\lambda,\nu\lambda}$

configurations.

The asymptotic behavior of the off-diagonal couplings between the continuum channels are shown in Fig. A.5. Here $P_{\nu 1, \nu' 1}$ behave like $\sim 1/R^{1.5}$, while other P coupling terms behave like $\sim 1/R^3$. The Q couplings are of higher order as $\sim 1/R^{3.5}$. The W couplings generally behave like $\mathcal{O}(1/R^2)$.

As shown in this example, though the shape-diabatic representation is complete, it does not treat the asymptotic behaviors of the three-body systems very well. To represent the three-body physics correctly at large distances, lots of diabatic channels need to be coupled. However, since the main objective to invoke a diabatic representation is to avoid sharp

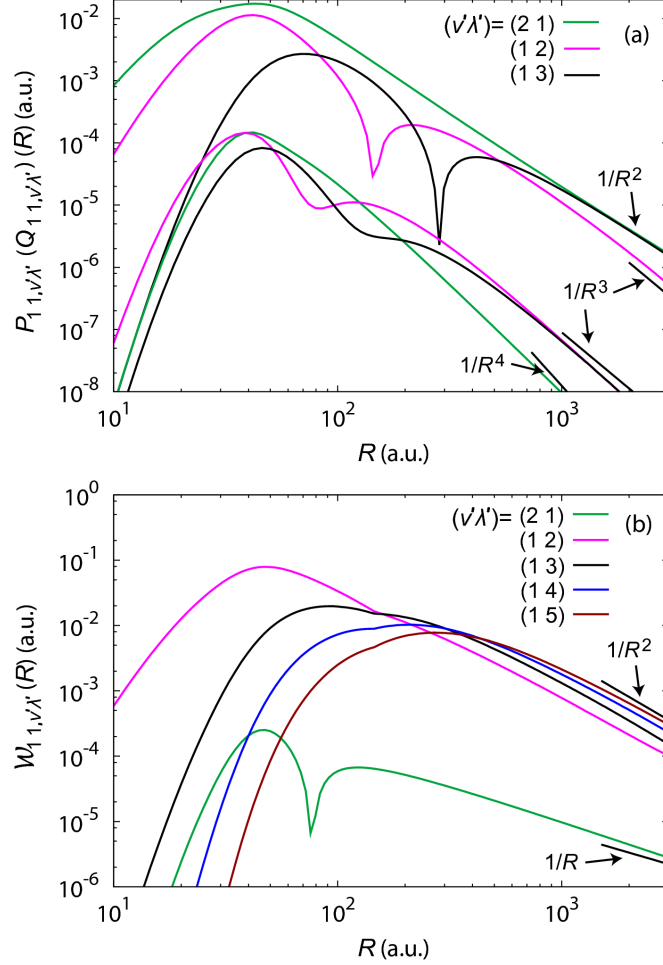


Figure A.4: The couplings between the bound channel and continuum channels. (a) $|P_{\nu\lambda,11}|$, $|Q_{\nu\lambda,11}|$ and (b) $|W_{\nu\lambda,11}|$, where $\nu' = 1$, $\lambda' = 1$ is for the bound channel. The sharp dips comes from the coupling terms passing through zero.

avoided crossings at short and intermediate distances, we will in the following demonstrate how the shape-diabatic representation gets rid of the sharp avoided crossings appearing in the adiabatic potentials.

System with high angular momentum bound channels

In the three-body systems where the two-body subsystems have high angular momentum states, the adiabatic hyperspherical potentials usually have sharp avoided crossings between the channels bearing different two-body angular momentum characteristics. In Fig. A.6, we

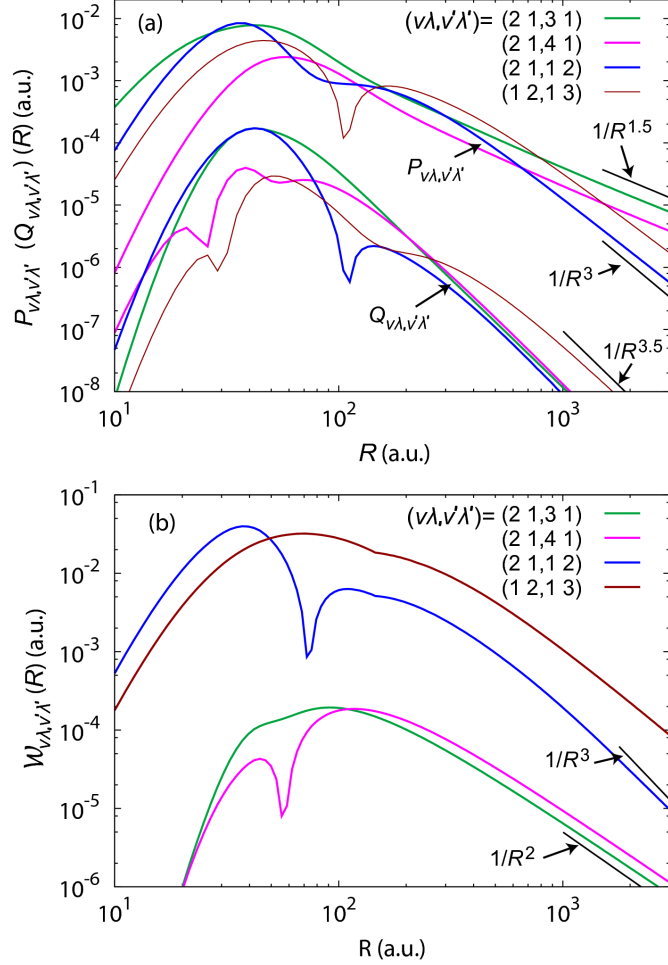


Figure A.5: The off-diagonal couplings between the continuum channels. (a) $|P_{\nu\lambda,\nu'\lambda'}|$, $|Q_{\nu\lambda,\nu'\lambda'}|$ and (b) $|W_{\nu\lambda,\nu'\lambda'}|$. The sharp dips comes from the coupling terms passing through zero.

show both the adiabatic potentials and the shape-diabatic potentials for such a three-body system. For the adiabatic potentials, the second lowest channel ($n=2$), which is an asymptotic d -wave bound channel, has an avoided crossing with the third channel ($n=3$) which is an asymptotic s -wave bound channel at $R \approx 24$ a.u.. The diabatic potentials following closely to these two adiabatic potentials ($\nu = 2, \lambda = 3$ and $\nu = 1, \lambda = 2$) cross smoothly here. The corresponding non-adiabatic and diabatic couplings are shown in Fig. A.7.

The non-adiabatic couplings in the adiabatic representation $P_{2,3}$ peaks sharply around $R \approx 24$ a.u., while the shape non-diabatic couplings $\mathcal{P}_{21,12}$, $\mathcal{Q}_{21,12}$ and the diabatic cou-

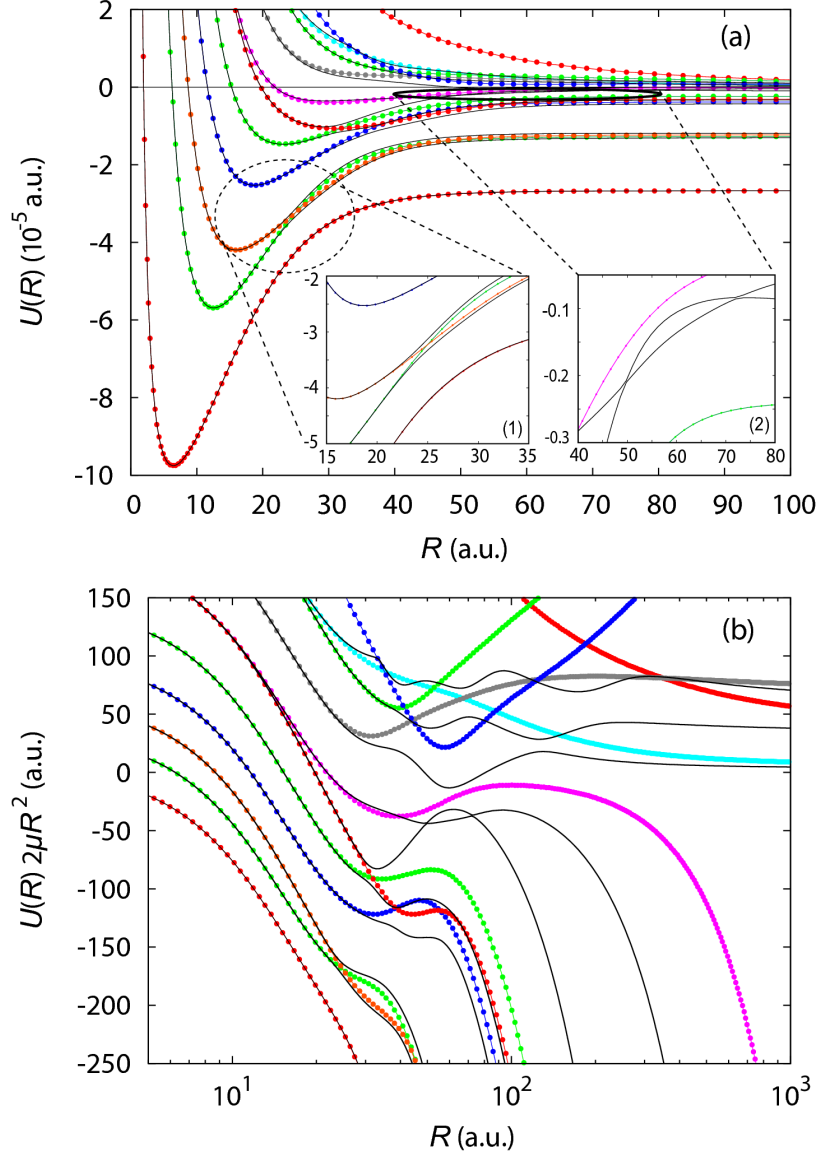


Figure A.6: The shape-diabatic potentials (lines with symbols) and the adiabatic ones (black lines). (a) The potentials at small distances. The inset shows the details in the region where the adiabatic potentials have avoided crossings. (b) The potentials multiplied by $2\mu R^2$ to identify the $1/R^2$ tail region of the continuum channels. Here, $m = 7292.3$ a.u., $r_0 = 15$ a.u. and $D = 4 \times 10^{-5}$ a.u.

pling $\mathcal{W}_{21,12}$ always exhibits smooth behavior. The avoided crossing between the adiabatic channels $n = 6$ and $n = 7$ shows even sharper behavior near $R \approx 50$ a.u. and $R \approx 72$ a.u. as shown in Fig. A.8(b). The couplings for the nearby diabatic potentials $\nu = 4$, $\lambda = 1$ and

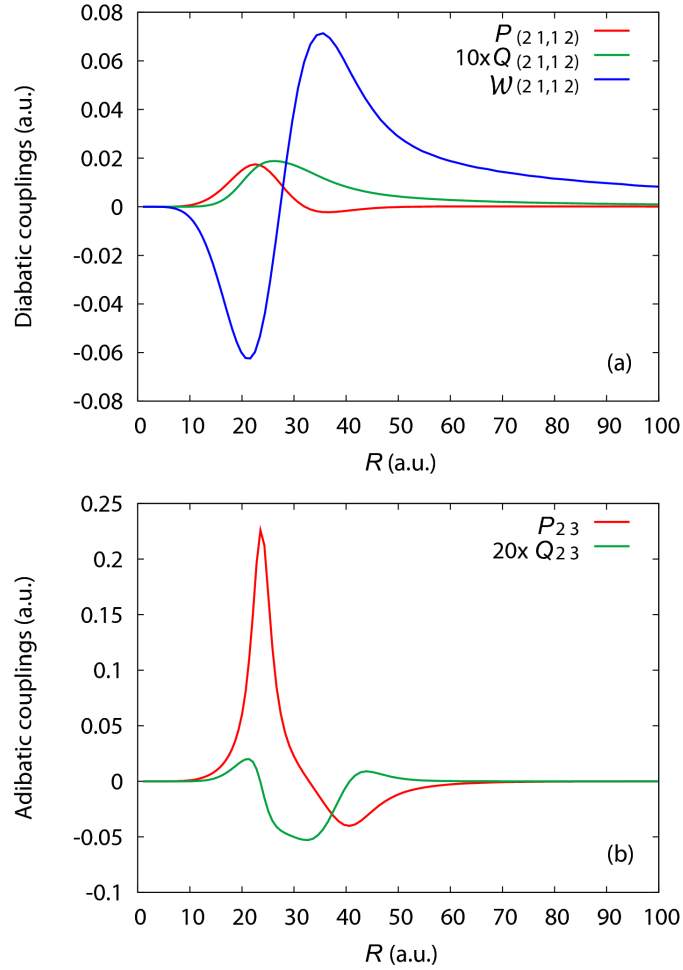


Figure A.7: The couplings in the shape-diabatic representation (a) and adiabatic representation (b) for the channels near the crossing shown in the inset (1) of Figure A.6(a). Note that to show the couplings together, the shape non-adiabatic coupling $Q_{23,12}$ is multiplied by 10 and the non-adiabatic coupling $Q_{2,3}$ is multiplied by 20 to make them comparable to other couplings.

$\nu = 2, \lambda = 2$ still show smooth behavior.

Since the reason that the diabatic potentials trace through the avoided crossings is because they usually carry the information of *nearly* conserved symmetry, we can get more physical insight into the origin of the sharp avoided crossings in the adiabatic potentials by looking at the diabatic channel functions. In Fig. A.9, we show the diabatic channel functions Φ_{21} and Φ_{12} near the crossing point $R \approx 24$ a.u.. For $\Phi_{1,2}$, the two nodal lines in φ direction asymptotically shrink into the region where two particles are close together, forming a *d*-wave

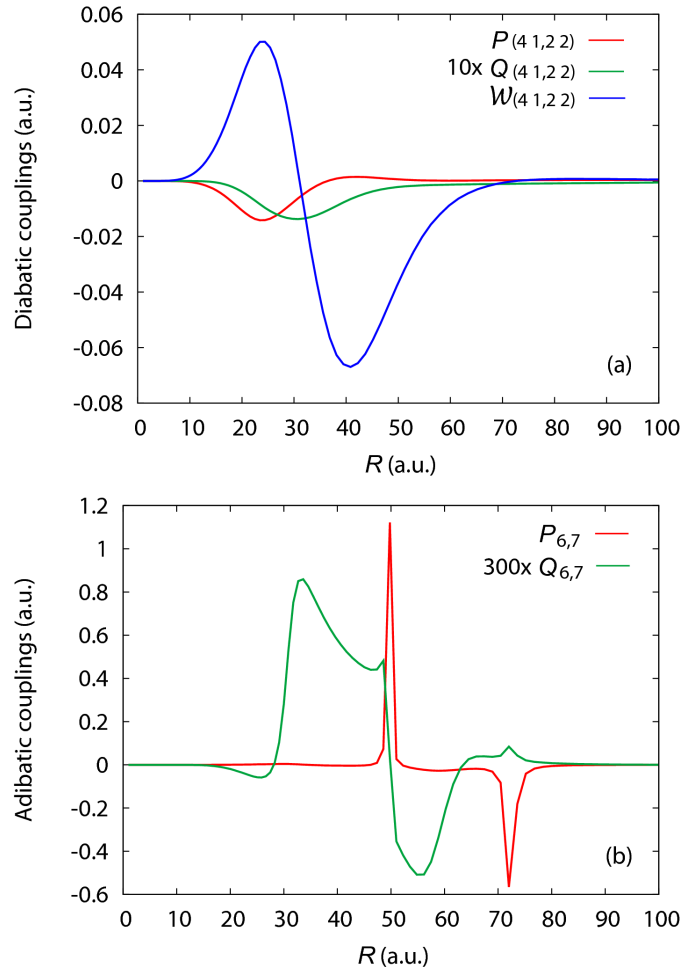


Figure A.8: The diabatic (a) and adiabatic (b) couplings for the channels near the crossing shown in the inset (2) of Fig. A.6(a). Note that the shape non-diabatic coupling $Q_{4,1,2,2}$ is multiplied by 10 and the non-adiabatic coupling $Q_{6,7}$ is multiplied by 300 to make them comparable to other couplings.

like bound channel. The channel wave-function $\Phi_{2,1}$ though, shows an isotropic distribution near the two-body coalescence region. This channel then naturally connects to an s -wave like bound channel asymptotically. Both channel functions have large amplitudes for the linear geometric configurations ($\theta = \pi/2$), but their distinct structures in φ make the transition between the two channels unlikely. Further, $\Phi_{1,2}$ has only negligible amplitude for equilateral and isosceles triangle shapes, making transitions via these configurations unlikely either.

Through this example, we see that in the diabatic representation each channel pertains

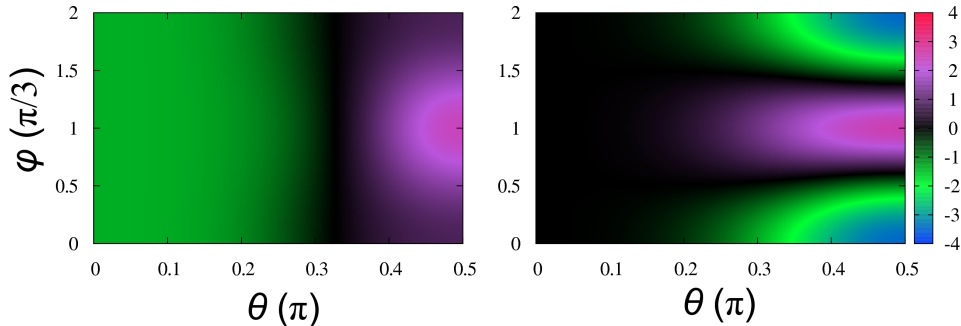


Figure A.9: Diabatic hyperangular wave-functions $\Phi_{2,1}$ (left column) and $\Phi_{1,2}$ (right column) at $R \approx 24$ a.u. where the potentials cross.

the same partial angular momentum characteristic at all hyperradii. This property helps trace out the angular momentum related sharp avoided crossings appearing in the adiabatic potentials diabatically, giving smooth behavior in both potentials and couplings. The corresponding hyperradial channel functions $F_{\nu,\lambda}$ are then expected to be free of drastic changes.

Systems with large two-body scattering length

In three-body systems with large two-body scattering length a , Efimov physics shows up through the long-range behavior of the adiabatic hyperradial potentials [12, 164, 230, 231]. Especially, the weakly-bound channel exhibits attractive $1/R^2$ scaling behavior when $r_0 \ll R \ll a$. We have calculated both adiabatic and diabatic potentials for the three-body system with large a , but with only one s -wave two-body bound state. The depth of the two-body potential D is tuned to give the specific scattering lengths. The diabatic potentials are calculated for $a = 500, 3000$ a.u. and ∞ . As shown in Fig. A.10, unlike the adiabatic potentials, the diabatic potentials do not show attractive $1/R^2$ long-range behavior. The long-range scaling is not observed in the couplings either, showing that the Efimov physics can only be represented as a multi-channel phenomenon in the shape-diabatic representation. This can be expected, though, as the manifestation of the Efimov physics depends crucially on the exact binding energy of the two-body states; yet this information is not shown clearly

as a single-channel property in the shape diabatic representation.

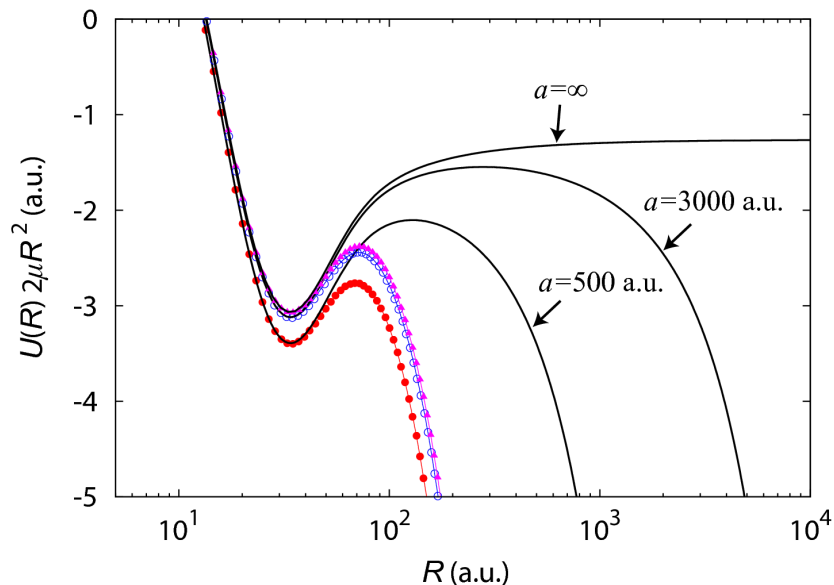


Figure A.10: The shape-diabatic potentials (lines with symbols) and the adiabatic ones (black lines) for $a=500$ a.u. (red balls), $a=3000$ a.u. (blue circles) and $a=\infty$ (purple triangles). The potentials are multiplied by $2\mu R^2$ to show the long-range scaling behavior of the potentials. Here, $m = 7292.3$ a.u., $r_0 = 15$ a.u.

System with strong short-range repulsions

In three-body systems with strong inter-particle short-range repulsions, different geometric configurations usually give a different energy scaling with the hyperradius for small or intermediate distances. The adiabatic potentials are then seen to be composed of families of curves embedded within each other and characterized by distinct geometric configurations, evolving a complicated structure and giving rise to some interesting features like double wells [232–234]. Since it is difficult for a three-body system to change the geometric configurations drastically within a narrow range of distance, the crossings between the potentials belonging to different families will usually give rise to sharp avoided crossings.

In the shape-diabatic representation, since each channel has its own “sense” of the geometric configuration, the diabatic potentials are expected to be more physical than the

adiabatic ones at small and intermediate distances. To study the behavior of the shape-diabatic potentials under such conditions, we use a Morse potential for the inter-particle interaction:

$$V(r_{ij}) = D \left[\left(1 - e^{-3(r_{ij}/r_0 - 1)} \right)^2 - 1 \right]. \quad (\text{A.10})$$

The three-body potentials are shown in Fig. A.11

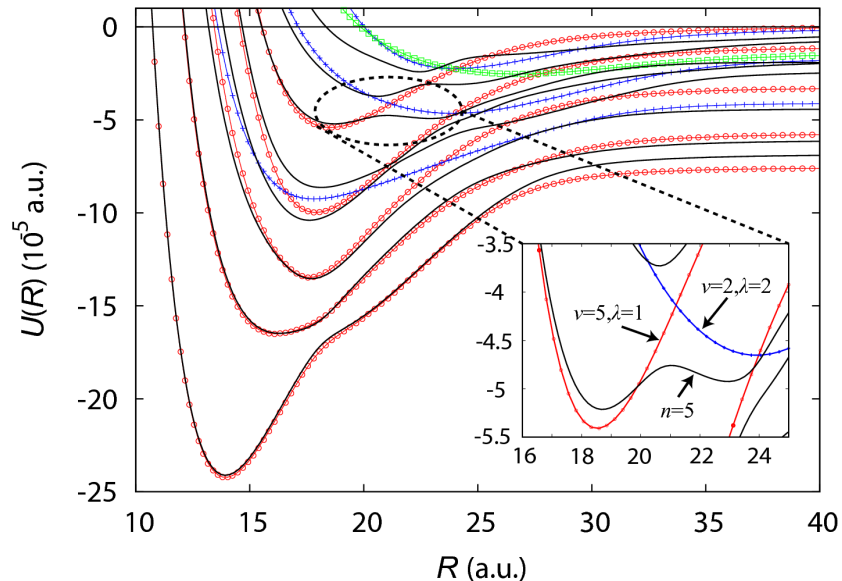


Figure A.11: The lowest few shape-diabatic potentials (lines with symbols) and the adiabatic ones (black lines) for a three-body system interacting with a Morse potential. The family of diabatic curves with $\lambda = 1$ are shown by red balls, the curves with $\lambda = 2$ are shown by blue circles, the curve with $\lambda = 3$ is shown by green triangles. The inset shows the details in one of the double-well region. Here, $m = 7292.3$ a.u., $r_0 = 10$ a.u. and $D = 10^{-4}$ a.u.

We see that the families of diabatic potential curves, labeled by λ , trace out a series of real crossings where the adiabatic potentials have avoided crossings. The origin of the double-well structure in the adiabatic potentials can be understood by the nearby diabatic potentials. As seen in the inset of Fig. A.11, the double-well structure appearing in the $n = 5$ adiabatic channel corresponds to single wells in the $\nu = 5, \lambda = 1$ and $\nu = 2, \lambda = 2$ diabatic channels at $R \approx 18.5$ and 24 a.u., respectively. The corresponding channel functions $\Phi_{5,1}$ and $\Phi_{2,2}$ near the double-well region are shown in Fig. A.12. In both of

the channel functions, the “black hole” centered at the two-body coalescence position ($\theta = \pi/2, \varphi = \pi/3$) comes from the strong inter-particle repulsion. The channel function $\Phi_{2,2}$ has a large amplitude in the two-body potential well around the repulsive region, showing that the geometric configuration of this channel corresponds to two particles close together. Compared with $\Phi_{2,2}$, the channel function $\Phi_{5,1}$ has the most amplitude in the region where all three particles are far apart. Clearly, at small hyperradius where all the particles are within the repulsive interaction region, the configurations of $\Phi_{5,1}$ reduce the repulsion thus give lower energy; at large hyperradius though, two particles close enough to be within the attractive interaction range gives configurations of lower energy. These two sets of geometric configurations generally have different equilibrium distances, leading to double-well structure in the adiabatic potentials.

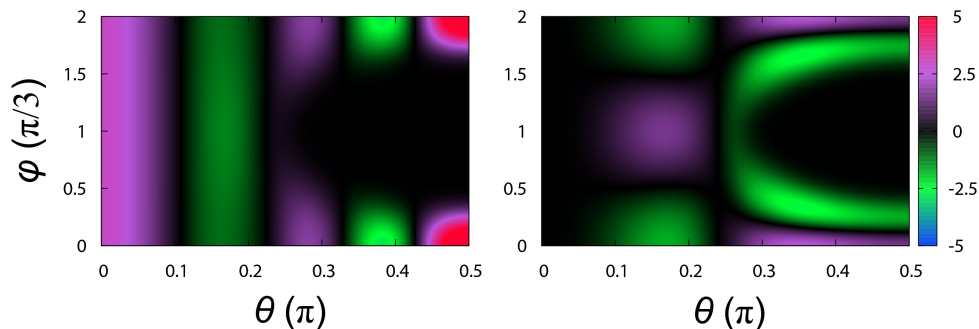


Figure A.12: Diabolic hyperangular wave-functions $\Phi_{5,1}$ (left column) and $\Phi_{2,2}$ (right column) at $R = 21$ a.u.

The couplings in the adiabatic representation, due to the crossings between the families of potentials, show drastic changes in small and intermediate distances. We make a comparison of the couplings between the diabatic and adiabatic representations in Fig. A.13. The couplings in the diabatic representation generally show slowly-varying behavior except in the range of very small hyperradii where the three-body potentials are dominated by the inter-particle repulsions. However, the peaks shown in this region are not expected to cause numerical problems since they are deep inside the classically forbidden region of the potentials.

For the lowest two channels in Fig. A.11, the diabatic and adiabatic potentials match closely up to $R \approx 25$ a.u., and the avoided crossings are seen in both diabatic and adiabatic potentials. But the couplings in the diabatic representation between these two channels behave a little smoother than the couplings in the adiabatic representation, as shown in Fig. A.14.

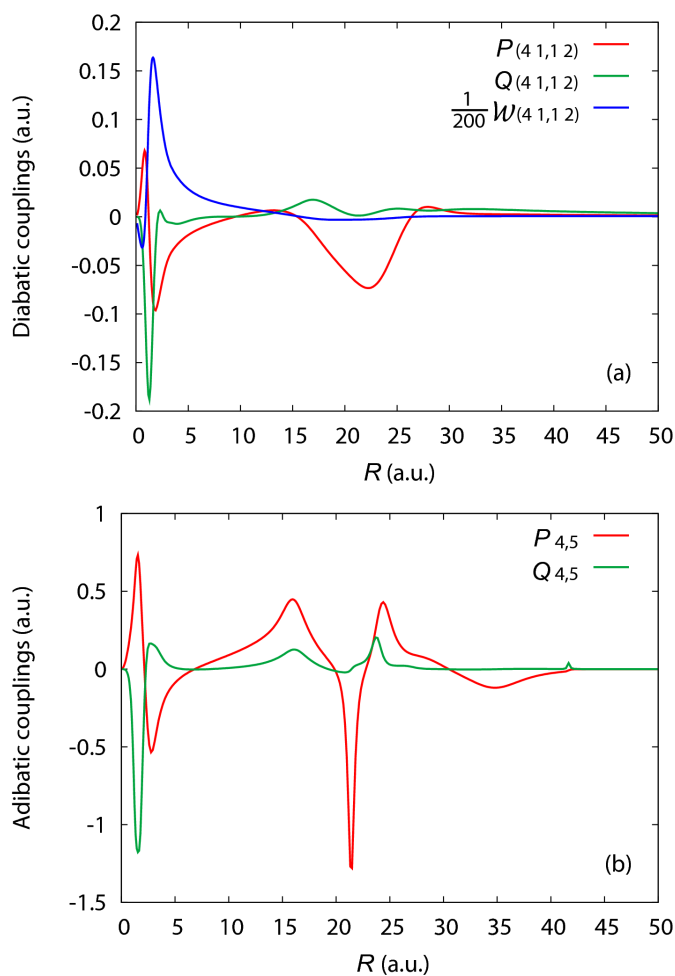


Figure A.13: (a) The couplings in diabatic picture between channels $\nu = 4, \lambda = 1$ and $\nu = 1, \lambda = 2$. Note $W_{41,12}$ has been divided by 200 to make it have similar magnitude as other couplings. (b) Couplings in the adiabatic picture between the channels $n = 4$ and $n = 5$.

The origin of the avoided crossing appearing in the lowest two diabatic channels can be understood by the following arguments. Though generally the geometric configurations in each diabatic channel do not change much for different hyperradius, due to the existence of

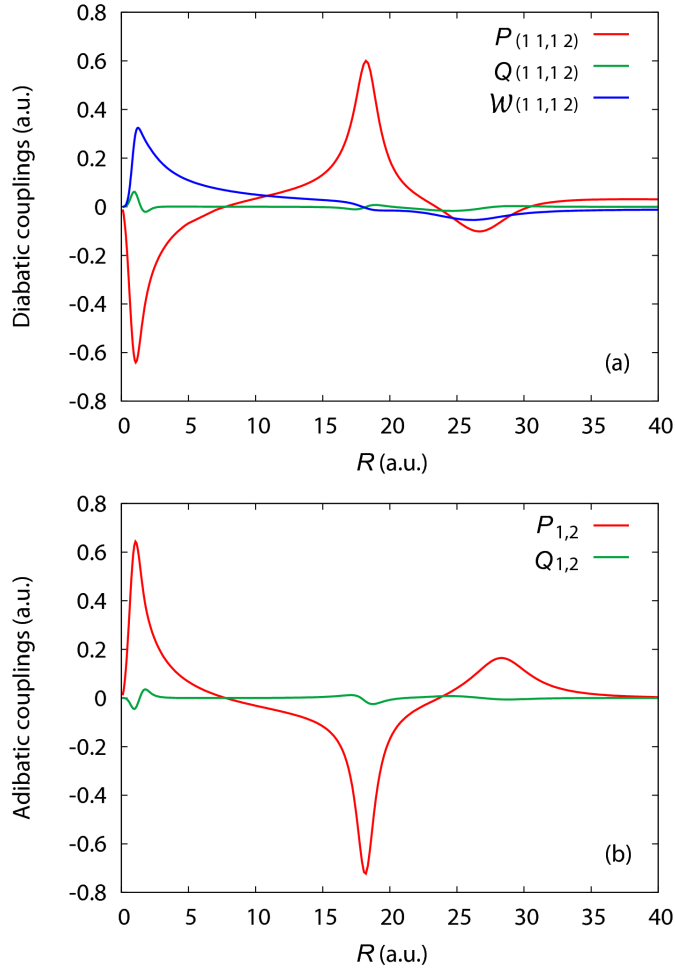


Figure A.14: (a) The couplings in the diabatic picture between channels $\nu = 1, \lambda = 1$ and $\nu = 2, \lambda = 1$. (b) Couplings in the adiabatic picture between the channels $n = 1$ and $n = 2$.

strong short-range inter-particle repulsions the geometric configurations in lowest diabatic channels are forced to change across a small range of hyperradii. We show in Fig. A.15 the diabatic channel function $\Phi_{1,1}$ near the potential minimum ($R \approx 14$ a.u.) and the potential shoulder ($R \approx 20$ a.u.). Near the potential minimum, the geometric configuration of the three particles are dominantly equilateral triangle, while near the potential shoulder the particles change to mainly linear shapes.

The preceding examples show that the shape-diabatic representation is potentially numerically superior to the adiabatic representation in the hyperradial region involving compli-

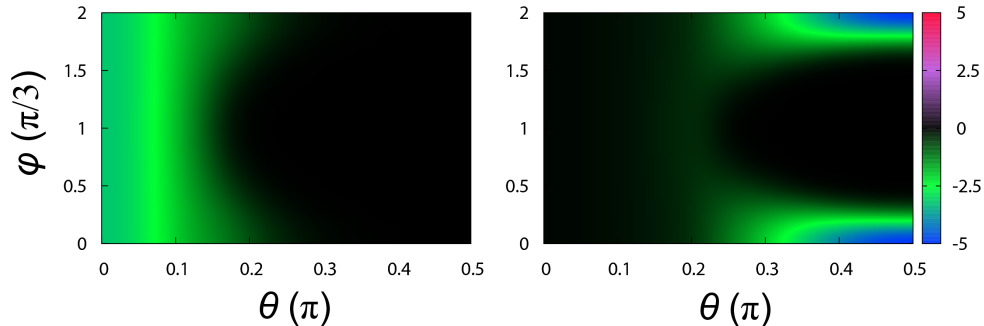


Figure A.15: The diabatic hyperangular wave-functions $\Phi_{1,1}$ at $R = 14$ a.u. (left column) and $R = 20$ a.u. (right column).

cated three-body dynamics. In the asymptotic region though, the adiabatic representation is more advantageous since different channels decouple. Since both representation form complete hyperangular basis, the solutions in the two representations can be transformed into each other without loss of information. A practical scheme for solving the three-body equation then would be combining the two representations in different hyperradial regions. The solutions at the boundary can then be matched by unitary transformation between the two representations.

A.2.2 Two identical particles

In the three-body systems where not all the particles are identical, the loss of complete exchange symmetry introduces complications: different affinities between the particle pairs can lead to drastic change in their geometric configurations. The behavior of the solutions to Eq. A.2 is expected to have drastic changes, making the diabatic basis also suffer from the difficulty of the sharp avoided crossings.

We demonstrate this effect by a system of two identical bosonic particles and one distinguishable particle. The inter-particle interactions are of the form of Eq. A.9, with different parameters for distinct pairs. For some range of hyperradii, sharp avoided crossings show up in the θ -potentials $u_\lambda(R, \theta)$ from Eq. A.2, upon which the diabatic hyperradial potentials and couplings are calculated. As shown in Fig. A.16, the avoided crossings appearing in

the low-lying θ -potentials are extremely sharp. The corresponding diabatic hyperangular channels function is shown in Fig. A.17(a). The abrupt change in the potentials and wave-functions, on the other hand, provides convenience for simple diabaticization. This can be simply achieved by reordering the channel index λ at the boundary of the sharp avoided crossings. The hyperangular channel function after diabaticization is shown in Fig. A.17(b), where we can see that the diabaticized wave-function behave smoothly. The resulting diabatic potentials and couplings are again free of sharp-varying structures.

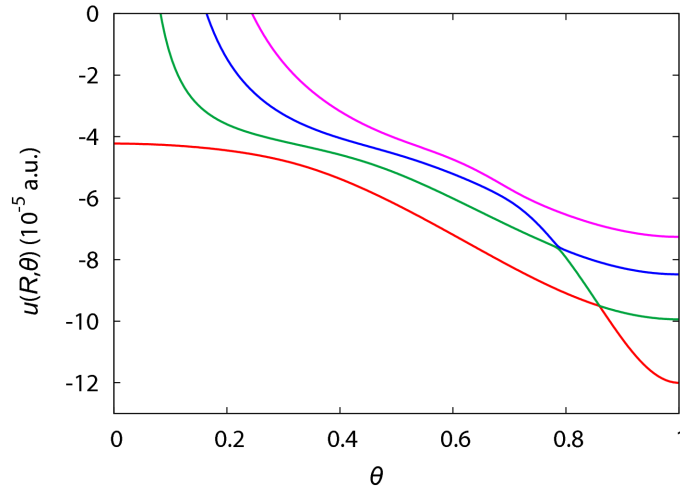


Figure A.16: The “ θ -potentials” $u_\lambda(R, \theta)$ at $R = 40$ a.u.. Here we take $D = 10^{-4}$ a.u., $r_0 = 10$ a.u. for identical pair, and $r_0 = 20$ a.u. for distinguishable pairs.

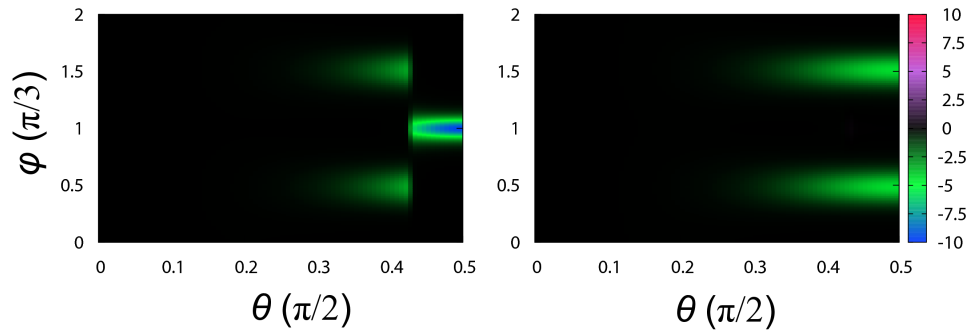


Figure A.17: The diabatic hyperangular channel function $\Phi_{1,1}$ at $R = 40$ a.u.. (a) The channel function without diabaticizing $u_\lambda(R, \theta)$ in θ . (b) The channel function after diabaticization.

A.2.3 Calculating adiabatic potentials

In the shape-diabatic representation, the 2-D equation in θ and φ is solved consecutively as 1-D equations. This dramatically increases the computational efficiency and reduces the consumption of the computational resources. The diabatic representation can then be adapted to calculating the three-body adiabatic potentials and couplings. One way for applying this idea is to calculate the adiabatic Hamiltonian matrix in the diabatic representation; the adiabatic potentials and hyperangular wave-functions can then be obtained by diagonalizing the matrix. An equivalent way is to expand the adiabatic wave-functions in the φ -basis ϕ_λ obtained from Eq. A.2:

$$\Phi_{\text{ad},n} = \sum_{\lambda} \vartheta_{n,\lambda}(R; \theta) \phi_{\lambda}(\varphi). \quad (\text{A.11})$$

The adiabatic equation then reduces to a set of coupled 1-D equations:

$$\left[-\frac{2}{\mu} \frac{\partial^2}{\partial \theta^2} + u(\theta)_{\nu,\lambda} \right] \vartheta_{n,\lambda}(R; \theta) - \frac{2}{\mu} \sum_{n',\lambda'} \left[\mathcal{Q}_{\lambda,\lambda'}(\theta) + 2(\mathcal{P}_{\lambda,\lambda'}(\theta) + \cot 2\theta) \frac{d}{d\theta} \right] \vartheta_{n',\lambda'}(R; \theta) = U_n(R) \vartheta_{n,\lambda}(\theta) \quad (\text{A.12})$$

In the following, we apply the two different methods to the three-body system in Sec. A.2.1 as example to calculate the adiabatic potentials. We first calculate the potentials by solving Eq. A.12 and compare them with the results calculated by solving the full 2-D equations. We use fifth order B-spline as spatial basis in all the calculations. The memory usage for 1-D calculations scales as $(N_{\theta} + N_{\varphi})N_c$, where N_{θ} , N_{φ} are the number of spline functions in θ and φ directions and N_c is the number of φ -channels. For 2-D calculations though, with our banded storage scheme, the memory usage grows as $N_{\theta}^2 N_{\varphi}$. In Table A.1, we show the comparison of lowest three adiabatic potentials at $R = 10$ a.u.. In solving the consecutive 1-D equations and 2-D calculation, we both use 10 B-spline functions in the φ and θ directions. For the 1-D calculations the lowest two φ -channels are included in the expansion A.11, giving 12 digits convergence for the lowest, 13 digits for the second and 10 digits for the third adiabatic potential energy. While in the 2-D calculation the potential

	1-D	2-D
U_1 (10^{-6} a.u.)	-6.90021495060(7)	-6.90021495060(8)
U_2 (10^{-5} a.u.)	3.108177885162	3.108177885162
U_3 (10^{-5} a.u.)	6.425280473(911)	6.425280473(253)

Table A.1: The lowest three adiabatic potential energies calculated at $R = 10$ a.u. by Eq. A.12 and by solving the full 2-D equation directly.

	1-D	2-D
U_1 (10^{-6} a.u.)	-1.122833546613	-1.12283354661(2)
U_2 (10^{-8} a.u.)	6.235902031(769)	6.23590203(2121)
U_3 (10^{-7} a.u.)	4.5162647094(78)	4.5162647094(10)

Table A.2: The lowest three adiabatic potential energies calculated at $R = 100$ a.u. by Eq. A.12 and by solving the full 2-D equation directly.

energies are converged to 12 digits, 13 digits and 10 digits, respectively. We performed the calculations on a single core of a 2.4GHz Intel Core2 cpu. The cpu time and memory usage for the 1-D calculation are 5.3×10^{-2} s and 1.3 MB, respectively. For the 2-D calculation though, the calculation takes 2×10^{-2} s of cpu time and 1.9 MB of memory. In this case, solving the 1-D equations does not show obvious advantages over solving the 2-D equation.

However, the resource usage changes quite a lot at larger hyperradii. We show the adiabatic potentials energies calculated at $R = 100$ a.u. in Table A.2. For the 1-D calculation, 100 spline functions are used in φ direction and 50 spline functions are used in θ direction. The lowest 20 φ -channels are included, giving 13 digits convergence for the lowest, 10 digits for the second and 11 digits for the third adiabatic potential energy. While in the 2-D calculation, 40 B-spline functions are used in θ and 30 spline functions are used in φ directions. The potential energies are converged to 12 digits, 9 digits and 11 digits, respectively. The cpu time and memory usage for the 1-D calculation are 6.8 s and 4.7 MB. The 2-D calculation though, takes 0.6 s and 14 MB. Finally, we list the potential energies calculated at $R = 500$ a.u. in Table A.3. For 1-D, we use 250 spline functions in both θ and φ directions with 50 φ channels included to get 11, 9 and 10 digits convergence. For

	1-D	2-D
U_1 (10^{-6} a.u.)	-1.1107884746(30)	-1.1107884746(45)
U_2 (10^{-9} a.u.)	1.92049209(5984)	1.92049209(3543)
U_3 (10^{-8} a.u.)	1.738091016(859)	1.738091016(214)

Table A.3: The lowest three adiabatic potential energies calculated at $R = 500$ a.u. by Eq. A.12 and by solving the full 2-D equation directly.

the 2-D calculation, 100 spline functions are used in both θ and φ directions. The potential energies are converged to 11 digits, 9 digits and 10 digits, respectively. The cpu time and memory usage for the 1-D calculation are 412 s and 102 MB. The 2-D calculation though, takes 117 s and 215 MB.

Generally, it is more difficult to obtain converged potentials at larger hyperradius. For 2-D calculations, more spline functions are required, while for 1-D calculations, both the number of spline functions and φ channels need to be increased. From the above comparisons, we see that it takes more cpu time but less memory to calculate the adiabatic potentials by solving the 1-D equations.

A.3 Summary

The sharp avoided crossings appearing in the adiabatic curves are an awkward problem to handle: the sharp crossings imply the existence of *nearly* exact symmetry which can be used to simplify the problem, but the loss of that symmetry information in adiabatic representation makes solving the problem much harder. Though a diabatic representation can generally by-pass the problem of sharp avoided crossings, it is unfortunately hard to find a general-purposed representation that can be migrated from one system to another. Further, if the diabatic channels do not build-in enough physical information from the system, other numerical difficulties may occur instead.

In this paper, we have presented a method for generating a diabatic representation for any three-body systems. Because the information of the particles' geometric configurations is

“built-in”, the potential curves in the shape-diabatic representation cross smoothly through the sharp avoided crossings observed in the adiabatic representation. In the asymptotic region though, the diabatic channels do not de-couple completely, making the representation less suitable to describe the asymptotic behavior of the particles. This also make it hard to represent the Efimov physics in the case of large two-body scattering length. But, by applying the shape-diabatic representation and adiabatic representation separately in the region of small and intermediate hyperradii and in the asymptotic region, the three-body systems with complicated short-range dynamics can be solved with much less numerical difficulty.

Computationally, the diabatic basis can be generated very efficiently since it is calculated from two consecutive 1-D equations. We also apply the idea of reducing the 2-D adiabatic equation into coupled 1-D equations for calculating adiabatic potentials. The convergence tests show that the 1-D calculations take less memory, but more cpu time.

Appendix B

Single-channel approach for deriving three-body inelastic rates

For the three-body recombination and relaxation processes we are working on, the inelastic transitions take place predominantly when the hyperradius is comparable with size of final two-body bound state. For the cases where the final state is deeply bound, the size of the three-body system needs to go down to the short-range distances to make the transition. Near a Feshbach resonance the adiabatic hyperspherical potential for the initial channel—either the lowest continuum channel for recombination at $a < 0$ or the weakly-bound atom-dimer channel at $a > 0$ for relaxation—has long-range scaling with the increasing size of $|a|$. The short-range behavior, for both the potentials and the couplings, has negligible change because of the tiny changes in the interactions. For low scattering energies $k \ll 1/r_0$, the de-Broglie wave length in the initial channel is much larger than the size of the short-range distance, the scaling of the inelastic rates is then determined by the amplitude of the wavefunction in the initial channel. These three-body inelastic processes reduce to essentially single-channel problems.

B.1 Zero-energy recombination ($a < 0$) and relaxation ($a > 0$) for large effective-range

The three-body recombination and relaxation rates for small effective-range $|r_{\text{eff}}|$ are given in Eqs. (1.6) and (1.7). These expressions have been derived by using different methods in the literature [52], here we derive the expressions for these rates for large $|r_{\text{eff}}|$. First we work on identical bosons. In Fig. 3.5, we show the schematic scaling of the adiabatic hyperspherical potentials for both $a > 0$ and $a < 0$. The only difference for the two cases is the asymptotic behavior in the potentials. This difference can be simply characterized by assigning effect angular momentum l for each of the asymptotic potential. In particular, $l = 0$ for relaxation and $l = 3/2$ for recombination. We use a model which connects directly different regions of the potentials, as the following:

$$W_0(R) = \begin{cases} W_0(r_0) & R = r_0, \\ 0 & r_0 < R < \alpha|r_{\text{eff}}|, \\ -\frac{s_0^2 + 1/4}{2\mu_3 R^2} & \alpha|r_{\text{eff}}| < R < \beta|a|, \\ E_{th} + \frac{l(l+1)}{2\mu_3 R^2} & R > \beta|a| \end{cases}, \quad (\text{B.1})$$

where the threshold energy for the initial channel E_{th} is zero for recombination and $-1/2\mu_2 a^2$ for relaxation. The parameters α and β , as mentioned in Sec. 3.1.2, are used to adjust the boundaries of the hyperradial regions. The behavior of the potential for the final channel is not shown since it does not scale with a . By neglecting the couplings between the initial and the final channel for $R > r_0$, the hyperradial wavefunction in the initial channel near zero scattering energy can be written down by sectors:

$$F_0 R = \begin{cases} C_1 \sin[kR + \delta_s(k)] & r_0 \ll R \ll \alpha|r_{\text{eff}}|, \\ C_2 R^{1/2} \{J_{is_0}(kR) + \tan[\delta_2(k)]N_{is_0}(kR)\} & \alpha|r_{\text{eff}}| \ll R \ll \beta|a|, \\ C_3 R^{1/2} \{J_{l+1/2}(kR) + \tan[\delta(k)]N_{l+1/2}(kR)\} & R \gg \beta|a|, \end{cases} \quad (\text{B.2})$$

For $k \rightarrow 0$ and $|a| \gg |r_{\text{eff}}|$ the short-range phase shift δ_s can be taken as

$$\delta_s(k) = -Ak, \quad (\text{B.3})$$

where A is the short-range scattering length. Due to the inelastic transitions at $R \leq r_0$, A acquires an imaginary part which determines the strength of the transition. By matching the hyperradial wavefunction $F_0(R)$ at $\alpha|r_{\text{eff}}|$ and $\beta|a|$, the asymptotic phase shift δ can be expressed in terms of $\alpha|r_{\text{eff}}|$, $\beta|a|$ and A . The probability for elastic scattering \mathcal{R} is the reflection coefficient:

$$\mathcal{R} = \left| \frac{1 + i \tan \delta}{1 - i \tan \delta} \right|^2. \quad (\text{B.4})$$

The probability for inelastic transition is then determined as

$$1 - \mathcal{R} = \frac{2\pi}{\Gamma(l + \frac{3}{2})\Gamma(l + \frac{1}{2})} \left(\frac{k\beta|a|}{2} \right)^{2l+1} \frac{\sin 2\varphi_0 \sinh 2\eta}{\sinh^2 \eta + \sin^2 [s_0 \ln(|a/r_{\text{eff}}|) + \Phi + \varphi]}, \quad (\text{B.5})$$

where the parameters Φ , η , φ and the constant phase φ_0 are defined through Eq. (3.6)-(3.8). The recombination rate K_3 and the relaxation rate V_{rel} are expressed by the inelastic transition probability through

$$K_3 = \frac{192\pi^2}{\mu_3 k^2} (1 - \mathcal{R}), \quad (\text{B.6})$$

$$V_{\text{rel}} = \pi(1 - \mathcal{R})/\mu k. \quad (\text{B.7})$$

For mixed-spin fermionic system FFF' , we are interested in the three-body relaxation process $(FF')^* + F \rightarrow FF' + F$, where $(FF')^*$ is a weakly-bound Feshbach molecule and FF' is a deeply-bound molecule. The adiabatic hyperspherical potential for this system is different from the potential for bosons only in the region $\alpha|r_{\text{eff}}| \ll R \ll \beta|a|$, as

$$W_0(R) = \frac{p_0^2 - 1/4}{2\mu_3 R^2}, \quad (\text{B.8})$$

where p_0 is determined by Eq. (3.11). The corresponding hyperradial wavefunction is thus changed to

$$F_0 = C_2 R^{1/2} \{ J_{p_0}(kR) + \tan[\delta_2(k)] N_{p_0}(kR) \} \quad \alpha|r_{\text{eff}}| \ll R \ll \beta|a|. \quad (\text{B.9})$$

Following exactly the same analysis for identical bosons, we get the relaxation rate for FFF' system Eq. (3.12).

B.2 Recombination at finite energies ($a < 0$)

Following essentially the same streamline in the previous section, we can derive the three-body recombination rate K_3 at finite energies for both small and large $|r_{\text{eff}}|$. For simplicity we first derive K_3 for small $|r_{\text{eff}}|$, the expression for large $|r_{\text{eff}}|$ can be obtained by extending the analysis for small $|r_{\text{eff}}|$. We model the adiabatic hyperspherical potential as the following:

$$W_0(R) = \begin{cases} -\frac{s_0^2 + 1/4}{2\mu_3 R^2} & r_0 < R < \beta|a|, \\ \frac{15/4}{2\mu_3 R^2} & R > \beta|a|. \end{cases}, \quad (\text{B.10})$$

With the solutions Eq. (B.2) in these regions, we obtain

$$\mathcal{R} = - \left\{ \frac{H_2^{(2)'}(k\beta|a|)[J_{is_0}(k\beta|a|) + \tan \delta_2(k)N_{is_0}(k\beta|a|)]}{H_2^{(2)}(k\beta|a|)[J'_{is_0}(k\beta|a|) + \tan \delta_2(k)N'_{is_0}(k\beta|a|)]} - 1 \right\} / \left\{ \frac{H_2^{(1)'}(k\beta|a|)[J_{is_0}(k\beta|a|) + \tan \delta_2(k)N_{is_0}(k\beta|a|)]}{H_2^{(1)}(k\beta|a|)[J'_{is_0}(k\beta|a|) + \tan \delta_2(k)N'_{is_0}(k\beta|a|)]} - 1 \right\}, \quad (\text{B.11})$$

where $H_l^{(1)}(x)$ and $H_l^{(2)}(x)$ are the first and second kind of Hankel's function of order l , respectively. The derivatives are taken on the whole argument. When the scattering energy satisfies $k \ll 1/r_0$, $\tan \delta_2(k)$ is independent of k

$$\tan \delta_2(k) \approx \frac{\cosh(\frac{\pi}{2}s_0) \tan \Phi - i \sinh(\frac{\pi}{2}s_0)}{i \sinh(\frac{\pi}{2}s_0) \tan \Phi + \cosh(\frac{\pi}{2}s_0)}, \quad (\text{B.12})$$

where Φ is the short-range phase. For energies such that $k \gg 1/|a|$, the recombination probability simplifies to Eq. (3.32) which shows log-periodic oscillations.

Near narrow Feshbach resonances where $|r_{\text{eff}}|$ is large, the adiabatic hyperspherical potential behave as in Eq. (B.1) and the the hyperradial wavefunction is given in Eq. (B.2). By matching the wavefunction at $R = \alpha|r_{\text{eff}}|$, the recombination probability in the energy range $1/|a| \ll k \ll 1/|r_{\text{eff}}|$ takes the same form as in Eq. (3.32), with the parameters Φ and η written in terms of r_{eff} and the short-range scattering length A as in Eq. (3.35). For energies $kk \gg 1/|r_{\text{eff}}|$, Eq. (B.11) reduces to

$$\mathcal{R} = 1 - 4k|\text{Im}A|. \quad (\text{B.13})$$

Appendix C

A multi-channel approach for deriving three-body inelastic rates

C.1 General formalism

Following the idea for solving the three-body hyperradial equation separately in each region, we formulate a rigorous multi-channel approach for solving Eq. (2.40) and extracting the scattering matrix. For simplicity we restrict our discussion to the case for small $|r_{\text{eff}}|$, the generalization for large $|r_{\text{eff}}|$ can be obtained by following the same streamline. Since a multi-channel description is necessary for three-body recombination when $a > 0$, we will formulate our method explicitly for this process. This method, however, can be applied to other processes with only minor modifications. Based on the physical insight obtained in Sec. 3.2.1 that the inelastic transitions occur predominantly near $R \approx a$, we divide the hyperradial regions as the following and we assume the couplings are non-zero only near $R \approx a$.

1. Short-range region ($R \leq r_0$). The solutions F_ν in this region is non-universal, so we parametrize the short-range solutions by a $N \times N$ R -matrix \mathbf{R}_s at $R = r_0$, where N is the number of the adiabatic channels under consideration.
2. Efimov region ($r_0 \leq R \leq \beta_1 a$). The coefficients β_1 reflects the uncertainty in determining the right boundary. The universal adiabatic potentials for $J = 0^+$ behave like

the following :

$$W_\nu = \begin{cases} -\frac{s_0^2 + 1/4}{2\mu_3 R^2}, \\ \frac{s_\nu^2 - 1/4}{2\mu_3 R^2} \quad (\nu > 0), \end{cases} \quad (\text{C.1})$$

where s_0 is determined by Eq. (2.73) and s_ν is determined by the same equation by replacing s_0 with is_ν . By neglecting the couplings in this region, we write the solutions in this region by a $N \times N$ matrix:

$$F_{\nu,\nu'}(R) = u_{\nu,\nu'} = (\boldsymbol{\chi} + \boldsymbol{\xi} \mathbf{K}_s)_{\nu,\nu'}. \quad (\text{C.2})$$

where the regular and irregular solution matrices are

$$\chi_{\nu,\nu'} = \delta_{\nu,\nu'} \chi_\nu(R), \quad (\text{C.3})$$

$$\xi_{\nu,\nu'} = \delta_{\nu,\nu'} \xi_\nu(R). \quad (\text{C.4})$$

For the Efimov channel where the potential is attractive, we take the sin-like and cos-like solutions as

$$\chi_\nu = \sqrt{\frac{\pi}{2}} R^{1/2} \left[\cosh\left(\frac{\pi}{2} s_0\right) J_{is_0}(kR) - i \sinh\left(\frac{\pi}{2} s_0\right) N_{is_0}(kR) \right], \quad (\text{C.5})$$

$$\xi_\nu = \sqrt{\frac{\pi}{2}} R^{1/2} \left[\cosh\left(\frac{\pi}{2} s_0\right) J_{is_0}(kR) - i \sinh\left(\frac{\pi}{2} s_0\right) N_{is_0}(kR) \right], \quad (\text{C.6})$$

The short-range reactance matrix \mathbf{K}_s is related to the R -matrix \mathbf{R}_s by

$$\mathbf{K}_s = (\mathbf{R}_s^{-1} \boldsymbol{\xi} - \boldsymbol{\xi}')^{-1} (\mathbf{R}_s^{-1} \boldsymbol{\chi} - \boldsymbol{\chi}'), \quad (\text{C.7})$$

where the derivative is taken respect to R .

3. Transitional region ($\beta_1 a \leq R \leq \beta_2 a$). The coefficients β_2 reflects the uncertainty in determining the right boundary. The adiabatic potentials in this region are also universal, but they cannot be written down in an analytical form. Without matching to solutions in other regions, there are $2N$ independent solutions in this region. For the convenience of the derivation, we split the $2N$ solutions into two arbitrary solution

matrices: \mathbf{M}_1 and \mathbf{M}_2 . The N physical solutions $F_{\nu,\nu'}$ are then written as the linear combinations of the $2N$ solutions:

$$F_{\nu,\nu'}(R) = (\mathbf{M}_1 \mathbf{B}_1 + \mathbf{M}_2 \mathbf{B}_2)_{\nu,\nu'}. \quad (\text{C.8})$$

The combination matrices B_1 and B_2 will finally be eliminated by matching the solutions for all regions.

4. Asymptotic region ($R > \beta_2 a$). The adiabatic channels decouple and the behaviors of the potentials for the continuum channels and the bound channels are given by Eq. (2.69) and (2.70), respectively. We directly write the solutions in a $N \times N$ matrix form:

$$F_{\nu,\nu'}(R) = (\mathbf{f} + \mathbf{g}\mathbf{K})_{\nu,\nu'}, \quad (\text{C.9})$$

where

$$f_{\nu,\nu'} = \delta_{\nu,\nu'} f_{\nu}(R), \quad g_{\nu,\nu'} = \delta_{\nu,\nu'} g_{\nu}(R), \quad (\text{C.10})$$

and \mathbf{K} is the reactance matrix, f_{ν} and g_{ν} are the energy normalized regular and irregular solutions:

$$f_{\nu}(R) = \sqrt{\frac{\pi}{2}} R^{1/2} J_{\ell_{\text{eff}}+1/2}(k_{\nu}R), \quad g_{\nu}(R) = \sqrt{\frac{\pi}{2}} R^{1/2} N_{\ell_{\text{eff}}+1/2}(k_{\nu}R), \quad (\text{C.11})$$

where the effective angular momentum $\ell_{\text{eff}} = \lambda + 3/2$ for the continuum channels and $\ell_{\text{eff}} = l + 1/2$ for the bound channels.

By matching the solution matrices and their derivatives at $\beta_1 a$ and $\beta_2 a$, we obtain the reactance matrix K in the asymptotic region:

$$\mathbf{K} = - \left\{ \left[\mathbf{u}\mathbf{u}'^{-1}(\mathbf{M}'_1)_L - (\mathbf{M}_1)_L \right] (\mathbf{M}_1^{-1})_R \mathbf{g} + \left[\mathbf{u}\mathbf{u}'^{-1}\mathbf{C} - \mathbf{D} \right] [\mathbf{g}' - (\mathbf{M}'_1)_R (\mathbf{M}_1^{-1})_R \mathbf{g}] \right\}^{-1} \left\{ \left[\mathbf{u}\mathbf{u}'^{-1}(\mathbf{M}'_1)_L - (\mathbf{M}_1)_L \right] (\mathbf{M}_1^{-1})_R \mathbf{f} + \left[\mathbf{u}\mathbf{u}'^{-1}\mathbf{C} - \mathbf{D} \right] [\mathbf{f}' - (\mathbf{M}'_1)_R (\mathbf{M}_1^{-1})_R \mathbf{f}] \right\}, \quad (\text{C.12})$$

where

$$\mathbf{C} = [(\mathbf{M}'_2)_L(\mathbf{M}_2^{-1})_R - (\mathbf{M}'_1)_L(\mathbf{M}_1^{-1})_R] [(\mathbf{M}'_2)_R(\mathbf{M}_2^{-1})_R - (\mathbf{M}'_1)_R(\mathbf{M}_1^{-1})_R]^{-1}, \quad (\text{C.13})$$

$$\mathbf{D} = [(\mathbf{M}_2)_L(\mathbf{M}_2^{-1})_R - (\mathbf{M}_1)_L(\mathbf{M}_1^{-1})_R] [(\mathbf{M}'_2)_R(\mathbf{M}_2^{-1})_R - (\mathbf{M}'_1)_R(\mathbf{M}_1^{-1})_R]^{-1}. \quad (\text{C.14})$$

In the above expressions, the subscript “ L ” and “ R ” indicate that the value or the derivative of a matrix is taken at $R = \beta_1 a$ or $\beta_2 a$, respectively. The value or derivative of the \mathbf{u} related matrices are evaluated at $R = \beta_1 a$, those of the \mathbf{f} or \mathbf{g} related matrices are evaluated at $R = \beta_2 a$.

The three-body recombination rate K_3 can finally be calculated after obtaining the reactance matrix \mathbf{K} . In particular, K_3 can be calculated by using Eq. (2.67), where the scattering matrix \mathbf{S} is connected with \mathbf{K} by:

$$\mathbf{S} = (\mathbb{1} + i\mathbf{K})(\mathbb{1} - i\mathbf{K})^{-1}, \quad (\text{C.15})$$

where $\mathbb{1}$ is the unit matrix.

C.2 An analytical model

With the general formalism set up in the previous section for studying the Efimov physics, we can study the scaling of K_3 at finite energies without numerically solving the three-body Schrödinger equation. To implement this method, we want to find a simple model which can facilitate the derivation or calculation but still have all necessary Efimov physics built in. Within our formalism, the solutions in the Efimov region and the asymptotic region are already known, the rest input will be from the short-range region and the transitional region.

For the short-range region, the potentials and couplings are non-universal which leaves a lot of freedom for parametrization. For instance, transitions to deeply-bound channels, which has been parametrized through the η parameter in Eq. (1.5), can be build in the matrix \mathbf{R}_s or \mathbf{K}_s in our formalism. For the purpose of studying universal behavior, however, we

assume there is no deeply-bound channels. Further, for the energy range we are interested in ($k \ll 1/r_0$), the continuum channels are all classically forbidden so that the inelastic transitions between the Efimov channel and the continuum channels are negligible. Without losing generality, we construct the following \mathbf{K}_s matrix:

$$(K)_{0,0} = -\tanh\left(\frac{\pi}{2}s_0\right) \tan\left[\Phi + \gamma - s_0 \ln\left(\frac{kr_0}{2}\right)\right], \quad (\text{C.16})$$

$$(K)_{\nu,\nu'} = 0 \quad \text{all other } \nu, \nu'. \quad (\text{C.17})$$

With this construction, the short-range scattering involving any the continuum channels is forbidden. More importantly, the wavefunction in the Efimov channel at $R = r_0$ is set by the convention of the short-range phase Φ used in the previous studies. The constant γ is defined in Eq. (3.30).

We next model the potentials and the couplings in the transitional region. From our numerical calculations we have learned that the non-adiabatic couplings $P_{\nu,\nu'}$ peak near $R \approx a$, with peak values scale like $1/a$. The non-adiabatic couplings $Q_{\nu,\nu'}$ which have the similar structure with peak values scale like $1/a^2$, which are negligible when $a \gg r_0$. We thus model the non-adiabatic couplings $P_{\nu,\nu'}$ by step functions which are non-zero only in the transitional region with constant values $c_{\nu,\nu'}/a$. The constants $c_{\nu,\nu'}$ are universal and their values can be obtained from the numerical calculations. We also set the adiabatic potentials in this region to be constants with values $w_\nu^2/2\mu_3a^2$, which between the values of the potentials in the adjacent regions. The coupled hyperradial equations take the following form:

$$-F_\nu'' = k_\nu^2 F_\nu + \sum_{\nu' \neq \nu} k_{\nu,\nu'} F_{\nu'} \quad \nu = 0, 1, \dots, N-1, \quad (\text{C.18})$$

where

$$\begin{aligned} k_{\nu,nu}^2 &= 2\mu_2 E - w_\nu^2, \\ k_{\nu,\nu'} &= 2c_{\nu,\nu'}/a \quad \nu \neq \nu'. \end{aligned} \quad (\text{C.19})$$

ν'	$c_{0,\nu'}$	$c_{1,\nu'}$	$c_{2,\nu'}$	$c_{3,\nu'}$	$c_{4,\nu'}$
0	0	-0.17	-0.041	-0.035	-0.025
1	0.17	0	-0.068	-0.030	-0.022
2	0.041	0.068	0	-0.030	-0.019
3	0.035	0.030	0.030	0	-0.047
4	0.025	0.022	0.019	0.047	0

Table C.1: Universal coefficients $c_{\nu,\nu'}$ for non-adiabatic couplings $P_{\nu,\nu'}$ ($J = 0^+$).

Eq. (C.18) can be solved by transforming into a set of coupled first order differential equations by defining $F_{N+\nu} = F'_\nu$:

$$\begin{cases} -F'_{N+\nu} &= k_\nu^2 F_\nu + \sum_{\nu' \neq \nu} k_{\nu,\nu'} F_{N+\nu'} & \nu = 0, 1, \dots, N-1, \\ F'_\nu &= F_{N+\nu} & \nu = 0, 1, \dots, N-1. \end{cases}$$

Writing the coupled equations in a matrix form $\vec{F}' = \mathbf{A}\vec{F}$, we can find a unitary transformation matrix \mathbf{U} such that $\mathbf{U}^\dagger \mathbf{A} \mathbf{U}$ is diagonal. The transformed solution vector $\vec{G} = \mathbf{U}^\dagger \vec{F}$ can be written explicitly as

$$G_\nu = b_\nu e^{a_\nu R} \quad \nu = 0, 1, \dots, 2N-1, \quad (\text{C.20})$$

where a_i are the eigenvalues of \mathbf{A} . All the $2N$ linearly independent solutions which make up the solution matrices \mathbf{M}_1 and \mathbf{M}_2 can be obtained by letting $b_\nu = \delta_{\nu,\nu'}$ with $\nu' = 0, 1, \dots, 2N-1$.

In the full numerical results as shown in Sec. 3.2.2, we have found that for $J = 0^+$ the recombination rates are converged to 95% by including the lowest four continuum channels in the calculations. The convergence for higher partial waves calculations is even quicker. In Table C.1 we list the values of the $c_{\nu,\nu'}$ for the lowest five channels: We have calculated the recombination rates K_3 for $J = 0^+$ by including the lowest five adiabatic channels where we use $w_0^2 = -s_0^2 - 1/4$ and $w_\nu^2 = s_\nu^2 - 1/4$ ($\nu \neq 0$). We notice that these results are not sensitive to the choice of the values for w_ν^2 . The results are shown in Fig. 3.16.

To get a simple analytical expression for the energy-dependent oscillations seen in Sec. 3.2 by using a multi-channel approach, we include only the lowest two channels in our model.

The solutions in the transitional region Eq. (C.20) is further simplified and in the energy range of interest ($1/a \ll k \ll 1/r_0$), the w_ν s drop off the expression and the scattering matrix element $(S)_{12}$ which determines the probability of the recombination reduces to

$$(S)_{12} = \frac{e^{i\pi/4}(e^{4c\beta_1} - e^{4c\beta_2})}{2ie^{2c(\beta_1+\beta_2)} \cot(\phi_0 + s_1\pi/2) + e^{4c\beta_1} + e^{4c\beta_2}}, \quad (\text{C.21})$$

where $c = c_{12}$. This finally leads the expression for the three-body recombination rate in Eq. (3.28).